Risk-analysis of global climate tipping points

Umwelt Bundesamt

Risk-analysis of global climate tipping points

by

Katja Frieler, Malte Meinshausen, N. Braun, A. Golly, W. Hare, M. Mengel, K. van der Merwe, B. Poulter, M. Schaeffer, C.-F. Schleussner, T. Schneider von Deimling
PRIMAP Research Group, Potsdam Institute for Climate Impact Research e.V., Potsdam

On behalf of the German Federal Environment Agency

UMWELTBUNDESAMT

This publication is only available online. It can be downloaded from
http://www.uba.de/uba-info-medien-e/4354.html.

The contents of this publication do not necessarily
reflect the official opinions.

Impressum
PRIMAP Research Group, Potsdam Institute for Climate Impact Research e.V., July 2011
Project Lead: Katja Frieler, Malte Meinshausen
Special Honour Medal: A. Golly.
Researchers: K. Frieler, M. Meinshausen, N. Braun, A. Golly, W. Hare, M. Mengel, K. van der Merwe, B. Poulter, M. Schaeffer, C.-F. Schleussner, T. Schneider von Deimling

Table of Contents

Zusammenfassung

Zusammenfassung Kipppunkte des Klimasystems – Eine Risikoanalyse.

K. Frieler, M. Meinshausen, N. Braun, A. Golly, W. Hare, M. Mengel, K. van der Merwe, M. Perrette, M. Schaeffer, C.-F. Schleussner, T. Schneider von Deimling

Einleitung[1]

Von vielen Elementen des Erdsystems wird erwartet, dass sie sich mit zunehmender globaler Erwärmung stetig verändern. Diese graduellen Veränderungen könnten sich als reversibel erweisen, wenn die globale Erwärmung zurückgehen sollte. Andere Elemente des Klimasystems hingegen könnten ein Kippverhalten zeigen, bei dem relativ kleine Störungen des Hintergrundklimas ausreichen, um einen (abrupten) Wechsel vom Ausgangszustand in einen qualitativ völlig anderen Zustand auszulösen (2). Von vielen dieser möglichen Kippvorgänge wird erwartet, dass sie sich nicht einfach rückgängig machen lassen, indem die globale Erwärmung etwa von einem höheren auf das heutige Niveau zurückgeht. Das liegt vor allem daran, dass vielen dieser Kippelemente ein sich selbst-stabilisierender Prozess zu Grunde liegt. Wird dieser einmal unterbrochen, kippt das System in einen neuen, völlig andersartigen Zustand, der sich dann allerdings auch selbst intern stabilisiert.

Zu den gegenwärtig als potenzielle Kippelemente identifizierten Prozessen gehören die Masseverluste des grönländischen und westantarktischen Eisschildes, der Rückgang des arktischen Seeeises im Sommer, verschiedene Monsunsysteme, der Rückgang des Amazonasregenwaldes, der Biodiversitätsschwund in Korallenriffen, das Auftauen der Permafrostböden sowie die Freisetzung mariner Methanhydraten (3).

Allen Elementen gemein ist, dass von ihrem Kippen regionale bis globale Auswirkungen auf die menschliche Gesellschaft, die Biodiversität und / oder Leistungen des Ökosystems zu erwarten sind. Einige der aufgeführten Elemente haben zudem das Potential, durch ihr Kippen die globale Erwärmung über positive Rückkopplungsprozesse weiter zu beschleunigen.

---

[1] Die Arbeit an diesem Teil unseres UFOPLAN-Berichts wurde von M. Schaeffer und B. Hare durchgeführt.

Die nicht zu vernachlässigende Wahrscheinlichkeit des Kippens einiger dieser Elemente sowie die schwerwiegenden, zum Teil kaum absehbaren Folgen machen Kippprozesse zu Hochrisikoereignissen. Verschiedenste Möglichkeiten der Schadensvermeidung müssen bedacht werden. In vielen der aufgeführten Beispiele scheinen die Anpassungsmöglichkeiten jedoch begrenzt. So könnte die einzig verantwortungsvolle Strategie darin zu bestehen, das Eintreten des Kippens zu verhindern. Aufgrund des potentiell immensen Ausmasses möglicher Folgen, ist ein besseres Verständnis der inneren Dynamik dieser Systeme und der auslösenden Mechanismen unerlässlich. Die Liste der hier aufgeführten Kippelemente ist nicht vollständig. Zudem wird es wahrscheinlich noch nicht identifizierte Kippelemente geben, die möglicherweise sogar größere Risiken bergen. Diese könnten auch innerhalb unserer sozio-ökonomischen Systeme liegen. Hier beschränken wir uns allerdings auf die Betrachtung von physikalischen oder biologischen Kippelementen.

In den folgenden beiden Abschnitten werden wir zunächst zwei eher methodische Entwicklungen in Bezug auf die Projektion globaler Niederschlags- und regionaler Klimaänderungen vorstellen. Diese beiden Ansätze bilden die Grundlage für die nachfolgende Analyse großräumiger Klimafolgen wie die Masseverluste des Grönländischen Eisschildes, die Freisetzung von Treibhausgasen durch das Auftauen von Permafrostgebieten und die Bedrohung der Korallenpopulationen.

Methodische Basis I: Globale Niederschlagsänderungen[2]

Viele Folgen des Klimawandels gehen auf Niederschlagsveränderungen zurück. Sie stellen einen möglichen Auslöser von Kippprozessen dar. Der Masseverlust der Grönländischen Eisschildes etwa hängt nicht nur von der regionalen Erwärmung ab, die zu einer Verstärkung des Abschmelzens führt, sondern auch von regionalen Niederschlagsänderungen, die die Verluste durch Abschmelzen über eine zusätzliche Akkumulation von Eis zumindest innerhalb bestimmter Grenzen ausgleichen können. Obwohl regionale Niederschlagsänderungen ohne Zweifel die entscheidende Größe bei dieser Art der Analyse sind, lohnt sich auch ein Blick auf die Änderungen des global gemittelten Niederschlags. Sie bieten die Möglichkeit, wesentliche Einflussfaktoren, auch für regionale Niederschlagsveränderungen, zu identifizieren.

Generell wird erwartetet, dass die Niederschläge im globalen Mittel mit der Erwärmung zunehmen. Tatsächlich war 2010 nicht nur das bisher wärmste Jahr in den Beobachtungen (mit 2005), sondern auch das niederschlagreichste (National Oceanic and Atmospheric Administration (NOAA), Global Historical Climatology Network). Eine erste Erklärungsmöglichkeit für den Zusammenhang zwischen Temperaturen und Niederschlägen besteht darin, dass warme Luft

---

[2] Dieser Teil unseres UFOPLAN-Berichts ist inzwischen als Artikel veröffentlicht: K. Frieler et al. "Changes in Global-mean Precipitation in Response to Warming, Greenhouse Gas Forcing and Black Carbon", Geophysical Research Letters, Vol. 38, L04702, 5 pp., 2011.

mehr Feuchtigkeit aufnehmen kann als kalte. Modellsimulationen zeigen jedoch, dass die Änderungen des global gemittelten Niederschlags nicht allein von der Änderung der globalen Mitteltemperatur bestimmt werden. Vielmehr variiert die globale Hydrologische Sensitivität, d.h. die relative Änderung der globalen Niederschläge pro Grad globaler Erwärmung, mit dem betrachteten Emissionsszenario und auch im Zeitverlauf. Basierend auf den Simulationen von 20 gekoppelten Atmosphäre-Ozean-Klimamodellen und bis zu 7 verschiedenen Emissionsszenarien haben wir analysiert, bis zu welchem Grad diese Variationen durch Veränderungen im Treibhausgasforcing und Emissionen von Rußpartikeln erklärt werden können. Die Ergebnisse unserer Analyse stützen frühere Ergebnisse, dass durch die Absorption sowohl kurzwelliger als auch langwelliger Strahlung durch Rußaerosole und Treibhausgase die Niederschläge anfänglich zurückgehen, bevor sie mit der globalen Erwärmung zunehmen (*4-6*). Durch die Aufnahme dieser Absorber als erklärende Variablen in ein multivariates Regressionsmodell wird es möglich, die simulierten Variationen der hydrologischen Sensitivität sehr genau nachzubilden (siehe die durchgezogenen Linien in Abbildung 1). Der Regressionsansatz liefert eine Abschätzung des durch Treibhausgase verursachten von Temperaturveränderngen unabhängigen Effektes von -0.42 ± 0.23 %/(W/m^2) sowie des durch Rußemissionen [Mt/Jahr] induzierten Effektes von -0.07 ± 0.02 % / (Mt/Jahr). In Kombinationen mit diesen beiden zusätzlichen Prädiktoren ergibt sich ein langfristiger Effekt der globalen Temperaturänderung auf die globalen Niederschläge von 2.2 ± 0.52 % pro Grad globaler Erwärmung – ein deutlich geringerer Wert als die 6.5% / °C, die sich aus der Clausius Clapeyron-Beziehung zwischen der Temperatur und dem möglichen Feuchtegehalt der Luft ableiten lassen (*4, 7*). Im Ergebnis wurden also neben der Änderung der globalen Mitteltemperatur auch das troposphärische Treibhausgasforcing und Rußemission als wichtige Prädiktoren für die Änderung des globalen Niederschlagsmittels identifiziert. Über einen weiten Bereich von Simulationen unterschiedlicher Klimamodelle bieten sie eine konsistente Erklärung für die globalen Niederschlagsänderungen.
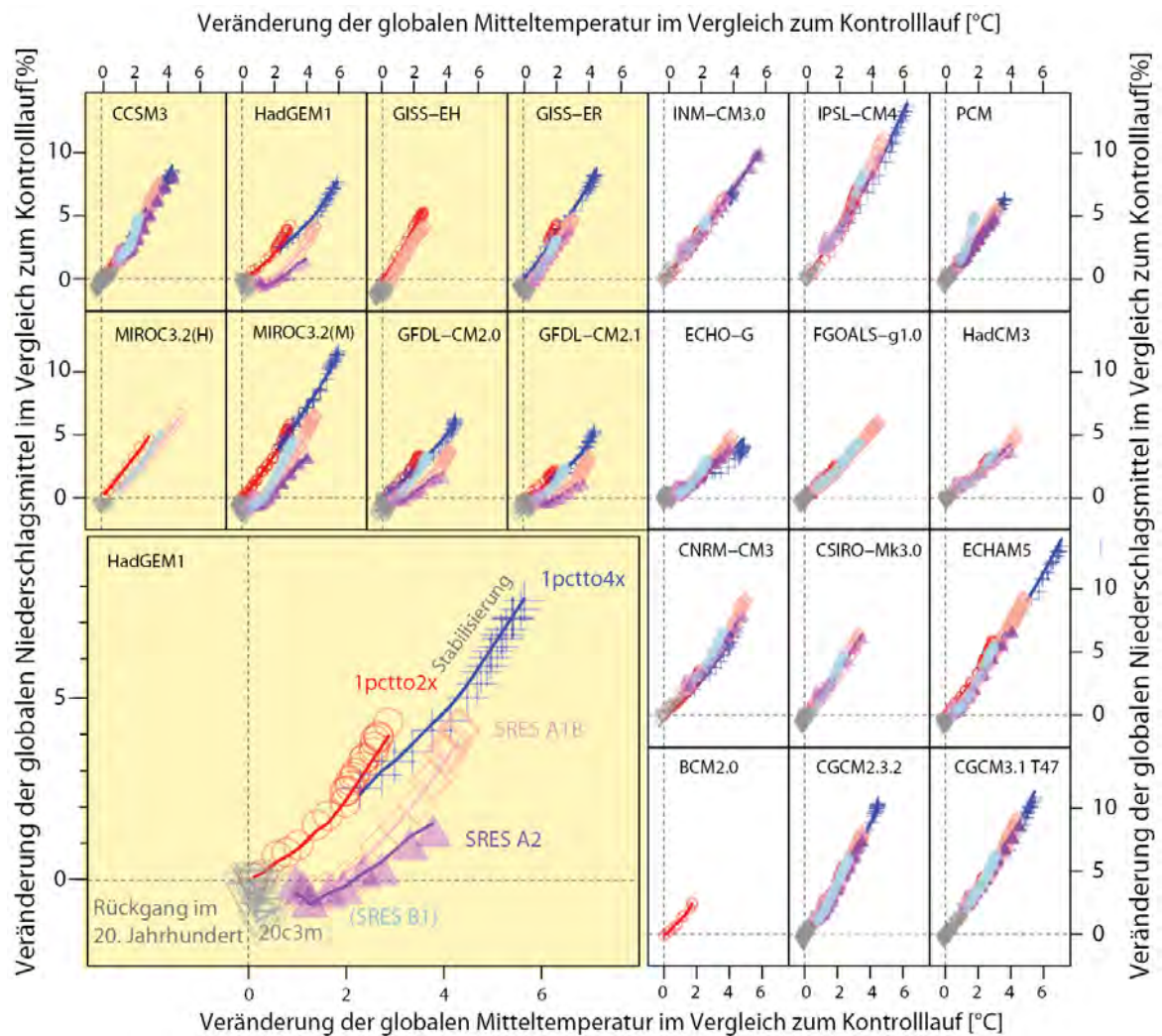
Abbildung 1 – Prozentuale Änderungen der global gemittelten Niederschläge in Abhängigkeit von Änderungen der globalen Mitteltemperatur. Verschiedenfarbige Symbole beziehen sich auf unterschiedliche Szenarien. Die Projektionen des statistischen Modells basierend auf den drei Prädiktoren globale Temperaturänderungen, Veränderungen im troposphärischen Treibhausgasforcing und Emissionen von Rußteilchen sind als durchgezogene Linien dargestellt. Die Klimamodelle, deren Simulationsergebnisse auf der linken Seite dargestellt sind (gelb schattierter Bereich), berücksichtigen Rußaerosole. Viele dieser Simulationen zeigen über das 20. Jahrhundert (graue Dreiecke) zurückgehende Niederschläge, während die Niederschläge in den

Zukunftsprojektionen zunehmen – ein Merkmal, das durch den Einfluss des troposphärischen Treibhausgasforcings und durch Aerosoleffekte erklärt werden kann.

Methodische Basis II: Probabilistische Projektionen regionaler Klimaveränderungen[3]

Auch wenn erwartet wird, dass die Niederschläge im globalen Mittel zunehmen, ist davon auszugehen, dass erhebliche regionale Unterschiede auftreten. So gibt es Gebiete, wie etwa den Mittelmeerraum, für die die globalen Klimamodelle übereinstimmend einen Rückgang der Niederschläge vorraussagen. In anderen Regionen sind die erwarteten Niederschlagszunahmen dagegen deutlich höher als im globalen Durchschnitt von 1-3% pro Grad globaler Erwärmung. Ganz ähnlich verhält es sich mit den regionalen Temperaturänderungen. So bedeutet etwa eine Begrenzung der globalen Erwärmung auf 2°C, dass die zu erwartende Erwärmung über Land durchaus höher, nämlich bei ungefähr 2.6 °C liegen könnte. Die Simulationen legen zudem nahe, dass die Erwärmung der Nordpolargebiete mit dem Grönländischen Eisschild und dem arktischen Meereis als besonders verwundbaren Elementen des Klimasystems noch deutlich stärker ausfallen könnte. Es ist gerade dieses regionale Muster der Klimaveränderungen, das sowohl für die Planung von Anpassungsmaßnahmen als auch für die Abschätzung des Kipppotentials bestimmter Elemente des Klimasystems entscheidend ist. Will man etwa analysieren mit welcher Wahrscheinlichkeit ein Kippen unter einem vorgegebenen globalen Emissionspfad auftritt, so ist dafür häufig auch eine probabilistische Projektion der auslösenden regionalen Klimaveränderungen eine wichtige Grundlage.

Derartige probabilistische Projektionen für verschiedenste Emissionsszenarien können nicht einfach auf Basis globaler Klimamodelle mit hoher räumlicher Auflösung durchgeführt werden[4]. Die Vielzahl benötigter Läufe würde zu viel Rechenzeit beanspruchen. Allerdings zeigen die vorhandenen Simulationen einen quasi linearen Zusammenhang zwischen der globalen Temperaturänderung und regionalen Temperatur- und Niederschlagsänderungen, der für die begrenzte Anzahl betrachteter Emissionsszenarien für viele Regionen kaum variiert (*1, 9, 10*). Probabilistische Projektionen der *globalen* Temperaturänderung können jedoch über vereinfachte Klimamodelle für unterschiedlichste Emissionspfade berechnet werden. Kombiniert man diese globalen Werte mit den entsprechenden regionalen Skalierungskoeffizienten, die wir aus den globalen Klimamodellen abgeleitet haben, wird es möglich, auch probabilistische Projektionen regionaler Klimaveränderungen zu liefern (zur Methode siehe Box 1).

---

[3] Dieser Teil der UFOPLAN-Berichts ist dokumentiert in dem Manuskript "A scaling approach to probabilistic assessment of regional climate change" von K. Frieler et al., das bei Drucklegung des Berichtes beim Journal of Climate eingereicht war.

[4] Eine erwähnenswerte Ausnahme bilden die viele tausend Löufe umfassenden Experimente des climateprediction.net Projektes (D. A. Stainforth *et al., Nature* **433** (2005).

In herkömmlichen Ansätzen wird dabei in der Regel nur die globale Temperaturänderung als erklärende Variable für regionale Klimaänderungen herangezogen. Da wir die Änderung im Strahlungshaushalt aufgrund von Treibhausgasen und Aerosolemissionen als zusätzliche Prädiktoren in ein multivariates Regressionsmodell miteinbeziehen kann jedoch die Reproduktion der Simulationsergebnisse globaler Klimamodelle, insbesondere bezüglich regionaler Niederschlagsvorhersagen, noch einmal erheblich verbessern. Obwohl die Emissionen von Sulfat-Aerosolen im Gegensatz zu Ruß-Aerosolen keinen großen Einfluss auf die simulierten globalen Niederschlagsveränderungen haben, wurden sie hier in das statistische Modell aufgenommen, da ihr Einfluss auf regionale Niederschlagsänderungen erheblich sein kann. Tatsächlich zeigt sich, dass diese zusätzlichen Prädiktoren eine mögliche Erklärung für die Variation der hydrologischen Sensitivität (relative Änderung der regionalen Niederschläge pro Grad globaler Erwärmung) von Szenario zu Szenario liefern. Insbesondere in Ostasien, wo die Niederschlagsveränderungen stark von hohen Aerosolemissionen beeinflusst zu sein scheinen, kann diese Variation der hydrologischen Sensitivität um mehr als 50% reduziert werden. Abbildung 3 zeigt die auf dem neuen statistischen Modell basierten probabilistischen Projektionen der Temperatur- und Niederschlagsänderung für verschiedene Weltregionen. Dabei wurden jeweils zwei unterschiedliche Emissionspfade vorgegeben. In Blau dargestellt sind die Projektionen unter Annahme starker Emissionsreduktionen (RCP3-PD-Szenario – siehe Referenzen zu RCP-Szenarien: (*11-13*)) während die Ergebnisse unter Annahme hoher „business as usual"-Emissionen (RCP8.5) in orange dargestellt sind. Die Abbildung zeigt deutlich den besonders starken Temperaturanstieg für die Nordpolarregion sowie die Niederschlagsabbnahme im Mittelmeerraum.

Box 1 – Projektion von regionalen Klimaänderungen
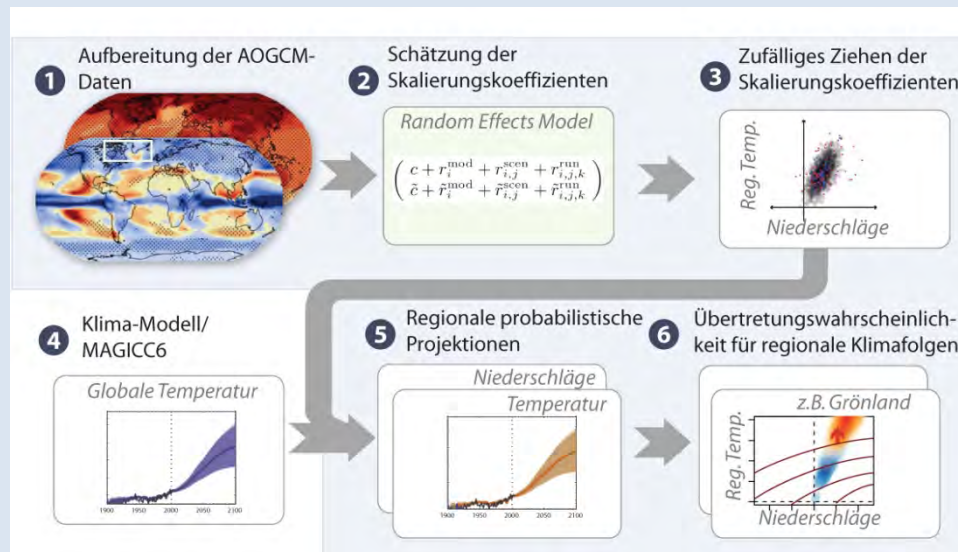
Abbildung 2 – Schematische Darstellung der verschiedenen analytischen Schritte auf dem Weg zu probabilistischen regionalen Klimaprojektionen. Nach der Aufbereitung der Simulationsergebnisse der globalen Klimamodelle (regionale/globale Mittelung etc.) (1) wird ermittelt, mit welchen Faktoren die globalen Temperaturveränderung multipliziert werden müssen, um die regionalen Klimaänderungen zu beschreiben (2). Aus der Variation dieser Skalierungskoeffizienten von Klimamodell zu Klimamodell ergibt sich eine Unsicherheitsverteilung der Koeffizienten. Aus dieser Verteilung werden anschließend zufällig Elemente gezogen (3) und mit Elementen aus der Unsicherheitsverteilung der globalen Temperaturentwicklung kombiniert (4), um so zu einer Unsicherheitsverteilung für die regionalen Temperatur- und Niederschlagsprojektionen zu kommen. Über diese zweidimensionalen Verteilungen wird es schließlich möglich, Überschreitungswahrscheinlichkeiten für bestimmte Impactschwellenwerte zu bestimmen. Die Abbildung zeigt als Beispiel eine Funktion, die den Masseverlust des Grönländischen Eisschildes beschreibt (6).

Abbildung 2 gibt einen Überblick über den neu entwickelten statistischen Ansatz zur Erzeugung probabilistischer regionaler Klimaprojektionen. Ähnlich zu bereits existierenden "Pattern-Scaling"-Ansätzen beruht diese Methode auf dem quasi-linearen Zusammenhang zwischen globalen Temperatur- und regionalen Klimaänderungen, wie er in vielen globalen Klimamodellen (AOGCMs) zu finden ist. Dieser lineare Zusammenhang ermöglicht eine Aufteilung der Frage nach probabilistischen regionalen Klimaprojektionen in zwei separate Teile: (1) Probabilistische Analyse der globalen Temperaturentwicklung unter Vorgabe eines beliebigen Emissionspfades, (2) probabilistische Analyse der regionalen Klimaänderungen unter Vorgabe einer globalen Temperaturänderung.

Die neue Methode zur Schätzung der Skalierungskoeffizienten hat drei wesentliche Vorteile gegenüber vorhanden Ansätzen: (1) Während auch in

anderen Studien, die Unsicherheit der Skalierungskoeffizienten aus der Variation der Skalierungskoeffizienten für unterschiedlichste Klimamodelle geschätzt wird, wird in dem neuen Ansatz zusätzlich die Korrelation zwischen temperatur- und niederschlagsbezogenen Unsicherheitskomponenten berücksichtigt. D.h., es wird der Tatsache Rechnung getragen, dass etwa Modelle, die einen besonders hohen Temperaturskalierungskoeffizienten aufweisen, möglicherweise auch hohe Niederschlagsskalierungskoeffizienten liefern oder anders herum. (2) Andere relevante Einflussgrößen wie etwa das Treibhausgasforcing und Aerosole können neben der globalen Temperaturänderung berücksichtigt werden. (3) Die Methode bietet die Möglichkeit, die Validität des Skalierungsansatzes zu überprüfen, d.h. die Annahme, dass die Skalierungskoeffizienten nahezu unabhängig vom betrachteten Szenario sind.
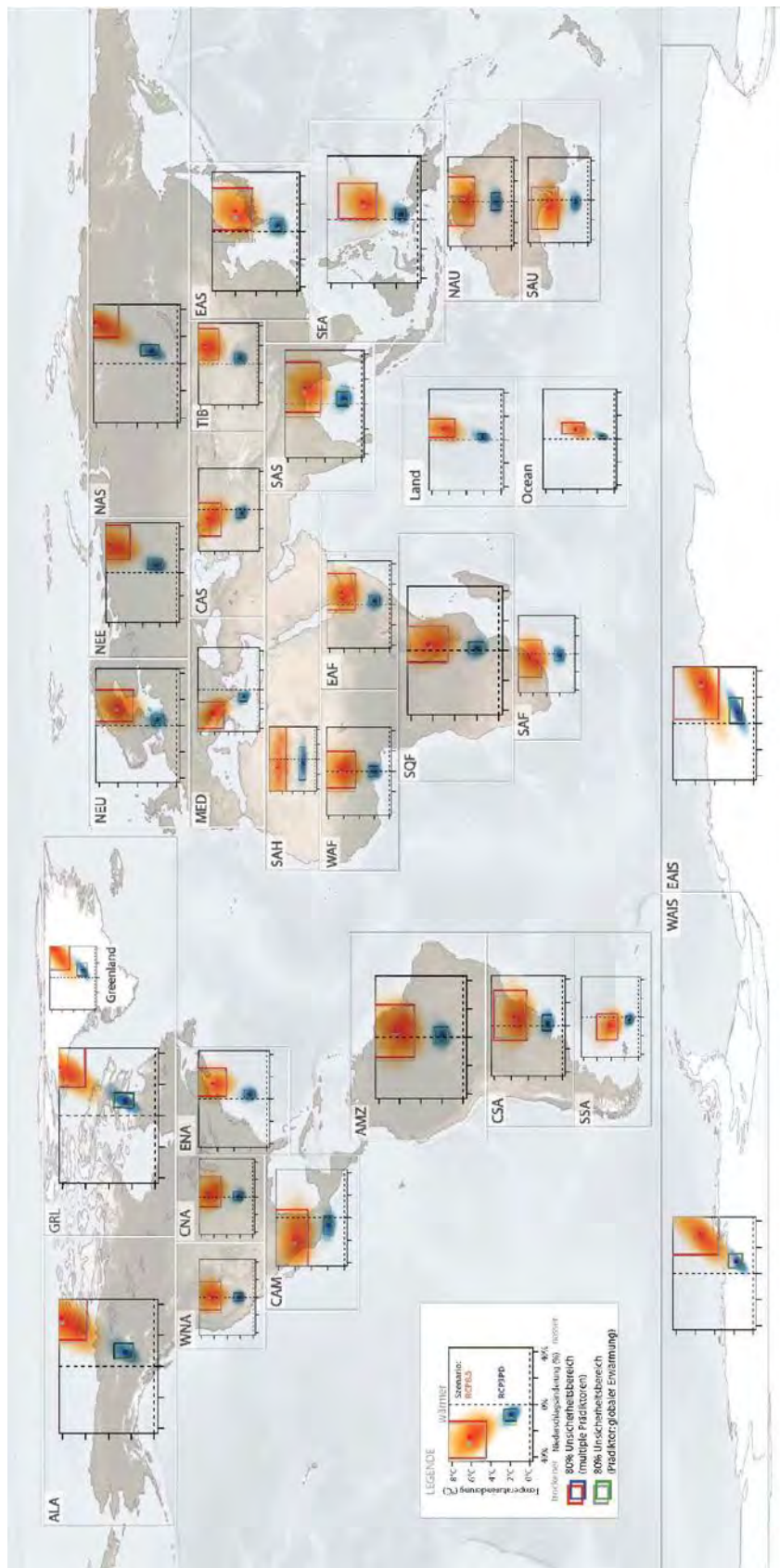
Abbildung 3 Zweidimensionale Unsicherheitsverteilung der regionalen Temperatur- und Niederschlagsänderungen für das Jahr 2100 unter dem niedrigen Emissionsszenario RCP3-PD in blau (Median der globalen Erwärmung im Jahr 2100: ≈ 1.5 °C) und dem hohen Emissionsszenario RCP8.5 in orange (Median der globalen Erwärmung im Jahr 2100: ≈ 5°C). Die Definition der Regionen geht auf Ref. (1) zurück und wurde lediglich ergänzt durch das West- und Ost-Antarktische Eisschild (WAIS and EAIS) getrennt durch die transantarktische Bergkette. (Hintergrund: NASA Blue Marble Bild nach R. Stöckli)

Folgen der Klimaveränderungen: Bedrohung der Korallenriffe, Rückgang der Permafrostgebiete und regionaler Meeresspiegelanstieg.

Aufbauend auf die in den beiden vorausgehenden Abschnitten vorgestellte methodische Vorarbeit steht im Folgenden die Analyse großräumiger Klimafolgen im Vordergrund, sowie die Wahrscheinlichkeit ihres Eintretens unter verschiedenen Erwärmungsszenarien.

Korallenriffe, die "Kanarienvögel des Klimasystems" werden wahrscheinlich schon in naher Zukunft, d.h. in ein oder zwei Jahrzehnten, gravierend geschädigt werden und in manchen Regionen ganz verschwinden. Der gegenwärtige Stand der Forschung legt nahe, dass zumindest die Hälfte der Korallenriffe den durch CO_2-Emissionen ausgelösten Veränderungen im Ozean nicht wird standhalten können. Auch die andere Hälfte scheint selbst bei sehr optimistischen Annahmen bezüglich ihre Toleranz gegenüber der Ozeanerwärmung nur unter den stärksten Reduktionsszenarien erhalten zu bleiben.

Nicht alle Kipppunkte liegen zeitlich in so naher Zukunft. Unsere Analyse zum Auftauen der Permafrostgebiete legt vielmehr nahe, dass sich dieser Prozess über Jahrhunderte erstrecken wird anstatt über Jahrzehnte.

In den abschließenden beiden Teilen unseres Forschungsprojektes geht es um den Anstieg des Meeresspiegels unter globaler Erwärmung. Dabei betrachten wir zum einen die mögliche Abschwächung der atlantischen Thermohalinen Zirkulation (*THC*)[5], die zu einem dynamisch bedingten Anstieg des Meeresspiegels an der nordamerikanischen Ostküste führen könnte.

Das dominante Problem, der „Gorilla im Zimmer", sind allerdings die Wassermassen, die im Grönländischen Eisschild oder im West-Antarktischen Eisschild gebunden sind und abzuschmelzen drohen. Das Schmelzen dieser Eisschilde würde den Meeresspiegel auf einer zeitlichen Skala von Jahrhunderten bis Jahrtausenden um mehrere Meter ansteigen lassen. Wir konzentrieren uns auf die Betrachtung des Grönländischen Eispanzers und insbesondere seiner Oberflächen-Massebilanz, wobei dynamische Eisverluste[6] ausgeklammert werden. Die Massebilanz an der Eisoberfläche kann als Indikator eines Kippprozesses betrachtet werden. Erreicht sie einen Wert von Null oder wird negativ (d.h., geht mehr Eis durch Abschmelzen verloren als durch die Akkumulation von Niederschlägen gewonnen wird), so wird das Grönländische Eisschild auf lange Sicht zum Großteil verschwinden. Ein Wiederaufbau ist nur unter deutlich kälteren Bedingungen als den heutigen möglich.

---

[5] Durch Temperatur- und Salzkonzentrationsunterschiede angetriebene Ozeanzirkulation. Sie führt Wassermassen oberflächennah von den Süd- bis in die Nordpolarregionen und als Tiefenwasser wieder zurück.
[6] Etwa durch ein beschleunigtes Abfließen der Eismassen über Gletscher.

Im letzten Kapitel werden alle potenziellen Beiträge zum Meeresspiegelanstieg aggregiert und in ein regionales Muster übersetzt. Mit besonders gravierenden Auswirkungen für die kleinen Inselstaaten und die Küstenlinien der Welt macht eine probabilistische Untersuchung der regionalen Meeresspiegelveränderungen deutlich, was auf dem Spiel steht, wenn Kipppunkte in Bezug auf die großen Eisschilde überschritten werden. Aufgrund der Trägheit der Prozesse können diese Meerespiegelveränderungen zumindest auf einer Zeitskala von Jahrhunderten als irreversibel betrachtet werden.

Korallenriffe: Die Kanarienvögel des Klimasystems[7]

Besonders hohe Wassertemperaturen stellen einen der dominierenden Stressfaktoren für Korallenriffe dar. Korallen leben in einer engen Symbiose mit bestimmten Algenarten (*Dinoflagellaten*), die ihnen ihre Farbe verleihen. Akkumulierter Hitzestress führt zum Verlust der Photosynthesefähigkeit des Gastes und schließlich zum Zusammenbruch der Symbiose der Korallen mit den Dinoflagellaten. Diese sogenannten Bleichungsereignisse können zu einem Sterben der Korallen führen, wenn sie mit einer Häufigkeit erfolgen, die eine Regeneration der Symbiose verhindert. Bisherige Zukunftsprojektionen zum Auftreten von Bleichungsereignissen waren auf die Analyse einzelner IPCC-Emissionsszenarien begrenzt und beruhten nur auf den Temperaturprojektionen einzelner Klimamodelle (*14*). In diesem Abschnitt diagnostizieren wir den kumulativen Temperaturstress in Form von „Hitze-Monaten" (DHMs)[8] an 2160 verschiedenen Korallenriffpunkten und leiten einen funktionalen Zusammenhang zwischen der Häufigkeit von Bleichungsereignissen und der globalen Erwärmung ab. Dabei werden die Simulationen von 19 gekoppelten IPCC-Klimamodellen berücksichtigt. Basierend auf früheren Studien wird eine zur Regeneration erforderliche Erholungszeit von 5 Jahren zwischen schweren Bleichungsereignissen (DHM>2°C*Monat) angenommen (*16*). Bei häufigerem Auftreten starker Erwärmungen ist anzunehmen, dass die Korallen dem thermischen Stress nicht standhalten können. Unsere Ergebnisse legen nahe, dass die globale Erwärmung auf 1.2°C (Unsicherheitsbereich: 1.1-1.4°C) gegenüber dem vorindustriellen Niveau begrenzt werden muss, um zumindest 50% der Korallenriffe zu schützen. Selbst unter dem stärksten Emissionsreduktionsszenario, das gegenwärtig vom IPCC betrachtet wird, ist aufgrund unserer Analyse zu erwarten, dass 72% (46-89%) der betrachteten Korallengitterzellen bis 2030 von schweren Langzeitschäden betroffen sein werden. Eine mögliche Anpassung der Korallen an veränderte Temperaturbedingungen könnte den Bereich der tolerierbaren Erwärmung

---

[7] Dieser Teil der UFOPLAN-Arbeit ist dokumentiert in dem Manuskript "80% of coral reefs at risk of disappearance already at 1.5°C global warming levels" von K. Frieler et al., das bei Drucklegung des Berichtes vor der Einreichung an eine internationale wissenschaftliche Fachzeitschrift stand.

[8] Dabei wird davon ausgegangen, dass eine Stresssituation für Korallen eintritt, wenn die mittlere Temperatur eines Monats die über eine Referenzperiode (1980-1999) gemittelten höchsten Monatsmitteltemperaturen eines Jahres übersteigt. Anhand von Beobachtungsdaten konnte auf dieser Basis ein Indikator (DHM) entwickelt werden, der es erlaubt Bleichungsereignisse zu projizieren (O. Hoegh-Guldberg, *International Coral Reef Symposium* (October 23-27, 2000, Bali, Indonesia, 2001).

ausdehnen und den Bereich der langfristig geschädigten Gebiete unter gleichzeitiger Annahme starker Emissionsreduktionen (RCP3-PD-Szenario mit einer maximalen globalen Erwärmung von 1.7 °C) auf 31% (9-60%) beschränken. Allerdings gibt es Hinweise darauf, dass der Temperaturschwellenwert für Bleichungsereignisse auch von der Ozeanversauerung abhängen könnte (*17*). Eine mit zunehmender Versauerung abnehmende Aragonite-Sättigung könnte demnach den Temperaturtoleranzwert für Bleichungsereignisse herabsetzten. Dies könnte bis 2030 zu einem Verlust von 86% (67-96%) der Korallen weltweit unter dem RCP3-PD-Szenario führen. Unter allen weiteren vom IPCC betrachteten höheren Emissionsszenarien erscheinen die Temperaturverläufe und chemischen Bedingungen ein Überleben der Korallen unwahrscheinlich zu machen – sollte sich die thermische Toleranz der Korallen nicht als höher als bisher bekannt herausstellen.
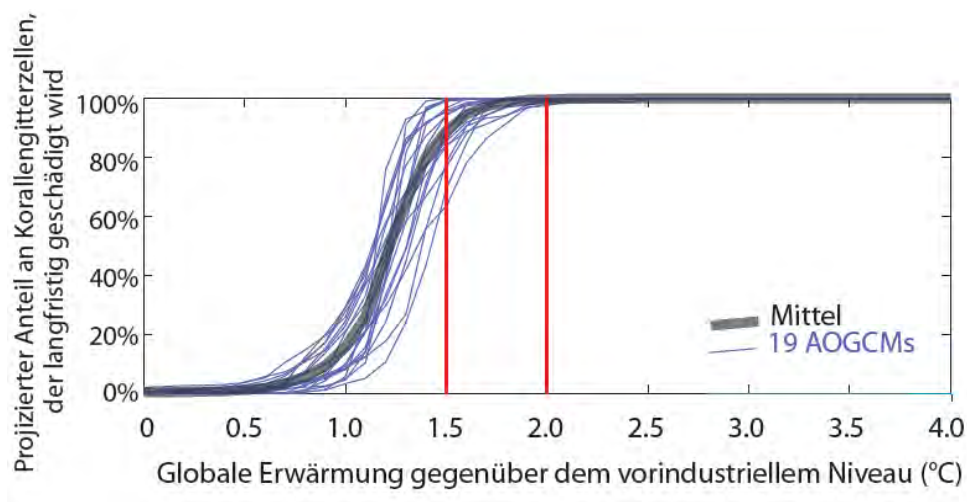
Abbildung 4 – Anteil der weltweiten Korallenriffe, der aufgrund von zu häufigen Bleichungsereignissen schwer geschädigt werden könnten. Der graue breite Streifen beschreibt das Mittel über die verschiedenen Klimamodelle. Dieser Mittelwert legt nahe, dass schon bei einer Zunahme des globalen Temperaturmittels von 2°C praktisch alle Korallenriffe mit Umweltbedingungen konfrontiert sein könnten, die schlussendlich zu ihrem Verschwinden führen könnten. Selbst bei 1.5°C globaler Erwärmung könnten sich bereits 90% der heutigen Korallengebiete von schweren langfristigen Schäden betroffen sein.
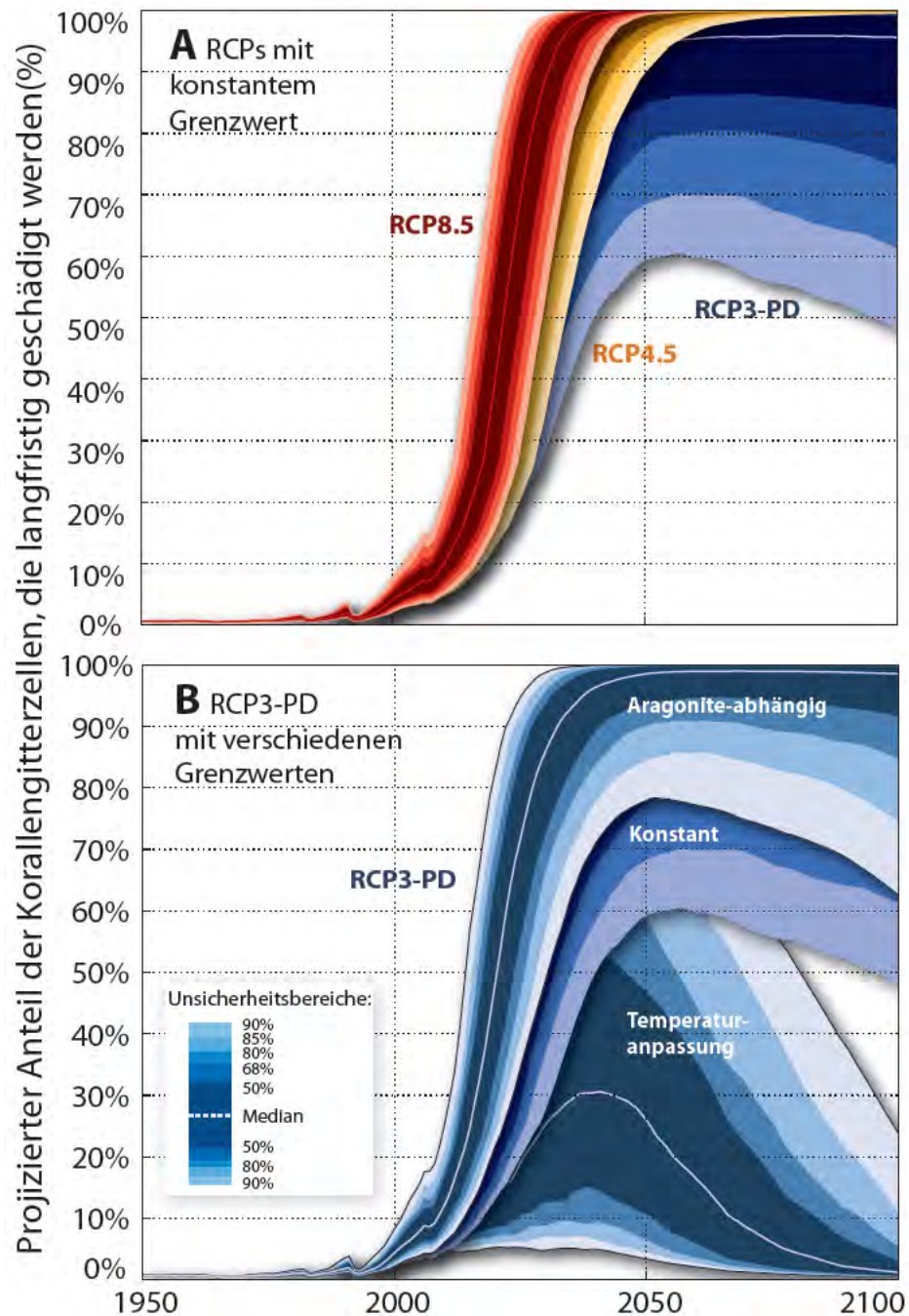
Abbildung 3 – Projektion der langfristigen Schädigung von Korallenriffen unter den "Representativen Emissionspfaden" (RCPs, siehe (11-13)). Grundlage der Berechnungen ist die Annahme, dass Korallen auf lange Sicht einem Hitzestress von 2°C*Monaten auf der Hitze-Monate-Skala nicht gewachsen sind, wenn diese Stressereignisse öfter als einmal in 5 Jahren auftreten. Selbst unter der Annahmen, dass sich die Korallen in einem gewissen Rahmen an die Ozeanerwärmung anpassen können, wären unter dem strengsten Emissionsreduktionsszenario, das gegenwärtig vom Weltklimarat betrachtet wird (RCP3-PD, Abbildungsteil B), ein Drittel der Korallen schon vor 2050

langfristig geschädigt. Schon unsere Standardannahme eines konstanten Temperaturschwellenwertes für das Auftreten von Bleichungsereignissen könnte sich allerdings als zu optimistisch erweisen, da sie mögliche Effekte der Ozeanversauerung nicht berücksichtigt (obere Trajektorie in Abbildungsteil B)

Permafrost: Ein langsam erwachender Riese[9]

Das Auftauen der Permafrostgebiete und die damit verbundene Freisetzung von Kohlendioxid und Methan stellt einen positiven Rückkopplungsmechanismus für das Klimasystem dar. Durch die anthropogenen Treibhausgasemissionen erwärmt sich das Klima, wodurch zusätzlicher Kohlenstoff – welcher bisher in Permafrostböden gebunden war – in Form von Treibhausgasen freigesetzt wird. Bisher hat eine Vielzahl unterschiedlicher Faktoren eine Quantifizierung dieser Rückkopplung verhindert. Der Prozess wird in den Klimamodellen der CMIP3-Generation und den Modellen zum Kohlenstoffkreislauf der C^4MIP-Generation, welche der Erstellung des vierten Weltklimaberichts als Modellgrundlage dienten, nicht berücksichtigt. Beträchtliche Unsicherheiten bestehen hinsichtlich der Geschwindigkeit und des Ausmaßes des Permafrost Auftauens, sowie in Bezug auf die resultierenden Veränderungen der Bodenhydrologie und Vegetationsbedeckung. Ebenso unsicher sind die Zeitskalen für den Abbau des frisch aufgetauten organischen Materials sowie der Anteil des Kohlenstoffs, welcher als CO_2 über aerobe (unter Beteiligung von Sauerstoff) Verfallsprozesse oder als Methan über anaerobe (unter Ausschluss von Sauerstoffzufuhr) Zerfallsprozesse freigesetzt wird. Hinzu kommt, dass der Grad der Verstärkung der globalen Erwärmung in hohen Breiten (Ausmaß der Erwärmung in hohen Breiten pro Grad globaler Erwärmung) unsicher ist. Eine weitere Rolle spielen die ausgeprägte und nur unzureichend erfasste Heterogenität der Bodenbeschaffenheit, des Kohlenstoffgehalts und der Hydrologie.

In der hier vorgestellten Studie koppeln wir ein Permafrostmodul an ein vereinfachtes Kohlenstoffkreislauf – Klimamodell. Dies erlaubt uns, ein großes Ensemble von Simulationen zu rechnen, wobei den oben erwähnten Unsicherheiten Rechnung getragen wird. Die Ergebnisse liefern Abschätzungen der möglichen Stärke der Permafrost-Kohlenstoff Rückkopplung. Für das hohe „Weiter-so" Emissionsszenario RCP8.5 werden bis zum Jahre 2100 zusätzliche 12-52 PgC (Petagramm Kohlenstoff) vorausgesagt (68% Unsicherheitsbereich). Dieser Betrag entspricht 3-11% der Netto-CO_2-Emissionen aus der Rückkopplung des terrestrischen Kohlenstoffkreislaufs und führt zu einer zusätzlichen Erwärmung von 0.02-0.11°C. Über das 21. Jahrhundert sind die geschätzten zusätzlichen Emissionen noch relativ moderat. Im weiteren Verlauf bis 2300 führt das Auftauen des Permafrosts und die langsame aber stetige Freisetzung

---

des im Boden gebundenen Kohlenstoffs zu einem deutlich höheren Beitrag. Bis zu diesem Zeitpunkt könnte mehr als die Hälfte des potenziell freisetzbaren Kohlenstoffs, der in den oberen 3 m der Permafrostböden gespeichert ist (600-1000PgC (*18*)), in Form von CO_2 freigesetzt sein und weitere 1-3% in Form von Methan. Unsere Ergebnisse legen nahe, dass Emissionsreduktionen in Übereinstimmung mit dem RCP3-PD-Szenario dafür sorgen können, dass der Temperaturanstieg in der Arktis hinreichend beschränkt werden könnte, um das Auftauen der Permafrostgebiete auf 15-30% zu begrenzen. In diesem Fall erreicht der zusätzliche Kohlenstoff induzierte Temperaturanstieg in unseren Simulationen nicht mehr als 0.01-0.07°C bis 2300.
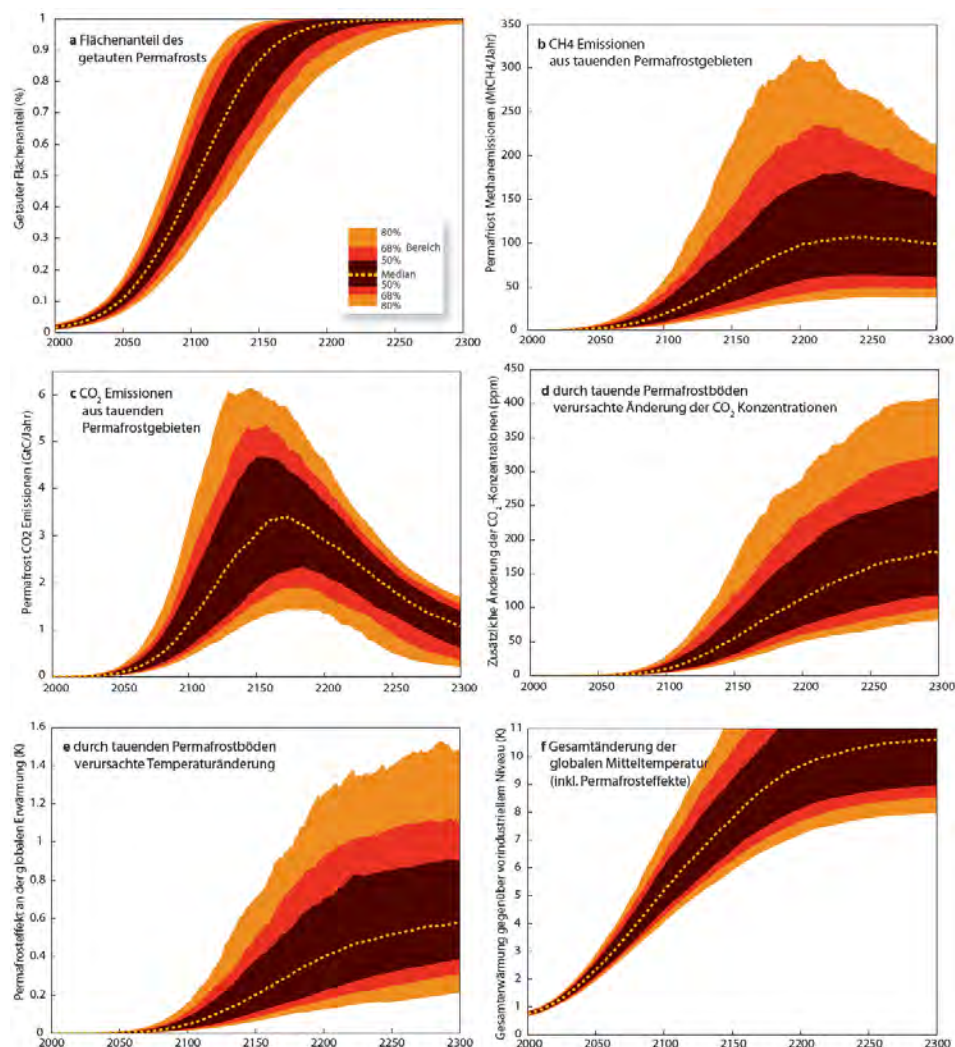

Abbildung 4 – Geschätzte Unsicherheitsbereiche für den Anteil des aufgetauten Permafrostbodens (a), die zugehörigen Methan- (b) und CO_2-Emissionen (c), die durch das Auftauen verursachte zusätzliche CO_2-

Konzentrationsänderung (d) und die entsprechende zusätzliche Erwärmung (e), sowie die gesamte anthropogen verursachte globale Erwärmung (f). Die Ergebnisse basieren auf einer Analyse des RCP8.5-Szenarios. Die Unsicherheitsabschätzung beruht auf einem Ensemble von 600 Simulationen bei denen die wichtigsten Parameter des Klimamodells sowie des neu entwickelten Permafrostmoduls innerhalb ihrer Unsicherheiten variiert wurden.

Ein einschlafender Riese: Die Abschwächung der Thermohalinen Zirkulation im Nordatlantik[10]

Die Thermohaline Zirkulation im Nordatlantik (THC) ist Teil des globalen Ozeanzirkulationssystems. Ihr kommt eine Schlüsselfunktion im globalen Klimasystem zu. So wird über diese Ozeanströmung ungefähr ein 1 PW (1 Petawatt = 10^{15} Watt) an Wärme in hohe nördliche Breiten transportiert, die zu dem relativ milden Klima in Nord-West-Europa beiträgt. Eine Abschwächung der THC, wie sie mit zunehmender globaler Erwärmung vorausgesagt wird, hat mit hoher Wahrscheinlichkeit starke Auswirkungen auf das globale Klimasystem (*19, 20*). Probabilistische Projektionen dieser Abschwächung, die nicht nur Mittelwerte sondern auch die entsprechenden Unsicherheitsbereiche beinhalten, sind deshalb von besonders großem Interesse nicht nur für die Wissenschaft, sondern auch für die Politik.

Für das Emissions-Reduktionsszenario RCP3-PD mit einer mittleren globalen Erwärmung von weniger als einem Grad bis 2100 gegenüber dem Jahr 2000 (ca. 1.5°C gegenüber vor-industriellem Niveau) liefert unsere Analyse des THC-Verhaltens eine mittlere Abschwächung von 11% über das 21. Jahrhundert. Im Vergleich: unter dem RCP4.5-Szenario mit einer mittleren globalen Erwärmung von 1.9°C im Verlauf des 21. Jahrhunderts (2.4°C im Vergleich zum vor-industriellen Niveau), erwarten wir eine Abschwächung von ca. 22% im Mittel. Zusätzliche Frischwassereinträge von 10 bzw. 20 cm Meeresspiegel-Äquivalent durch das Abschmelzen des Grönlandeises würden die THC um weitere 4.5% bzw. 10% abschwächen. Diese Verlangsamung der Ozeanströmung hat Einfluss auf den Meeresspiegel an der Ostküste der USA sowie in Europa und führt dort zusätzlich zum mittleren erwärmungsbedingten Meeresspiegelanstieg zu einer dynamisch bedingten Zunahme. Durch die Kopplung unserer Projektionen der THC-Abschwächung mit den Ergebnissen einer multi-Modellstudie zum Meeresspiegelanstieg (*21*) wurde es möglich, den dynamisch bedingten Meeresspiegelanstieg entlang der New Yorker Küste abzuschätzen. Für das 21. Jahrhundert liegen die vorausgesagten Werte bei 4 cm unter dem RCP3-PD und bei 8 cm unter dem RCP4.5-Szenario. Schließt man auch den durch thermische

[10] Dieser Teil unserer Arbeit ist dokumentiert in: "Emulating Atlantic overturning strength for low emission scenarios: consequences for sea-level rise along the North American east coast", C.F. Schleussner et al., Earth System Dynamics Discussions, www.earth-syst-dynam-discuss.net/1/357/2010/.

Expansion bedingten Meeresspiegel in die Abschätzung ein, so ergibt sich unter dem RCP3-PD-Szenario ein Gesamtanstieg von 24 cm für New York City im zeitlichen Verlauf bis 2100 (Abbildung 7b). Dies kann als eine untere Abschätzung des regionalen Meeresspiegelanstiegs verstanden werden, da mögliche Effekte durch das Abschmelzen des Grönlandeises und des Antarktischen Eisschildes in dieser Rechnung nicht berücksichtigt wurden.
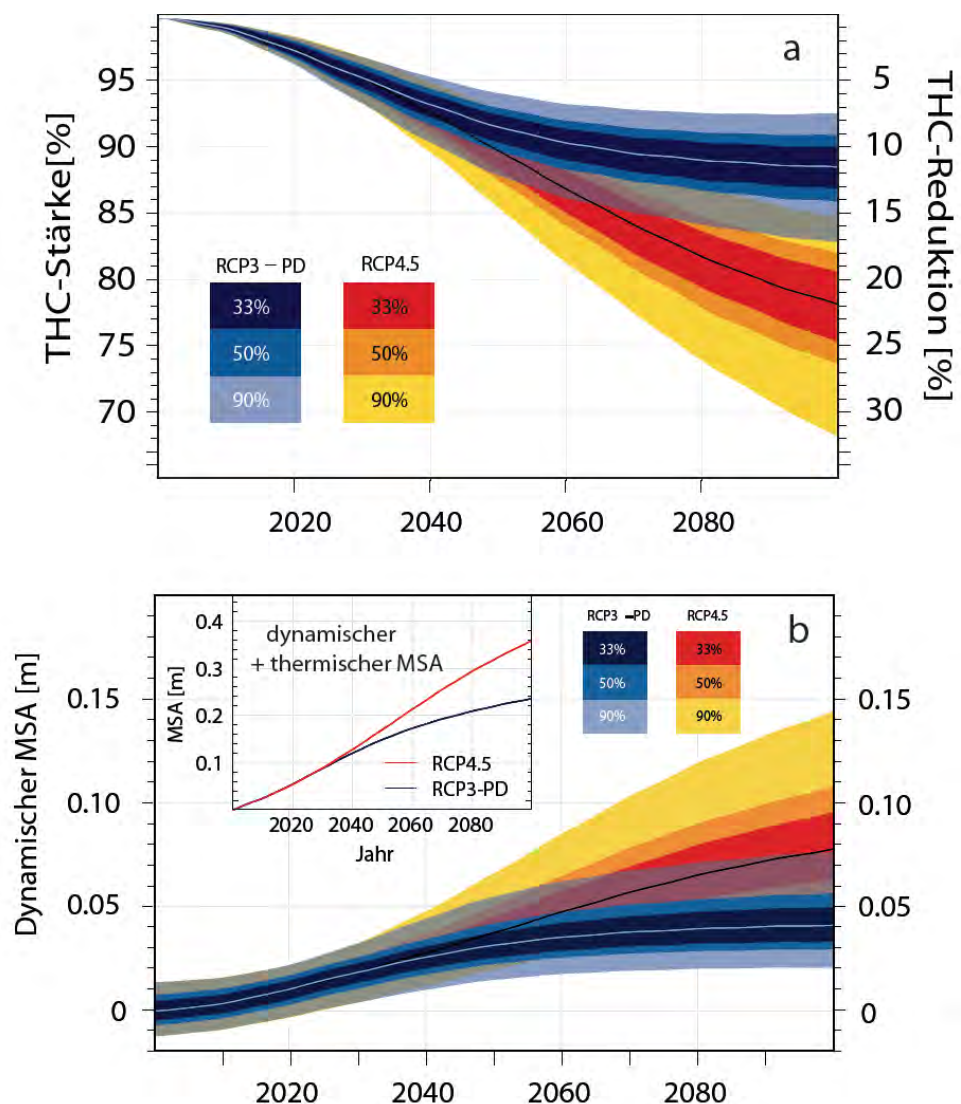
Abbildung 5 - a) Probabilistische Projektionen der THC-Abschwächung für zwei relativ niedrige Emissionsszenarien, das RCP3-PD-Szenario in blau und das RCP4.5-Szenario in rot/gelb. Die Farbschattierungen beschreiben jeweils die inneren 33, 50 und 90% der Unsicherheitsverteilung. b) Projektionen des entsprechenden dynamisch induzierten Meeresspiegelanstiegs. Kleiner Graph: Abschätzung der Summe aus der sterischen (durch thermische Expansion bedingten) und der dynamischen Komponente des mittleren

Meeresspiegelanstiegs an der New Yorker Küstenlinie durch die Kombination unserer Abschätzungen mit Ergebnissen von (*22*).

Grönlands Oberflächen-Massebilanz[11]

Das Abschmelzen und der substanzielle Rückgang des Grönländischen Eisschildes können einen wesentlichen Anteil am Meeresspiegelanstieg haben. Würde das gesamte Eisschild vollständig verschwinden, steigt der globale Meeresspiegel um 6 bis 7 m an. Die Massenbilanz des Eisschildes wird vom Abschmelzen des Eises, der Akkumulation durch Niederschläge und den Abfluss von Eis ins Meer bestimmt. Wenn mehr Eis schmilzt oder der Abfluss von Eis sich beschleunigt, und die Verluste nicht durch zunehmende Niederschläge ausgeglichen werden, steigt der Meeresspiegel. In diesem Abschnitt betrachten wir nur die Oberflächen-Massenbilanz und klammern dynamische Verluste durch die Beschleunigung des Eisabflusses und das Abschmelzen von unten (basales Schmelzen) aus. Änderungen der Oberflächen-Massenbilanz durch oberflächliches Schmelzen oder die Akkumulation von neuem Eis durch Niederschlagsänderungen allein können bereits Hinweise auf das Kipppotenzial des Grönländischen Eisschildes liefern: Erreicht die Oberflächen-Massenbilanz einen Wert von Null, können die anderen Verluste über den dynamischen Abfluss von Eis und basales Schmelzen nicht mehr ausgeglichen werden. Auf lange Sicht, d.h. über hunderte oder tausende von Jahren, würde das Grönländische Eisschild verschwinden. Wir kombinieren hier die Ergebnisse von zwei verschiedenen Modellen (*23, 24*) zur Beschreibung der Oberflächen-Massenbilanz, um die Wahrscheinlichkeit abzuschätzen, mit der diese Nulllinie unterschritten wird. Erreicht die globale Erwärmung 4°C, so ist es sehr wahrscheinlich, dass dieser Kipppunkt überschritten wird und ein irreversibler Auflösungsprozess des Grönländischen Eisschildes in Gang gesetzt wird. Aber schon bei einer deutlich geringeren globalen Erwärmung von 2.3°C liegt diese Wahrscheinlichkeit bei immerhin 20% (siehe Abbildung 8).

[11] Dieser Teil des UFOPLAN-Berichts ist dokumentiert in der Diplomarbeit von N. Braun, beaufsichtigt u.a. durch M. Meinshausen and B. Hare.
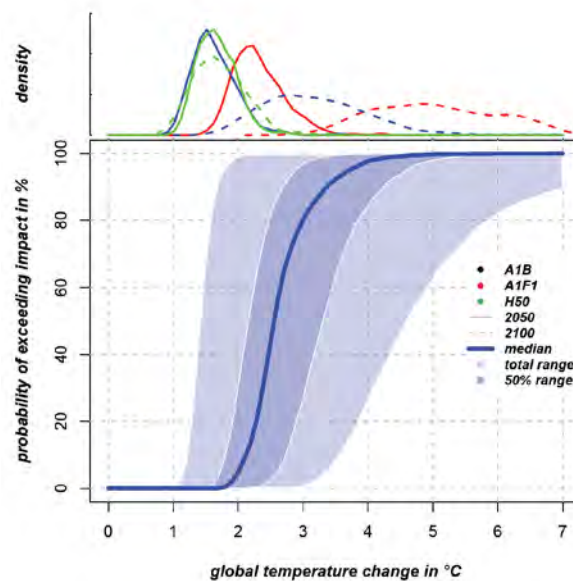
Abbildung 8 – Die Wahrscheinlichkeit, dass die Oberflächen-Massenbilanz Grönlands negativ wird - unter den Annahmen der in Ref. (23) beschriebenen „Methode 1". Der hellblau schattierte Bereich in der unteren Teilabbildung beschreibt die durch unterschiedliche Klimaprojektionen verursachte Streuung. In einem Erwärmungsbereich von 1.4 bis 4.6°C könnte der Kipppunkt mit einer Wahrscheinlichkeit von 50% überschritten werden. Die obere Teilabbildung zeigt geschätzte globale Erwärmungsniveaus für das IPCC SRES A1B und A1FI-Szenario (25) sowie ein Szenario, in dem die globalen Emissionen bis 2050 halbiert werden.

Regionaler Meeresspiegelanstieg[12]

Bei Projektionen des Meeresspiegelanstiegs werden häufig nur Änderungen im globalen Mittel betrachtet oder regionale Muster untersucht, die auf einzelne beitragende Komponenten zurückgehen. Hier bieten wir eine probabilistische Abschätzung, die alle Komponenten umfasst. Eine weitere Neuerung ist, dass wir den regionalen Meeresspiegelanstiegs erstmals probabilistisch für die neuen „Repräsentativen Emissionspfade" (RCPs) (*11-13*) prognostizieren. Dabei werden Projektionen des globalen Meerespiegelanstiegs in die einzelnen Beiträge, hauptsächlich thermische Expansion und Verluste von verschiedenen Landeis-massen aufgeteilt. Die zugehörigen räumlich aufgelösten Änderungsmuster (sog. Fingerabdrücke) des Meerespiegels werden entsprechend skaliert und zu einem Gesamtbild des regionalen Meeresspiegelanstiegs zusammengefügt. Während die Beiträge durch thermische Expansion und das Abschmelzen von Gletschern direkt berechnet werden, ergeben sich die Anteile des Antarktischen und Grönländischen Landeises (einschließlich der zugehörigen Gletscher)

---

[12] Dieser Teil der Arbeit ist dokumentiert in dem Manuskript "Probabilistic projections of regional sea-level rise" von M. Perrette et al., das bei Drucklegung des Berichtes vor Einreichung bei einer internationalen Fachzeitschrift stand.

anschließend aus der Differenz des globalen Meeresspiegelanstieg und der ersten beiden Beiträge. Im „Standardfall" beruhen die globalen Projektionen auf einem semi-empirischen Ansatz (*26*). Insgesamt zeigen die Muster einen verstärkten Anstieg des Meeresspiegels in niedrigen Breiten, da die Eisschilde in polaren Breiten an Masse und damit an Anziehungskraft verlieren. Außerdem unterscheiden sich die Anstiege auch zonal. So ist auf gleicher Breite der Meeresspiegelanstieg entlang der Chinesischen Küste um 20% stärker als entlang der europäischen Küste. Veränderungen der Ozeandynamik spielen in diesem Kontext nur eine untergeordnete Rolle. Sie verstärken einen Ost-West-Gradienten des Meeresspiegelanstiegs im Pazifik und steigern den Meeresspiegelanstieg im Indischen Ozean. Die dynamischen Veränderungen haben jedoch einen wesentlichen Anteil an der Unsicherheit der Projektionen.
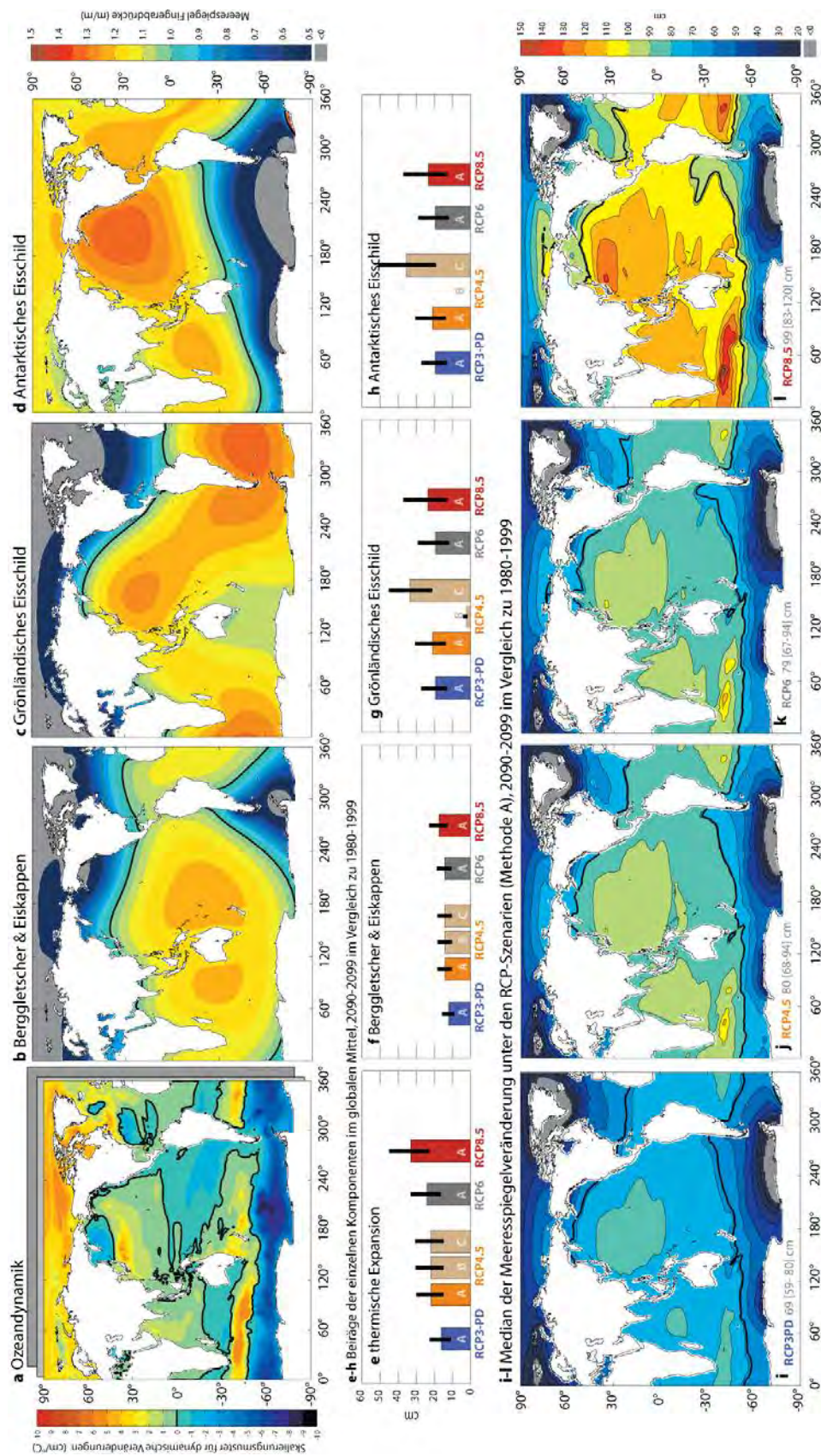
Wir vergleichen unsere „Standard-Abschätzungen" mit Mustern, die sich unter geänderten Annahmen über den Beitrag der Eisschilde zum globalen Meeresspiegelanstieg ergeben. Dazu nutzen wir die im IPCC AR4 (*27*) benutzte Abschätzung sowie eine „obere" Abschätzung, die auf Maximalannahmen an den Eisabfluss über Gletscher zurückgeht (*28*). Die im IPCC-Bericht vorgestellte regionale Verteilung des Meeresspiegelanstiegs wird in erster Linie durch Änderungen in der Ozeandynamik und die Masseverluste an Gletschern in hohen Breiten verursacht, während die großen Eisschilde über das 21. Jahrhundert nur einen geringen Beitrag liefern. Im anderen Fall, unter der „oberen" Abschätzung für den Anteil der Eisschilde am globalen Meeresspiegelanstieg, sind die regionalen Muster sehr ähnlich zu unserem „Standardfall". Betrachtet man die gegenwärtig beobachtete Beschleunigung der Massenverluste, so kann das Eintreten der „oberen" Abschätzung nicht ausgeschlossen werden (*28*). Unsere Studie ist der erste Schritt in Richtung einer probabilistischen Projektion der regionalen Meeresspiegeländerungen, basierend auf globalen Größen und den regionalen Mustern der einzelnen Komponenten. Die Abschätzungen können leicht aktualisiert werden, wenn etwa neue Erkenntnisse zum Beitrag der Landeismassen verfügbar werden, die die beobachteten Masseverluste besser repräsentieren.

Abbildung 9 (Nächste Seite) – Obere Reihe: Meeresspiegel-Fingerabdrücke (regionaler Meeresspiegelanstieg pro global gemitteltem Beitrag aus derselben Quelle (b-d) bzw. pro Grad globaler Erwärmung (a)) für sterische Expansion (a), Gletscher (b), Antarktis (c) und Grönland (d). Mittlere Reihe: Beitrag der einzelnen Komponenten zum globalen Meeresspiegelanstieg unter verschiedenen Annahmen an den globalen Meeresspiegelanstieg (A: semi-empirische Methode, B: IPCC-AR4, C: high-end Abschätzung für Anteil der Eisschilde). Untere Reihe: Räumlich aufgelöste Projektionen des Meeresspiegelanstiegs unter den verschiedenen Emissionsszenarien.

a Ozeandynamik

b Berggletscher & Eiskappen

c Grönländisches Eisschild

d Antarktisches Eisschild

e–h Beiträge der einzelnen Komponenten im globalen Mittel, 2090-2099 im Vergleich zu 1980-1999

e thermische Expansion

f Berggletscher & Eiskappen

g Grönländisches Eisschild

h Antarktisches Eisschild

i–l Median der Meeresspiegelveränderung unter den RCP-Szenarien (Methode A), 2090-2099 im Vergleich zu 1980-1999

i RCP3PD 69 [59–80] cm

j RCP4.5 80 [68–94] cm

k RCP6 79 [67–94] cm

l RCP8.5 99 [83–120] cm

Meeresspiegel Fingerabdrücke (m/m)

Skalierungsmuster für dynamische Veränderungen (cm/°C)

Globale Mittel

Melbourne   Kappstadt   Tuvalu   Hong Kong   Lissabon
             Mauritius   Golf von Bengalen   New York
                          Malediven   Tokyo   Vancouver
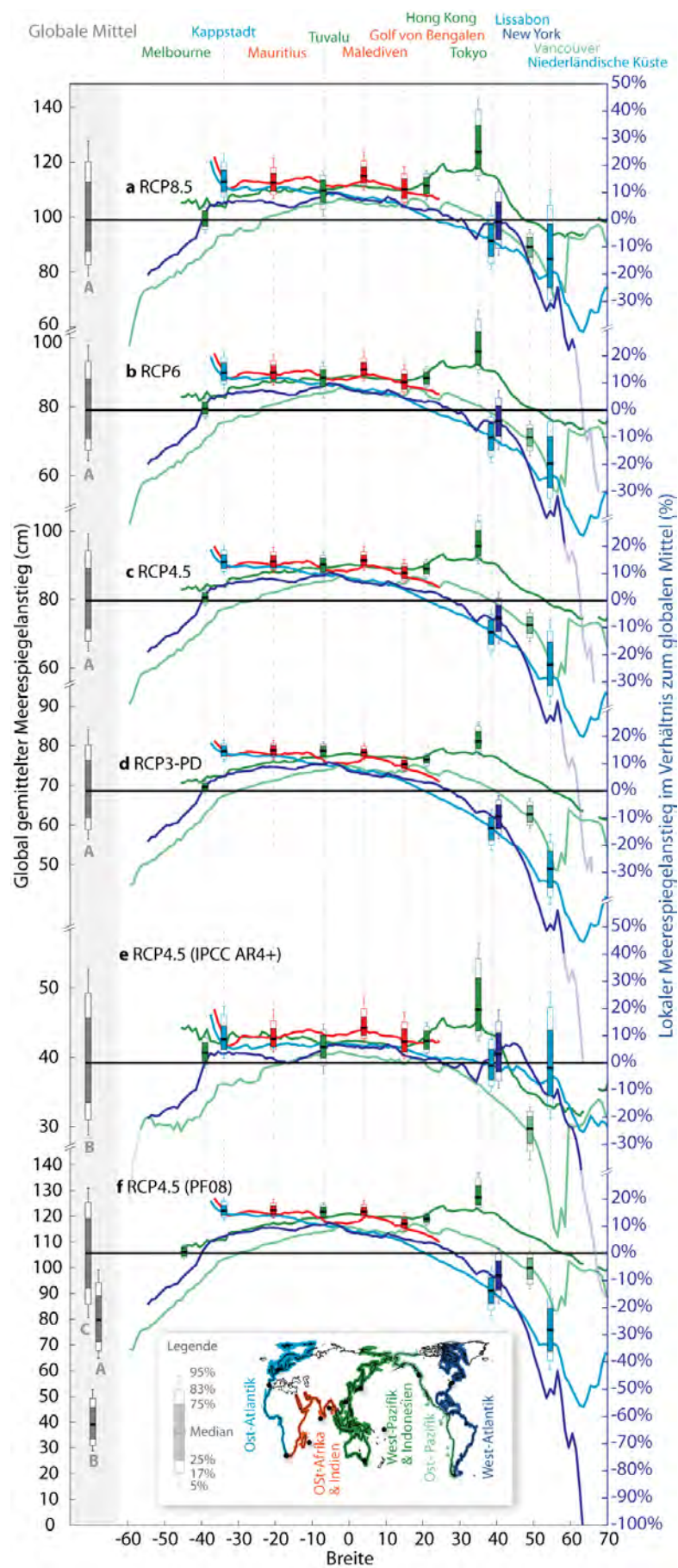   Niederländische Küste

Abbildung 10 (Previous Page) - Erwarteter Meeresspiegelanstieg entlang der Küstenlinien. Die farbigen Linien beschreiben regionale Meerespiegelprojektionen, gemittelt über Küstenregionen in Abhängigkeit von der Breite und aufgeteilt nach verschiedenen Ozeanregionen (siehe kleine Weltkarte unten). Der horizontale schwarze Balken am linken Rand jeder Szenariozeile gibt den gemittelten Meeresspiegelanstieg (cm) mit Fehlerbalken wieder, die den 50%, 68% und 80% Unsicherheitsbereich beschreiben. Zudem werden die Position einzelner Orte in den Küstenregionen angezeigt (siehe oberer Rand der Abbildung und gestrichelte Linien). Die Unsicherheitsbereiche, die zu den Projektionen an diesen Orten angegeben sind, beschreiben die Unsicherheit in der relativen Abweichung vom global gemittelten Meeresspiegelanstieg und erfassen damit die Unsicherheit in den einzelnen „Fingerabdrücken" nicht aber die Unsicherheit im globalen Meerespiegelanstieg selbst.

Abschließende Worte

In diesem Forschungsprojekt wurden Schlüsselelemente des Klimasystems untersucht, die gegenüber anthropogenen Treibhausgasemissionen besonders anfällig sind (*2*). Unsere Liste ist bei Weitem nicht vollständig, viele weitere dieser Elemente existieren: das Arktische Meereis, der Amazonasregenwald, sowie Monsunniederschläge, um nur einige der in diesem Bericht nicht betrachteten Prozesse zu erwähnen. Lenton und Kollegen bieten dazu etwa einen weiteren Überblick (*3*).

Alle hier betrachteten Prozesse erscheinen als "Riesen" im Gesamtklimasystem -- einige von ihnen noch schlafend, andere noch sehr wach. Betrachtet man etwa die Gesamtmenge des Kohlenstoffs, der bisher dauerhaft im gefrorenen Boden der Permafrostgebiete gebunden ist, so ergibt sich ein Wert von 800PgC oder mehr. Allein diese Menge an Kohlenstoff würde ausreichen, um die globale Temperatur um zusätzliche 2°C ansteigen zu lassen. Weitere schlafende Riesen sind das Antarktische und das Grönländische Eisschild. Einmal in den Zustand dauerhaften Abschmelzens gekippt, wird allein Grönland den Meeresspiegel auf lange Sicht um mehrere Meter ansteigen lassen. Beide Riesen werden durch die anthropogen erzeugten Veränderungen des Klimasystems „geweckt" werden, wenn die Treibhausgasemissionen nicht entscheidend reduziert werden. Sie werden langsam erwachen und die Folgen werden sich im Laufe von Jahrhunderten entfalten. Wir wissen sehr wenig darüber, ob diese Prozesse wieder gestoppt werden können, wenn sie einmal angestoßen wurden. Die Permafrostregionen etwa könnten wieder einfrieren, wenn die Temperaturen weit genug sinken. Der freigesetzte Kohlenstoff wird jedoch mit hoher

Wahrscheinlichkeit nicht wieder im Boden der Tundra gebunden. Das Verschwinden der Landeismassen könnte verlangsamt werden. Um sie allerdings wieder anwachsen zu lassen, scheinen deutlich niedrigere Temperaturen notwendig als die heute herrschenden.

Andere, gegenwärtig noch sehr wache Riesen, könnten einschlafen: Die Thermohaline Zirkulation im Nordatlantik transportiert riesige Wärmemengen nach Europa und sorgt damit für ein deutlich milderes Klima und günstigere Bedingungen für die Landwirtschaft als in anderen Gebieten auf gleicher Breite. Klimaveränderungen könnten diese riesenhafte Ozeanzirkulation zumindest zeitweilig in einen schläfrigeren Zustand versetzen. Diese Abschwächung könnte die Temperatur- und Niederschlagsverteilung beeinflussen. Wir sind in diesem Bericht allerdings einer anderen Auswirkung nachgegangen: Den regionalen Änderungen des Meeresspiegels, die mit einer Abschwächung der THC verbunden sein könnten. Insbesondere für die Ostküste der USA ist eine Verstärkung des Meeresspiegelanstiegs zu erwarten, wenn sich der Golfstrom abschwächt.

Während diese „Riesen" noch als relativ robust erscheinen, sind andere Komponenten im Ökosystem Erde deutlich zerbrechlicher. So sind etwa die Korallenriffe so etwas wie die Kanarienvögel in der Kohlemine in Bezug auf den Klimawandel. Sie könnten die ersten Ökosysteme sein, die in großer Anzahl von unserem Planeten verschwinden. Ohne großen zeitlichen Puffer oder Abfederungsmöglichkeiten scheinen die Korallenriffe tatsächlich vom Aussterben bedroht zu sein – in nur 10 bis 20 Jahren. Einige Korallengebiete sind wahrscheinlich bereits verloren, auch wenn die Treibhausgasemissionen morgen dramatisch reduziert würden. Diese extrem artenreichen und kostbaren Ökosysteme werden die ersten Opfer sein – Opfer der anhaltenden Unfähigkeit der Menschheit entschieden zu handeln, um gefährliche anthropogene Wechselwirkungen mit dem Klimasystem zu verhindern.

Referenzen

1. F. Giorgi, *Journal of Climate* **21**, 1589 (Apr, 2008).
2. H. J. Schellnhuber, *Proceedings of the National Academy of Sciences of the United States of America* **106**, 20561 (Dec 8, 2009).
3. T. M. Lenton *et al.*, *Proceedings of the National Academy of Sciences of the United States of America* **105**, 1786 (Feb 12, 2008).
4. M. I. Allen, W., *Nature* **419**, 224 (2002).
5. Y. Ming, V. Ramaswamy, G. Persad, *Geophysical Research Letters* **37** (Jul).
6. P. L. Wu, R. Wood, J. Ridley, J. Lowe, *Geophysical Research Letters* **37** (Jun).
7. J. F. B. Mitchell, C. A. Wilson, W. M. Cunnington, *Quarterly Journal of the Royal Meteorological Society* **113**, 293 (Jan, 1987).

8.   D. A. Stainforth *et al.*, *Nature* **433** (2005).
9.   J. F. B. Mitchell, T. C. Johns, M. Eagles, W. J. Ingram, R. A. Davis, *Climatic Change* **41**, 547 (Mar, 1999).
10.   T. D. Mitchell, *Climatic Change* **60**, 217 (Oct, 2003).
11.   M. Meinshausen *et al.*, *Climatic Change* (eingereicht).
12.   R. H. Moss *et al.*, *Nature* **463**, 747 (Feb, 2010).
13.   D. P. van Vuuren *et al.*, *Climatic Change* (eingereicht).
14.   S. D. Donner, *Plos One* **4** (Jun 3, 2009).
15.   O. Hoegh-Guldberg, *International Coral Reef Symposium* (October 23-27, 2000, Bali, Indonesia, 2001).
16.   S. D. Donner, W. J. Skirving, C. M. Little, M. Oppenheimer, O. Hoegh-Guldberg, *Global Change Biology* **11**, 2251 (Dec, 2005).
17.   K. R. N. Anthony, D. I. Kline, G. Diaz-Pulido, S. Dove, O. Hoegh-Guldberg, *Proceedings of the National Academy of Sciences of the United States of America* **105**, 17442 (Nov 11, 2008).
18.   C. Tarnocai *et al.*, *Global Biogeochemical Cycles* **23, GB2023** (2009).
19.   A. Timmermann, S. I. An, U. Krebs, H. Goosse, *Journal of Climate* **18**, 3122 (Aug, 2005).
20.   M. Vellinga, R. A. Wood, *Climatic Change* **54**, 251 (Aug, 2002).
21.   J. J. Yin, M. E. Schlesinger, R. J. Stouffer, *Nature Geoscience* **2**, 262 (Apr, 2009).
22.   J. Schewe, A. Levermann, M. Meinshausen, *Earth System Dynamics* **2**, 25 (2011).
23.   X. Fettweis, E. Hanna, H. Gallee, P. Huybrechts, M. Erpicum, *Cryosphere* **2**, 117 (2008).
24.   J. M. Gregory, P. Huybrechts, *Philosophical Transactions of the Royal Society a-Mathematical Physical and Engineering Sciences* **364**, 1709 (Jul, 2006).
25.   N. Nakicenovic *et al.*, *Cambridge University Press, Cambridge, UK* (2000).
26.   M. Vermeer, S. Rahmstorf, *Proceedings of the National Academy of Sciences* **106**, 21527 (2009).
27.   G. A. Meehl *et al.*, in *Climate Change 2007: The Physical Science Basis. Contribution of Working Group I to the Fourth Assessment Report of the Intergovernmental Panel on Climate Change* S. Solomon *et al.*, Eds. (Cambridge University Press, Cambridge, United Kingdom and New York, NY, USA., 2007) pp. 747--845.
28.   W. T. Pfeffer, J. T. Harper, S. O'Neel, *Science* **321**, 1340 (2008).

Summary

Tipping points in the climate system
– A Risk Analysis

K. Frieler, M. Meinshausen, N. Braun, A. Golly, W. Hare, M. Mengel, K. van der Merwe, M. Schaeffer, C.-F. Schleussner, T. Schneider von Deimling

Introduction[1]

There are many elements of the Earth system that are expected to change gradually with increasing global warming. Changes might prove to be reversible after global warming returns to lower levels. But there are others that have the potential of showing a threshold behavior. This means that these changes would imply a transition between qualitatively disparate states which can be triggered by only small shifts in background climate (2). These changes are often expected not to be reversible by returning to the current level of warming. The reason for that is, that many of them are characterized by self-amplifying processes that could lead to a new internally stable state which is qualitatively different from before.

There are different elements of the climate system that are already identified as potential tipping elements. This group contains the mass losses of the Greenland and the West-Antarctic Ice Sheet, the decline of the Arctic summer sea ice, different monsoon systems, the degradation of coral reefs, the dieback of the Amazon rainforest, the thawing of the permafrost regions as well as the release of methane hydrates (3).

Crucially, these tipping elements have regional to global scale effects on human society, biodiversity and/or ecosystem services. Several examples may have a discernable effect on global climate through a large-scale positive feedback. This means they would further amplify the human induced climate change. These tipping elements pose risks comparable to risks found in other fields of human activity: high-impact events that have at least a few percent chance to occur classify as high-risk events. In many of these examples adaptation options are limited and prevention of occurrence may be a more viable strategy. Therefore, a better understanding of the processes driving tipping points is essential.

There might be other tipping elements even more critical but not yet identified. These may also lie within our socio-economic systems that are vulnerable to

---

[1] This introductory part of our UFOPLAN work was performed by M. Schaeffer and B. Hare.

climate change impacts. Here we focus on tipping elements within the physical / biological system.

In the following two sections, we briefly highlight some of our methodological research regarding global mean precipitation and regional climate change. These methodological developments provided the underpinning for our subsequent analysis of individual large-scale climate impacts, as e.g. mass losses of the Greenland ice sheet, the release of greenhouse gases by the thawing of permafrost regions or the threat of coral reefs by high ocean temperatures.

Background I: Global-mean precipitation[2]

Precipitation changes are a key driver of climate change impacts and might trigger tipping processes. For example, the mass loss of the Greenland ice sheet does not only depend on regional temperature changes which would increase melting. It also depends on regional changes in precipitation that have the potential to at least partially balance increases in melting by additional accumulation of precipitation. Although regional precipitation changes are definitely of higher relevance for these kind of questions, the consideration of global mean precipitation changes may help to identify some of the important predictors.

On average, global mean precipitation is expected to increase with warming. That is what global climate models consistently show and, in fact, 2010 was not only the warmest (together with 2005) but also the wettest year in the observational record (National Oceanic and Atmospheric Administration (NOAA), Global Historical Climatology Network). One potential explanation for that increase is the fact that warmer air can take up more water than colder air. However, simulated global mean precipitation changes do not simply scale with global mean surface air temperature. Instead, global hydrological sensitivity, the relative change of global-mean precipitation per degree of global warming, seems to vary across different scenarios and even with time. Based on output from 20 coupled Atmosphere-Ocean-General-Circulation-Models (AOGCM) for up to 7 different emission scenarios, we analyzed to what extent these variations can be explained by changes in black carbon (BC) emissions and greenhouse gas (GHG) forcing. Our analysis supports earlier findings that these short- and longwave absorbers initially decrease global-mean precipitation before it increases with increasing surface air temperatures (4-6). Including these effects into a multivariate scaling approach allows to closely reproduce the simulated global-mean precipitation changes (solid lines in Figure 1). We find a sensitivity of global-mean precipitation to tropospheric greenhouse gas forcing of -0.42 ± 0.23 %/(W/m^2) (uncertainty given as one standard deviation of inter-model variability) and to black carbon emissions of -0.07 ± 0.02%/(Mt/yr). In combination with these two predictors the dominant longer-term effect would be that precipitation increases by 2.2 ± 0.52 % per degree (K) increase of surface air temperatures - much lower than the 6.5 %/K that may be expected from the theoretical Clausius-Clapeyron relationship between temperature and the amount of water that can be taken up by the air (4, 7). Overall, global mean temperatures, tropospheric GHG forcings and BC emissions are therefore identified as important additional predictors for precipitation changes. These three predictors provide a consistent explanation of global mean precipitation changes over a wide range of different models.

---

[2] This part of our UFOPLAN work is documented in K. Frieler et al. "Changes in Global-mean Precipitation in Response to Warming, Greenhouse Gas Forcing and Black Carbon", Geophysical Research Letters, Vol. 38, L04702, 2011, doi:10.1029/2010GL045953.
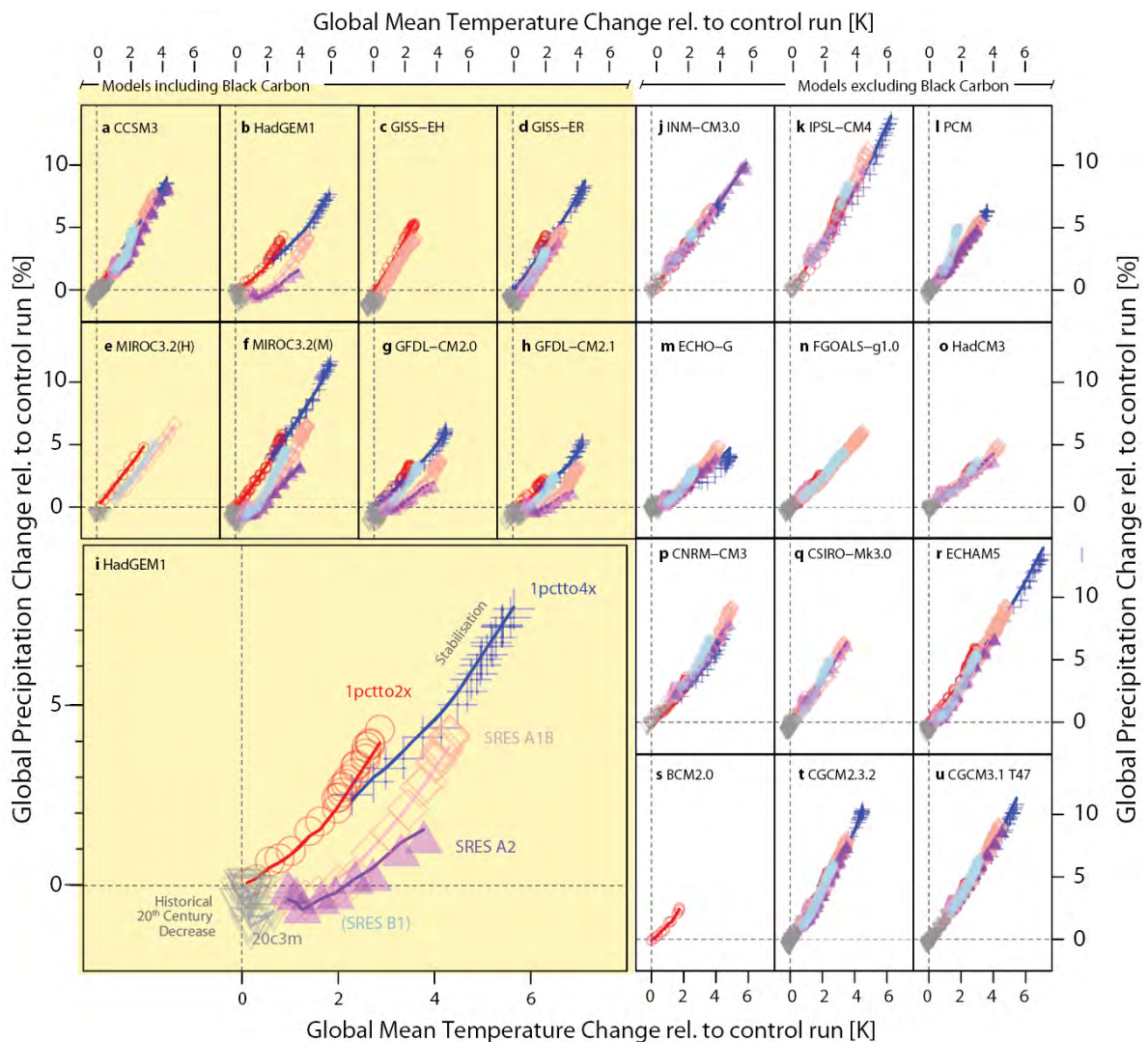
Figure 1 – Percentage changes of global-mean precipitation versus global-mean temperature changes. Color coding indicates different future IPCC scenarios. Projections of our model based on the three predictors: changes in global mean temperature, changes in tropospheric GHG forcing, and BC emissions are shown as solid lines. The models on the left (yellow shading) included BC aerosol emissions. Note how the 20th century simulations (grey symbols) often indicate decreasing precipitation, while future projections nevertheless show positive precipitation trends – a feature that can be explained when taking into account aerosol and GHG forcing effects.

Background II: Deriving Probabilistic Regional Climate Change[3]

Although precipitation is projected to increase in average over the globe, that will not happen uniformly everywhere. In contrast, there are regions as for example the Mediterranean region where models consistently show a decrease in precipitation while in other regions expected increases in precipitation are significantly higher than the global mean increase of 1-3% per degree of global warming. Temperature changes show similar features. Thus, even if we manage to limit global warming to 2°C, the warming over land areas is projected to be higher, i.e., reaching 2.6°C in the multi-model mean. Warming of the Arctic regions is expected to be even more pronounced, thereby affecting particularly vulnerable elements of the Earth System such as the Greenland ice sheet and the Arctic sea ice. It is this spatial pattern of climate change that is relevant for adaptation but also for the assessing the tipping potential of certain elements of the Earth System. Analyzing the probability of tipping associated with a given GHG emission pathway often builds on probabilistic assessment of the triggering regional climate changes.

These probabilistic climate projections for any given emission scenario cannot be simply done on the basis of Atmosphere-Ocean-General-Circulation-Models (AOGCM) with a high spatial resolution. These models can generally only be run for a very limited number of emission scenarios and parameter settings as they are too computationally expensive to do a large number of runs[4]. It turned out that current AOGCMs show a remarkably linear relationship between global mean temperature changes and regional changes in temperature and precipitation that do not differ strongly from emission scenario to emission scenario (*1, 9, 10*). That provides a possible way out of the problem as there are very efficient simplified climate models that allow to calculate probabilistic projections of global-mean temperature change for any given emission scenario (e.g. (*11*)). Combining these projections with the scaling coefficients derived from the available AOGCM simulations allows deriving probabilistic regional climate projections in spite of the limited computer resources (see Box 1).

Usually these scaling approaches are based on global mean temperature changes as single predictor for regional changes. As shown in the previous section simulated precipitation changes are also influenced by tropospheric GHG forcing and aerosol emissions. In fact, the inclusion of GHG forcing and aerosol emissions as additional predictors can significantly improve the emulation of AOGCM simulations even at the regional level. Although sulfate aerosols do not have such a strong influence on global mean precipitation as BC aerosols, they are included in the regional analysis as they might have strong effects on regional precipitation. Following such an approach, the variations of hydrological

---

[3] This part of our UFOPLAN work is documented in the manuscript "A scaling approach to probabilistic assessment of regional climate change" by K. Frieler et al. that was submitted to Journal of Climate, when this report was finalized.

[4] A notable exception are multi-thousand member ensembles by the climateprediction.net experiment in D. A. Stainforth *et al.*, *Nature* **433** (2005).

sensitivity (the percentage change of precipitation per degree of warming) across different AOGCM scenario simulations can for example be reduced by more than 50% in the East-Asian region.

Probabilistic regional climate projections for a strong mitigation scenario (RCP3-PD in blue) and a high emission business as usual scenario (RCP85 in orange) are shown in Figure 2 (references to the considered emission scenarios: (*12-14*)). Our results clearly indicate the high temperature increase to be expected over the Arctic region and the precipitation decrease projected for the Mediterranean region.

Box 1 – Projecting regional climate changes based on AOGCM simulations.
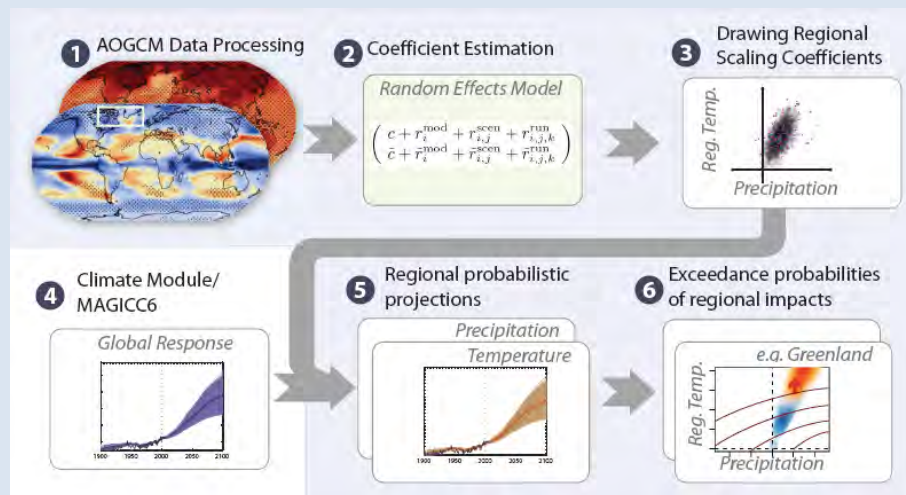
Figure 2 - Schematic illustration of this study's analytical steps. After processing (region / global averaging etc.) the output from AOGCM models (1), the statistical relationship between regional climate change and the three predictors global-mean temperatures, GHG forcing and aerosol emissions is estimated (2). The uncertainty of the associated scaling coefficients is estimated from their inter - AOGCM variability. Sampling scaling coefficients from the established uncertainty distributions (3) and combining them with global mean temperature projections (4) allows projecting probabilistic evolutions of regional temperatures and precipitation changes. Finally, these bi-dimensional regional uncertainty distributions allow deriving exceedance probabilities of specific regional impacts, here taking Greenland's ice sheet surface mass balance as an example (6).

Figure 2 represents a new statistical model for probabilistic projections of regional climate changes. As with earlier pattern scaling approaches it builds on the quasi-linear relation between global mean temperatures and regional climate changes found in many Atmosphere Ocean General Circulation Models (AOGCMs). This quasi-linearity enables us to split the problem of probabilistic regional climate projections into two separate parts: (1) Probabilistic assessment of the global mean temperature change associated with a given emission pathway, (2) Probabilistic assessment of regional climate changes given a fixed amount of global warming.

Our new approach to estimate the scaling coefficients has three main benefits in comparison to previous approaches: (1) The method takes correlations between temperature and precipitation scaling coefficients into account, i.e. it accounts for the fact that coupled climate models providing a high temperature scaling coefficients might at the same time also provide high scaling coefficients for precipitation or vice versa. (2) It enables scaling with other important predictors such as tropospheric GHG forcing and aerosol emissions, and (3) provides an inbuilt means of checking the validity of the scaling relationships, i.e., the assumption that the scaling coefficients do not differ strongly from scenario to scenario.
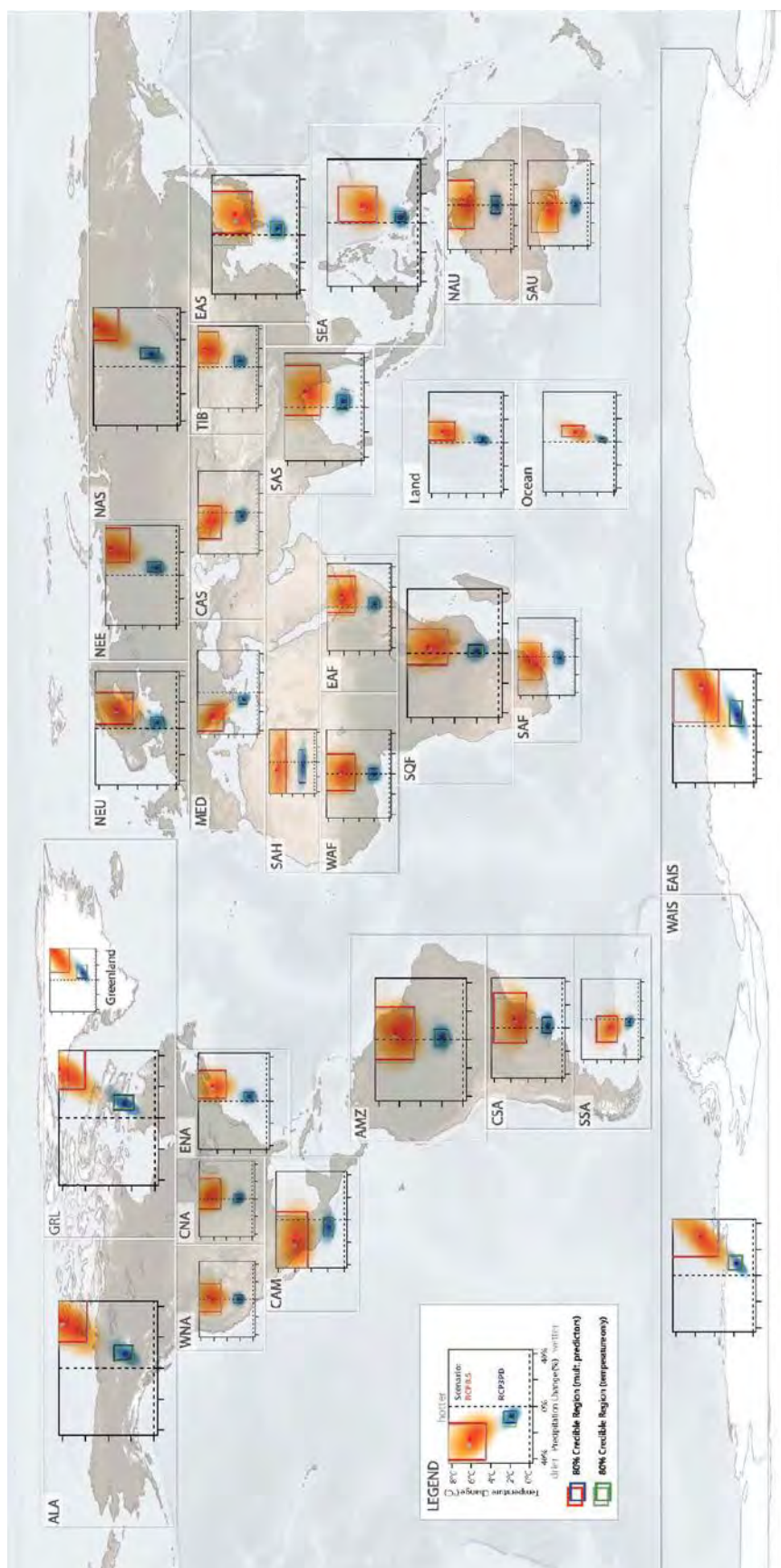
Figure 3 - Joint distributions of regional temperature and precipitation changes in 2100 under the low (RCP3-PD, median global mean warming in 2100: ≈ 1.5°C) and high (RCP85, median global mean warming in 2100: ≈ 5°C) scenarios. The region definitions are based on Ref. (*1*) and amended by those for the West and East Antarctic Ice Sheet (WAIS and EAIS) separated by the Transantarctic Mountains. Background NASA Blue Marble image by R. Stöckli.

Impacts: Coral reefs, permafrost degradation and regional sea level rise.

We now turn to individual large-scale climate impacts and their probability of occurrence under climate change. *Coral reefs*, the 'canaries in the climate system' are likely to shrink substantially, or disappear entirely in some places, on a very short time-scale of just one or two decades. Current research suggests that at least one third of today's corals might be subject to long-term degradation even under very optimistic assumptions concerning CO_2 emissions, thermal adaptation and their resistance to ocean acidification.

Not all tipping points have such near-term time scales as coral reef disappearance. Our analysis of *Permafrost* degradation for example shows that this process runs over centuries, not decades.

Turning to our focus area sea level rise, the remainder of the report illustrates the likely slow-down of the *Atlantic Meridional Overturning Circulation*, which can, for example, dynamically elevate sea level rise on the Eastern coast of North America. The 'gorilla' in the room is however the water frozen in the *Greenland* and *West-Antarctic ice sheets*. The melting of these ice sheets could elevate sea level by multiple meters, again, on the time-scale of centuries and millenia. Here, we focus on one sub-aspect of the Greenland ice sheet: its surface mass balance excluding dynamical losses. This surface mass balance suffices to indicate a tipping point. If the surface mass balance is zero or negative, the Greenland ice sheet will largely disappear, with recovery only possible in a much colder climate than today. In the final chapter, we aggregate all potential sea level rise contributions and investigate the *regional sea level rise* over the 21st century. Affecting small islands and coasts around the world, a probabilistic projection of regional sea level rise might best illustrate of what is at stake, if tipping points regarding ice sheets are crossed. Sea level rise, due to its inertia, is essentially irreversible on the timescales of centuries and possibly millenia.

Coral Reefs: Canaries in the climate system[5]

A dominant stress factor for coral reef ecosystems are peak water temperatures. Corals live in a close symbiotic relationship with a special type of algae (zooxanthellae) that make them appear colored. Cumulative thermal stress results in a loss of the photosynthetic functionality of the coral's endosymbiotic dinoflagellates and a break-down of the endosymbiosis. These so-called bleaching events can lead to the demise of coral reef ecosystems, if they occur with a sufficient frequency to prevent recovery. Future projections have so far been limited to individual future IPCC emission scenarios based on individual coupled climate models (*15*). In this section, we diagnose cumulative heat stress

---

[5] This part of our UFOPLAN work is documented in the manuscript "80% of coral reefs at risk of disappearance already at 1.5°C global warming levels" by K. Frieler et al., to be submitted to an international scientific journal, when this report was finalized.

(degree heating months, DHMs) at 2160 worldwide reef locations and establish a relationship to global-mean temperature levels, based on a comprehensive set of 19 IPCC AR4 coupled climate models. Following earlier studies, we assume a necessary recovery time of 5 years between severe bleaching events (DHM>2 °C*month)[6] to prevent to coral mortality (*17*). Our results suggest that global warming has to be limited to 1.2 °C (uncertainty range: 1.1 - 1.4 °C) above pre-industrial levels to protect at least 50% of the coral reefs. Even under the strongest mitigation scenario currently considered by IPCC, our analysis suggests that 72% (46-89%) of corals might be subject to long-term degradation by 2030. Thermal adaptation, sometimes hypothesized for coral reef systems, could increase the tolerable global mean temperature, theoretically limiting the fraction of affected regions to 31% (9-60%) under the strong mitigation scenario RCP3-PD with peak temperatures of around 1.7°C. However, the thermal threshold for bleaching might also depend on ocean acidification. Under RCP3-PD, we project that 86% (67-96%) of the corals could be seriously damaged until 2030 when assuming a thermal threshold that decreases with decreasing aragonite saturation, i.e., increasing acidification. Under any of the higher RCPs, the projected future thermal and chemical conditions suggest it unlikely for any coral reefs to survive in the absence of a – so far elusive – increase in the coral's thermal tolerance.
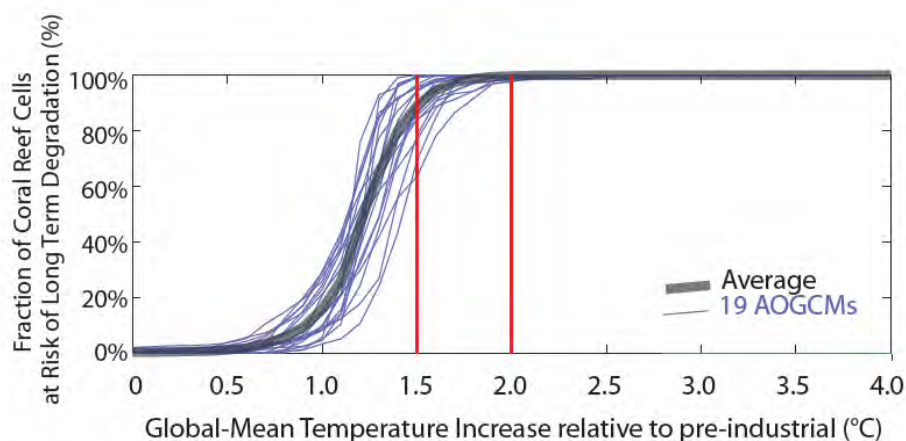
Figure 4 - Fraction of world coral reefs that might be subject to long term degradation due to too frequent coral bleaching events. The grey wide band indicates the average across the different climate models. At 2°C global-mean warming levels, this average suggest that essentially all coral reefs could face environmental conditions leading to their long-term degradation (vertical thick solid red line). At 1.5°C warming levels, the average suggests that 90% of today's

---

[6] The definition is based on the assumption that corals are exposed to thermal stress if monthly mean temperatures are higher than the average across all warmest months in a certain base period. The indicator was established on the basis of observational (16.   O.   Hoegh-Guldberg, *International   Coral   Reef Symposium* (October 23-27, 2000, Bali, Indonesia, 2001).

coral reef locations could be non-supportive of the further existence of coral communities (vertical thin solid red line).
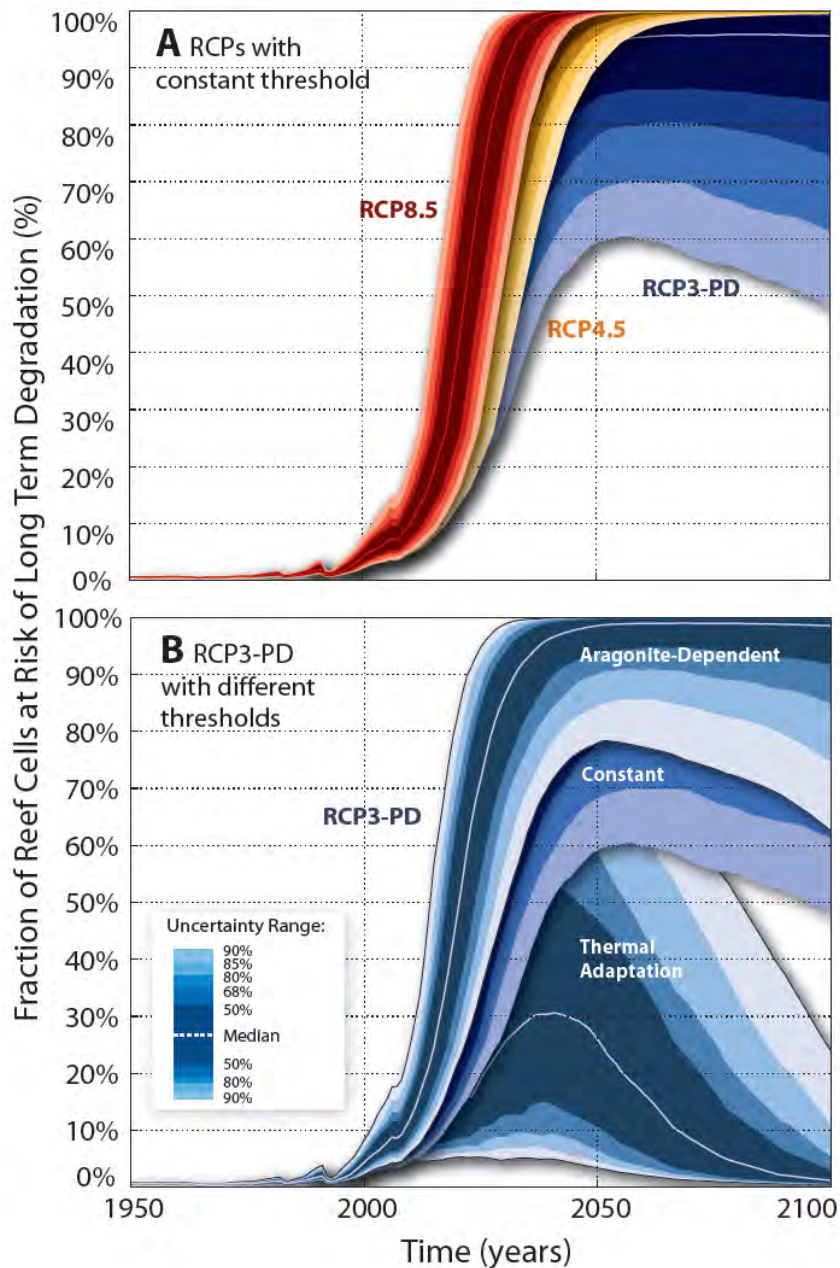
Figure 5 – Projected long term degradation of coral reefs under the "Representative Concentration Pathways" (RCPs: (12-14)). These calculations assume that corals can – in the longer term - not withstand heat stress that is equivalent to a degree-heating-month indicator of more than 2°C*months, if it occurs once every five years. Assuming that corals will be able to tolerate warmer maximal sea surface temperatures over time (thermal adaptation), we still project that one third of the coral reefs might be subject to long-term degradation before 2050 – even under the most stringent mitigation scenario

currently investigated by the IPCC, i.e. RCP3-PD (see lower trajectory of panel B). Our default assumption of constant thermal tolerance however might already be too optimistic, as it does not take into account ocean acidification (upper trajectory in panel B).

Permafrost: The slowly wakening giant[7]

Thawing of permafrost and the associated release of carbon constitutes a positive feedback in the climate system: Increasing temperatures caused by greenhouse gas emissions lead to additional greenhouse gas emissions by carbon release from thawing permafrost. The effect of anthropogenic GHG emissions on global-mean temperatures is hence amplified. Multiple factors have hindered the quantification of this feedback, which was not included in the CMIP3 and C[4]MIP generation of AOGCMs (Atmosphere Ocean General Circulation Models) and carbon-cycle models that form the modeling basis of the Fourth IPCC-Assessment Report. There are considerable uncertainties in the rate and extent of permafrost thaw, the hydrological and vegetation responses, the decomposition timescales of freshly thawed organic material, the proportion of soil carbon that might be emitted as carbon dioxide via aerobic (with participation of oxygen) decomposition or as methane via anaerobic (without participation of oxygen) decomposition, and in the magnitude of the high latitude amplification of global warming that will drive permafrost thaw. Additionally, there are extensive and poorly characterized regional heterogeneities in soil properties, carbon content, and hydrology. Here, we couple a permafrost module to a reduced-complexity carbon-cycle climate model, which allows us to perform a large ensemble of simulations. We design these simulations to account for the uncertainties listed above. The results hence can provide an estimate of the potential strength of the permafrost-carbon-feedback.

For the high business-as-usual scenario, RCP8.5, we project an additional release of 12-52 PgC by 2100 (68% uncertainty range). This amount represents 3-11% of the projected net CO_2 emissions from land carbon-cycle feedbacks. This leads to an additional warming of 0.02-0.11°C. Though projected 21st century emissions are relatively modest, ongoing permafrost thaw and slow, but steady, soil-carbon decomposition imply much more important contributions by 2300.

By then, more than half of the potentially vulnerable permafrost carbon stock in the upper 3m of the soil (600-1000PgC (*18*)) could be released as CO_2, with an extra 1%-3% being released as methane. Our results also suggest that mitigation action in line with the strong mitigation scenario RCP3-PD could limit Arctic temperature increase sufficiently in a way such that thawing of the permafrost

area is limited to 15-30% and the permafrost-carbon induced temperature increase does not exceed 0.01-0.07°C by 2300.
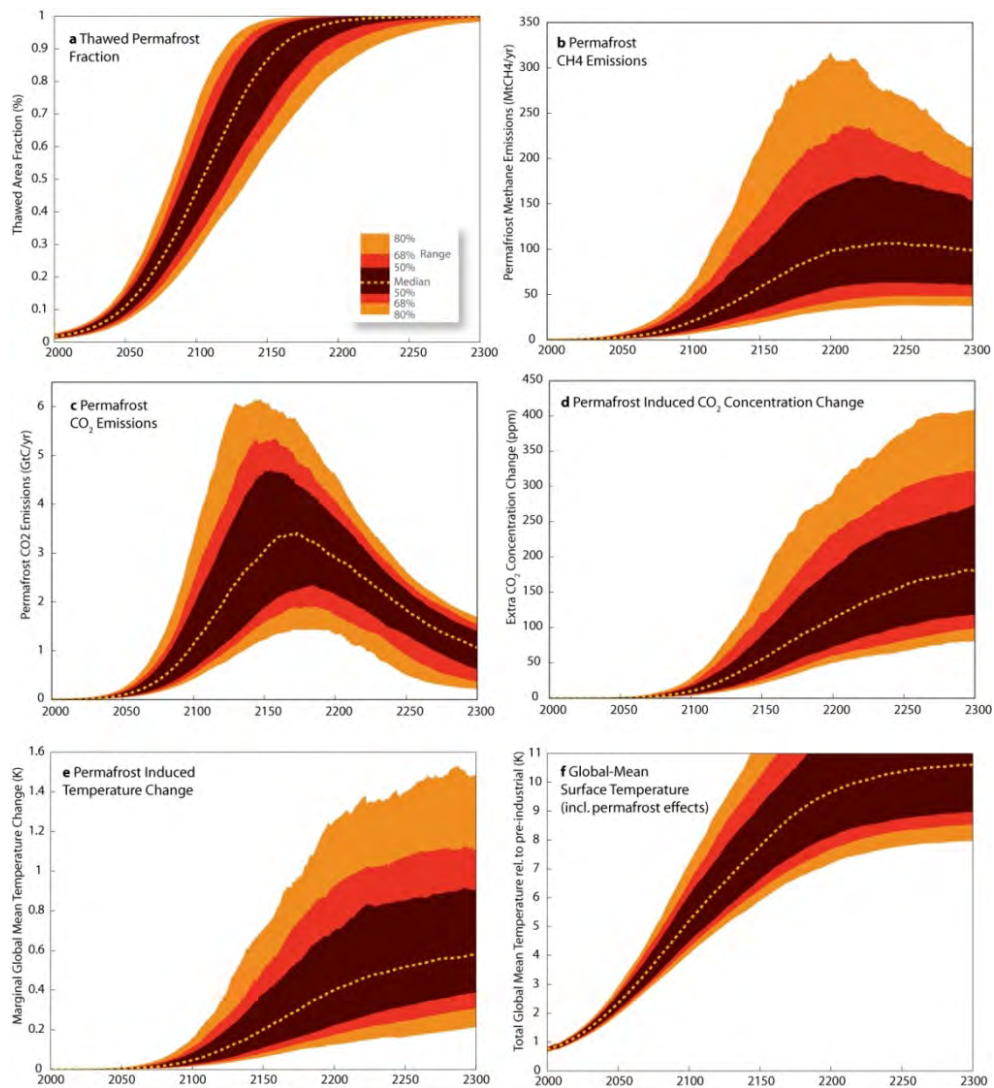
Figure 6 - This study's estimated ranges of thawed permafrost fraction (a), permafrost methane (b) and CO_2 emissions (c), permafrost induced CO_2 concentration (d) and temperature change (e), and the total anthropogenically induced global mean temperature anomaly (f). Results were obtained form an uncertainty analysis for the RCP8.5 scenario. The uncertainty ranges results from 600 member ensemble simulations, using a Monte Carlo sampling that combines the joint distribution of 82 climate model parameters, 9 sets of 17 carbon cycle parameters and 21 independently sampled parameters of our permafrost model.

A giant going asleep: Slowdown of the Meridional Overturning Circulation[8]

The Atlantic Meridional Overturning Circulation (AMOC) is a part of the global ocean-system circulation and is a key player in Earth's climate. It transports about 1 PW (1 Petawatt = 10^{15} Watt) of heat into high northern latitudes, contributing to the mild climate predominant in northwestern Europe. A reduction of the AMOC, as it is projected under global warming is likely to have strong implications on the global climate system (*19, 20*). Probabilistic projections of the AMOC slow-down under global warming that provide not only the mean weakening, but also uncertainty ranges, are therefore of great interest for the scientific community and policy makers likewise.

For the RCP3-PD emission pathway that will result in a global mean temperature rise around 1.0°C relative to the year 2000 (around 1.5°C relative to pre-industrial levels), we project an ensemble median weakening of up to 11% over the 21st century. For the higher RCP4.5 scenario, with a warming of about than 2.0°C over the 21st century, we project a weakening around 22%. Additional Greenland melt water of 10 and 20 cm of global sea-level rise equivalent would further weaken the AMOC by about 4.5% and 10%, respectively. This AMOC slow-down will also affect sea-level at the eastern coast of the U.S. and in Europe and will lead to a dynamical sea-level rise additional to the global mean. By combining our projections for the AMOC reduction with a multi-model sea-level rise study (*21*) we were able to project the dynamic sea-level rise along the New York City coastline. This dynamic effect might account for 4 cm local sea level rise under the RCP3-PD and 8 cm for the RCP4.5 scenario over the 21st century. We estimate the total steric and dynamic sea-level rise for New York City to be about 24 cm till 2100 for the RCP3-PD scenario (Figure 7b). This can hold as a lower bound for sea-level rise projections in this region, since it does not include contributions of Greenland and Antarctic ice-sheets.

---

[8] This part of our UFOPLAN work is documented in the manuscript published in Earth System Dynamics Discussions by C.F. Schleussner et al. "Emulating Atlantic overturning strength for low emission scenarios: consequences for sea-level rise along the North American east coast", available at www.earth-syst-dynam-discuss.net/1/357/2010/.
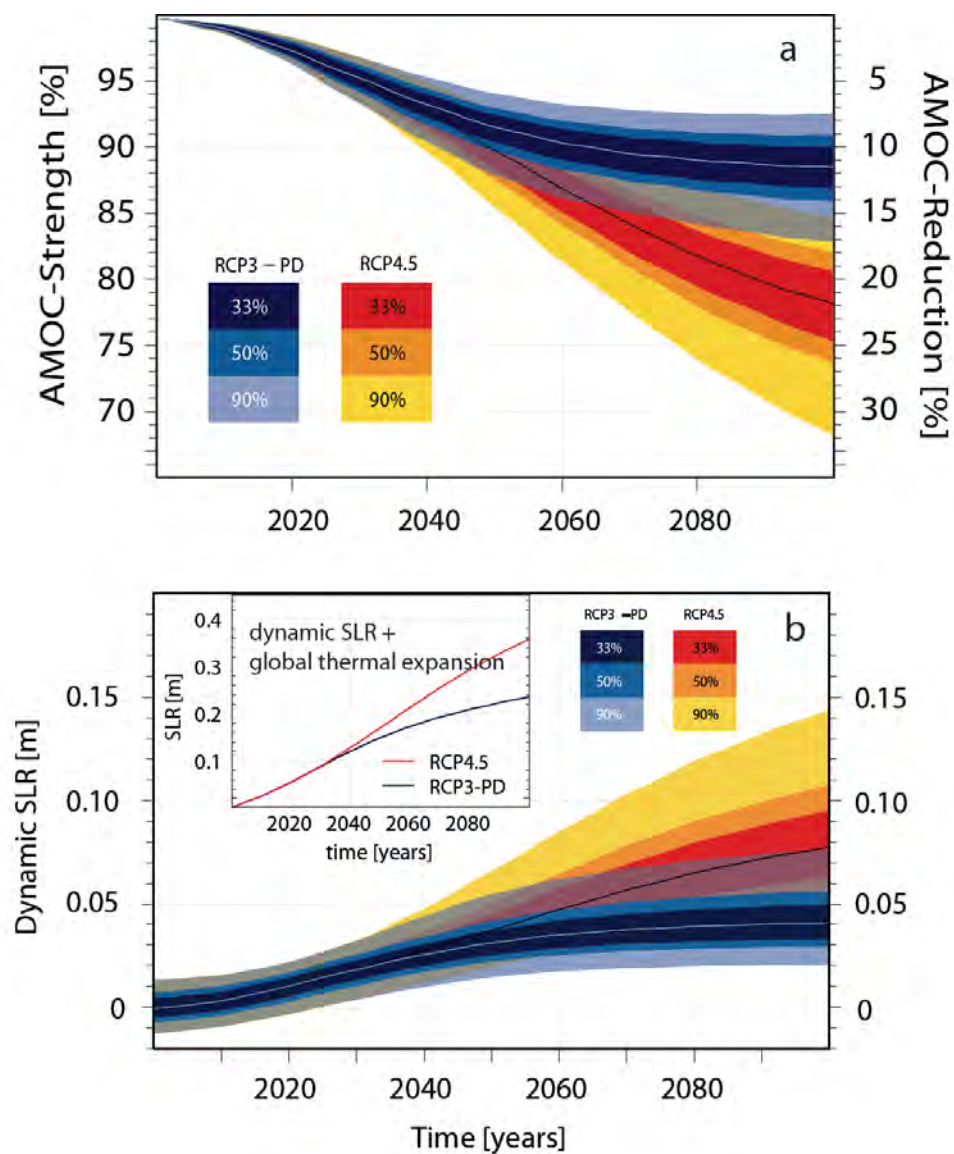
Figure 7 - a) Probabilistic projection of the AMOC reduction for two low concentration pathways (blue: RCP3-PD, red: RCP4.5). b) Dynamic sea-level rise induced by the AMOC slow-down. Inlay: Estimates of the steric and dynamic sea-level rise at the New York City coastline by combining our projections with simulations for the global steric sea-level rise by Schewe et al. (22).

Surface Mass Balance of Greenland[9]

The melting and disintegration of Greenland's ice sheet can contribute substantially to future sea level rise. If the whole ice sheet were to disappear completely, the global sea level would rise between 6 to 7 m. Melting of ice at the surface, accumulation of snow, and discharge of ice into the sea are the three main processes changing its overall mass. If more ice melts or discharges into the ocean and if this loss is not balanced by increasing precipitation, global-mean sea level is going to rise. Here, we look only at surface mass balance ignoring losses by increasing ice discharge or basal melting. Surface mass balance, i.e., the combination of melting at the surface and accumulation of new ice can alone already be an indicator for the tipping potential of the Greenland ice sheet. If the surface mass balance becomes zero, no other process could offset ice losses due to discharge or basal melting. Over long time scales of hundreds and thousands of years, the Greenland ice sheet would be lost under a surface mass balance of zero. We here combine results from two existing surface-mass balance models (*23, 24*) to determine the probability of exceeding such a zero surface mass balance tipping point. For a global temperature change of 4°C, it is very likely that the tipping point would be exceeded representing the onset of an irreversible ablation process. Already at lower warming levels around 2.3°C, there is a 20% chance (see Figure 9).

---

[9] This part of our UFOPLAN work is documented in N. Braun's diploma thesis, supervised by M. Meinshausen and B. Hare.
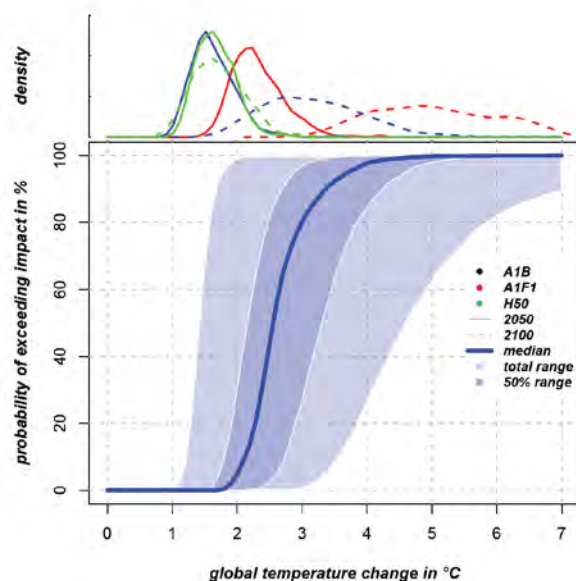
Figure 8 – The probability of net surface mass balance dropping below zero for one of our investigated methods (23). The light blue-shaded area in the lower panel shows the range of all AOGCMs (excluding the outliers). The tipping point could be exceeded with a 50% probability in a range from 1.4 to 4.6°C global mean temperature change. The upper panel illustrates warming levels in 2050 and 2100 for the IPCC SRES A1B, A1FI (25) and a mitigation scenario that halves global emissions by 2050.

Regional Sea Level Rise[10]

Sea-level projections for 21st century are often addressed in terms of global mean change or with a focus on spatial patterns resulting from a single component. Here we present an aggregated view of regional sea-level change in a probabilistic framework for the new Representative Concentration Pathways (RCP) scenarios (*12-14*). For this purpose we decompose the global mean rise into its individual contributions from thermal expansion and ice losses. The associated spatial patterns of change (the so-called fingerprints) are scaled accordingly and combined to an overall pattern. Unlike thermal expansion and glaciers, which are calculated directly, Antarctica and Greenland ice contributions (including nearby glaciers) are assumed in our default setting as residual from a semi-empirical model (*26*) for total sea-level rise. This results in a

---

[10] This part of our UFOPLAN work is documented in the manuscript by M. Perrette et al. "Probabilistic projections of regional sea-level rise", to be submitted to Proceedings of the National Academy of Sciences, when this report was finalized.

rapid rise at low latitudes driven by water that moves away from ice sheets and polar glaciers due to changes in the gravity field. A zonal structure is present as well. Sea-level rise is up to 20% greater along Chinese coast than along Europe at the same latitude. Changes in ocean dynamics are secondary in this context, but they tend to strengthen an east-west gradient in Pacific sea-level rise and amplify the rise in the Indian Ocean. However, they significantly contribute to the uncertainty of the regional projections. We compare our default results with patterns that we reconstructed from independent estimates of global mean ice-sheet contributions, namely from the IPCC AR4 "scaled up" estimate (27) and a high-end estimate based on glaciological constraints (28). The sea-level rise patterns based on the IPCC are influenced primarily by ocean dynamics and high-latitude glaciers because ice sheets are projected to have a small contribution over the 21st century. On the other hand, our "default" pattern is found to vary little as compared to the glaciological-limit estimate where land-ice plays a larger role. The latter cannot be ruled out in the context of their currently observed acceleration. Our study is a first step toward probabilistic forecast of regional sea-level from knowledge of global mean quantities and associated patterns, and could easily be updated with new estimates of land-ice contributions when process-based model simulations become available that more closely reflect observed ice-sheet behavior.

Figure 9 (Next Page) – First line: Sea-level-fingerprints for ocean dynamics (a), mountain glaciers and ice caps (b), Greenland ice sheet (c) and Antarctic ice sheet (d), expressed in unit of regional sea-level rise per unit of global mean temperature change (a) or per global mean contribution of the source used for scaling (b-c). Second line: Individual contributions to global mean SLR under different assumptions about global mean rise (A: semi-empirical method (26), B: IPCC-AR4 (27), C: high-end estimate concerning the ice sheets' contribution(28)). Third line: Projected total SLR for all components combined (contours every 10 cm). The thick black line corresponds to the global mean on all maps, and grey shading indicates areas of sea-level drop.

a Ocean Dynamics

b Mountain Glaciers & Ice Caps

c Greenland Ice Sheet

d Antarctic Ice Sheet

Sea-level fingerprint (m/m)

Ocean Dynamic Pattern (cm/°C)

e-h Global-Mean Contributions by 2090-2099 rel. 1980-1999

e Steric Sea Level Change

RCP3-PD   RCP4.5   RCP6   RCP8.5

f Mountain Glaciers & Ice Caps

RCP3-PD   RCP4.5   RCP6   RCP8.5

g Greenland Ice Sheet

RCP3-PD   RCP4.5   RCP6   RCP8.5

h Antarctic Ice Sheet

RCP3-PD   RCP4.5   RCP6   RCP8.5

i-l Median Sea Level Change under RCP scenarios (Approach A) 2090-2099 rel. 1980-1999

cm

i RCP3PD 69 [59-80] cm

j RCP4.5 80 [68-94] cm

k RCP6 79 [67-94] cm

l RCP8.5 99 [83-120] cm

Figure 10 - Projected sea-level rise along the world's coastlines. Coloured lines show regional sealevel projections, averaged over coastal areas over latitude, and for various oceans (selected coastlines are indicated in the inlet). Global mean SLR (cm) is indicated by a horizontal black bar on the left for each scenario, with error bars indicating 50%, 68% and 80% uncertainty ranges. Particular locations are also shown. The uncertainty ranges for these only describe the uncertainties in relative deviations from the global mean SLR (%), to highlight uncertainty in regional fingerprints. The uncertainty in global mean SLR is not covered.

Closing Words

This research project focused on some key parts of the climate system that are vulnerable to anthropogenic greenhouse gas emissions. Our list is by far not complete, in fact many more exist, which are not covered by this report: Arctic sea ice, the Amazon rain forest , monsoon changes, just to name a few. Lenton and colleagues (*3*) or the special issue in PNAS (*2*), for example, provide an overview.

The impacts we examine in this study are all 'climatic giants', some of them asleep, some of them much awake. For example, all carbon that is currently in perennial frozen grounds in permafrost regions amounts to 800PgC or more. This amount of carbon in itself is enough to raise global-mean temperatures by an extra 2°C. Other 'sleeping giants' are the ice sheets in Greenland and Antarctica. Once tipped to sustained melting, they will raise sea level by several meters. Both these giants are going to be 'woken up' by the human perturbation to the climate system, if emissions are not decisively reduced, though these triggered processes will unfold their full impact only over centuries. The giants will wake up slowly.Very little do we know about whether these processes can be stopped, once they start. Permafrost regions might freeze again, if temperatures are sufficiently lowered. The released carbon is however unlikely to return to the tundra soils, once emitted. Ice sheets might slow their ultimate disappearance but it might take substantially colder temperatures than today in order to see them grow to present levels again.

Yet other currently quite lively giants might be lulled. The Atlantic meridional circulation transports vast amount of heat towards Europe, making it more amenable for agriculture than any other area on the same latitude. Climate change might (temporarily) put this ocean circulation in a more 'sleepy' phase. Temperature and precipitation distributions might change, although here we focused on an altogether different effect. The regional sea level caused by a slowdown of the meridional overturning circulation. Specifically, more sea level rise can be expected on the Eastern North American coast if the Gulf Stream slows down.

While those giants are still quite robust, some impacted ecosystems appear to be much more fragile. Coral reefs, the canaries in the coalmines when it comes to climate change, are the first ecosystems to disappear in large numbers. Without much inertia and resilience, coral reefs seem indeed to run the danger to die back in only 10 or 20 years from now. Many coral reef systems are certain to be lost already, even if emissions were reduced dramatically tomorrow. These extremely biodiverse and precious ecosystems will be the first victims of the world's lasting inability to act decisively to prevent dangerous anthropogenic interference with the climate system.

References

1.   F. Giorgi, *Journal of Climate* **21**, 1589 (Apr, 2008).
2.   H. J. Schellnhuber, *Proceedings of the National Academy of Sciences of the United States of America* **106**, 20561 (Dec 8, 2009).
3.   T. M. Lenton *et al.*, *Proceedings of the National Academy of Sciences of the United States of America* **105**, 1786 (Feb 12, 2008).
4.   M. I. Allen, W., *Nature* **419**, 224 (2002).
5.   Y. Ming, V. Ramaswamy, G. Persad, *Geophysical Research Letters* **37** (2010).
6.   P. L. Wu, R. Wood, J. Ridley, J. Lowe, *Geophysical Research Letters* **37** (2010).
7.   J. F. B. Mitchell, C. A. Wilson, W. M. Cunnington, *Quarterly Journal of the Royal Meteorological Society* **113**, 293 (Jan, 1987).
8.   D. A. Stainforth *et al.*, *Nature* **433** (2005).
9.   J. F. B. Mitchell, T. C. Johns, M. Eagles, W. J. Ingram, R. A. Davis, *Climatic Change* **41**, 547 (Mar, 1999).
10.   T. D. Mitchell, *Climatic Change* **60**, 217 (Oct, 2003).
11.   M. Meinshausen *et al.*, *Nature* **458**, 1158 (2009).
12.   M. Meinshausen *et al.*, *Climatic Change* (submitted).
13.   R. H. Moss *et al.*, *Nature* **463**, 747 (Feb, 2010).
14.   D. P. van Vuuren *et al.*, *Climatic Change* (submitted).
15.   S. D. Donner, *Plos One* **4** (Jun 3, 2009).
16.   O. Hoegh-Guldberg, *International Coral Reef Symposium* (October 23-27, 2000, Bali, Indonesia, 2001).
17.   S. D. Donner, W. J. Skirving, C. M. Little, M. Oppenheimer, O. Hoegh-Guldberg, *Global Change Biology* **11**, 2251 (Dec, 2005).
18.   C. Tarnocai *et al.*, *Global Biogeochemical Cycles* **23, GB2023** (2009).
19.   A. Timmermann, S. I. An, U. Krebs, H. Goosse, *Journal of Climate* **18**, 3122 (Aug, 2005).
20.   M. Vellinga, R. A. Wood, *Climatic Change* **54**, 251 (Aug, 2002).
21.   J. J. Yin, M. E. Schlesinger, R. J. Stouffer, *Nature Geoscience* **2**, 262 (Apr, 2009).
22.   J. Schewe, A. Levermann, M. Meinshausen, *Earth System Dynamics* **2**, 25 (2011).
23.   X. Fettweis, E. Hanna, H. Gallee, P. Huybrechts, M. Erpicum, *Cryosphere* **2**, 117 (2008).
24.   J. M. Gregory, P. Huybrechts, *Philosophical Transactions of the Royal Society a-Mathematical Physical and Engineering Sciences* **364**, 1709 (Jul, 2006).
25.   N. Nakicenovic *et al.*, *Cambridge University Press, Cambridge, UK* (2000).
26.   M. Vermeer, S. Rahmstorf, *Proceedings of the National Academy of Sciences* **106**, 21527 (2009).
27.   G. A. Meehl *et al.*, in *Climate Change 2007: The Physical Science Basis. Contribution of Working Group I to the Fourth Assessment Report of the Intergovernmental Panel on Climate Change* S. Solomon *et al.*, Eds. (Cambridge University Press, Cambridge, United Kingdom and New York, NY, USA., 2007) pp. 747--845.
28.   W. T. Pfeffer, J. T. Harper, S. O'Neel, *Science* **321**, 1340 (2008).

Chapter 1 Overview Literature

Tipping point risks associated with global warming

M. Schaeffer[1], W. Hare[1,2]
[1] Climate Analytics GmbH, Potsdam, Germany and New York, USA
[2] Potsdam Institute for Climate Impact Research e.V., Potsdam, Germany

Introduction

At the global level most current climate change impacts are of a gradually increasing nature. However, a range of tipping points has been identified towards more abrupt transitions between qualitatively disparate states. Although spanning a wide variety of scales in time and space, these transitions are often irreversible on a human generation's time scale. At present-day warming levels, for example, the observed increase in high surface-ocean temperature events has led to the demise of coral reef systems and replacement by algae-dominated systems in several locations (e.g. Mumby et al. 2007).

Continuing warming will bring more elements of the Earth system closer to, or beyond tipping points. We will review here abrupt transitions that have a high impact on a sub-continental to continental scale. In several cases, these transitions will have a discernable effect on global climate through a large-scale positive feedback. We will map estimated global-mean temperature increases associated with the tipping points identified in literature and in research carried out under UFO-plan project FKZ 370841103 against global warming policy targets as formulated in the Copenhagen Accord and the level of warming implied by the current state-of-affairs of proposed emission reductions.

Note that this brief overview draws from diverse sources. The level of understanding is different for the various tipping point mechanisms and the level of warming associated with these is uncertain. Most of the mechanisms involve feedbacks between subsystems over different spatial scales. Surprises and unknowns will be the rule, rather than exceptions. This overview estimates the risks involved according to the present-day level of scientific understanding.

What is connecting all of the research sources is the fact that a plausible mechanism is identified that leads to a non-negligible probability of an abrupt high-impact event. In many cases, the geological history shows that these transitions have occurred before. In all fields of human activity, very high-impact events associated with a probability of at least a few percent classify as high-risk events and warrant serious policy considerations of options to reduce these risks. The risks may be reduced both by lowering the probability of occurrence (mitigation) and by reducing the impacts (adaptation). A second shared characteristic of large-scale tipping points discussed here is that adaptation options are limited and prevention of occurrence may be a more viable strategy.

Potential tipping points

For the following tipping points, plausible mechanisms have been identified in recent observations, geological reconstructions, models, or any combination of these.

West Antarctic Ice Sheet (WAIS)

Recent research on the relationship between Antarctic temperatures and global sea level over the last 520,000 years indicates that multi-metre sea level rise equivalent loss of ice over the next centuries from warming levels of only 2°C is likely (Rohling et al. 2009). Rapid sea level rise from loss

of ice from the Greenland or Antarctic ice sheets occurred during the last interglacial (warm) period, 125,000 years ago when temperatures were a little higher than at present. Average rates of sea level rise in this period were rapid, around 1.6 metres/century (Rohling et al. 2008a; Rohling et al. 2008b).

It has long been hypothesized that the WAIS is vulnerable to global warming and collapse (Mercer 1968; Mercer 1978). The WAIS is a marine ice sheet, grounded far below sea level, with the depth of the ice sheet increasing inland from the grounding line of its ice streams. Such ice sheets are thought to be inherently unstable (Goldberg et al. 2009; Mercer 1968; Schoof 2007; Weertman 1974; Weertman 1976). The persistence of such ice streams may be determined by the presence of ice shelves which are pinned or topographically constrained by embayments or submarine sills and rises (Bentley 1982; Goldberg et al. 2009; Hughes 1982; Mercer 1967; Thomas 1979). Mercer argued that the ice shelves fringing the ice sheet buttress or hold back the main ice streams and glaciers discharging from its interior. In this theory, collapse of the ice shelves would cause the ice sheet grounding line to retreat as accelerated discharge of ice occurred and eventually the ice sheet would float (Mercer 1978).

A further possible contributing element to the potential instability of the WAIS is the fact that the outlet ice streams are often grounded deep below sea level, making the grounding line region of the discharge glaciers vulnerable to high rates of basal melting. Melting of ice close to the grounding line can cause retreat inland, where a deepening bed will likely lead to an acceleration of the discharge from the ice stream. Warming deep ocean waters could lead to increasing rates of basal melting at the grounding line and the decay of buttressing ice shelves, both of which can have a destabilizing effect. These processes are presently not well included in ice sheet models (Huybrechts and Le Meur 1999), although it seems well established that increased basal melting would ultimately lead to the collapse of the ice sheet (Warner and Budd 1998).

Mercer proposed that one of the first consequences of global warming would be the collapse of the ice shelves fringing the Antarctic Peninsula, as there appeared to exist a surface temperature limit for the viability of these shelves (Mercer 1967; Mercer 1978). The 'ice shelf collapse – glacier discharge' theory has been controversial ever since it was raised and debate has raged back and forward (Bentley 1997; Bindschadler; and Bentley; 1997; Oppenheimer 1998).

In the last decade or so a collapse of ice shelves has been observed to lead to accelerated discharge of ice, notably in the Antarctic Peninsula. The observed collapse of the Larsen A ice shelf has been associated with a rapid retreat of the grounded ice streams that drained into the Larsen A ice shelf on the north eastern Antarctic peninsula (De Angelis and Skvarca 2003). Whilst the cause of the accelerated glacial discharges cannot be firmly established, De Angelis and Skvarca propose that it is due to the removal of the ice shelves that in turn removes the back stress from the glaciers. It is now clear that the glaciers draining into the former Larsen B ice shelf have accelerated rapidly following its collapse in year 2000 (Rignot et al 2004). The Antarctic Peninsula glaciers appear to be exhibiting behaviour consistent with an expectation that removal of ice shelf buttressing will lead to acceleration of glacier discharge (Pritchard and Vaughan 2007).

Recent observations in the Amundsen sea sector of the WAIS, which contains enough ice to raise sea level about 1.2 metres, show ongoing and accelerating loss of ice (Pritchard et al. 2009; Rignot and Thomas 2002; Scott et al. 2009; Velicogna 2009) that appears related to deep ocean warming and to collapse of ice shelves possible several decades in the past. The present rapid retreat of the grounding line of Pine Island Glacier (Scott et al. 2009), and widespread dynamic loss if ice from the other major glaciers in this region (Pritchard et al. 2009) could be a sign of an incipient disintegration of this sector of the WAIS.

Loss of the Filchner-Ronne and Ross ice shelves would affect larger regions of the WAIS.

Processes that could lead to a disintegration of the WAIS thus include surface air temperature increase or deep ocean warming that leads to the loss of the major ice shelves, and/or ocean warming sufficient to lead retreating grounding lines into deeper water in the interior of the WAIS.

Greenland ice sheet

This Greenland ice sheet is thought to be vulnerable to warming, but has quite different dynamics than the West Antarctic Ice Sheet. Without marine ice shelves, which in the case of the WAIS are thought to be pinning back large volumes of ice which are grounded below sea levels, and which if melted could destabilize interior ice streams (Oppenheimer 1998), Greenland does not appear to have the latent capacity for rapid collapse. It is know with some certainty that sustained modest warming over Greenland will lead to its decay contributing substantially to sea level rise over the coming centuries and millennia, but with relatively small contributions in the 21st century (Berger and Loutre 2002; Huybrechts and de Wolde 1999; Loutre M.F and Berger A 2000). Such decay could occur trigger a self-amplifying mechanism: a decrease of ice sheet height (currently up to 3500 m) due to melting brings the surface into contact with lower air layers, which are warmer and accelerate further melting ('surface-elevation feedback'). This self-amplifying mechanism implies that a stabilization of global warming, or even a return to pre-industrial levels, may not slow down GIS melting for centuries. IPCC AR4 estimated the tipping point to be reached if warming was to be sustained for millennia in the range of 1.9-4.6^{o}C above pre-industrial.

However, rapid changes are occurring in Greenland at present with accelerating ice loss, contemporaneous with recent warming, indicating that glaciers and ice streams are moving faster than models predict (Khan et al. 2010; Rignot et al. 2010; Velicogna 2009).

The changing gravitational pull of the ice sheet masses will affect the relative sea level change in far field locations. Sea-level rise due to melting of the GIS would be off-set in the North Atlantic by decreased gravitational pull and be relatively faster in other regions.

Arctic sea-ice

Aircraft, ship and satellite observations show that summer (annual minimum) Arctic sea-ice extent has decreased by 50% in the last 50 years (Stroeve et al. 2007). 2009 showed the third lowest extend on record, behind 2007 and 2008. Ice thickness has declined as well, by more than 40% on average over the Arctic basin between the 1970s and 1990s (Rothrock et al. 1999; Wadhams and Davis

2000). Sea ice melts as Arctic temperatures rise and summer ice is pre-conditioned for increased melting by thinner ice due to warmer winters. Reduced sea-ice extent amplifies Arctic warming by enhancing absorption of incoming solar radiation (ice-albedo feedback). Compensating mechanisms, involving more rapid cooling of the ocean surface if an insulating layer of ice is missing, may currently work against the potential of an abrupt change (Eisenman and Wettlaufer 2009). However, these mechanisms depend on the existence of sufficient sea-ice extent. Low sea-ice extent in the coldest periods of the year is expected to be unstable, in the sense that further warming may reduce sea-ice cover enough to allow an abrupt transition to an ice-free state, that is irreversible: Arctic temperatures need to drop significantly below the current threshold to allow re-growth. This has extremely negative consequences for Arctic sea ecosystems (including polar bears, seals, walrus and narwhales) and indigenous people's way of life. It may also further open up the Arctic seas for shipping routes and exploitation of natural resources. Recent studies suggest a tipping point is not likely to exist as long as sea-ice continues to exist for a sufficiently large part of the year and sea-ice extent will recover once warming is reduced (Eisenman and Wettlaufer 2009; Notz 2009). However, since in terms of impacts on ecosystems and society, a seasonally ice-free state is fundamentally different from a perennial ice cover, inclusion here of Arctic summer sea-ice as a system potentially undergoing a state transition is warranted. In addition, as sea-ice extent reduces, the thickness and extent is expected to enter a more erratic regime with much high inter-annual variability and much lower seasonal predictability (Notz 2009). Observed melt over the past 50 years has been faster than in climate models represented in IPCC AR4. A transition to an Arctic ice-free summer is estimated to occur between 1 to 2.5 °C of global warming above pre-industrial, while a sudden transition to a totally ice-free Arctic is not expected below 5°C global warming (Eisenman and Wettlaufer 2009; Lenton et al. 2008; Levermann et al. submitted).

Monsoon systems

The Monsoon system of southern Asia is highly dependent on temperature contrasts between the ocean and land surfaces. The Asian Monsoon may be strengthened by an increased warming of Eurasia relative to the oceans associated with global warming, but weakened by cooling over Asia due to aerosol emissions. The existence of a tipping point is supported by geological evidence of rapid changes in variability of the Monsoon strength during the last ice age and over the past 10,000 years (Gupta et al. 2003). The driving force may be a change in global planetary albedo around 0.5, but this is highly uncertain and difficult to unambiguously link to levels of future warming (Lenton et al. 2008). Over West Africa, the driving force for the Monsoon is the contrast of sea-surface temperatures between hemispheres. The tight coupling between climate and vegetation in the Sahel and Sahara may give rise to a transition from the current low-vegetation state to a much greener state, characterized by grasslands extending to a large part of the Sahara. In one model simulation a greening that extents over almost half of the Sahara's area occurs in a simulation covering a period 9,000 to 6,000 years ago, in agreement with supporting paleobotanic evidence (Claussen et al. 2003). The authors warn that today's climatic state and forcings are that much different from the period in question that this may not be a valid analogy to what may happen under future anthropogenic climate change. Nonetheless, this greening is one of the few examples of a

potentially beneficial tipping point that may occur around 3.5-5.5°C global warming above pre-industrial (Lenton et al. 2008).

Ocean acidification

Of current anthropogenic CO_2 emissions, about 30% is absorbed by the oceans, in response to the higher CO_2 concentration of the atmosphere (Denman et al. 2007 in IPCC AR4). The acidity of the ocean waters rises when additional CO_2 is absorbed. The atmospheric CO_2 concentration has surpassed 380 ppm recently, which has led to an increase of the ocean's acidity, estimated at a reduction of 0.1 units of pH since pre-industrial (Meehl et al. 2007 in IPCC AR4). Reduced reef calcification due to acidification has been observed in the last decade (Cooper et al. 2008; De'ath et al. 2009; Tanzil et al. 2009). IPCC AR4 projections for SRES scenarios indicate a further increase of the ocean's acidity of 0.14 to 0.35 units of pH over the 21st Century (Meehl et al. 2007 in IPCC AR4). Higher acidity of ocean waters leads to reduced availability of calcium carbonate (aragonite), the resource vital for coral species and ecosystems to build skeletons and shells. Especially vulnerable are warm-water coral reefs, cold-water corals and ecosystems in the Southern Ocean. Identified impacts of reduced pH on these systems are a reduction in coral calcification (reduced growth), coral skeleton weakening and stronger temperature sensitivity (potentially increasing the risk of bleaching due to rising temperature of surface waters) (Fischlin et al. 2007 in IPCC AR4). Recent research estimates that if atmospheric CO_2 reaches 450 ppm, coral reefs around the world will slow down growth considerably and at 550 ppm will start to dissolve (Cao and Caldeira 2008; Silverman et al. 2009). A deterioration of coral reefs will have negative impacts on dependent species, fisheries, coastal protection and tourism in many AOSIS regions, as well as in other countries with coral reef systems. In climate model runs of the RCP emission scenarios developed for IPCC AR5, exceeding a CO_2 concentration of 450 ppm is correlated with exceeding roughly 1.5°C above pre-industrial, while a concentration of 550 ppm is associated with approximately 2.3°C warming (median projections). Note that for long-term equilibrium climate change, long time-scale elements in the warming response will have caught up with concentration levels and the corresponding warming levels will be higher by roughly 0.5°C, depending on aerosols and concentrations of other greenhouse gases.

Amazon forest

Much of the precipitation over the Amazon basin is part of regional water recycling involving the rainforests. Under future climate change, which includes drying, probably due to an increased frequency and amplitude of El Niño, the rainforests may give way to open woodlands, seasonal forests, or savannah (Cox et al. 2004; Malhi et al. 2009; Salazar and Nobre 2010). A collapse of large areas of rainforest may reduce regional precipitation by 20-30% annually and up to 50% in the wet season (Avissar and Werth 2005; Kleidon and Heimann 2000), which may prevent rainforest from re-establishment. A tipping point is estimated to exist at 3-5°C global warming (Lenton et al. 2008; Malhi et al. 2009; Salazar and Nobre 2010), although not all climate models project increased drought. Although a CO_2 fertilization effect sustained beyond a decade, or so, continues to be questioned by experiments (Norby et al. 2010), it is included in the estimate of the threshold level here, reducing the sensitivity of Amazon rainforest to drought. Without the fertilization effect, the threshold level may be 2°C lower (Salazar and Nobre 2010). A positive regional feedback exists in which reduced forest cover further increases regional temperature through increased drying. On a

global level, warming is amplified by greenhouse gas emissions from decomposing soil and aboveground biomass following rainforest dieback. A collapse will have devastating consequences for biodiversity, livelihoods of indigenous people, Amazon basin hydrology and water security, nutrient cycling and other ecosystem services. Continuing deforestation in the region may enhance the sensitivity, by reductions in rainfall, and lower the system's threshold, to the extent that some studies argue a threshold has been passed already (Malhi et al. 2009).

Boreal forest

Northern-hemisphere forests at high latitudes are part of a dynamic and complex system involving pests, fires and other disturbances. Over the past decades, the frequency and severity of fires and pests have increased. Under further warming, an increase in variability is expected. Projected higher temperatures, increased drying, pests and wildfires may tip the system to a state in which grasslands and open woodlands dominate (e.g. Bonan 2008; Fischlin et al. 2007). This implies a major ecosystem shift and a positive feedback on global climate change by greenhouse gas emissions from decomposing soil and aboveground organic matter. A tipping point is estimated to exist at about 3-5°C, but is highly uncertain (Lenton et al. 2008).

Atlantic thermohaline circulation

As part of the global ocean circulation, Atlantic surface currents transport heat northward from the equator to high latitudes. Due to the prevailing westerly winds, this heat benefits especially northern Europe, which on average is much warmer than Asian or North American land areas at the same latitude. Water flows back south in the deeper ocean, driven by sinking of cold and salty water masses at high latitudes, principally in the Labrador and Nordic Seas. In the geological past, the Atlantic overturning circulation has been interrupted repeatedly, due to high fluxes of fresh water in polar and sub-polar regions, for instance during the last ice age (Rahmstorf 2002). The time scale of a collapse has been in the order of decades to centuries. A collapse may be induced by increased warming and fresh water input under continuing anthropogenic climate change, including projected increased precipitation over the Arctic basin and melt water from the Greenland ice sheet. A collapse will have severe consequences for marine life and CO_2 uptake by the ocean. For northern Europe the cooling will be masked by the global warming signal. However, since the time scale of a collapse may be in the order of decades, it implies an abrupt cooling superimposed on a much slower warming trend (Schaeffer et al. 2002), which seriously undermines adaptation activities in society and ecosystems. In addition, the abrupt change in ocean currents involves a rapid sea-level rise of up to 1 metre along the European and North American coastlines (Levermann et al. 2005). Finally, in the decades of approaching a tipping point the overturning may go through large fluctuations and enter a phase of high unpredictability (Schaeffer et al. 2002). Recent literature has shown that climate models represented in IPCC AR4 may be too conservative in the positioning of the current climate system relative to a tipping point of the Atlantic thermohaline circulation (Hofmann and Rahmstorf 2009). Whereas observations show that the Atlantic is a net *exporter* of fresh water southward of 30°S, Weber et al (2007) found that all but one of nine climate models showed a net fresh-water *import* across 30 ° S. Net export of fresh water indicates the real circulation may be bistable, i.e. may show tipping point transitions, whereas net import of fresh water indicates the system is monostable, i.e. does not have a tipping point to a different state.

Indeed, none of the AR4 models shows a collapse of the thermohaline in projections of 21st century climate change, although all project a significant gradual slowing down of the circulation. Recent analyses and expert elicitations estimate a roughly 10% probability of a collapse at a warming level exceeding 2°C above pre-industrial and about 25% for warming over 5°C (Kriegler et al. 2009; Levermann et al. submitted).

Marine methane hydrates

Large amounts of methane are stored in ice form as methane hydrates in ocean floor sediments. A warming of the deep ocean may trigger the release of methane to the atmosphere and act as a strong positive feedback for global warming. Inventories, observations and modelling of the effects of methane hydrates are in a very early stage of scientific development. Preliminary results point to a very important potential effect: if methane hydrates start to decompose once warming penetrates to the deep ocean, the global climate system may move to a different state, in which the continuing release of methane prevents warming from slowing down, or decreasing, for millennia, even if anthropogenic greenhouse-gas emissions cease (Archer et al. 2009). Such preliminary results show this may happen at warming levels above 2°C, but this is highly uncertain given the level of understanding.

Mapping of risks against plausible levels of warming in the 21st century

The figure below illustrates the risks associated with levels of global warming above pre-industrial levels, indicating today's level, two targets proposed in the international climate negotiation context and an estimate of projected warming resulting from a bottom-up analysis of current emission reduction proposals by individual countries (Rogelj et al. 2010). The tipping point phenomena with lowest level of understanding are printed grey. Note that the threshold level for all phenomena is uncertain.

The figure above and the text below provide a rough overview of the estimated threshold levels associated with several tipping elements. For references, see the sections above that discussed the literature on these phenomena.

Global warming above pre-industrial

Observed at current or recent warming levels (0.8°C)
- Observed increased frequency of coral reef bleaching due to thermal stress
- Accelerating loss of ice from West-Antarctic and Greenland ice sheets, faster than predicted by models
- Observed, rapid decline of summer Arctic sea-ice area and thickness, faster than predicted by models

1.5°C
- Coral reef bleaching a biannual to annual event in the Eastern Caribbean
- Risk of severe bleaching every five years in Indian Ocean
- CO_2 concentrations of around 350 ppm: Possible upper threshold of viability for coral reefs
- Sea level rise of about 0.6 m by 2100 (using models and methods of Meinshausen et al (2009) and Rahmstorf (2007))
- Risk of complete loss of summer sea ice in the Arctic with widespread adverse effects on species and ice based ecosystems

2°C
- Warming of 1 to 3°C: widespread mortality of coral reefs, with risk growing rapidly in the temperature range 1.5 to 2°C.
- CO_2 concentrations of around 450 ppm: coral reefs stop growing due to the effects of ocean acidification, caused by rising atmospheric CO_2.
- Release of methane, a powerful greenhouse gas, as ocean warming causes methane hydrates under the sea bed to dissolve and enter the atmosphere, accelerating warming.
- Large risk of Amazon forest dieback under assumptions of no sustained CO_2 fertilization effect.
- Sea level rise of about 0.8 m by 2100 (using models and methods of Meinshausen et al (2009) and Rahmstorf (2007))
- Roughly 10% chance of a collapse of the Atlantic meridional overturning circulation.
- Recent research on the relationship between Antarctic temperatures and global sea level rise over the last half million years indicate that multi-metre sea level rise from over 2°C warming over the coming centuries is likely, unless global mean temperatures are reduced very substantially.

3.2-3.5°C (rough estimate of global warming by 2100 under current emission reduction proposals by both developed and developing countries)

- Based on recent estimates, sea level rise exceeds 1.1 m by 2100 (using models and methods of Meinshausen et al (2009) and Rahmstorf (2007))
- CO_2 concentrations of around 550 ppm could be a level at which coral reefs start top dissolve due to the effects of ocean acidification, caused by rising atmospheric CO_2.
- Increased drought linked to increased warming leads to a rapid enhanced dieback of the Amazonian rainforest, leading to a loss in biodiversity and releasing carbon into the atmosphere
- Warming leads to increased pests and wildfires in northern high latitude (boreal) forests. A rapid dieback is possible in a transition to open woodlands and grasslands, but highly uncertain.
- The Greenland ice sheet is predicted to loose ice continuously for global warming in the range of 1.9 to 4.6°C above preindustrial leading ultimately to a 6-7 metre sea level over centuries to millennia. It would be better to stay outside of this warming range than to risk a major discharge of ice from this ice sheet on any timescale.

References

Archer, D., Buffett, B., and Brovkin, V. (2009). "Ocean methane hydrates as a slow tipping point in the global carbon cycle." *Proceedings of the National Academy of Sciences*, 106(49), 20596-20601.

Avissar, R., and Werth, D. (2005). "Global Hydroclimatological Teleconnections Resulting from Tropical Deforestation." *Journal of Hydrometeorology*, 6(2), 134-145.

Bentley, C. R. "The West Antarctic Ice Sheet: Diagnosis and Prognosis." *Presented at Carbon Dioxide Research Conference: Carbon Dioxide, Science and Consensus*, Berkeley Springs, West Virginia.

Bentley, C. R. (1997). "Rapid Sea-Level Rise Soon from West Antarctic Ice Sheet Collapse?" *Science*, 275(5303), 1077-1078.

Berger, A., and Loutre, M. F. (2002). "CLIMATE: An Exceptionally Long Interglacial Ahead?" *Science*, 297(5585), 1287-1288.

Bindschadler;, R., and Bentley;, C. E. (1997). "West Antarctic Ice Sheet Collapse?" *Science*, 276(5313), 661d-665.

Bonan, G. B. (2008). "Forests and Climate Change: Forcings, Feedbacks, and the Climate Benefits of Forests." *Science*, 320(5882), 1444-1449.

Cao, L., and Caldeira, K. (2008). "Atmospheric CO_2 stabilization and ocean acidification." *Geophysical Research Letters*, 35, L19609.

Claussen, M., Brovkin, V., Ganopolski, A., Kubatzki, C., and Petoukhov, V. (2003). "Climate change in northern Africa: The past is not the future." *Climatic Change*, 57, 99-118.

Cooper, T. F., De'Ath, G., Fabricius, K. E., and Lough, J. M. (2008). "Declining coral calcification in massive Porites in two nearshore regions of the northern Great Barrier Reef." *Global Change Biology*, 14(3), 529-538.

Cox, P. M., Betts, R. A., Collins, M., Harris, P. P., Huntingford, C., and Jones, C. D. (2004). "Amazonian forest dieback under climate-carbon cycle projections for the 21st century." *Theoretical and Applied Climatology*, 78(1), 137-156.

De Angelis, H., and Skvarca, P. (2003). "Glacier Surge After Ice Shelf Collapse." *Science*, 299(5612), 1560-1562.

De'ath, G., Lough, J. M., and Fabricius, K. E. (2009). "Declining Coral Calcification on the Great Barrier Reef." *Science*, 323(5910), 116-119.

Denman, K. L., Brasseur, G., Chidthaisong, A., Ciais, P., Cox, P. M., Dickinson, R. E., Hauglustaine, D., Heinze, C., Holland, E., Jacob, D., Lohmann, U., Ramachandran, S., da Silva Dias, P. L., Wofsy, S. C., and Zhang, X. (2007). "Couplings Between Changes in the Climate System and Biogeochemistry", in S. Solomon, D. Qin, M. Manning, Z. Chen, M. Marquis, K. B. Averyt, M. Tignor, and H. L. Miller, (eds.), *Climate Change 2007: The Physical Science Basis. Contribution of Working Group I to the Fourth Assessment Report of the Intergovernmental Panel on Climate Change*. Cambridge, United Kingdom and New York, NY, USA: Cambridge University Press, pp. 499-587.

Eisenman, I., and Wettlaufer, J. S. (2009). "Nonlinear threshold behavior during the loss of Arctic sea ice." *Proceedings of the National Academy of Sciences*, 106(1), 28-32.

Fischlin, A., Midgley, G. F., Price, J. T., Leemans, R., Gopal, B., Turley, C., Rounsevell, M. D. A., Dube, O. P., Tarazona, J., and Velichko, A. A. (2007). "Ecosystems, their properties, goods, and services", in O. F. C. M.L. Parry, J.P. Palutikof, and P. J. v. d. L. a. C. E. Hanson, (eds.), *Climate Change 2007: Impacts, Adaptation and Vulnerability. Contribution of Working Group II to the Fourth Assessment Report of the Intergovernmental Panel on Climate Change*. Cambridge: Cambridge University Press, pp. 211-272.

Goldberg, D., Holland, D. M., and Schoof, C. (2009). "Grounding line movement and ice shelf buttressing in marine ice sheets." *J. Geophys. Res.*, 114(F4), F04026.

Gupta, A. K., Anderson, D. M., and Overpeck, J. T. (2003). "Abrupt changes in the Asian southwest monsoon during the Holocene and their links to the North Atlantic Ocean." *Nature*, 421(6921n), 354-357.

Hofmann, M., and Rahmstorf, S. (2009). "On the stability of the Atlantic meridional overturning circulation." *Proceedings of the National Academy of Sciences*, 106(49), 20584-20589.

Hughes, T. "The Stability of the West Antarctic Ice Sheet: What has happened and what will happen." *Presented at Carbon Dioxide Research Conference: Carbon Dioxide, Science and Consensus*, Berkeley Springs, West Virginia.

Huybrechts, P., and de Wolde, J. (1999). "The dynamic response of the Greenland and Antarctic ice sheets to multiple-century climatic warming." *Journal of Climate*, 12(8), 2169-2188.

Huybrechts, P., and Le Meur, E. (1999). "Predicted present-day evolution patterns of ice thickness and bedrock elevation over Greenland and Antarctica." *Polar Research*, 18(2), 299-306.

Khan, S. A., Wahr, J., Bevis, M., Velicogna, I., and Kendrick, E. (2010). "Spread of ice mass loss into northwest Greenland observed by GRACE and GPS." *Geophysical Research Letters*, 37(6), L06501.

Kleidon, A., and Heimann, M. (2000). "Assessing the role of deep rooted vegetation in the climate system with model simulations: mechanism, comparison to observations and implications for Amazonian deforestation." *Climate Dynamics*, 16(2), 183-199.

Kriegler, E., Hall, J. W., Held, H., Dawson, R., and Schellnhuber, H. J. (2009). "Imprecise probability assessment of tipping points in the climate system." *Proceedings of the National Academy of Sciences*.

Lenton, T. M., Held, H., Kriegler, E., Hall, J. W., Lucht, W., Rahmstorf, S., and Schellnhuber, H. J. (2008). "Tipping elements in the Earth's climate system." *Proceedings of the National Academy of Sciences*, 105(6), 1786-1793.

Levermann, A., Bamber, J., Drijfhout, S., Ganopolski, A., Haeberli, W., Harris, N. R. P., Huss, M., Krüger, K., Lenton, T., Lindsay, R. W., Notz, D., Wadhams, P., and Weber, S. (submitted). "Potential climatic transitions with profound impact on Europe - Review of the current state of six 'tipping elements of the climate system'."

Levermann, A., Griesel, A., Hofmann, M., Montoya, M., and Rahmstorf, S. (2005). "Dynamic sea level changes following changes in the thermohaline circulation." *Climate Dynamics*, 24(4), 347-354.

Loutre M.F, and Berger A. (2000). "Future Climatic Changes: Are We Entering an Exceptionally Long Interglacial?" *Climatic Change*, 46(1/2), 61-90(30).

Malhi, Y., Aragão, L. E. O. C., Galbraith, D., Huntingford, C., Fisher, R., Zelazowski, P., Sitch, S., McSweeney, C., and Meir, P. (2009). "Exploring the likelihood and mechanism of a climate-change-induced dieback of the Amazon rainforest." *Proceedings of the National Academy of Sciences*, 106(49), 20610-20615.

Meehl, G. A., Stocker, T. F., Collins, W. D., Friedlingstein, P., Gaye, A. T., Gregory, J. M., Kitoh, A., Knutti, R., Murphy, J. M., Noda, A., Raper, S. C. B., Watterson, I. G., Weaver, A. J., and Zhao, Z.-C. (2007). "Global Climate Projections", in S. Solomon and M. M. D. Qin, Z. Chen, M. Marquis, K.B. Averyt, M. Tignor and H.L. Miller, (eds.), *Climate Change 2007: The Physical Science Basis. Contribution of Working Group I to the Fourth Assessment Report of the Intergovernmental Panel on Climate Change*. Cambridge, United Kingdom and New York, NY, USA: Cambridge University Press.

Meinshausen, M., Meinshausen, N., Hare, W., Raper, S. C. B., Frieler, K., Knutti, R., Frame, D. J., and Allen, M. R. (2009). "Greenhouse-gas emission targets for limiting global warming to 2[thinsp][deg]C." *Nature*, 458(7242), 1158-1162.

Mercer, J. H. "Antarctic Ice and Sangamon Sea Level." *Presented at Commission of Snow and Ice: Reports and Discussions*, Bern.

Mercer, J. H. "Antarctic Ice and Sangamon Sea Level." *Presented at Commission of Snow and Ice: Reports and Discussions*, Bern.

Mercer, J. H. (1978). "West Antarctic Ice Sheet and Co2 Greenhouse Effect - Threat of Disaster." *Nature*, 271(5643), 321-325.

Mumby, P. J., Hastings, A., and Edwards, H. J. (2007). "Thresholds and the resilience of Caribbean coral reefs." *Nature*, 450(7166), 98-101.

Norby, R. J., Warren, J. M., Iversen, C. M., Medlyn, B. E., and McMurtrie, R. E. (2010). "CO2 enhancement of forest productivity constrained by limited nitrogen availability." *Proceedings of the National Academy of Sciences*, 107(45), 19368-19373.

Notz, D. (2009). "The future of ice sheets and sea ice: Between reversible retreat and unstoppable loss." *Proceedings of the National Academy of Sciences*, 106(49), 20590-20595.

Oppenheimer, M. (1998). "Global warming and the stability of the West Antarctic Ice Sheet." *Nature*, 393(6683), 325-332.

Pritchard, H. D., Arthern, R. J., Vaughan, D. G., and Edwards, L. A. (2009). "Extensive dynamic thinning on the margins of the Greenland and Antarctic ice sheets." *Nature*, advance online publication.

Pritchard, H. D., and Vaughan, D. G. (2007). "Widespread acceleration of tidewater glaciers on the Antarctic Peninsula." *Journal of Geophysical Research-Earth Surface*, 112(F3), -.

Rahmstorf, S. (2002). "Ocean circulation and climate during the past 120,000 years." *Nature*, 419(6903), 207-214.

Rahmstorf, S. (2007). "A Semi-Empirical Approach to Projecting Future Sea-Level Rise." *Science*, 315(5810), 368-370.

Rignot, E., Koppes, M., and Velicogna, I. (2010). "Rapid submarine melting of the calving faces of West Greenland glaciers." *Nature Geoscience*, 3(3), 187-191.

Rignot, E., and Thomas, R. H. (2002). "Mass Balance of Polar Ice Sheets." *Science*, 297(5586), 1502-1506.

Rogelj, J., Nabel, J., Chen, C., Hare, W., Markmann, K., Meinshausen, M., Schaeffer, M., Macey, K., and Hohne, N. (2010). "Copenhagen Accord pledges are paltry." *Nature*, 464(7292), 1126-1128.

Rohling, E. J., Grant, K., Bolshaw, M., Roberts, A. P., Siddall, M., Hemleben, C., and Kucera, M. (2009). "Antarctic temperature and global sea level closely coupled over the past five glacial cycles." *Nature Geosci*, 2(7), 500-504.

Rohling, E. J., Grant, K., Hemleben, C., Kucera, M., Roberts, A. P., Schmeltzer, I., Schulz, H., Siccha, M., Siddall, M., and Trommer, G. (2008a). "New constraints on the timing of sea level fluctuations during early to middle marine isotope stage 3." *Paleoceanography*, 23.

Rohling, E. J., Grant, K., Hemleben, C., Siddall, M., Hoogakker, B. A. A., Bolshaw, M., and Kucera, M. (2008b). "High rates of sea-level rise during the last interglacial period." *Nature Geosci*, 1(1), 38-42.

Rothrock, D. A., Yu, Y., and Maykut, G. A. (1999). "Thinning of the Arctic sea‐ice cover." *Geophys. Res. Lett.*, 26(23), 3469-3472.

Salazar, L. F., and Nobre, C. A. (2010). "Climate change and thresholds of biome shifts in Amazonia." *Geophys. Res. Lett.*, 37(17), L17706.

Schaeffer, M., Selten, F. M., Opsteegh, J. D., and Goosse, H. (2002). "Intrinsic limits to predictability of abrupt regional climate change in IPCC SRES scenarios." *Geophysical Research Letters*, 29(16), 14:1-14:4.

Schoof, C. (2007). "Marine ice-sheet dynamics. Part 1. The case of rapid sliding." *Journal of Fluid Mechanics*, 573(-1), 27-55.

Scott, J. B. T., Gudmundsson, G. H., Smith, A. M., Bingham, R. G., Pritchard, H. D., and Vaughan, D. G. (2009). "Increased rate of acceleration on Pine Island Glacier strongly coupled to changes in gravitational driving stress." *The Cryosphere*, 3, 125–131.

Silverman, J., Lazar, B., Cao, L., Caldeira, K., and Erez, J. (2009). "Coral reefs may start dissolving when atmospheric CO_2 doubles." *Geophysical Research Letters*, 36, L05606.

Stroeve, J., Holland, M. M., Meier, W., Scambos, T., and Serreze, M. (2007). "Arctic sea ice decline: Faster than forecast." *Geophys. Res. Lett.*, 34(9), L09501.

Tanzil, J., Brown, B., Tudhope, A., and Dunne, R. (2009). "Decline in skeletal growth of the coral Porites lutea from the Andaman Sea, South Thailand between 1984 and 2005." *Coral Reefs*, 28(2), 519-528.

Thomas, R. H. (1979). "The dynamics of marine ice sheets." *Journal of Glaciology*, 24, 167-177.

Velicogna, I. (2009). "Increasing rates of ice mass loss from the Greenland and Antarctic ice sheets revealed by GRACE." *Geophys. Res. Lett.*, 36.

Wadhams, P., and Davis, N. R. (2000). "Further evidence of ice thinning in the Arctic Ocean." *Geophys. Res. Lett.*, 27(24), 3973-3975.

Warner, R. C., and Budd, W. F. (1998). "Modelling the long-term response of the Antarctic ice sheet to global warming." *Annals of Glaciology*, 27, 161-168.

Weber, S. L., Drijfhout, S. S., Abe-Ouchi, A., Crucifix, M., Eby, M., Ganopolski, A., Murakami, S., Otto-Bliesner, B., and Peltier, W. R. (2007). "The modern and glacial overturning circulation in the Atlantic ocean in PMIP coupled model simulations." *Clim. Past*, 3(1), 51-64.

Weertman, J. (1974). "Stability of the junction of an ice sheet and an ice shelf." *Journal of Glaciology*, 13(67), 3-11.

Weertman, J. (1976). "Glaciology's grand unsolved problem." *Nature*, 260, 284-286.

Chapter 2 Precipitation Scaling I Global

Projected Global-mean Precipitation in Response to Warming, Greenhouse Gas Forcing and Black carbon

K. Frieler, [1] M. Meinshausen, [1] T. Schneider von Deimling, [1] T. Andrews, [2] and P. Forster [2]

[1] Earth System Analysis, Potsdam Institute for Climate Impact Research, Potsdam, Germany

[2] School of Earth and Environment, University of Leeds, Leeds, United Kingdom

Abstract

Precipitation changes are a key driver of climate change impacts. On average, global precipitation is expected to increase with warming. However, model projections show that precipitation does not scale linearly with surface air temperature. Instead, hydrological sensitivity, the relative change of global-mean precipitation per degree of global warming, seems to vary across different scenarios and even with time. Based on output from 20 coupled Atmosphere-Ocean-General-Circulation-Models for up to 7 different scenarios, we discuss to what extent these variations can be explained by changes in the tropospheric energy budget. Our analysis supports earlier findings that long- and shortwave absorbers initially decrease global-mean precipitation. Including these absorbers into a multivariate scaling approach allows to closely reproduce the simulated global-mean precipitation changes. We find a sensitivity of global-mean precipitation to tropospheric greenhouse gas forcing of -0.42 $\pm$ 0.21 % $W^{-1}m^2$ (uncertainty given as one std of inter-model variability) and to black carbon emissions of -0.07 $\pm$ 0.02% $Mt^{-1}yr$. In combination with these two predictors the dominant longer-term effect of surface air temperatures on precipitation is estimated to be 2.2 $\pm$ 0.51 % K^{-1} – much lower than the 6.5 % K^{-1} that may be expected from the Clausius-Clapeyron relationship. While scattering aerosols and changes in solar forcing are expected to have a minor influence on global-mean precipitation, their influence cannot be excluded.

1 Introduction

Relative humidity is observed to stay approximately constant under global warming (*Trenberth et al.*, 2007). Therefore, if precipitation was driven by the availability of moisture, one would expect an increase of about 6.5%/K from the Clausius Clapeyron relationship between temperature change and saturation vapor pressure (*Mitchell et al.*, 1987; *Allen and Ingram*, 2002). 20-yr long satellite observations seem to support such an increase (*Wentz et al.*, 2007), although observed precipitation trends strongly differ across data sources (*Trenberth et al.*, 2007; *Arkin et al.*, 2010). On a longer timescale, current Atmosphere-Ocean-General-Circulation-Models (AOGCMs) show a much weaker hydrological sensitivity (HS) of about 1-3%/K (median = 1.7%/K after *Held and Soden* (2006) and 1.4%/K after *Liepert and Previdi* (2009)). The tropospheric energy budget seems to set a more severe constraint on simulated precipitation changes than availability of moisture (e.g. *Mitchell et al.*, 1987; *Allen and Ingram*, 2002; *Held and Soden*, 2006; *Liepert and Previdi*, 2009).

Changes in forcing agents might change global-mean precipitation in two ways (see Figure 1):

(1) via changes in global-mean surface air temperature on a "slow" timescale of years or (2) by practically simultaneous changes of the tropospheric energy budget on a "fast" timescale of days or weeks.

The "slow" response has been shown to be well described by $\alpha \Delta T$, with ΔT being the change in global-mean surface air temperature (e.g. *Andrews et al.* (2009); *Ming et al.* (2010)) and α being approximately independent of the forcing agent (*Andrews et al.*, 2010). A "fast" response occurs as soon as purely radiative top of the atmosphere (TOA) and surface forcing differ as in the case of CO_2 where TOA forcing is higher than radiative surface forcing. Given the small heat capacity of the troposphere, conservation of its energy budget dictates that any tropospheric radiative forcing has to be balanced by sensible or latent heat fluxes – with the latter shown to be dominant, mainly on the basis of instantaneous CO_2 doubling experiments (e.g. *Mitchell et al.* (1987); *Allen and Ingram* (2002); *Yang et al.* (2003); *Lambert and Faull* (2007); *Andrews et al.* (2009)). Additional tropospheric heating will decrease the vertical temperature gradient (lapse rate) – thereby damping convection and ultimately precipitation (*Lambert and Allen*, 2009; *Dong et al.*, 2009).

Other GHGs are expected to have a qualitatively similar effect as CO_2 on the tropospheric energy budget and hence on precipitation. Recently, black carbon (BC) aerosols gained more attention in the context of HS (*Lambert and Allen*, 2009; *Andrews et al.*, 2010; *Ming et al.*, 2010). Absorbing shortwave radiation BC shows a positive TOA forcing (therefore increasing global-mean temperature) while radiative surface forcing is estimated to be negative (*Ramanathan et al.*, 2001). In addition to decreasing sensible heat fluxes at lower layers, BC also induces strong near-instantaneous reductions in latent heating (*Andrews et al.*, 2010; *Lambert and Allen*, 2009), which can even cancel the increase in precipitation expected from the associated warming (*Ming et al.*, 2010).

For scattering aerosols (e.g. tropospheric sulfate aerosols or stratospheric volcanic aerosols) and changes in solar irradiance, TOA forcings are very similar to surface radiative forcings. Not considering possible interactions with BC, their "fast" effects on global precipitation are shown to be small (*Lambert and Faull*, 2007; *Andrews et al.*, 2010), although they might play an important role for regional precipitation (*Ramanathan et al.*, 2001).

Usually, individual climate models were used to analyze the effects of different forcing agents separately. To our knowledge there is only one approach to extract the individual contributions from nine transient multi-forcing 20th century AOGCM runs (*Lambert and Allen*, 2009). We build on this approach, test various predictors and quantify the unexplained inter-scenario variability.

2 Tropospheric energy budget

The energy balance equation for the troposphere can be written as:

$$L\Delta P + \Delta SH = \alpha \Delta T + \Delta R, \tag{1}$$

with specific latent heat L, $L\Delta P$ being the change in latent heat release due to changes in precipitation ΔP, ΔSH the change in sensible heat flux, $\alpha \Delta T$ the net change of radiative fluxes in and out of the troposphere due to changes in global-mean surface air temperature and associated climate feedbacks, and ΔR being the near-instantaneous tropospheric radiative flux divergence. We split ΔR according to the forcing agents expected to be most relevant for precipitation changes, namely GHGs and BC. We furthermore assume that ΔSH can be split into additive components ($\Delta SH = \Delta SH_T + \Delta SH_{GHG} + \Delta SH_{BC}$) and that each of them can be related to the latent heat flux contribution by agent- or temperature specific Bowen Ratios ($B_X = L\Delta P_X / SH_X$, with X being T, GHG or BC). Thus, for relative precipitation change $\Delta P/P$ equation (1) can be rewritten as:

$$\Delta P/P = k_T * \Delta T + k_{GHG} * \Delta R_{GHG} + k'_{BC} * \Delta R_{BC}, \tag{2}$$

where $k_T = \alpha/LP(1 + B_T)$, $k_{GHG} = 1/LP(1 + B_{GHG})$ and $k'_{BC} = 1/LP(1 + B_{BC})$.

3 Data and the statistical model

To test whether equation (2) is able to explain variations in simulated HS we apply a multivariate regression to data from 20 AR4 AOGCMs as available from the CMIP3 model archive (http:\\www-pcmdi.llnl.gov\ipcc\about_ipcc.php). We use the complete set of past (20c3m), future (commit, sresb1, sresa1b, sresa2), and idealized CO_2-only scenarios (1pctto2x, 1pctto4x), if available, including up to 5 ensemble runs for each of the seven scenarios. For each simulation we calculate decadal averages $(\Delta P/P)_{i,j}$ of global-mean precipitation changes (relative to the linear trend of the log-transformed control run data) with i indicating the model and j the scenario. To explain $(\Delta P/P)_{i,j}$, we include the following three predictors, henceforth called "basic" predictors:

1. ΔT: decadal average of global-mean temperature change with respect to the linear trend of the control run.
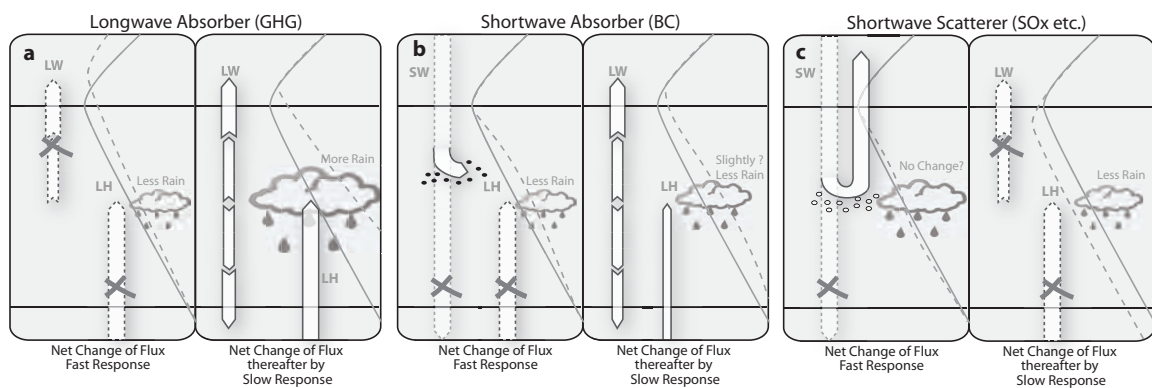
Figure 1: Schematic overview over the "fast" (left hand side of panels a-c) and "slow" (right hand side of panels a-c) effects of different forcing agents on global-mean precipitation. The lapse rate changes on the right hand side combine the "fast" and "slow" response. Panel a) longwave absorbers, b) shortwave absorbers, c) shortwave scattering aerosols. Illustrative changes in the tropospheric energy budget are indicated by arrows; The lapse rates are indicated for the unperturbed state (solid thin lines) and after the forcing perturbation occurred (dashed lines). Figure 1 of the Supplementary shows global energy fluxes for the unperturbed situation.

2. R_{GHG}: weighted sum of TOA forcings based on the assumption that the tropospheric forcing of each GHG component is proportional to its TOA forcing. Agent-specific weightings account for the fact that the ratio of R_{GHG} to F^{TOA} may differ from forcing agent to forcing agent (see Supplementary, Figure 2). TOA forcings are taken from AOGCM-specific emulations (*Meinshausen et al.*, 2008).

3. E_{BC}: global BC emissions, as provided by the AOGCM groups (see Supplementary, Figure 3). Given the relatively short atmospheric residence time of BC, E_{BC} is assumed to be proportional to tropospheric BC forcing ($\Delta R_{BC} \approx \beta E_{BC}$). High correlations between GHG and BC forcings in the 20c3m run that hindered *Lambert and Allen* (2009) analysing BC as separate regressor are less a problem in this study because we analyse both idealized and several multi-forcing scenarios.

With these approximations, the model is given by:

$$
\begin{aligned}
(\Delta P/P)_{i,j} \;=\;\; & (k_T + r_T^{mod,i} + r_T^{scen,i,j}) * \Delta T \\
+ \;\; & (k_{GHG} + r_{GHG}^{mod,i}) * R_{GHG} \\
+ \;\; & (k_{BC} + r_{BC}^{mod,i}) * E_{BC} + \varepsilon_{i,j}
\end{aligned}
\tag{3}
$$

with k_T, k_{GHG}, and $k_{BC} = \beta k'_{BC}$ being the central (multi-AOGCM mean) estimates of the scaling coefficients that are equal or proportional to the coefficients introduced in equation (2). ε describes the residual variability of $\Delta P/P$ not explained by the predictors. The "random effects" framework (*Pinheiro and Bates*, 2000) applied here explicitly allows for AOGCM specific deviations ($r_X^{mod,i}$) from the central scaling coefficients, assumed to stem from normal distributions around zero. We optionally allow for normally distributed scenario-dependent random effect $r_T^{scen,i,j}$ to quantify the remaining scenario-dependency of the HS. That random effect should ideally be small, if the predictors explain precipitation changes sufficiently well. The models excluding and including $r_T^{scen,i,j}$, are subsequently called "standard" and "extended", respectively. All scaling coefficients k_X and standard deviations σ_X^{mod} (and σ_T^{scen}) of the random effects are estimated by a restricted maximum likelihood approach using the R-package "nlme" (*Pinheiro and Bates*, 2000). To assist comparison of the resulting coefficients, we normalized R_{GHG} and E_{BC} by the reciprocal of the averages across all AOGCMs in 1999. Besides σ_T^{scen} the Bayesian information criterion (BIC) is used to describe the performance of the statistical model.

4 Performance of the basic model including T, GHG and BC

For some AOGCMs the relation between global-mean precipitation and temperature clearly depends on the considered emission scenario (see Figure 2). There is a pronounced difference between the idealized CO_2 doubling and quadrupling runs and the multi-forcing runs, especially for models including BC effects. For some of the BC runs the forcing effect even leads to a reduction in precipitation in the 20c3m run, an effect also found in some of the BC experiments by *Ming et al.* (2010). During stabilization, the solely temperature driven increase in precipitation is particularly strong while near-instantaneous radiative effects dampen the increase during other periods (*Wu et al.*, 2010).

Our "standard" model including our set of "basic" predictors provides a very good fit to the AOGCM data. HS is estimated to be 2.2 %/K, with $\sigma_T^{mod} = 0.51\%/K$ (see Table 1). This value is slightly smaller than the 2.4%/K found for the stabilization periods of the idealized model runs (*Andrews and Forster*, 2010). The difference might be due to shortcomings of the fixed weightings applied to TOA GHG forcings (see section 5) or a slightly different set of AOGCMs. Increasing GHG forcing and BC emissions leads to a strong near-instantaneous change in precipitation of -0.42 $\pm$ 0.21 %/(W/m^2) for R_{GHG} and $-0.07 \pm 0.02\%/(Mt/yr)$ for E_{BC}. The central value of the scaling coefficients is close to or larger than $2\sigma_X^{mod}$ for all three predictors indicating that the effects are basically consistent across the range of considered AOGCMs (see Table 1).

The inter-scenario variability estimated by the "extended" model versions can be reduced by more than 50% (from 0.37 %/K to 0.16 %/K) by including R_{GHG} and E_{BC}. The central estimates are not strongly affected by the inclusion of the scenario dependent random effect r_T^{scen}. Comparing the different models by the BIC clearly shows that the model containing the three "basic" predictors is superior to the reduced one only including ΔT (see Supplementary, Table 1).

5 Sensitivity analysis

One shortcoming using R_{GHG} are the fixed weightings to calculate the aggregate R_{GHG} from individual TOA forcings (see Supplementary). Ideally, each TOA forcing component would be included separately into the regression allowing for AOGCM-specific scaling coefficients for each forcing agent individually. The high correlation of the TOA forcing time series does
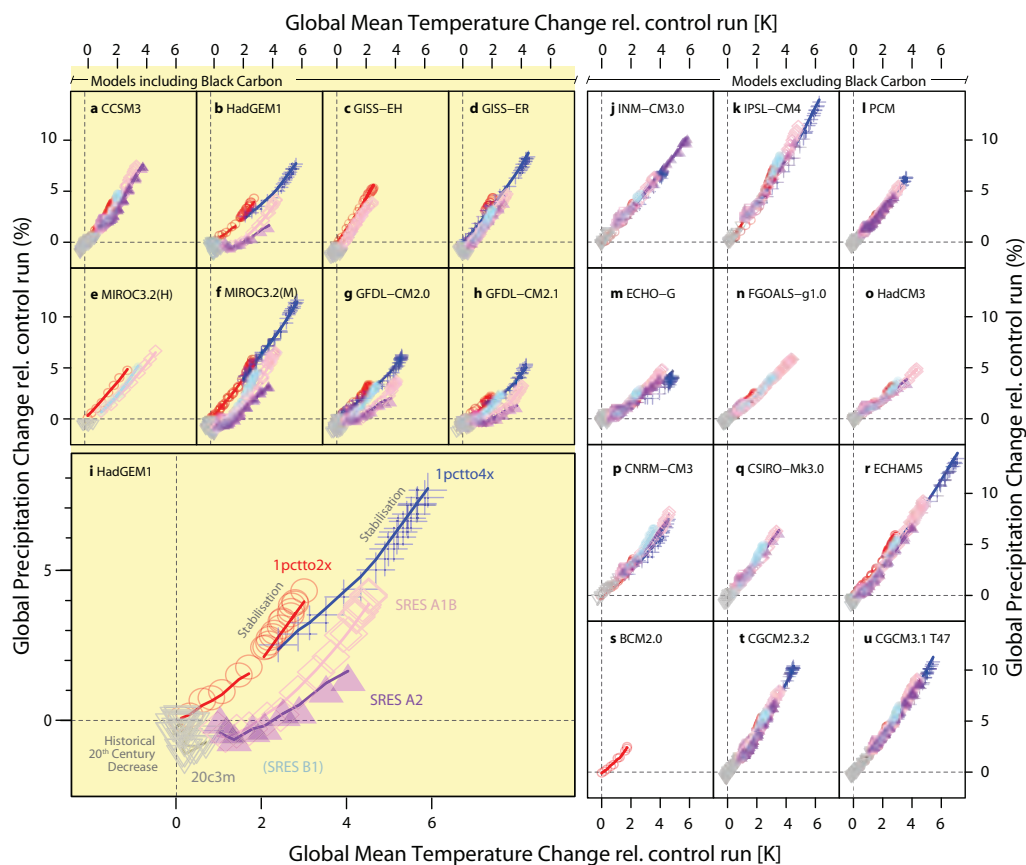
Figure 2: Ten-year averages of relative change in global-mean precipitation with respect to the pre-industrial control run (except of the idealized runs of CCSM3, ECHO-G, CGCM2.3.2, and PCM that branch from the present-day control run) plotted against global-mean temperature change. Eight AOGCMs took BC into account (panels a to i). Projections of our "standard" model (best linear unbiased estimates) are shown in solid lines, using the three "basic" predictors: T, R_{GHG}, and E_{BC}. The HadGEM1 diagnosis (panel b) is enlarged for illustrative purposes (panel i).

however not allow that approach. Because we include the idealized runs, in which only CO_2 is varied, we can at least split up R_{GHG} into the tropospheric forcing induced by CO_2, R_{CO_2}, and the remainder, $R_{GHG \setminus CO_2}$. Including both components into the statistical model provides larger coefficients for the CO_2 component and smaller ones for $R_{GHG \setminus CO_2}$ (see Table 1). This indicates that our weights for aggregating R_{GHG}, which are based on the available literature on surface forcings, might have to be reduced for the other GHGs in comparison to CO_2. The estimated HS of 2.3%/K is slightly closer to the estimate of *Andrews and Forster* (2010).

We also tested an array of additional predictors. These are sulfate emissions (E_{SOx}), volcanic forcing (F_{volc}), solar forcing (F_{solar}), interaction effects between BC and sulfate aerosols (i.e., the product of normalized BC and sulfate emissions, $I_{BC,SOx}$), and analogously $I_{BC,volc}$ and $I_{BC,solar}$. While E_{SOx} and F_{solar} were normalized analogously to E_{BC} and R_{GHG}, F_{volc} was normalized with respect to 1991, the year of the Pinatubo eruption. Stepwise inclusion of these predictors still reduces the BIC but in smaller steps (see Supplementary, Table 1). The "standard" model including additional predictors improves only slightly on the model with the "basic" predictors (see Supplementary, Figure 7). There is nearly no further reduction in σ_T^{scen} estimated by the "extended" model.

While the scaling coefficients of the basic predictors are relatively stable across the different model versions, the effects of the additional components turn out to be smaller and less consistent across AOGCMs as evident from the comparison of the central estimates and their inter-AOGCM variations σ_X^{model} (shown for a selected set of model versions in Table 1). The effect of E_{SOx} per unit mass of emissions is more then one order of magnitude smaller than the BC effect and not significantly different from zero. That is expected from TOA and surface forcings being nearly identical for sulfate aerosols. However, there seems to be a larger interaction effect indicating that precipitation is reduced when SOx emissions are increased in presence of BC. This might be due to more absorption of shortwave radiation by BC when shortwave radiation is scattered by sulfate aerosols - an interaction effect that depends on the vertical distribution of both BC and sulfates. The sign of the scaling coefficient related to F_{volc} is consistent with the expectation that a reduction in shortwave radiation passing the troposphere leads to less absorption of shortwave radiation. The absolute value of the scaling coefficients is relatively small as expected from the fact that TOA and surface forcing of volcanic aerosols do not differ strongly.

The signs of the other scaling coefficients found for $I_{BC,volc}$, F_{solar}, and $I_{BC,solar}$ are not consistent with our expectation based on tropospheric energy budget considerations. Increases in stratospheric aerosols should reduce the amount of shortwave radiation reaching the troposphere, which in turn should lead to less absorbtion of shortwave radiation by BC particles and increased precipitation. Similarly, increasing solar forcing should lead to (slightly) more

| Predictor | Sensitivity Coefficient | Normalized | | |
	Central Est.	Central Est.	Std.Error	σ^{mod}
Standard model				
$\Delta T_{\mathrm{global}}$	2.203 %/K	2.203	0.115	0.509
R_{GHG}	-0.424 %/(W/m ^{2})	-0.815	0.094	0.411
E_{BC}	-0.069 %/(Mt/yr)	-0.943	0.092	0.256
$\Delta T_{\mathrm{global}}$	2.294 %/K	2.294	0.119	0.526
R_{CO_2}	-0.531 %/(W/m ^{2})	-1.021	0.154	0.682
$R_{GHG\backslash CO_2}$	-0.158 %/(W/m ^{2})	-0.304	0.201	0.849
E_{BC}	-0.087 %/(Mt/yr)	-1.188	0.155	0.425
$\Delta T_{\mathrm{global}}$	2.238 %/K	2.238	0.109	0.481
R_{GHG}	-0.476 %/(W/m ^{2})	-0.916	0.113	0.492
E_{BC}	-0.070 %/(Mt/yr)	-0.952	0.273	0.720
E_{SOx}	0.001 %/(MtS /yr)	0.042	0.117	0.485
$I_{\mathrm{BC, SOx}}$	< -0.001 %/(Mt*MtS/yr^2)	-0.272	0.094	0.199
F_{volc}	-0.188 %/(W/m ^{2})	-0.183	0.121	0.337
$I_{\mathrm{BC, volc}}$	0.046 %/(Mt/yr*W/m ^{2})	0.610	0.155	0.264
F_{solar}	2.135 %/(W/m ^{2})	0.289	0.150	0.560
$I_{\mathrm{BC, solar}}$	0.049 %/(Mt/yr*W/m ^{2})	0.091	0.238	0.551
Extended model with inter-scenario variability				
$\Delta T_{\mathrm{global}}$	2.324 %/K	2.324	0.115	0.506
R_{GHG}	-0.488 %/(W/m ^{2})	-0.939	0.127	0.563
E_{BC}	-0.068 %/(Mt/yr)	-0.933	0.062	0.156
$\Delta T_{\mathrm{global}}$	2.330 %/K	2.330	0.102	0.444
R_{CO2}	-0.500 %/(W/m ^{2})	-0.961	0.132	0.583
$R_{GHG\backslash CO_2}$	-0.363 %/(W/m ^{2})	-0.699	0.202	0.832
E_{BC}	-0.077 %/(Mt/yr)	-1.052	0.095	0.227

Table 1: Central estimates of the scaling coefficients (fixed effects), their standard errors and the standard deviation of the associated inter-model variabilities estimated by the "standard" and "extended" model. Central estimates are provided in standard units and normalized towards 1999 or 1991 in the case of volcanic forcing, respectively.

shortwave absorption in the troposphere and small decreases in precipitation as also seen in the experiments by *Andrews et al.* (2010). In both cases, we find however a positive scaling coefficient with the reasons for this disagreement being presently unclear. The common feature of these "problematic" forcings is that their variations are limited to the 20c3m run which represents a relatively small part of the whole data set. Analysing the 20c3m runs *Lambert and Allen* (2009) also found positive scaling coefficients for their forcing component that combines volcanic and tropospheric sulfate aerosol forcings. There might be correlated forcings that influence these scaling coefficients. As well, the regression could erroneously relate a part of the temperature dependent response to these forcing components.

We trained our statistical model on all available CMIP3 scenarios. Thus, the question is how suitable our approach might be for projecting changes for non-calibrated scenarios. We tested the prediction skill of the "standard" model with our "basic" predictors by excluding one scenario after another from the regression and by predicting changes in relative precipitation for the excluded scenario. As illustrative goodness of fit measure, we computed a root mean square error (RMSE) of 0.34% precipitation changes across all scenarios. This can be compared to a RMSE of 0.24% when all available datapoints are used for calibration. Given the overall magnitude of modelled precipitation changes of up to 5% and 10%, the prediction skill of our statistical approach is comparatively good (see Supplementary, Figure 8).

6 Conclusions

Our study contributes to the theoretical understanding of modelled global-mean precipitation changes. Going beyond a simple linear scaling with global-mean temperatures, we have shown that modelled HS and its variations across scenarios are remarkably well reproduced by three predictors: global-mean temperature change, tropospheric GHG forcing and BC emissions. We presented here the first study analyzing a comprehensive set of AOGCMs across the full range of future SRES and idealized scenarios from the CMIP3 archive. We were able to quantify the distinct precipitation sensitivities by drawing information from the time-varying information within and the comparison across different scenarios.

Given the skill for predicting global-mean precipitation changes, multiple scenarios could now be modeled including those not yet run by a comprehensive set of AOGCMs. The forthcoming datasets of CMIP5, for which AOGCMs are likely driven with a more standardized and comprehensive set of forcings for more model years, will allow a verification and refinement of this statistical approach to project and explain global-mean precipitation changes across a wide range of future scenarios.

Acknowledgments

Literature

Allen M. R., W. J. Ingram, "Constraints on future changes in climate and the hydrological cycle," *Nature,* **419,** (2002).

Andrews T., P. M. Forster, O. Boucher, N. Bellouin, A. Jones, "Precipitation, radiative forcing and global temperature change," *Geophysical Research Letters,* **37,** 14, L14701 (2010).

Andrews T., P. M. Forster, "The transient response of global-mean precipitation to increasing carbon dioxide levels," *Environmental Research Letters,* **5,** 025212 (2010).

Andrews T., P. M. Forster, J.M. Gregory, "A surface energy perspective on climate change," *Journal of Climate,* **22,** 2557–2570 (2009).

Arkin P. A., T. M. Smith, M. R. P. Sapiano, J. Janowiak, "The observed sensitivity of the global hydrological cycle to changes in surface temperature," *Environmental Research Letters,* **5,** 035201, doi:10.1088/1748-9326/5/3/035201 (2010).

Dong B., J.M. Gregory, R.T, Sutton, "Understanding land-sea warming contrast in response to increasing greenhouse gases. Part I: Transient Adjustment," *Journal of Climate,* **22,** 3079–3097 (2009).

Held I. M., B. J. Soden, "Robust responses of the hydrological cycle to global warming," *Journal of Climate,* **19,** 5686–5699 (2006).

Lambert F. H., M. R. Allen, "Are changes in global precipitation constrained by the tropospheric energy budget?," *Journal of Climate,* **22,** doi:10.1175/2008JCLI2135.1 (2009).

Lambert F. H., N. E. Faull, "Tropospheric adjustment: The response of two general circulation models to a change in insolation," *Geophysical Research Letters,* **34,** L03701, doi:10.1029/2006GL028124 (2007).

Liepert B. G., M. Previdi, "Do models and observations disagree on the rainfall response to global warming?," *Journal of Climate,* **22,** doi:10.1175/2008JCLI2472.1 (2009).

Meinshausen M., S. C. B. Raper, T. M. L. Wigley, "Emulating IPCC AR4 atmosphere-ocean and carbon cycle models for projecting global-mean, hemispheric and land/ocean temperatures: MAGICC 6.0," *Atmos. Chem. Phys. Discuss.,* **8,** 6153–6272 (2008).

Ming Y., V. Ramaswamy, G. Persad, "Two opposing effects of absorbing aerosols on global-mean precipitation," *Geophysical Research Letters,* **37,** L13701, doi:10.1029/2010GL042895 (2010).

Mitchell J. F. B., C. A. Wilson, W. M. Cunnington, "On CO_2 climate sensitivity and model dependence of results," *Q.J.R. Meteorol. Soc.,* **113,** 293–322 (1987).

Pinheiro J. C., D. M. Bates, "Mixed-effects models in S and S-PLUS," *Statistics and Computing, Springer, New York* (2000).

Ramanathan V., P. J. Crutzen, J.T. Kiehl, D. Rosenfeld, "Aerosols, climate, and the hydrological cycle," *Science,* **294,** 2119–2124 (2001).

Trenberth, K.E., P.D. Jones, P. Ambenje, R. Bojariu, D. Easterling, A. Klein Tank, D. Parker, F. Rahimzadeh, J.A. Renwick, M. Rusticucci, B. Soden and P. Zhai, "Observations: Surface and atmospheric climate change. In: Climate Change 2007: The Physical Science Basis. Contribution of Working Group I to the Fourth Assessment Report of the Intergovernmental Panel on Climate Change," *Cambridge University Press,* Cambridge, United Kingdom and New York, NY, USA (2007).

Wentz, F.J., L. Ricciardulli, K. Hilburn, C. Mears, "How much more rain will global warming bring?," *Nature,* **317,** 233–235 (2007).

Wu P., R. Wood, J. Ridley, J. Lowe, "Temporary acceleration of the hydrological cycle in response to a CO_2 rampdown," *Geophysical Research Letters,* **37,** L12705, doi:10.1029/2010GL043730 (2010).

Yang F., A. Kumar, M. E. Schlesinger, W. Wang, "Intensity of hydrological cycles in warmer climates," *J. Climate,* **16,** 2419–2423 (2003).

Supplementary Material – Projected Global-mean Precipitation in Response to Warming, Greenhouse Gas Forcing and Black carbon

K. Frieler, [1] M. Meinshausen, [1] T. Schneider von Deimling, [1] T. Andrews, [2] and P. Forster [2]

[1] Earth System Analysis, Potsdam Institute for Climate Impact Research, Potsdam, Germany

[2] School of Earth and Environment, University of Leeds, Leeds, United Kingdom

1 Global energy fluxes

Our schematic illustrations of the forcing agent effects (see Figure 1 in the main article) show the net change of fluxes departing from the "base" case of global energy fluxes shown in Figure 1 below.
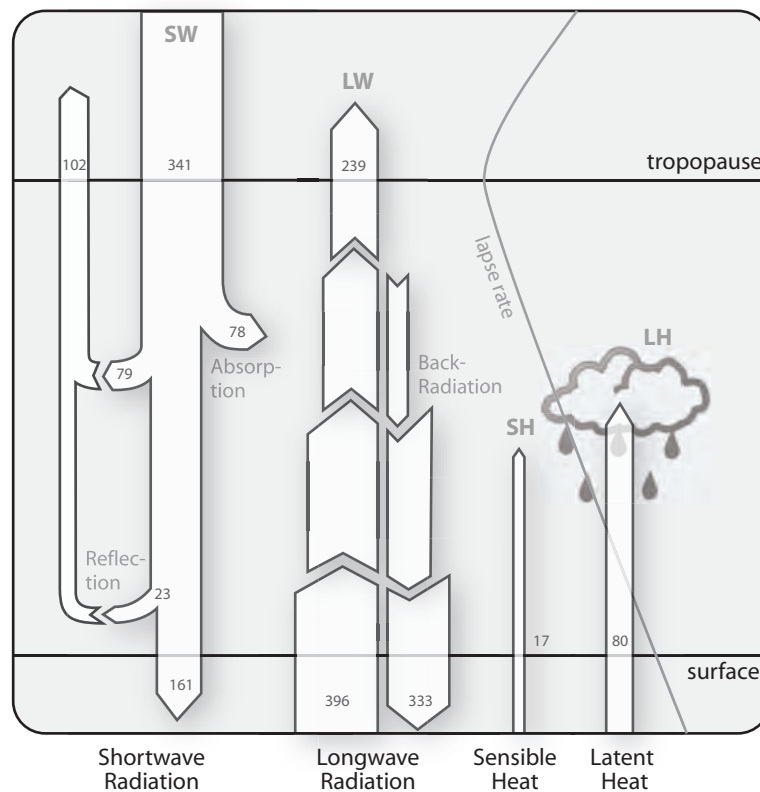
Figure 1: Global energy fluxes following *Trenberth et al.* (2009) with flux sizes provided in Wm^{-2}

2 Tropospheric GHG forcing

We use transient forcing information for CO_2, CH_4, N_2O, halocarbons (HALO), flourinated (FGAS), and tropospheric ozone (*Meinshausen et al.*, 2008) and define the second predictor R_{GHG} as a weighted sum of these forcings. As mentioned in Section 3 of the main article, weightings are introduced to account for the fact that the ratio of R_{GHG} to F^{TOA}, i.e. the

part of the adjusted TOA-forcing which is modifying the tropospheric energy budget, may differ from forcing agent to forcing agent. Actually, R_{GHG} is the difference between the top of the atmosphere forcing F^{TOA} and the surface radiative forcing F^{surf}. Thus, our weights are chosen to approximate $Q = 1 - F^{surf}/F^{TOA}$. Based on Figure 2.23 of *Forster et al.* (2007) Q is set to 0.8 except for CH_4 and tropospheric ozone. *Andrews et al.* (2010) calculated a separate value of $Q = 0.5$ for CH_4 which was used for our study. In case of tropospheric ozone Q was set to 0.4 according to Figure 2.23 of *Forster et al.* (2007). Thus, our default aggregation is $R_{GHG} = 0.8F_{CO2}^{TOA} + 0.8F_{N2O}^{TOA} + 0.8F_{HALO}^{TOA} + 0.8F_{FGAS}^{TOA} + 0.5F_{CH4}^{TOA} + 0.4F_{trop.ozone}^{TOA}$ for each of the considered 20 AOGCMs (see Figure 2). Most of the AOGCM simulation include a (relatively short) stabilization period where GHG concentrations are held constant after a transient increase (see Figure 2). As BC does not vary during these periods, associated changes in global-mean precipitation are solely due to temperature changes. When the R_{GHG} is split up (see section 5 of the main article) $R_{CO2} = 0.8F_{CO2}^{TOA}$ and $R_{GHG\backslash CO2} = 0.8F_{N2O}^{TOA} + 0.8F_{HALO}^{TOA} + 0.8F_{FGAS}^{TOA} + 0.5F_{CH4}^{TOA} + 0.4F_{trop.ozone}^{TOA}$.
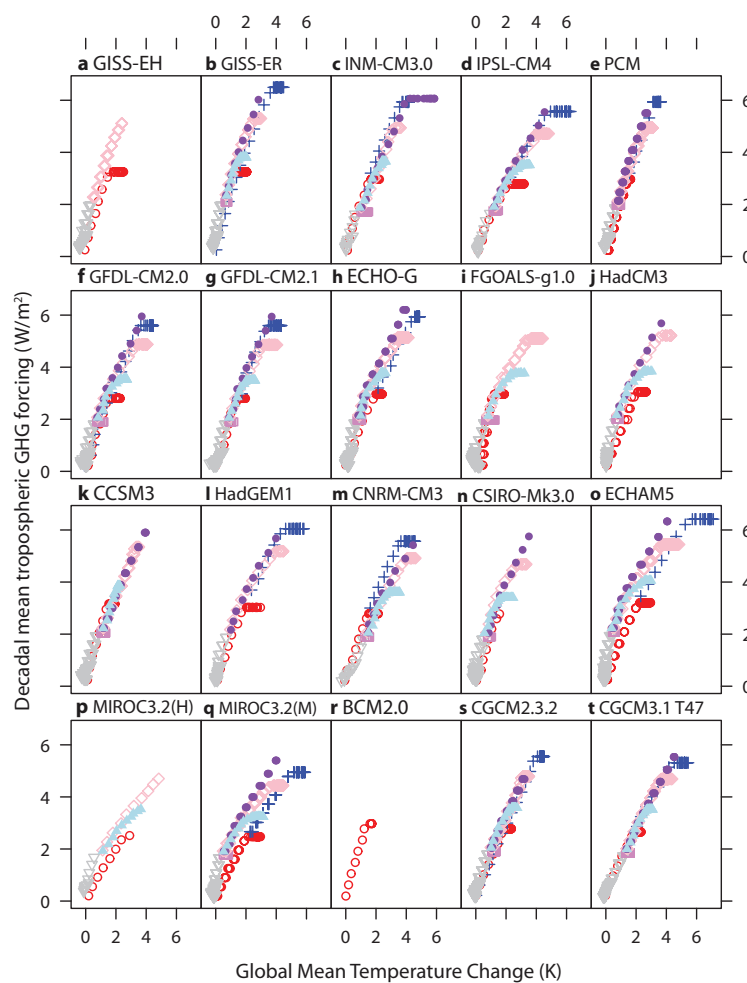
Figure 2: Ten-year averages of tropospheric GHG forcing R_{GHG} estimated from adjusted TOA forcings as: $R_{GHG} = 0.8F_{CO2}^{TOA} + 0.8F_{N2O}^{TOA} + 0.8F_{HALO}^{TOA} + 0.8F_{FGAS}^{TOA} + 0.5F_{CH4}^{TOA} + 0.4F_{trop.ozone}^{TOA}$. Each box represents the results of one AOGCM and color coding indicates the different scenarios (red = 1pctto2x, blue = 1pctto4x, grey = 20c3m, violet = commit, pink = sresa1b, purple = sresa2, lightblue = sresb1).

3 Black carbon emissions

For the CMIP3 experiments, no standardized set of BC emission time series has been applied by the AOGCMs. Therefore, our third predictor is defined by the globally averaged information directly provided by the eight individual modelling groups that include BC in their simulations. Emissions for the 20c3m GISS-simulations were taken as the mean value of the data used by the other AOGCMs. After 2000 BC was held constant in the GISS simulations independent of the considered SRES scenario. In case of the CCSM3 model we also adjusted BC emissions towards matching the mean BC emission data reported for the other AOGCMs in the year 2000. To describe the temporal evolution of the emissions we applied the scaling factors which were used to describe the temporal evolution of BC loadings within the simulations.
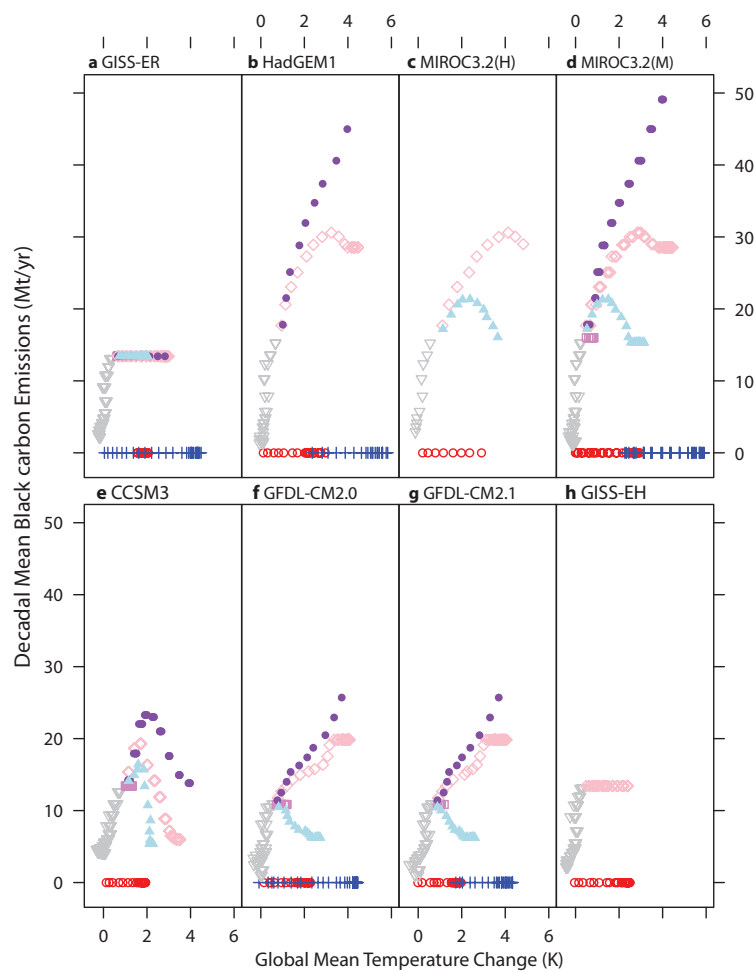
Figure 3: Globally averaged black carbon emission time series (ten-year averages, [Mt/yr]) used within the regression approach. Color coding indicates the different scenarios (red = 1pctto2x, blue = 1pctto4x, grey = 20c3m, violet = commit, pink = sresa1b, purple = sresa2, lightblue = sresb1).

4 Additional predictors

In this Appendix, we briefly show the numerical values of the additional predictors investigated for each of the 20 AOGCMs, namely SOx emissions (see Figure 4), solar forcing (see Fig. 5), and volcanic forcing (see Fig. 6). These additional predictors are either taken directly from the SRES emissions scenarios (SOx emissions), or applied as in previous calibration studies (solar and volcanic forcing), taking into account AOGCM-specific volcanic forcing amplitudes based on the analysis by *Forster and Taylor* (2006) as described in *Meinshausen et al.* (2008). The Bayesian Information Criterion (BIC) calculated with the "standard" statistical model and the inter-scenario variability (σ_T^{scen}) calculated with the "extended" statistical model for the different sets of predictors is provided in Table 7 below. The graphical comparison between AOGCM data and the projected precipitation changes under the "standard" model using all predictors is provided in Figure 8.

Figure 4: As Figure 3, but for globally averaged SOx emissions.

Figure 5: As Figure 3, but for solar TOA forcing time series.

Figure 6: As Figure 3, but for stratospheric volcanic aerosol TOA forcing time series.

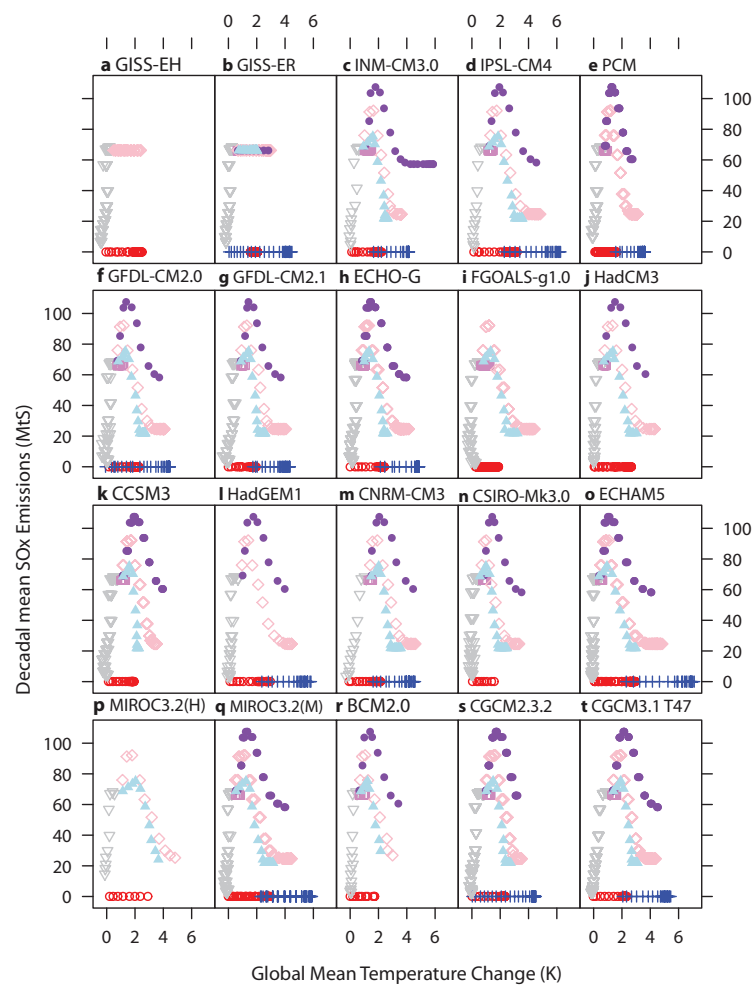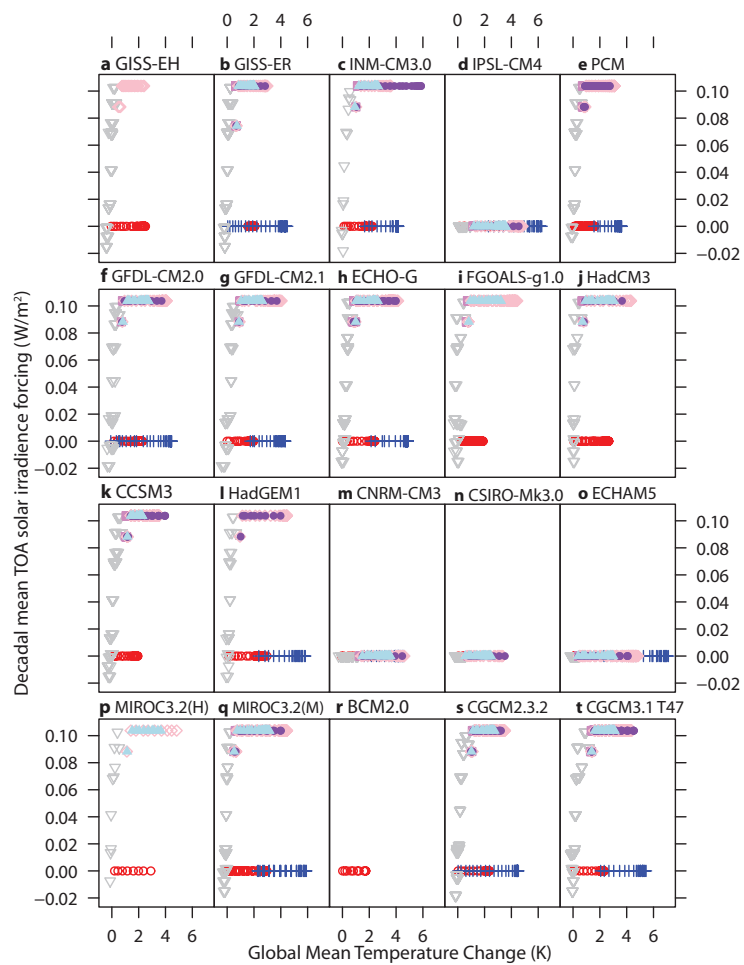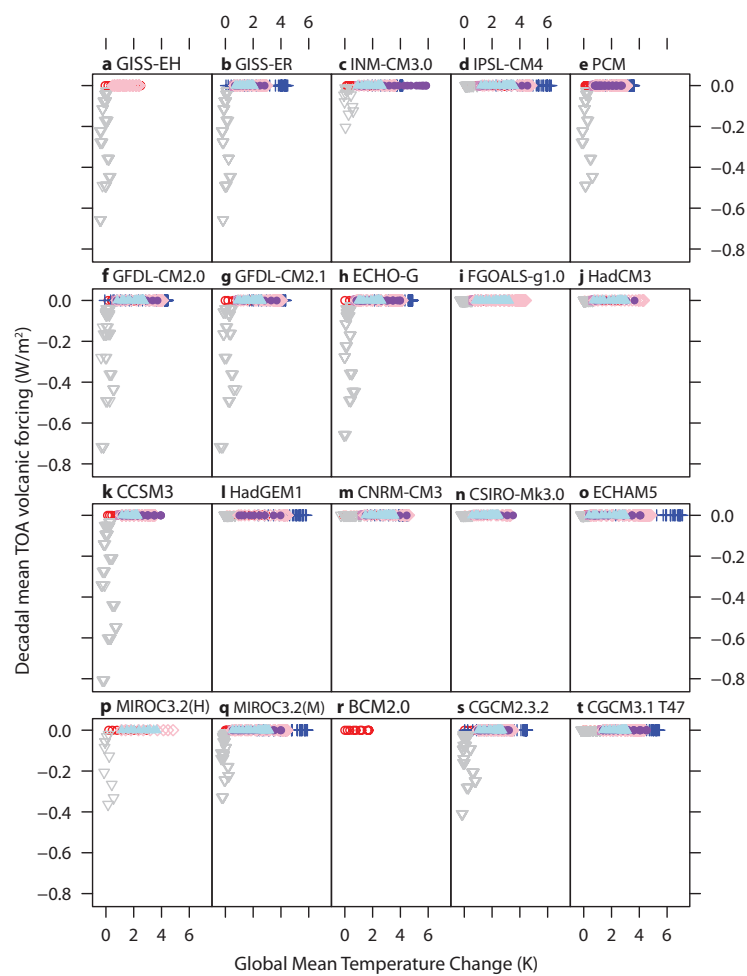| model	BIC	σ_{scen}
ΔT_{global}	4930.090	0.373
$\Delta T_{\text{global}} + R_{\text{GHG}}$	1646.869	0.255
$\Delta T_{\text{global}} + R_{\text{GHG}} + E_{\text{BC}}$	-343.659	0.156
$\Delta T_{\text{global}} + R_{\text{GHG}} + E_{\text{BC}} + E_{\text{SOx}}$	-611.357	0.153
$\Delta T_{\text{global}} + R_{\text{GHG}} + E_{\text{BC}} + I_{\text{BC, SOx}} + E_{\text{SOx}}$	-806.473	0.145
$\Delta T_{\text{global}} + R_{\text{GHG}} + E_{\text{BC}} + I_{\text{BC, SOx}} + E_{\text{SOx}} + F_{\text{solar}}$	-1654.878	0.148
$\Delta T_{\text{global}} + R_{\text{GHG}} + E_{\text{BC}} + I_{\text{BC, SOx}} + E_{\text{SOx}} + I_{\text{BC, solar}} + F_{\text{solar}}$	-1659.893	0.148
$\Delta T_{\text{global}} + R_{\text{GHG}} + E_{\text{BC}} + I_{\text{BC, SOx}} + E_{\text{SOx}} + I_{\text{BC, solar}} + F_{\text{solar}} + F_{volc}$	-1741.821	0.137
$\Delta T_{\text{global}} + R_{\text{GHG}} + E_{\text{BC}} + I_{\text{BC, SOx}} + E_{\text{SOx}} + I_{\text{BC, solar}} + F_{\text{solar}} + F_{volc} + I_{volc,BC}$	-1759.413	0.128
$\Delta T_{\text{global}} + R_{CO_2} + R_{GHG \backslash CO_2} + E_{\text{BC}}$	-1140.178	0.160
$\Delta T_{\text{global}} + R_{CO_2} + R_{GHG \backslash CO_2} + E_{\text{BC}} + E_{\text{SOx}}$	-1810.197	0.145
$\Delta T_{\text{global}} + R_{CO_2} + R_{GHG \backslash CO_2} + E_{\text{BC}} + I_{\text{BC, SOx}} + E_{\text{SOx}}$	-1949.164	0.139
$\Delta T_{\text{global}} + R_{CO_2} + R_{GHG \backslash CO_2} + E_{\text{BC}} + I_{\text{BC, SOx}} + E_{\text{SOx}} + F_{\text{solar}}$	-2326.065	0.139
$\Delta T_{\text{global}} + R_{CO_2} + R_{GHG \backslash CO_2} + E_{\text{BC}} + I_{\text{BC, SOx}} + E_{\text{SOx}} + I_{\text{BC, solar}} + F_{\text{solar}}$	-2326.198	0.138
$\Delta T_{\text{global}} + R_{CO_2} + R_{GHG \backslash CO_2} + E_{\text{BC}} + I_{\text{BC, SOx}} + E_{\text{SOx}} + I_{\text{BC, solar}} + F_{\text{solar}} + F_{volc}$	-2419.800	0.126
$\Delta T_{\text{global}} + R_{CO_2} + R_{GHG \backslash CO_2} + E_{\text{BC}} + I_{\text{BC, SOx}} + E_{\text{SOx}} + I_{\text{BC, solar}} + F_{\text{solar}} + F_{volc} + I_{\text{BC, volc}}$	-2437.472	0.116

Figure 7: Two indicators to measure appropriateness of statistical model: Bayesian information criterion values derived from stepwise inclusion of the different predictors into our "standard" model (second column) and the inter-scenario variability σ^{scen} estimated by the "extended" statistical model (third column). The BIC decreases with improved model versions. It represents a measure of the model fit adding a penalty term for the number of parameters to avoid overfitting.
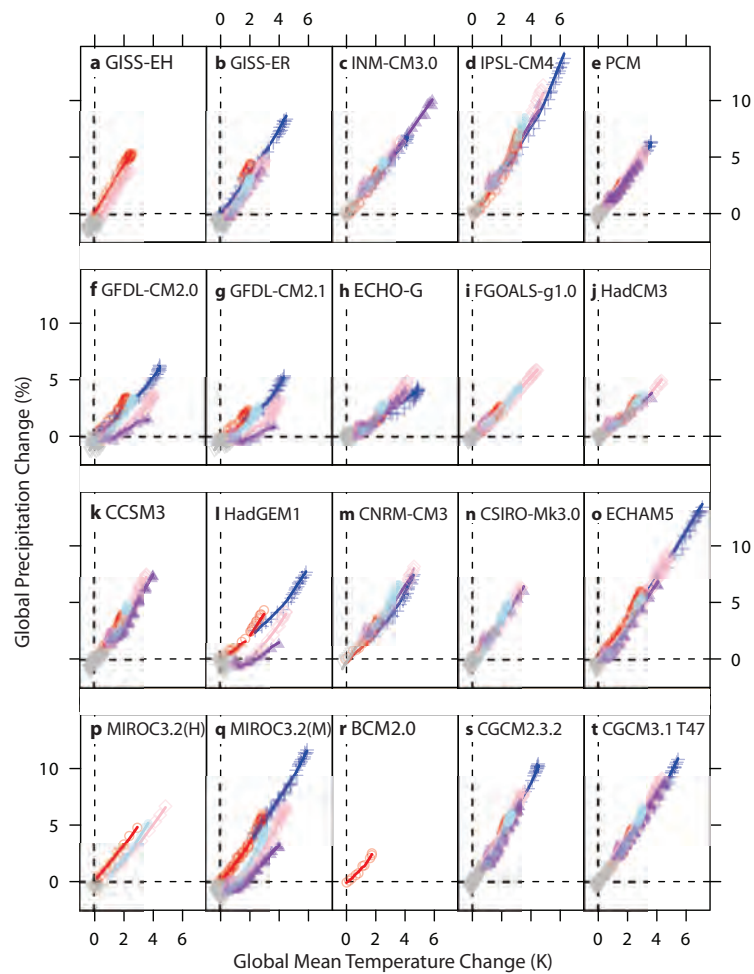
Figure 8: Analogously to Figure 2 in the main article, but using all predictors listed in Table 7.

5 Cross validation

Here, we present the comparison between AOGCM data and the "standard" model (analogously to Figure 2 in the main article) for the our sensitivity calibrations. In these sensitivity calibrations, the AOGCM data for one of the SRES or idealized scenarios has not been used for calibrating the statistical "standard" model. For the scenario that has been left out, the global-mean precipitation changes were then predicted based on the parameters estimated for the remaining scenarios. The below Figure 9 shows all scenarios for the 20 AOGCMs and these corresponding predictions - illustrating that the prediction skill is slightly less good for each scenarios, but still relatively good (i.e. average RMSE of 0.34% instead of 0.24 % in the case presented in Figure 2 in the main article).
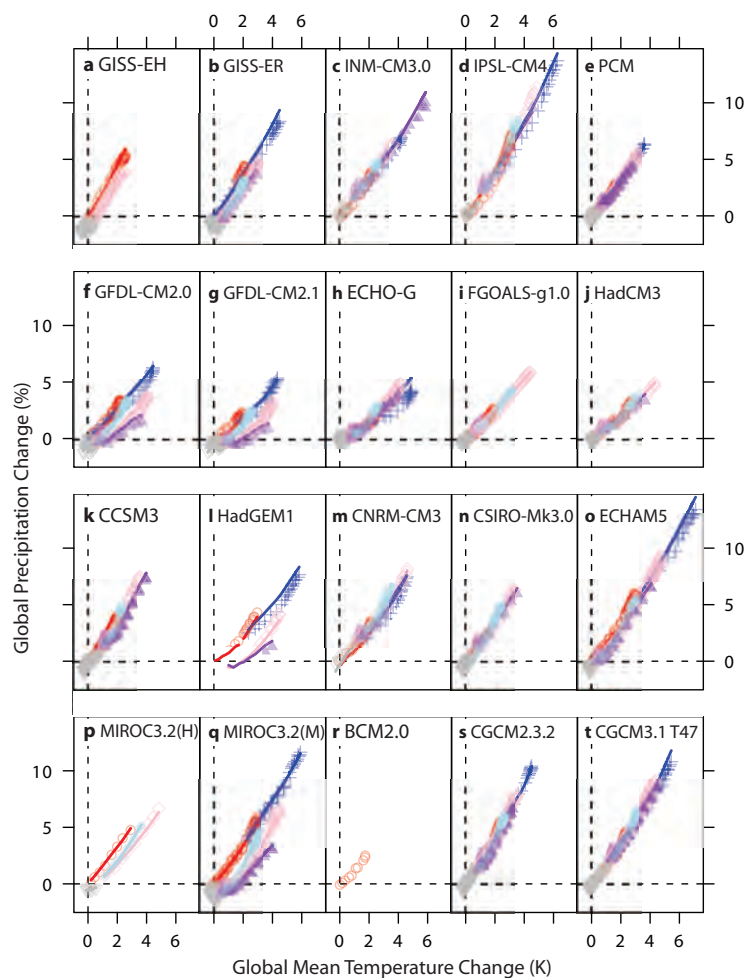
Figure 9: As Figure 2, but using for each individual scenario projection the "standard" model's parameters that have been calibrated on the basis of all AOGCM scenario, except the one predicted. See text.

Literature

Andrews T., P. M. Forster, O. Boucher, N. Bellouin, A. Jones, "Precipitation, radiative forcing and global temperature change," *Geophysical Research Letters,* **37,** 14, L14701 (2010).

Forster P., V. Ramaswamy, P. Artaxo, T. Berntsen, R. Betts, D.W. Fahey, J. Haywood, J. Lean, D.C. Lowe, G. Myhre, J. Nganga, R. Prinn, G. Raga, M. Schulz, R. Van Dorland, "Changes in atmospheric constituents and radiative forcing", In: Climate Change 2007: The Physical Science Basis. Contribution of WG I to the fourth Assessment Report of the Intergovernmental Panel on Climate Change, *Cambridge University Press,* Cambridge, United Kingdom and New York, NY, USA, (2007).

Forster, P. M. D., K. E. Taylor, "Climate forcings and climate sensitivities diagnosed from coupled climate model integrations," *Journal of Climate, 19,* **23,** 6181–6194 (2006).

Meinshausen M., S. C. B. Raper, T. M. L. Wigley, "Emulating IPCC AR4 atmosphere-ocean and carbon cycle models for projecting global-mean, hemispheric and land/ocean temperatures: MAGICC 6.0," *Atmos. Chem. Phys. Discuss.,* **8,** 6153–6272 (2008).

Trenberth, K. E., J. T. Fasullo, J. Kiehl, "Earth's Global Energy Budget," *Bulletin of the American Meteorological Society,* **90,** 3, 311-323, doi:10.1175/2008BAMS2634.1 (2009).

Chapter 3 Precipitation Scaling Regional

A scaling approach to probabilistic assessment of regional climate change

K. Frieler, [1] M. Meinshausen, [1] M. Mengel, [1] N. Braun, [2] W. Hare [3]

[1] Potsdam Institute for Climate Impact Research (PIK), Potsdam, Germany.

[2] Ecofys, Cologne, Germany

[3] Climateanalytics, Potsdam, Germany.

This part of our UFOPLAN work is documented in the manuscript "A scaling approach to probabilistic assessment of regional climate change" by K. Frieler et al., submitted to Journal of Climate, when this report was finalized.

Abstract

A new approach to probabilistic projections of regional climate change is introduced. It builds on the already established quasi-linear relation between global mean temperature and regional climate change found in Atmosphere Ocean General Circulation Models (AOGCMs). The new approach (a) it takes correlations between temperature and precipitation related uncertainty distributions into account, (b) enables to include predictors other than global mean temperature, (c) and checks the validity of the scaling relationships. We test SOx and black carbon emissions and greenhouse gas forcings as additional predictors of precipitation changes. These changes are found to deviate substantially from linear relationship with global mean temperature change in some regions. Thereby the two main limitations of a simple linear scaling approach – ignoring regional aerosol effects and changes in scaling coefficients when approaching equilibrium conditions – are addressed. The additional predictors can markedly improve the emulation of AOGCM simulations. In some regions, the variations of hydrological sensitivity (the percentage change of precipitation per degree of warming) across different scenarios can be reduced by more than 50%. Coupled to probabilistic projections of global mean temperatures and greenhouse gas forcings, bi-dimensional distributions of regional temperature and precipitation changes accounting for multiple uncertainties are derived. Based on 20 AR4-AOGCMs, probabilistic projections are provided for the RCP scenarios and 31 world regions (online database at: www.pik-potsdam.de/∼frieler/regional). As an example application of further impact, adaptation and vulnerability studies changes in surface mass balance of the Greenland ice sheet are computed.

1. Introduction

Probabilistic assessment of regional climate change for future emission scenarios is challenging as there are multiple sources of uncertainty that have to be taken into account. The cause effect chain reaches from emissions via the carbon cycle and atmospheric chemistry to atmospheric abundances, radiative forcings, and the induced regional patterns of temperature and precipitation response. In the context of simple climate models, a synthesis of uncertainties along the cause-effect chain linking emissions to global mean temperature changes can be performed [Allen et al., 2009, Meinshausen et al., 2009]. Unfortunately, comprehensive uncertainty assessments are usually too computationally intensive to be performed within AOGCMs that provide regional information, although some larger perturbed physics studies exist [e.g. Stainforth et al., 2005].

It is a remarkable property of the climate change signal simulated by AOGCMs that various regional surface climate variables are fairly linearly related to global mean temperature change where scaling coefficients are largely independent of the underlying emission scenario [Santer et al., 1990, Mearns et al., 2001, Mitchell, 2003, Giorgi, 2008, Solomon et al., 2009]. This relation provides an efficient way to obtain regional, probabilistic climate projections: The scaling coefficients can be used to derive regional climate projections for emissions scenarios not simulated by AOGCMs using reduced complexity climate models that only project large scale aggregated quantities. Furthermore, estimating these scaling coefficients for a large number of different AOGCMs provides a way to capture the spread of sensitivities of regional climate change to changes in global mean temperature due to different parameterizations and model architectures. In other words, these scaling coefficients can allow a formal treatment of scientific uncertainty in regional climate responses by "parameterizing" structural uncertainties apparent in multi-AOGCM ensemble results.

Apart from this so-called "inter-AOGCM" variability of the scaling coefficients, two other distinct types of variability can be distinguished. Firstly, for the same AOGCM, different ensemble runs of the same scenario might differ in their regional climate, giving rise to the henceforth called "inter-run" variability. Secondly, estimating the scaling coefficients for different scenario runs from the same AOGCM should ideally result in identical scaling coefficients, but generally will not, which is henceforth called the "inter-scenario" variability.

The validity of the scaling approach is supported, if these latter two variabilities are small compared to the first "inter-AOGCM" variability or central estimates of the scaling coefficients. High inter-scenario variability of the scaling coefficients provides a hint that there might be other processes not closely correlated with global mean temperature change that influence the regional climate change.

Once an uncertainty distribution for the scaling coefficients is determined it can be coupled to probabilistic projections of global mean temperature change (or other possible predictors provided by the simple climate model) to finally derive probabilistic regional climate projections [e.g. Dessai et al., 2005].

The focus of our work lies on the development of a new scaling approach which - building on and going beyond previous work [e.g. Giorgi, 2008] - explicitly allows to:

1. estimate and compare the inter-AOGCM, inter-scenario, and inter-run variability of the scaling coefficients derived from AOGCM simulations

2. take into account the correlation between the temperature and precipitation component of these variations to provide bi-dimensional uncertainty distributions

3. consider further co-variates to broaden the predictor variables beyond global mean temperature alone.

The third point, i.e. the inclusion of additional co-variates other than global mean temperature is motivated by a number of studies [e.g. Ramanathan et al., 2001, Dong et al., 2009, Bala et al., 2010] that showed both aerosol emissions and greenhouse gas forcing to have the potential to influence regional precipitation beyond the "slow" effect of induced surface air temperature changes. Thus, these co-variates are candidates to explain some of the inter-scenario variability of the regional hydrological sensitivity (HS) apparent in AOGCMs. The aerosol effect on precipitation is based on four (micro-) physical mechanisms [cf. Ramanathan et al., 2001]: (1) Reduction of the amount of incoming solar radiation at the ground by scattering (e.g. sulfate aerosols with a single scattering albedo of nearly one) or absorption of short wave radiation (mainly black carbon, BC). This direct aerosol effect can result in reduced evaporation that in turn lowers precipitation. (2) Increased number of cloud particles (mainly due to sulfate and organic aerosols) resulting in brighter clouds. These clouds reflect more shortwave radiation back to space which in turn does not reach the earth's surface (first indirect effect [Twomey, 1977]). (3) Increased life time of clouds as the increased number of cloud nuclei makes them less efficient in releasing precipitation [Albrecht, 1989]. This second indirect effect also contributes to a reduction of shortwave radiation at the surface. (4) Changes in the atmospheric temperature structure due to absorbing particles (mainly BC) that might lead to an increased atmospheric stability and less convection.

In addition, GHG radiative forcing has the potential to induce changes in precipitation that occur on a short time scale within days or weeks [Allen and Ingram, 2002, Wu et al., 2010, Frieler et al., 2011]. On global average, this "fast" effect can be understood in terms of the tropospheric energy budget: The perturbed system balances variation in tropospheric radiative cooling by the change of latent heat release. CO_2 is the most prominent example of a GHG having a higher top of the atmosphere (TOA) than surface forcing. Thus, increasing CO_2 concentrations lead to a reduced radiative cooling that is mainly balanced – on a global scale – by a reduction in latent heat release, i.e. less precipitation [Allen and Ingram, 2002, Andrews et al., 2010]. Due to considerable energy exchange with the adjacent regions [Lambert and Webb, 2008, Andrews et al., 2009] regional precipitation changes cannot simply be described within the framework of the global energy budget. However, we allow for a "fast" response that simply scales linearly with the tropospheric GHG forcing (Subsection 2.2).

The paper is structured along the methodological steps from diagnosing AOGCM data to retrieving thresholds for exceeding regional impacts, as schematically highlighted in Figure 1: In the following methods section (Section 2), we first describe the data processing applied
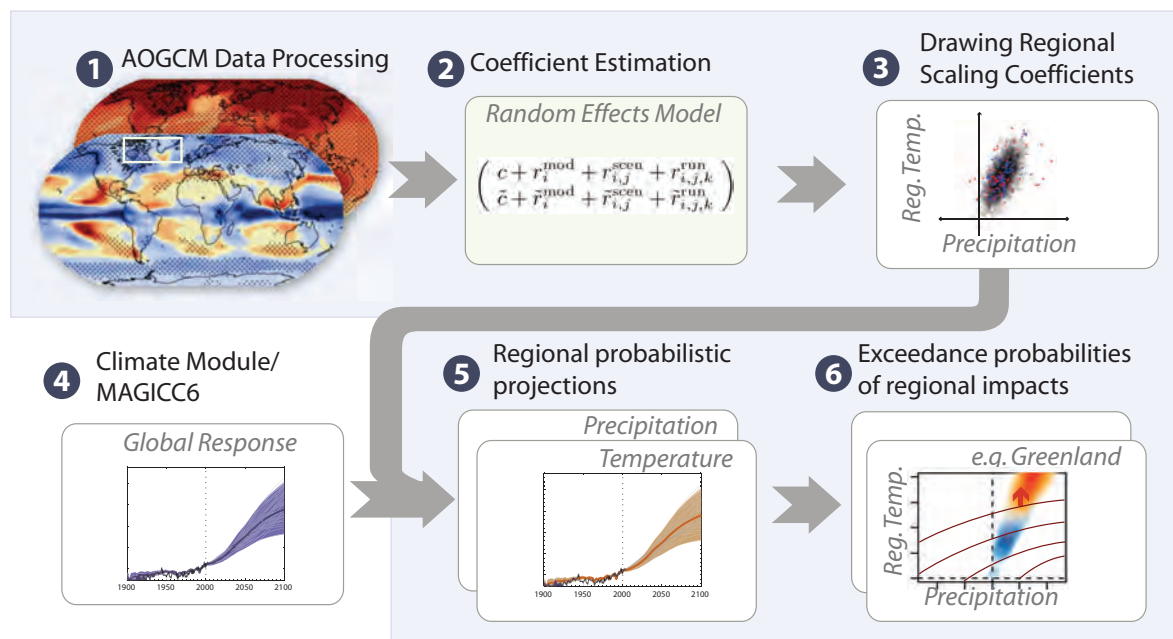
Figure 1: Schematic illustration of this study's analytical steps. After processing the output from AOGCM models (1), the statistical relationship between global temperatures and the regional climate is estimated (2). Drawing the scaling coefficients from the established distributions (3) and combining them with global mean temperature projections (4) allows to project probabilistic evolutions of mean regional temperatures and precipitation changes. Finally, these bi-dimensional regional uncertainty distributions allow to derive exceedance probabilities of specific regional impacts, here taking Greenland surface mass balance as an example (6).

to the spatial temperature and precipitation AOGCM output (Subsection 2.1). The data on additional predictors is presented in Subsection 2.2. We then introduce the random effects statistical model to retrieving uncertainty distributions of the scaling coefficients. We distinguish between a basic model that only includes global mean temperature as predictor (Subsection 2.3) and an extended version that optionally includes further predictors for the precipitation component (Subsection 2.4). We describe how to draw from these uncertainty distributions to obtain a sample of scaling coefficients in (Subsection 2.5). This is combined with a sample that we draw from the uncertainty distributions related to global mean temperature (and GHG forcing) projections based on simulations by the reduced complexity climate model MAGICC6, as briefly introduced in Subsection 2.6. In the results section (Section 3), bi-dimensional distributions of regional temperature and precipitation changes are provided for 31 world regions under the strong mitigation scenario RCP3-PD and the highest RCP business as usual scenario, RCP8.5 (RCP = Representative Concentration Pathway for use in the

CMIP5 AOGCM intercomparison exercise in preparation of the IPCC Fifth Assessment Report [van Vuuren et al., submitted]) (Subsection 3.3). Taking Greenland's surface mass balance as an example, we demonstrate the usefulness of bi-dimensional uncertainty distributions when determining exceedance probabilities for certain impact thresholds (Subsection 3.4). Limitations, sensitivities and further development of our scaling approach are discussed in Section 4. Section 5 concludes.

2. Methods

2.1. AOGCM Data pre-processing

Our raw data stems from the AOGCM simulations performed as part of the Coupled Model Intercomparison exercise Phase 3 (CMIP3), assessed by the Intergovernmental Panel of Climate Change (IPCC) Fourth Assessment Report (AR4) and stored within the framework of the Program for Climate Model Diagnosis and Intercomparison (PCMDI: http:\\www-pcmdi.llnl.gov). The available monthly data were averaged to obtain annual data giving equal weight to each month. We used all available scenario runs, i.e. the idealized runs ("1pctto2x" and "1pctto4x") assuming increasing CO_2 concentrations of 1% per year up to doubled and quadrupled levels, respectively, the 20th century run ("20c3m"), the run that keeps concentrations constant at year 2000 levels ("commit"), and the SRES scenarios ("sresb1", "sresa2", and "sresa1b"). If there were multiple runs per scenario from a single AOGCM, we used up to five ensemble members in our analysis.

Regional averages were calculated as area weighted mean over all AOGCM grid points falling into the polygons specifying our 31 world regions, which are an extended set based on the region definitions by Giorgi and Bi [2005], by including West and East-Antarctica, land and ocean regions and a region representing the geographical Greenland ($\overline{\text{GRL}}$), as opposed to the larger GRL region defined by Giorgi and Bi [2005].

For two AOGCMs (UKMO-HadCM3 and BCCR-BCM2.0) negative precipitation data appear at individual grid points. The data were set to zero as long as their absolute values were smaller than $10^{-11}\,\text{kg} * \text{m}^{-2} * \text{s}^{-1}$. When absolute values were larger, negative precipitation values were set to missing. Similarly, when precipitation values were larger than 1, we set them to missing, given that precipitation values are generally of the order of 10^{-7} to $10^{-5}\,\text{kg} * \text{m}^{-2} * \text{s}^{-1}$. As long as the number of missing values for one specific year was smaller than 5% of the total number of grid points falling into the specified areas, regional averages were calculated on the basis of the remaining data. Otherwise the regional average for that particular year and model

run was considered to be missing.

Percentage precipitation and absolute temperature changes were calculated with respect to the corresponding sections of the control runs (as recommended by Mitchell [2003]). In most of the cases, this is the preindustrial control run ("picntrl") while the idealized scenario runs of the CCSM3, ECHO-G, CGCM2.3.2, and PCM models branch off the present day control run ("pdcntrl"). We smoothed the raw control data by linear regression before subtracting it from the scenario runs in order to avoid an artificial inflation of the variability. If the control run was too short, we extended it with the last valid data point in the smoothed timeseries. For technical reasons we used ten year averages of these annual data to reduce the data set that is otherwise too large for fitting the bi-dimensional statistical model (1).

We did not log-transform the AOGCM precipitation data. Although this transformation provides a way of regarding positivity constraints (projected precipitation must not become negative), there are potential drawbacks. In particular, a log-transformation assumes an exponential relation between changes in the predictors (as e.g. global mean temperature) and regional precipitation changes [Watterson, 2008]. Instead, we assumed both regional temperature and precipitation data to follow a Gaussian distribution without any further transformation and QQ-plots were used to verify this assumptions (see Figure 8 of Appendix B).

2.2. Data on co-variables, aerosols and GHG forcing

AOGCM simulations include aerosol effects to a varying degree depending on the model (see Table 10.1 in Meehl et al. [2007]) except for the idealized "1pctto2x" and "1pcttp4x" scenarios. While effects of sulfate aerosols are represented in all AOGCMs there are only eight CMIP3 models that took BC effects into account. In addition, indirect effects are not generally simulated. Table 1 gives an overview of the aerosol forcing agents and mechanisms included in the different models.

Given the relatively short atmospheric residence time of black carbon and sulfate aerosols we use emissions time series (E_{BC} and E_{SOx}, respectively) as additional predictors in our statistical model. In the framework of the SRES scenarios regional information about SOx emissions is only provided for four regions (OECD, ASIA, REF, and ALM). We map the finer-scale Giorgi regions to these SRES regions as indicated in Table 2. BC is not prescribed in the SRES scenarios. Thus, we use information provided by the individual groups, as described in the Supplementary Material of Frieler et al. [2011]. Similar to the SRES regions, emissions were averaged over the large scale areas ASIA, REF, $OECD_{north}$, $OECD_{europe}$, $OECD_{south}$, LAM and MAF, defined as an aggregation Giorgi regions listed in Table 2).

Table 1: The forcing agents included in the individual CMIP3 AOGCMs and considered in this study as covariates for explaining regional precipitation. We distinguish between greenhouse gas forcing (GHG), black carbon (BC), and sulfate emissions (SOx). Although our analysis does not include the 20th century runs, we show as well volcanic forcing (VOLC) with model specific relative amplitudes provided in brackets based on Forster and Taylor [2006] (cf. Table 2 in Meinshausen et al. [2011] and Table 10.1 in Meehl et al. [2007]). For sulphate, we provide the background information in brackets, whether the AOGCMs included the direct (D) and/or first (I^1) and second (I^2) indirect effects, although our method does not distinguish between these cases.

AOGCM	Forcing agents
BCCR-BCM2.0	GHG - SOX(D)
CCSM3	GHG - SOX(D) - BC - VOLC$_{(0.86)}$
CGCM3.1(T47)	GHG - SOX(D) - VOLC$_{(0.0)}$
CGCM3.1(T63)	GHG - SOX(D) - VOLC$_{(0.0)}$
CNRM-CM3	GHG - SOX(D)
CSIRO-Mk3.0	GHG - SOX(D)
ECHAM5/MPI-OM	GHG - SOX(D,I^{1*})
ECHO-G	GHG - SOX(D,I^1)- VOLC$_{(0.70)}$
FGOALS-g1.0	GHG - SOX(D)
GFDL-CM2.0	GHG - SOX(D)-BC- VOLC$_{(0.70)}$
GFDL-CM2.1	GHG - SOX(D)-BC- VOLC$_{(0.70)}$
GISS-AOM	GHG - SOX(D)
GISS-EH	GHG - SOX(D,I^2) - VOLC$_{(0.70)}$
GISS-ER	GHG - SOX(D,I^2) - VOLC $_{(0.70)}$
INM-CM3.0	GHG - SOX(D) - VOLC$_{(0.2)}$
IPSL-CM4	GHG - SOX(D,I^1)
MIROC3.2(H)	GHG - SOX(D,$I^{1,2}$) - BC - VOLC $_{(0.52)}$
MIROC3.2(M)	GHG - SOX(D,$I^{1,2}$)- BC - VOLC $_{(0.35)}$
MRI-CGCM2.3.2	GHG - SOX(D) - VOLC $_{(0.40)}$
PCM	GHG - SOX(D) - VOLC$_{(0.7)}$a
UKMO-HadCM3	GHG - SOX(D,I I^{1*}) - VOLC $_{(0.0)}$
UKMO-HadGEM1	GHG - SOX(D,$I^{1,2}$) - BC - VOLC $_{(0.0)}$

Table 2: Mapping of the Giorgi regions [Giorgi and Bi, 2005] and the geographical Greenland ($\overline{\text{GRL}}$) (column one) to the large scale emission regions for SO_X emissions defined within the SRES scenarios (column two) and to the large scale BC emission regions defined by column 2.

region	SOx emission region	BC emission region
GRL	OECD	$\text{OECD}_{\text{north}}$
ALA	OECD	$\text{OECD}_{\text{north}}$
GRL	OECD	$\text{OECD}_{\text{north}}$
NEU	OECD	$\text{OECD}_{\text{europe}}$
MED	OECD	$\text{OECD}_{\text{europe}}$
WNA	OECD	$\text{OECD}_{\text{north}}$
CAN	OECD	$\text{OECD}_{\text{north}}$
ENA	OECD	$\text{OECD}_{\text{north}}$
CAM	OECD	$\text{OECD}_{\text{north}}$
NAU	OECD	$\text{OECD}_{\text{south}}$
SAU	OECD	$\text{OECD}_{\text{south}}$
SAS	ASIA	ASIA
TIB	ASIA	ASIA
EAS	ASIA	ASIA
SEA	ASIA	ASIA
NEE	REF	REF
NAS	REF	REF
CAS	REF	REF
AMZ	ALM	LAM
CSA	ALM	LAM
SSA	ALM	LAM
SAH	ALM	MAF
WAF	ALM	MAF
EAF	ALM	MAF
EQF	ALM	MAF
SQF	ALM	MAF
SAF	ALM	MAF

Beyond aerosol forcings, we test tropospheric GHG forcing as a second additional predictor for precipitation changes. We introduced the co-variate ΔR_{GHG} as a weighted sum of TOA forcings in Frieler et al. [2011] to describe the *tropospheric* fraction of the GHG forcing, i.e. the difference between the TOA and the surface radiative forcing. The TOA forcing information stems from the emulation of the AOGCM simulations [Meinshausen et al., 2011] except of the model "BCM2.0" that was not emulated but where we used a idealized forcing time series for the "1pctto2x" run (3.7 W/m^2 at doubling). While Figure 2 and 3 show the complete data set, Figure 5 shows the reduced data set the actual model fitting is based on. It excludes the 20c3m run (Section 3, Subsection 3.2) and multi-forcing runs of "BCM2.0". We use a normalized and a not normalized set of predictors. In the first case, GHG forcing, BC and SOx emissions were normalized with respect to the multi-model mean of the 1999's values to assist the comparison of their effects (Table 4). However, probabilistic projections are based on absolute values of GHG forcing in W/m^2, SOx emissions (MtS/yr) and BC emissions (Mt/yr) and scaling coefficients were adjusted accordingly.

2.3. The basic statistical model

This section describes the basic random effects model [e.g. Pinheiro and Bates, 2000] solely including global mean temperature change as predictor for the regional changes in temperature and precipitation. In our context the random effects model can be understood as a linear regression model allowing for inter-model, inter-scenario or inter-run variations of the scaling coefficients. These are handled as random deviations (random effects) from the central scaling coefficients (fixed effects). In contrast to time slice approaches (e.g. Giorgi [2008], Hulme et al. [2000]) the regression approach makes use of the full time series of data (as recommended by Mitchell [2003]). While a simple least square fit to the full time series of *one* (AO)GCM was used e.g. by Mitchell et al. [1999] or by Huntingford and Cox [2000] the random effects approach allows to fit one unique model to *all* time series of the 20 AOGCMs, different scenarios, and different runs per scenario. The method, which to our knowledge has not been used in pattern scaling approaches before, has the advantage a) of correcting the standard errors of the scaling coefficients $(c, \tilde{c})$ (see equation (1)) for the dependency structure of the data due to their clustering in different AOGCMs, scenarios and runs, and b) of explicitly estimating the inter-AOGCM, inter-scenario, and inter-run variability of the scaling coefficients. Advantage b) is important as it directly tests the validity of the scaling approach: The pattern scaling approach can only be confidently applied if inter-scenario and inter-run variabilities are small.

Our random-effects model combining temperature and precipitation data is described by the following equation:

$$
\begin{pmatrix} \Delta T_{\text{regional}} \\ \Delta P_{\text{regional}} \end{pmatrix}_{ijk} = \begin{pmatrix} c + r_i^{\text{mod}} + r_{ij}^{\text{scen}} + r_{ijk}^{\text{run}} \\ \tilde{c} + \tilde{r}_i^{\text{mod}} + \tilde{r}_{ij}^{\text{scen}} + \tilde{r}_{ijk}^{\text{run}} \end{pmatrix} * \Delta T_{\text{global } ijk} + \begin{pmatrix} \varepsilon_{ijk} \\ \tilde{\varepsilon}_{ijk} \end{pmatrix} \tag{1}
$$

Within this modelling framework it is assumed that there are fixed "population based" scaling coefficients for temperature (c) and precipitation $(\tilde{c})$, respectively. The scaling coefficients for individual AOGCMs (i), scenarios (j) and ensemble runs (k) are assumed to deviate randomly from the fixed effects. Each model run provides one realization of these random effects that are described by $(r, \tilde{r})$, where $(r^{\text{mod}}, \tilde{r}^{\text{mod}})$ describes the inter-AOGCM, $(r^{\text{scen}}, \tilde{r}^{\text{scen}})$ the inter-scenario and $(r^{\text{run}}, \tilde{r}^{\text{run}})$ the inter-run variability. The residuals ε_{ijk} and $\tilde{\varepsilon}_{ijk}$ are assumed to follow a normal distribution with AOGCM specific variances σ_i and $\tilde{\sigma}_i$ (see Appendix A).

We do not assume that there is a common scenario effect across all AOGCMs (in the sense that scenarios with a high scaling coefficient, i.e. positive r^{scen} or $\tilde{r}^{\text{scen}}$, for one AOGCM need to have the same random effect for another AOGCM) but the scenario effects are assumed to be AOGCM specific and therefore also indexed by i in equation (1). This assumption is supported for most of the considered regions when plotting estimates of $r_{i,j}^{\text{scen}}$ and $\tilde{r}_{i,j}^{\text{scen}}$ for fixed scenarios j and varying AOGCMs i (see Figure 9 and 10 of the Appendix C). All random effects are assumed to follow a bivariate normal distribution:

$$
\begin{pmatrix} r^{\text{mod}} \\ \tilde{r}^{\text{mod}} \end{pmatrix} \sim N((0,0), C_{\text{mod}})
$$

$$
\begin{pmatrix} r^{\text{scen}} \\ \tilde{r}^{\text{scen}} \end{pmatrix} \sim N((0,0), C_{\text{scen}})
$$

$$
\begin{pmatrix} r^{\text{run}} \\ \tilde{r}^{\text{run}} \end{pmatrix} \sim N((0,0), C_{\text{run}})
$$

It turns out that the inter-run variability of the scaling coefficients is very low for some of the considered regions. This causes problems in estimating the correlation between the temperature and precipitation related component of the random effects (i.e. r^{run} and $\tilde{r}^{\text{run}}$). Whenever these problems occurred the bi-variate model was first restricted to a model where the two components of the inter-run variabilities were assumed to be independent. If this does not ensure convergence of the fitting routines the inter-run variability of the precipitation component was excluded from the model. Whenever a restricted model was used, the field of the associated parameter in Table 3 was left empty.

2.4. The extended statistical model

In contrast to the basic model (1) the temperature component of the bi-dimensional model is simplified by ignoring the inter-run variability which turned out to be small within the basic model. The same was done for the precipitation component for which aerosol emissions and GHG forcing were included as additional predictors. The additional scaling coefficients are allowed to vary between AOGCMs (inter-AOGCM variability) but we exclude inter-scenario variations:

$$
\begin{aligned}
\Delta T_{\text{regional } ij} &= (c + r_i^{\text{mod}} + r_{ij}^{\text{scen}}) * \Delta T_{\text{global } ij} + \varepsilon_{ij} \\
\Delta P_{\text{regional } ij} &= (\tilde{c} + \tilde{r}_i^{\text{mod}} + \tilde{r}_{ij}^{\text{scen}}) * \Delta T_{\text{global } ij} \\
&+ (\tilde{d} + \tilde{s}_i^{\text{mod}}) * \Delta R_{\text{GHG } ij} \\
&+ (\tilde{e} + \tilde{t}_i^{\text{mod}}) * E_{\text{SOx, region } ij} \\
&+ (\tilde{f} + \tilde{u}_i^{\text{mod}}) * E_{\text{BC, region } ij} + \tilde{\varepsilon}_{ij}
\end{aligned}
\tag{2}
$$

In the most general setting, the inter-AOGCM variations $(r^{mod}, \tilde{r}^{mod}, \tilde{s}^{mod}, \tilde{t}^{mod}, \tilde{u}^{mod})$ stem from a multivariate normal distribution with a covariance matrix C_{mod}. However, the covariance matrix does not seem to be well defined by the data, leading to convergence problems of the fitting algorithm. To reduce the degrees of freedom, the general structure of C_{mod} was restricted to the following one:

$$
C_{\text{mod}} = \begin{pmatrix}
a_{1,1} & a_{1,2} & a_{1,3} & 0 & 0 \\
a_{2,1} & a_{2,2} & a_{2,3} & 0 & 0 \\
a_{3,1} & a_{3,2} & a_{3,3} & 0 & 0 \\
0 & 0 & 0 & d_{4,4} & 0 \\
0 & 0 & 0 & 0 & d_{5,5}
\end{pmatrix}
$$

with the five rows and columns corresponding to, in that order, the covariance of the random effects associated with the scaling factors for ΔT_{global} onto (1) $\Delta T_{\text{regional}}$ and (2) $\Delta P_{\text{regional}}$, as well as (3) ΔR_{GHG}, (4) E_{SOx}, and (5) E_{BC}, onto $\Delta P_{\text{regional}}$ (i.e. $a_{1,1} = var(r^{mod})$, $a_{2,1} = cov(r^{mod}, \tilde{r}^{mod})$ etc.). Thus, only the global- mean temperature and GHG forcing related random effects are allowed to be correlated. The covariance matrix C_{scen} for the inter-scenario variabilities is assumed to be diagonal, i.e. r^{scen} and $\tilde{r}^{\text{scen}}$ are assumed to be independent.

While the above model is our starting point, it may be further reduced by (a) excluding predictors or (b) further restrictions of the covariance structure of the random effects. Concerning (a) we used the Bayesian information criterion (BIC) as model selection criterion. The BIC

decreases with improved model versions. It represents a measure of the model fit while adding a penalty term for the number of estimated parameters to avoid overfitting.

Further restrictions of the Covariance Matrix C_{mod} (point (b)) become necessary when the high correlation of the GHG forcing component and the temperature component raises problems for the parameter estimation. The correlation only decreases during the relatively short stabilization periods at the end of the scenario runs (Figure 1 of the supplementary material of Frieler et al. [2011]). When fitting the extended model we thus may find parts of the temperature related response spuriously attributed to the GHG forcing component. The anti-correlation of the inter-AOGCM variations of the random effects associated with the temperature and the GHG forcing component $\tilde{r}^{\mathrm{mod}}$ and $\tilde{s}^{\mathrm{mod}}$ ($\sqrt{a_{3,2}}$) provides a hint to some compensatory effects. We decided to set a limit of -0.8 for this anti-correlation. In all cases where the anti-correlation was estimated to be higher or not estimated due to convergence problems we fit a reduced model that excludes the GHG forcing component. In some cases the scaling coefficient $\tilde{c}$ estimated for the normalized GHG forcings and aerosol emissions differs from $\tilde{c}$ estimated for the non normalized additional predictors providing a hint that the model is not stable. In these cases the GHG forcing component was also excluded from the fitting. For some of the remaining cases it happens that the approximated variance covariance matrix describing the uncertainties associated with the estimation of the (co-) variances of the random effects is not positive definite. Nonetheless we did not change the model in these cases. The problem is related to the estimation of $a_{3,2}$ as it disappears when the GHG forcing random effects are assumed to be independent from the global mean temperature related ones. The estimated scaling coefficients of both model versions do not differ by more than 10%.

In case of the West and East Antarctic Ice Sheets (WAIS and EAIS, respectively) we do not include aerosol effects. We furthermore exclude the GHG-forcing component from the WAIS model because of a strong anti-correlation of the random effects. We thus only provide scaling coefficients estimated by the basic model (1) for this region.

2.5. Drawing the scaling coefficients

To get a sample of the uncertainty distribution associated with the scaling coefficients we randomly draw from the multivariate normal distribution associated with the estimation of the fixed effects. In addition, we draw from the multivariate normal distributions $N(0, C_{\mathrm{mod}})$, $N(0, C_{\mathrm{scen}})$, and $N(0, C_{\mathrm{run}})$, where C_{mod}, C_{scen}, and C_{run} are the estimated covariance matrices of the random effects and 0 stands for a two- or more dimensional vector of zeros. These four components are assumed to be independent and additive.

2.6. Coupling to probabilistic global mean temperature changes

This section briefly describes our approach to generate (bi-dimensional) uncertainty distributions of global mean temperature change ΔT_{global} (as well as ΔR_{GHG}) and how these are merged to the previously derived uncertainty distribution of scaling coefficient.

We generate uncertainty distributions of ΔT_{global} and ΔR_{GHG} using the reduced complexity coupled carbon cycle climate model MAGICC, which has been used within the past IPCC Assessment reports and several integrated assessment models [Wigley and Raper, 2001]. Its reduced complexity makes it highly efficient whilst being able to closely emulate more complex carbon cycle models (C4MIP) and global climate models (CMIP3), respectively, as shown for its most recent version MAGICC6 [Meinshausen et al., 2011]. For generating our joint distributions of ΔT_{global} and ΔR_{GHG}, we use here the identical setup as in the "illustrative default" case in Meinshausen et al. [2009]: The most relevant input parameters of the model were a priori varied according to our current level of knowledge reflected by the IPCC AR4. In addition, the model is constrained by observational data, i.e., time series of hemispheric land/ocean temperatures [Brohan et al., 2006] and ocean heat uptake [Domingues et al., 2008]. Carbon cycle feedback strength parameterisations are drawn at random from 10 C^4MIP [Friedlingstein et al., 2006] emulations as described in Meinshausen et al. [2011]. The Bayesian approach finally provides an updated (a posteriori) distribution of annual global mean temperature changes and ΔR_{GHG} given a fixed emission scenario.

For deriving regional climate projections, the distributions of global temperature changes and ΔR_{GHG} on the one side and the regional scaling coefficients on the other side need to be combined. Here, we employ a simple Monte Carlo technique, drawing independently from the bi- or multi-dimensional distribution of scaling coefficients (as described above) and the (bi-dimensional) uncertainty distribution of global mean temperature changes and ΔR_{GHG}. Each vector of scaling coefficients is multiplied by a randomly drawn (paired) time series of global mean temperature change (and ΔR_{GHG}) to get a bi-dimensional time series of regional temperature and precipitation changes.

3. Results

In this section, we first show examples of regional temperature and precipitation data we diagnosed from AOGCMs (see Subsection 3.1). Then, we present the results provided by the statistical models described above. We focus on the uncertainty distribution of scaling coefficients (Subsection 3.2) and show the associated distribution of regional climate changes

under the RCP8.5 and RCP3-PD emission scenarios (Subsection 3.3). The associated impacts on Greenland's contribution to sea level rise (SLR) from surface mass balance changes are described in Subsection 3.4.

3.1. Diagnosed AOGCM data

For illustrative purposes, we chose the regional temperature and precipitation changes over Greenland ($\overline{\text{GRL}}$) and East Asia (EAS) as an example, see Figure 2 and Figure 3.

Regional temperature changes show a close linear relation to global mean temperature but we find pronounced deviations from linearity for precipitation changes.

Over Greenland, we find a linear relationship between global mean temperature change and regional precipitation changes over the main part of the simulations. But some AOGCMs show a change of the slope at the end of some scenario runs, e.g. in year 2100 in the SRES scenarios when concentrations were held constant afterwards or in the idealized runs after stabilization (see arrows in Figure 2d).

In the EAS region global mean temperature changes alone cannot explain the decline in precipitation over the 20th century and the following increase within the SRES simulations of some AOGCMs. Aerosol emissions might provide an explanation for the non-linear relation. In contrast to Greenland, aerosol emissions have strongly increased during the region's industrialization in the 20th century. This explanation is particularly supported by the fact that the decrease in precipitation shown for some AOGCMs over the EAS region over the 20th century does not appear in the corresponding idealized "1pctto2x" and "1pctto4x" scenarios that do not include aerosol effects.

"Fast" dampening effects of tropospheric GHG forcings may provide one possible explanation for the change in regional hydrological sensitivity over Greenland during the stabilization periods of the different scenarios runs. Based on CCSM3 simulations, Bala et al. [2010] found that the "fast" effect of CO_2 forcing on precipitation can be more than 50% of the total response. As opposed to our results they found a slight increase in precipitation over Greenland as "fast" response to CO_2 forcing. Unfortunately, the stabilization periods simulated by the CCSM3 model are very short. Therefore it is not possible to assess whether this AOGCM would show a slower increase in precipitation during these periods.

Figure 2: Greenland ($\overline{\text{GRL}}$): Ten year averages of regional temperature (left panels a) and precipitation changes (right panels b) plotted against the global mean temperature changes from 20 of the CMIP3 AOGCMs. Color coding indicates different scenarios: red = 1pctto2x, blue = 1pctto4x, grey = 20c3m, violet = commit, pink = sresa1b, purple = sresa2, lightblue = sresb1. Note that the Greenland region definition is here taken from Gregory and Huybrechts [2006] unlike as in Figure 6, where the Giorgi and Bi [2005] definition is used.

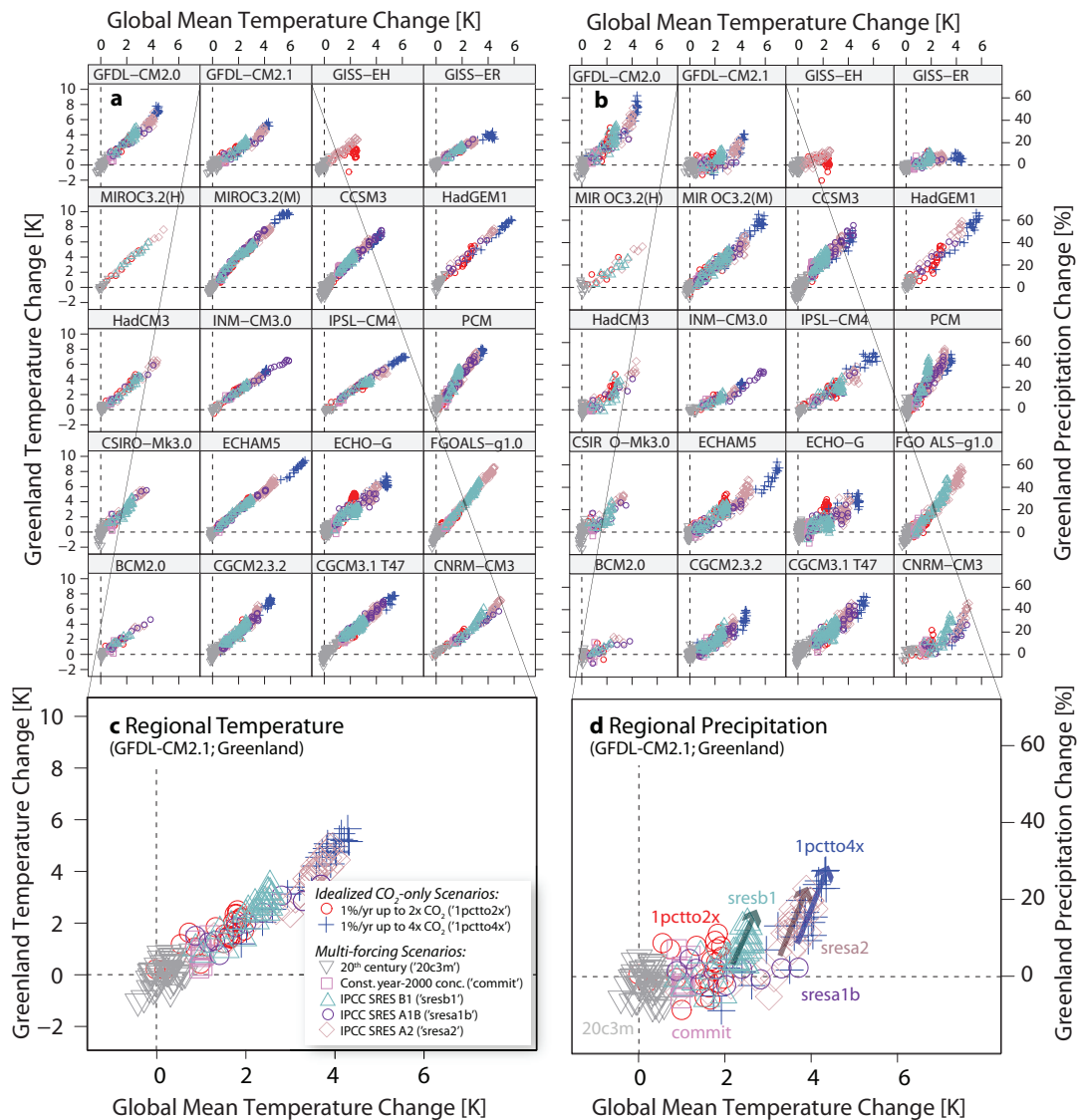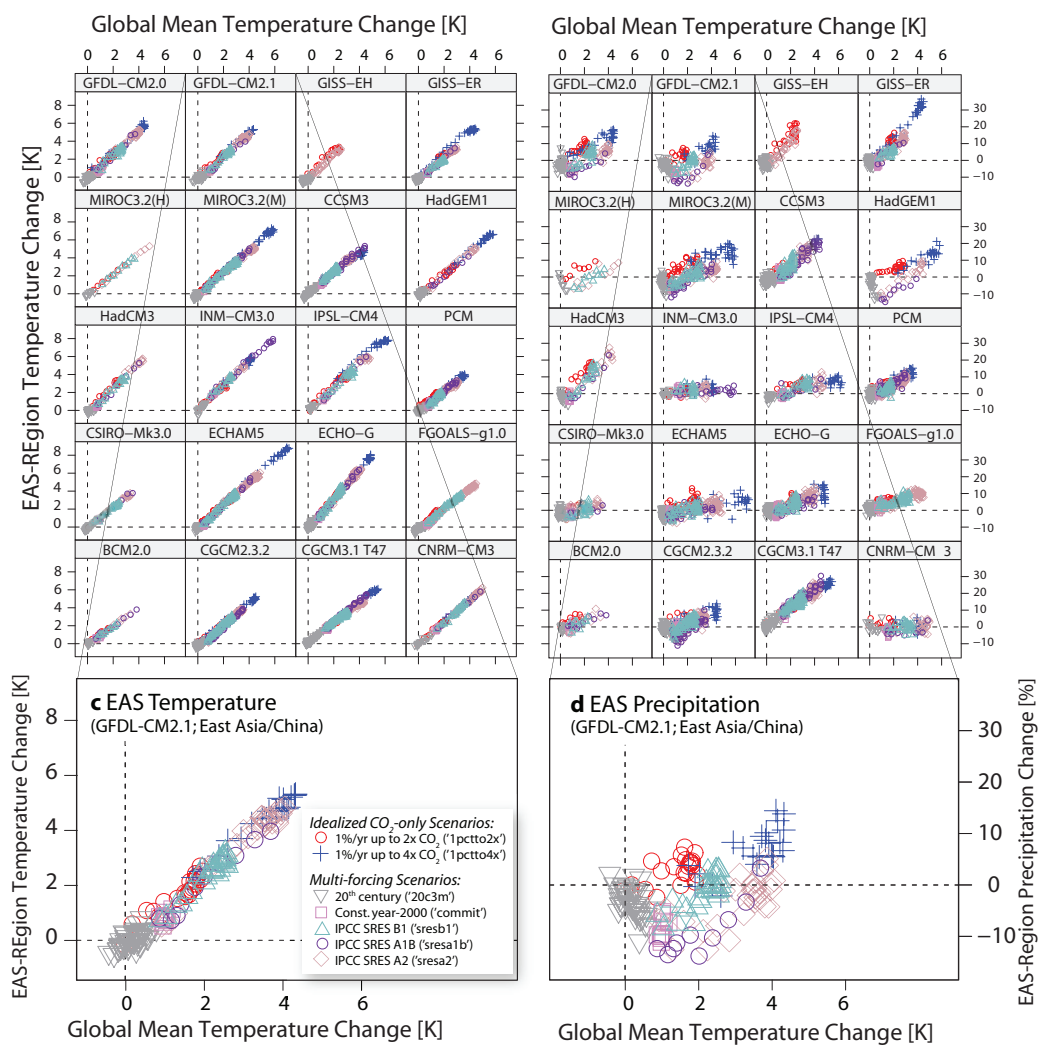Figure 3: East Asia (EAS) region: Ten year averages of regional temperature (left panels a) and precipitation changes (right panels b) plotted against the associated global mean temperature changes from 20 of the CMIP3 AOGCMs. Color coding is the same as in Figure 2. The EAS region is defined by Giorgi and Bi [2005].

3.2. Resulting Scaling Coefficients

Figure 4 shows the uncertainty distribution of the global mean temperature scaling coefficients obtained by fitting the basic statistical model (equation (1)) to the regional changes in temperature and precipitation as provided by 20 CMIP3 AOGCMs for the Greenland and EAS area.
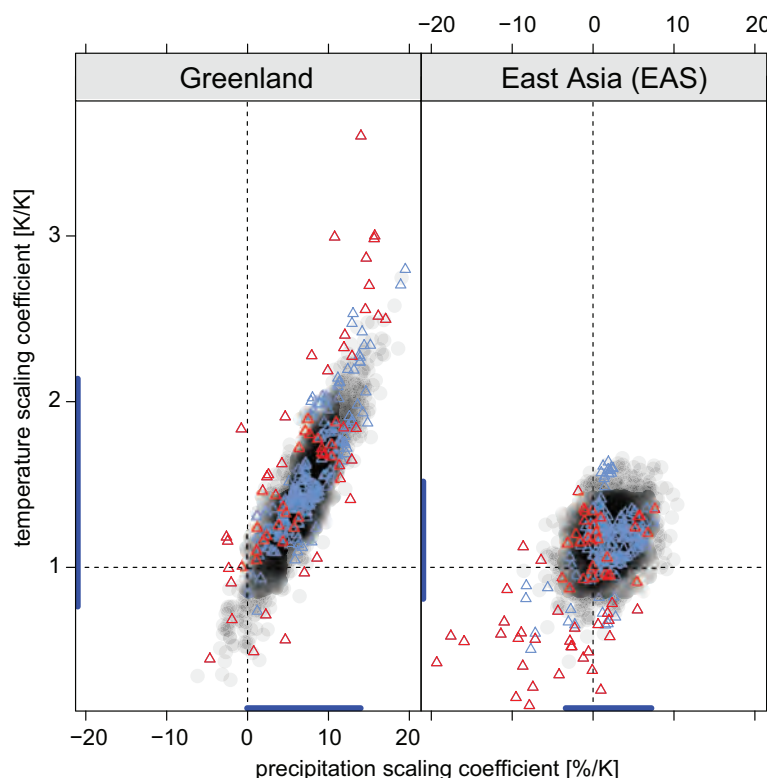
Figure 4: Scaling coefficients for $\overline{GRL}$ and EAS regions. Grey dots: Sample of the temperature and precipitation scaling coefficients calculated for Greenland and the EAS region based on the basic model solely including global mean temperature change as predictor. Blue dots: pairs of scaling coefficients estimated by separate linear regressions applied to the individuals model runs except the "20c3m" run. Red Dots: Pairs of scaling coefficients estimated only from the "20c3m" run. The blue lines at the axis mark the 2 σ uncertainty ranges as calculated by formula 3.

We also calculated individual pairs of scaling coefficients by fitting separate linear regression models to the temperature and precipitation data for each individual model run. The scaling coefficients calculated from the 20c3m runs (see red triangles in Figure 4) show a high variability without a systematic pattern in Greenland. In the EAS region the precipitation scaling coefficients are systematically lower for the 20c3m run compared to the other scenarios. This

is in line with Figure 3 showing decreasing precipitation for the 20th century and increases afterwards. This systematic effect is probably due to tropospheric aerosol effects that strongly increase within the 20th century. While the unsystematic effects might be due to (a) a lower signal to noise ratio and (b) the fact that the 20c3m run is especially short in comparison to the SRES runs there might be other systematic effects not included in our model, e.g., solar or volcanic forcing. For that reason, we left out the 20c3m run when determining our regression coefficients.

There is a strong correlation between the temperature and the precipitation scaling coefficients for $\overline{\text{GRL}}$ while it is weaker for the EAS region. This high correlation for the $\overline{\text{GRL}}$ area is apparent across AOGCMs as well as across different scenarios (see the correlation coefficients of the random components in the third line of Table 3), possibly indicating a moisture-limited precipitation over Greenland. Having assumed Gaussian distributions of our variabilities, the "overall" uncertainty of the temperature and precipitation component can be estimated by

$$\sigma = \sqrt{\sigma_{\text{fixed effects}}^2 + \sigma_{\text{mod}}^2 + \sigma_{\text{scen}}^2 + \sigma_{\text{run}}^2} \tag{3}$$

For the Greenland region, this "overall" uncertainty is $\sigma = 0.3$ K/K and $\sigma = 3.5\%$/K for the temperature and precipitation coefficients, respectively. The inter-AOGCM variability has the largest contribution to this uncertainty for both components in case of $\overline{\text{GRL}}$ (see Table 3). The inter-scenario variability is less than half of the inter-AOGCM variability. That is different for the EAS region where the inter-scenario variability of the precipitation scaling coefficients is larger than the inter-AOGCM variability.

The extended model shows that the high inter-scenario variability may be largely explained by varying aerosol loadings. The inter-scenario variability for precipitation in the East-Asian region decreased from 1.9 to 0.4 for the temperature-related scaling coefficient when aerosol emissions and GHG forcing are included in the regression. Starting from the comprehensive version that includes ΔR_{GHG}, E_{BC}, and E_{SO_x} as additional predictors for the precipitation component (equation (2)) the model was stepwise reduced whenever this decreased the BIC. In case of $\overline{\text{GRL}}$ only the GHG forcing component improved the model in comparison to the basic temperature-only model (indicated by the missing rows for the $\tilde{e}$ and $\tilde{f}$ scaling coefficients in Table 4 related to E_{SO_x} and E_{BC}, respectively). The estimated scaling coefficient $\tilde{d}$ is negative, indicating a relatively strong possible dampening of the purely temperature induced increase in precipitation by tropospheric GHG forcing. Figure 5a shows the fit of the precipitation model to the $\overline{\text{GRL}}$ data.

Table 3: The estimated coefficients from the basic model with global mean temperature being the only predictor for projecting precipitation and temperature changes in 31 world regions. The table provides the fixed effects c (regional temperature change per change in global mean temperature) and $\tilde{c}$ (percentage regional precipitation change per change in global mean temperature), their standard errors and their correlation as well as the elements of the correlation matrices of the random effects as estimated by the basic model (1).

		fixed effects			random effects					
		value	Std.E	corr	$\sigma(r^{\mathrm{mod}})$ $\sigma(\tilde{r}^{\mathrm{mod}})$	corr	$\sigma(r^{\mathrm{scen}})$ $\sigma(\tilde{r}^{\mathrm{scen}})$	corr	$\sigma(r^{\mathrm{run}})$ $\sigma(\tilde{r}^{\mathrm{run}})$	corr
land	c	1.307	0.013		0.055		0.030		0.007	
	$\tilde{c}$	1.503	0.260	-0.125	1.108	-0.181	0.718	0.586	0.038	-0.500
sea	c	0.873	0.005		0.022		0.012		0.003	
	$\tilde{c}$	1.443	0.106	0.640	0.458	0.679	0.246	0.087	0.059	0.776
GRL	c	1.451	0.070		0.306		0.137		0.026	
	$\tilde{c}$	6.964	0.717	0.889	3.117	0.894	1.378	0.940	0.373	
WAIS	c	1.094	0.051		0.218		0.134		0.024	
	$\tilde{c}$	5.849	0.485	0.790	2.088	0.789	1.043	0.946		
EAIS	c	1.062	0.051		0.223		0.075		0.019	
	$\tilde{c}$	5.705	0.877	0.864	3.889	0.868	0.920	0.942	0.297	
NEU	c	1.198	0.028		0.106		0.135		0.013	
	$\tilde{c}$	2.474	0.325	-0.256	1.387	-0.441	0.863	0.763		
MED	c	1.204	0.025		0.105		0.091		0.004	
	$\tilde{c}$	-5.784	0.429	-0.359	1.761	-0.521	1.533	0.617	0.359	
NEE	c	1.509	0.053		0.223		0.150		0.018	
	$\tilde{c}$	4.371	0.338	-0.343	1.442	-0.444	0.858	0.752	0.096	-0.119
NAS	c	1.588	0.056		0.243		0.122		0.021	
	$\tilde{c}$	5.468	0.297	0.555	1.254	0.543	0.871	0.769	0.084	0.655
CAS	c	1.357	0.037		0.158		0.080		0.012	
	$\tilde{c}$	-1.999	0.551	-0.523	2.387	-0.569	1.087	0.232		
TIB	c	1.433	0.035		0.153		0.060		0.016	
	$\tilde{c}$	3.616	0.447	-0.264	1.917	-0.281	1.119	0.014	0.053	
EAS	c	1.164	0.030		0.121		0.125		0.010	
	$\tilde{c}$	1.912	0.439	-0.010	1.736	-0.231	1.939	0.895	0.154	-0.123
SAS	c	1.213	0.037		0.163		0.048		0.010	
	$\tilde{c}$	2.188	0.643	-0.265	2.796	-0.284	1.319	0.247		
SEA	c	0.989	0.022		0.096		0.034		0.008	
	$\tilde{c}$	1.980	0.334	0.109	1.435	0.122	0.792	-0.142	0.063	-0.905
NAU	c	1.241	0.025		0.108		0.040		0.017	
	$\tilde{c}$	0.307	0.708	-0.156	3.120	-0.155	0.816	-0.298		
SAU	c	1.078	0.025		0.108		0.049		0.015	
	$\tilde{c}$	-1.526	0.670	-0.025	2.941	-0.023	0.896	-0.116		

		fixed effects			random effects					
		value	Std.E	corr	$\sigma(r^{\mathrm{mod}})$ $\sigma(\tilde{r}^{\mathrm{mod}})$	corr	$\sigma(r^{\mathrm{scen}})$ $\sigma(\tilde{r}^{\mathrm{scen}})$	corr	$\sigma(r^{\mathrm{run}})$ $\sigma(\tilde{r}^{\mathrm{run}})$	corr
SAH	c	1.372	0.027		0.116		0.051		0.012	
	$\tilde{c}$	-3.093	2.148	-0.478	9.258	-0.538	4.816	0.572	0.316	
WAF	c	1.253	0.039		0.169		0.082		0.012	
	$\tilde{c}$	0.042	0.605	-0.190	2.579	-0.203	1.163	-0.026		
EAF	c	1.237	0.040		0.177		0.062		0.013	
	$\tilde{c}$	1.790	0.521	-0.364	2.229	-0.372	1.304	-0.274	0.204	-0.772
EQF	c	1.140	0.036		0.160		0.054		0.014	
	$\tilde{c}$	4.188	0.855	-0.660	3.748	-0.688	1.405	0.168		
SQF	c	1.235	0.034		0.148		0.049		0.011	
	$\tilde{c}$	0.645	0.364	-0.357	1.587	-0.380	0.685	0.243		
SAF	c	1.261	0.035		0.155		0.041		0.006	
	$\tilde{c}$	-0.992	0.659	0.250	2.912	0.250	0.714	0.337		
ALA	c	1.569	0.050		0.221		0.063		0.000	
	$\tilde{c}$	5.513	0.379	0.432	1.653	0.435	0.729	0.477	0.163	
GRL	c	1.627	0.050		0.219		0.081		0.026	
	$\tilde{c}$	5.757	0.308	0.840	1.337	0.843	0.617	0.942	0.133	0.376
WNA	c	1.317	0.037		0.163		0.060		0.010	
	$\tilde{c}$	0.069	0.539	0.002	2.373	0.009	0.702	-0.268	0.093	
CNA	c	1.334	0.036		0.154		0.101		0.012	
	$\tilde{c}$	0.735	0.538	-0.696	2.346	-0.710	0.968	-0.642		
ENA	c	1.300	0.030		0.129		0.068		0.013	
	$\tilde{c}$	2.305	0.331	-0.547	1.427	-0.610	0.739	0.389	0.100	-0.757
CAM	c	1.182	0.031		0.134		0.055		0.006	
	$\tilde{c}$	-4.387	0.802	-0.061	3.518	-0.064	1.347	0.032		
AMZ	c	1.252	0.036		0.160		0.045		0.010	
	$\tilde{c}$	0.488	0.551	-0.544	2.413	-0.557	0.964	-0.155	0.113	0.161
CSA	c	1.088	0.026		0.116		0.041		0.010	
	$\tilde{c}$	1.353	0.571	-0.400	2.523	-0.402	0.735	-0.378		
SSA	c	0.831	0.024		0.105		0.044		0.011	
	$\tilde{c}$	-2.082	0.399	-0.244	1.761	-0.239	0.514	-0.476	0.204	-0.170

Table 4: The scaling coefficients from the extended statistical model, including GHG forcing, SOx aerosol and black carbon emissions as additional predictors. Fixed effects c (change in temperature per change in global mean temperature), $\tilde{c}$ (percentage change in regional precipitation per change in global mean temperature), $\tilde{d}$ (percentage change in regional precipitation per change in GHG forcing), $\tilde{e}$ (percentage change in regional precipitation per change in SO_x emissions, normalized to the multi-model mean of SO_x emissions in 1999), and $\tilde{f}$ (percentage change in regional precipitation per change in BC emissions, normalized to the multi-model mean BC emissions in 1999), their standard errors and the their correlation. The correlations associated with $\tilde{e}$ and $\tilde{f}$ were omitted because their absolute values are in general very small and always smaller than 0.3. The right part of the table provides the elements of the correlation matrices of the random effects. The estimates are based on model (2) including or excluding the additional predictors following the Bayesian Information Criterion (BIC) and excluding the GHG forcing component whenever the correlation of the inter-AOGCM variations of the associated scaling coefficients were smaller than -0.8.

| | | fixed effects | | | | random effects | | | |
| | | | | correlations | | | correlations | | |
		value	Std.E	c	$\tilde{c}$	σ_{model}	r^{mod}	$\tilde{r}^{mod}$	σ_{scen}
land	c	1.307	0.013			0.055			0.029
	$\tilde{c}$	2.030	0.194	0.046		0.805	0.050		0.214
	$\tilde{d}$	-0.140	0.233	-0.129	-0.225	0.951	-0.146	-0.106	
	$\tilde{e}$	-0.430	0.185			0.713			
	$\tilde{f}$	-2.217	0.302			0.626			
sea	c	0.874	0.005			0.022			0.012
	$\tilde{c}$	2.524	0.132	0.423		0.577	0.448		0.203
	$\tilde{d}$	-1.297	0.132	0.130	-0.663	0.575	0.139	-0.666	
	$\tilde{e}$	0.298	0.085			0.346			
	$\tilde{f}$	-0.968	0.122			0.250			
GRL	c	1.453	0.071			0.308			0.135
	$\tilde{c}$	11.265	1.237	0.602		5.306	0.636		1.176
	$\tilde{d}$	-5.466	1.292	-0.029	-0.760	5.502	-0.026	-0.747	
EAIS	c	1.065	0.050			0.221			0.070
	$\tilde{c}$	9.691	1.115	0.615		4.870	0.637		0.949
	$\tilde{d}$	-5.120	1.089	0.195	-0.577	4.732	0.205	-0.561	
NEU	c	1.199	0.028			0.107			0.132
	$\tilde{c}$	3.290	0.358	0.164		1.352	0.217		0.551
	$\tilde{d}$	-0.852	0.597	-0.321	-0.664	2.401	-0.410	-0.598	
	$\tilde{e}$	0.949	0.467			1.599			
	$\tilde{f}$	-1.317	1.217			3.001			
MED	c	1.207	0.025			0.104			0.089
	$\tilde{c}$	-4.716	0.351	-0.404		1.502	-0.456		0.750
	$\tilde{e}$	-2.127	0.716			2.561			
	$\tilde{f}$	-4.735	1.253			2.923			

		fixed effects				random effects			
				correlations			correlations		
		value	Std.E	c	$\tilde{c}$	σ_{model}	r^{mod}	$\tilde{r}^{mod}$	σ_{scen}
NEE	c	1.508	0.052			0.219			0.148
	$\tilde{c}$	6.068	0.400	-0.473		1.518	-0.579		0.559
	$\tilde{d}$	-1.849	0.419	0.136	-0.533	1.391	0.183	-0.337	
	$\tilde{e}$	0.389	0.394			1.365			
	$\tilde{f}$	-1.552	0.736			1.623			
NAS	c	1.588	0.056			0.246			0.116
	$\tilde{c}$	6.427	0.372	0.660		1.554	0.722		0.352
	$\tilde{d}$	-0.718	0.369	-0.376	-0.666	1.451	-0.434	-0.623	
	$\tilde{e}$	-0.811	0.312			1.181			
	$\tilde{f}$	-1.012	0.592			1.431			
CAS	c	1.357	0.037			0.158			0.080
	$\tilde{c}$	-1.591	0.529	-0.554		2.312	-0.584		0.715
	$\tilde{e}$	0.107	0.536			1.844			
	$\tilde{f}$	-2.942	1.273			3.194			
TIB	c	1.432	0.035			0.153			0.061
	$\tilde{c}$	3.803	0.469	-0.368		2.069	-0.381		0.580
	$\tilde{e}$	-0.413	0.296			1.144			
	$\tilde{f}$	0.114	1.280			3.436			
EAS	c	1.171	0.030			0.123			0.115
	$\tilde{c}$	2.917	0.594	-0.133		2.467	-0.156		0.436
	$\tilde{d}$	0.290	0.593	0.104	-0.652	2.312	0.129	-0.595	
	$\tilde{e}$	-2.265	0.382			1.519			
	$\tilde{f}$	-3.010	0.347			0.001			
SAS	c	1.214	0.037			0.163			0.048
	$\tilde{c}$	1.129	0.999	-0.300		4.312	-0.314		0.640
	$\tilde{d}$	2.070	0.910	0.146	-0.805	3.764	0.160	-0.798	
	$\tilde{e}$	-3.049	0.329			1.264			
SEA	c	0.989	0.022			0.096			0.034
	$\tilde{c}$	2.314	0.343	0.151		1.500	0.157		0.510
	$\tilde{e}$	-0.840	0.197			0.722			
	$\tilde{f}$	-0.753	0.824			2.190			
NAU	c	1.242	0.024			0.107			0.043
	$\tilde{c}$	0.131	0.710			3.131			0.598
	$\tilde{e}$	1.554	0.788			2.447			
	$\tilde{f}$	-0.077	1.336			3.123			
SAU	c	1.078	0.025			0.107			0.051
	$\tilde{c}$	-1.622	0.656			2.885			0.705
	$\tilde{e}$	0.298	0.932			3.628			

		fixed effects				random effects			
				correlations			correlations		
		value	Std.E	c	$\tilde{c}$	σ_{model}	r^{mod}	$\tilde{r}^{mod}$	σ_{scen}
SAH	c	1.372	0.027			0.119			0.052
	$\tilde{c}$	2.431	2.438	-0.657		10.246	-0.711		3.204
	$\tilde{d}$	-7.105	1.390			4.140	0.877	-0.286	
	$\tilde{e}$	-0.119	1.157			4.568			
WAF	c	1.253	0.039			0.169			0.082
	$\tilde{c}$	0.311	0.834	-0.298		3.516	-0.322		0.633
	$\tilde{d}$	0.371	0.792	0.230	-0.736	3.193	0.260	-0.724	
	$\tilde{e}$	-0.209	0.197			0.694			
	$\tilde{f}$	-3.391	0.863			2.002			
EAF	c	1.236	0.040			0.177			0.062
	$\tilde{c}$	2.369	0.556	-0.356		2.437	-0.368		0.741
	$\tilde{e}$	-0.466	0.349			1.374			
	$\tilde{f}$	-2.176	0.903			1.983			
EQF	c	1.139	0.036			0.160			0.056
	$\tilde{c}$	4.536	0.902	-0.646		3.994	-0.662		0.780
	$\tilde{e}$	-0.144	0.331			1.246			
	$\tilde{f}$	-1.047	1.581			4.036			
SQF	c	1.235	0.034			0.148			0.050
	$\tilde{c}$	-0.131	0.480	0.052		1.994	0.056		0.392
	$\tilde{d}$	1.541	0.579	-0.360	-0.681	2.353	-0.401	-0.638	
	$\tilde{e}$	-0.644	0.208			0.787			
	$\tilde{f}$	-0.928	0.667			1.604			
SAF	c	1.261	0.035			0.156			0.041
	$\tilde{c}$	-0.854	0.648	0.283		2.868	0.288		0.555
	$\tilde{e}$	-0.473	0.317	-0.000	-0.022	1.284	0.000	0.000	
ALA	c	1.573	0.050			0.219			0.059
	$\tilde{c}$	7.268	0.467	0.128		1.997	0.135		0.443
	$\tilde{d}$	-1.885	0.411	0.246	-0.615	1.671	0.274	-0.583	
	$\tilde{e}$	-1.149	0.299	0.000	0.056	1.083			
GRL	c	1.630	0.050			0.218			0.081
	$\tilde{c}$	7.756	0.401	0.482		1.680	0.519		0.518
	$\tilde{d}$	-2.527	0.465	0.209	-0.639	1.960	0.230	-0.607	
WNA	c	1.317	0.037			0.163			0.061
	$\tilde{c}$	0.422	0.493	0.013		2.174	0.013		0.477
	$\tilde{e}$	0.197	0.678			2.534			
	$\tilde{f}$	-3.072	0.810			1.789			
CNA	c	1.334	0.036			0.155			0.097
	$\tilde{c}$	0.944	0.525	-0.659		2.318	-0.699		0.496
	$\tilde{e}$	1.419	0.772			2.979			
	$\tilde{f}$	-3.726	0.740			1.471			

		fixed effects				random effects			
				correlations			correlations		
		value	Std.E	c	$\tilde{c}$	σ_{model}	r^{mod}	$\tilde{r}^{mod}$	σ_{scen}
ENA	c	1.301	0.030			0.128			0.066
	$\tilde{c}$	2.388	0.481	-0.460		1.983	-0.514		0.325
	$\tilde{d}$	0.481	0.441	0.029	-0.662	1.630	0.033	-0.601	
	$\tilde{e}$	0.096	0.424			1.478			
	$\tilde{f}$	-2.652	0.649			1.483			
CAM	c	1.182	0.031			0.134			0.055
	$\tilde{c}$	-3.561	0.807	-0.064		3.565	-0.066		0.948
	$\tilde{e}$	-1.260	0.698			2.461			
	$\tilde{f}$	-4.300	1.443			3.607			
AMZ	c	1.251	0.036			0.161			0.046
	$\tilde{c}$	0.864	0.590	-0.549		2.617	-0.560		0.543
	$\tilde{e}$	0.125	0.209			0.797			
	$\tilde{f}$	-2.799	0.750			1.877			
CSA	c	1.088	0.026			0.115			0.042
	$\tilde{c}$	2.764	0.849	-0.115		3.686	-0.121		0.636
	$\tilde{d}$	-1.702	0.714	-0.297	-0.657	3.012	-0.320	-0.638	
SSA	c	0.827	0.023			0.100			0.044
	$\tilde{c}$	-1.752	0.390	-0.333		1.719	-0.348		0.474
	$\tilde{e}$	-0.214	0.165			0.620			
	$\tilde{f}$	-1.201	0.299			0.328			
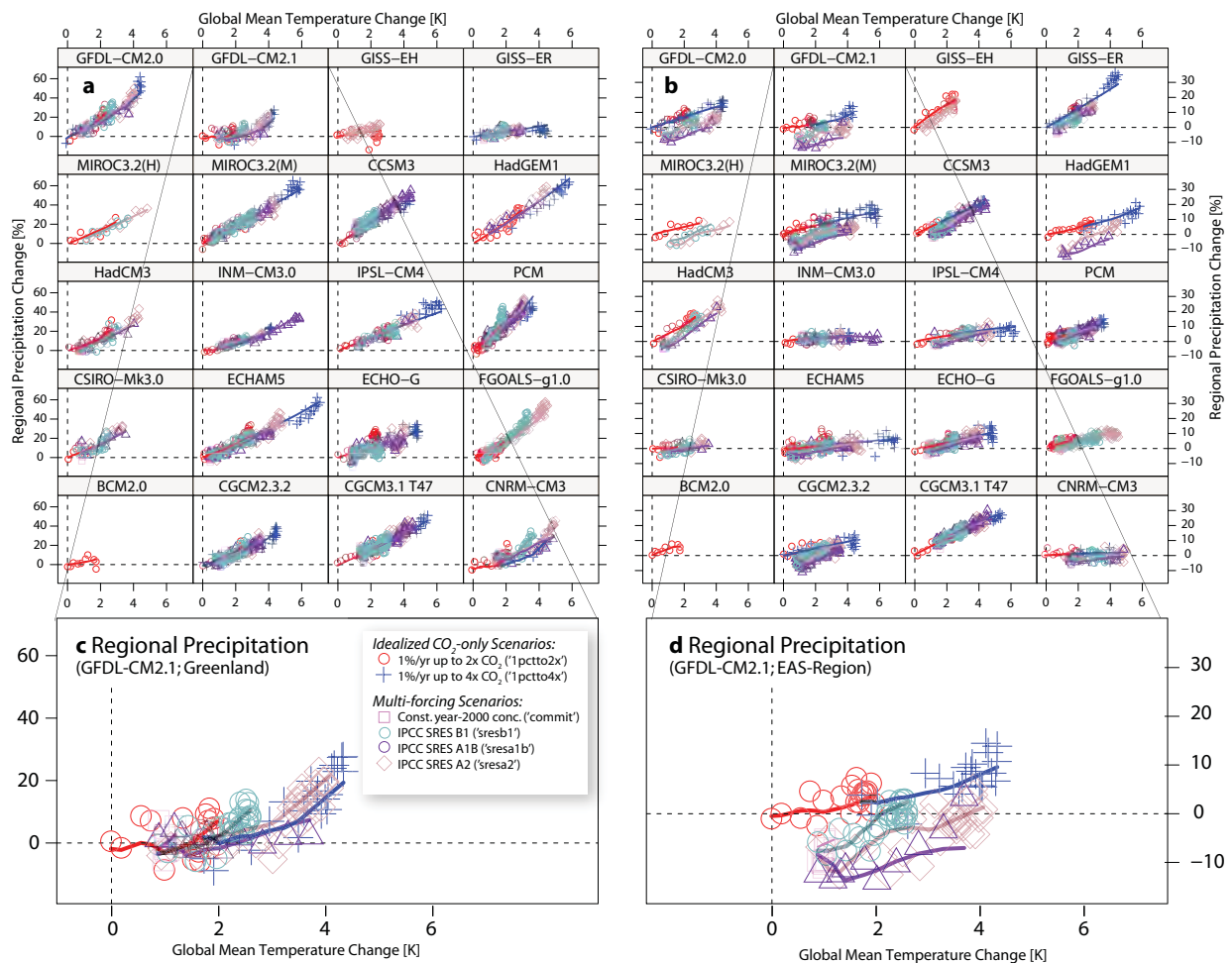
Figure 5: Regional precipitation changes for Greenland ($\overline{\text{GRL}}$) (a) and the East Asian region (EAS) (b). We added the predicted values of the extended precipitation model as solid lines to the precipitation part of Figures 2b and 3b. The data set used for fitting and shown here excludes the 20c3m runs and the BCM2.0 runs where there are no GHG forcing informations available. The predictions are based on the estimated fixed effect and the AOGCM specific random effects. Inter-scenario variations are not added.

To calculate the model fit, AOGCM specific estimates of r^{mod} and $\tilde{r}^{mod}$ were added to the fixed effects while the scenario or run specific random effects were ignored in Figure 5. GHG forcing effects could explain the change in hydrological sensitivity at the beginning of the stabilization periods for some of the AOGCMs as e.g. the GFDL-CM2.1 and the CNRM-CM3 model. However, for some models, e.g., GFDL-CM2.0 or ECHAM5, the inclusion of the tropospheric GHG forcing component does not sufficiently explain the steeper increase (the fitted lines in Figure 5 do not reproduce these AOGCM data points very well). That might be due to 1) further mechanisms that affect hydrological sensitivity but are not included in our

analysis 2) an inadequate approximation of the tropospheric GHG forcing by the weighted sum of TOA forcings. In case of the EAS region we found BC and SOx emissions to have a strong dampening effect on temperature driven precipitation increases (see the negative values for $\tilde{e}$ and $\tilde{f}$ in Table 4). A combination of BC and SOx effects thus provide a good explanation for the difference between the precipitation changes in the idealized runs and the SRES scenarios (Figure 5b).

The remaining inter-scenario variability of the scaling coefficients is generally lower than the inter-AOGCM variability but not completely negligible (in the order of 50% in case of temperature and in the order of 30% in case of precipitation when taking GHG forcing and aerosol effects into account). For temperature, the standard deviation of the inter-scenario variability is in the order of 5-10 % of the estimated scaling coefficients. The inter-run variability is estimated to be about one order of magnitude smaller than the inter-AOGCM variability and might be neglected given the other contributions to the overall uncertainty of the scaling coefficients.

In some regions the scaling coefficients of the additional predictors show a considerably larger inter-AOGCM variability than the multi-model-mean absolute value. This indicates that the effects are not consistent over the 20 AOGCMs.

We now discuss two distinct purposes for the scaling coefficients given in Table 3 and 4. First of all it becomes possible to derive regional probabilistic climate response estimates for any particular fixed warming level. Using our "temperature-only" model version provided in Table 3, any particular warming level can be transformed into a regional temperature and precipitation change and its uncertainty. For instance, we may multiply the provided "fixed effects" scaling coefficients for temperature (second column of Table 4) by 2 to yield the mean temperature change under a 2°C global warming level, recently adopted as climate target by the Copenhagen Accord. As an example the North Asia / Siberia region (NAS) is likely to be 3.18 °C (± 0.56°C) warmer at a 2 °C global mean warming level. However, we need the triplet of global mean warming level, GHG forcing and aerosol emissions to account for the non-linearities in the precipitation patterns. For the 2 $°C$ warming level, the associated fixed effect by temperature on precipitation has to be multiplied by 2 and merged with the scaled GHG forcing, BC and sulfate emission values.

In a second application we use the scaling coefficients in conjunction with uncertainty distributions of global mean temperatures and GHG forcings to derive transient probabilistic regional projections, as described in Subsection 2.6 and demonstrated in the following sections.

3.3. Probabilistic regional projections

The combination of probabilistic global projections with the scaling coefficient now allows to derive regional climate changes, as shown in Figure 7 for Greenland and other world regions in Figure 6. All projections are based on the extended model versions, i.e. the scaling coefficients given in Table 4.

Several implications for future regional climate change seem noteworthy. Firstly, if the new RCP scenarios are truly spanning the full range of literature scenarios - which was one of their design criteria - then the lower (RCP3-PD) and higher (RCP8.5) scenario results shown in Figure 6 do span the range from strong mitigation towards high emission no-climate-policy cases. With the possible exception of the South America (CSA and SSA), South East Asia (SEA), and South Australia (SAU), a temperature increase in excess of 8°C by 2100 cannot be excluded in any of the regions under the high RCP8.5 scenario. Secondly, even the low RCP3-PD emission scenario that implies strong and immediate mitigation actions results in best-guess land warming at or beyond 2°C, although median global warming remains below 2°C.

Our analysis reenforces earlier diagnoses [Meehl et al., 2007] in regard to the regional distribution of precipitation changes under climate change. While precipitation is increasing for Greenland and other polar regions, models suggest strongly decreasing precipitation for the Mediterranean region (MED) and possibly Central America (CAM). On contrary, the sign of the precipitation change is not clear for the Amazon due to the divergent result from the underlying set of AOGCMs. Confirming earlier studies, our results show that the occurrence of an Amazon dieback as both consequence and cause of a strong reduction in precipitation [Cox et al., 2004, Jones et al., 2009] are rather unique to the HadCM3 and HadGEM1 model. For the very dry Sahel Zone (SAH), the high uncertainty in relative precipitation changes reflects the very small current absolute precipitation levels which easily result in high relative deviations from pre-industrial levels. Note that these regions are not strictly defined climatic regions and therefore subregions with more pronounced precipitation changes might exist.

Overall, the projected median changes in precipitation (and the associated uncertainty ranges) based on the extended model are very similar to the basic model results for most of the regions. Differences between the basic and the extended models are most pronounced for the EAS, MED and $\overline{\text{GRL}}$ region. Except of small scaling coefficients for the aerosol and GHG components for some regions the similarity has two main reasons: 1) low aerosol emissions in 2100 for both RCP scenarios (see Figure 11 and 12 of the Appendix) and 2) the high correlation between the global mean temperature changes and the tropospheric GHG forcing component
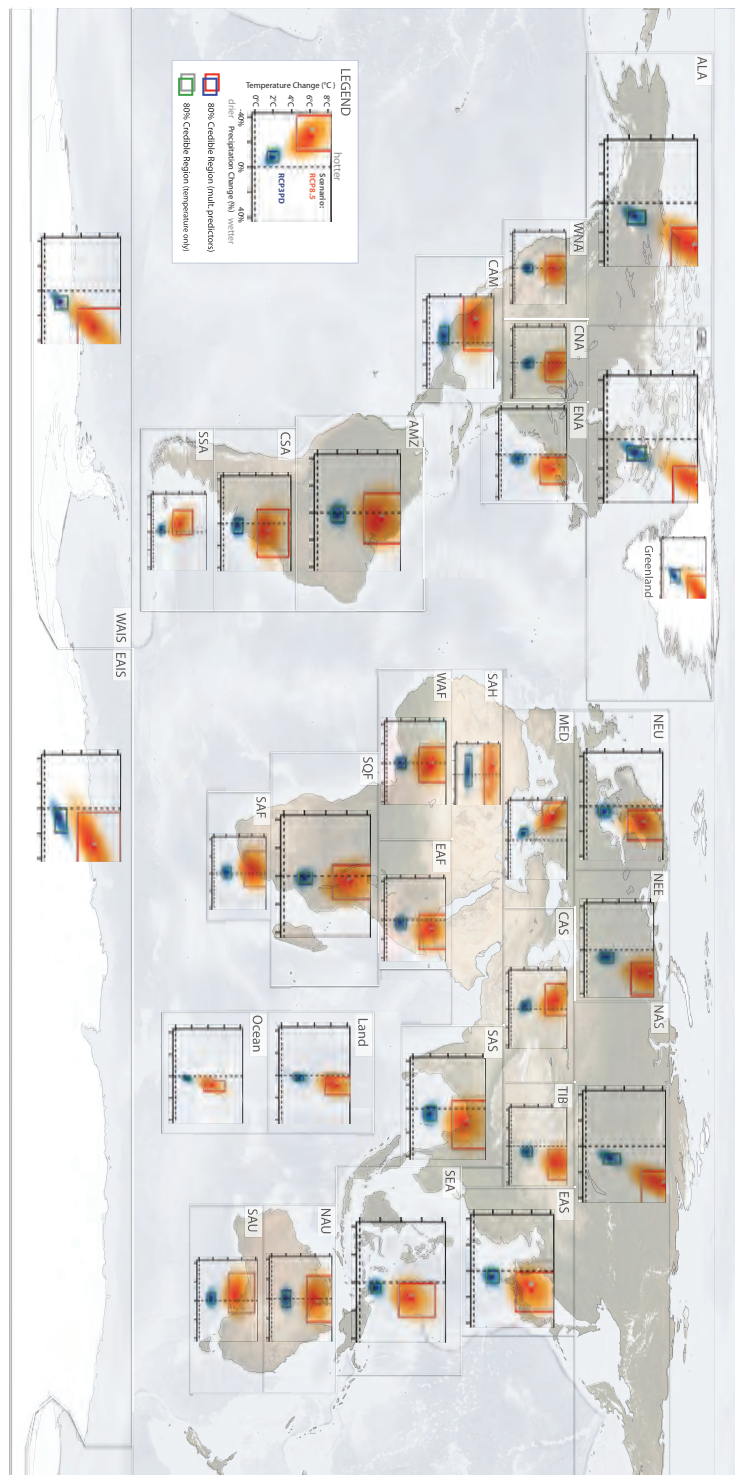
Figure 6: Joint distributions of regional temperature and precipitation changes in 2100 under the low (RCP3-PD, blue) and high (RCP8.5, orange) scenarios. The region definitions are based on Giorgi and Bi [2005] and amended by those for the West and East Antarctic Ice sheet (WAIS and EAIS) separated by the Transantarctic Mountains. The background is based on NASA Blue Marble image by R. Stöckli.

that do not diverge within the 21st century, at least not for the RCP8.5 scenario. Figure 13 and 14 of Appendix E show the time series of the individual contributions of tropospheric GHG forcing, aerosol effects and global mean temperature change to the overall change in precipitation for the EAS region and $\overline{GRL}$. In both cases the contributions of the additional explanatory variables are rather substantial.

In all our projections, we do not include any residual variation, i.e. the distributions describe the uncertainties of the projected $mean$ changes without taking into account internal variability.

3.4. Example of Greenland's ice sheet SLR contribution

While accurate simulation of ice sheet surface mass balance usually requires higher spatial resolution than provided by the AR4 AOGCM runs, Gregory and Huybrechts [2006] developed a method for calculating mass balance changes in dependence of ice-sheet averaged temperature and precipitation changes from AOGCM simulations by combining them with high resolution climate model runs and an ice-sheet mass balance model. Their model uses the integrated sum of expected positive degree days, based on annual averages of temperature, and different degree-day factors (DDFs) for snow and ice to calculate surface melt and the following runoff. The model was applied to calculate the $change$ of surface mass balance for a range of regional climate changes ΔT and $\Delta P/P_0$, where changes were described with respect to "present day" values (T_0 and P_0) averaged over the 1960-1990 period. Increasing precipitation produces a negative sea level contribution, because of higher accumulation rates. Increasing temperatures produce a positive contribution, because of accelerated melting rates.

Table 5: Exceedance probabilities for different contributions to sea level rise from changes in Greenland's surface mass balance. The calculations are based on the parametric scaling approach coupled to the impact function provided by Gregory and Huybrechts [2006].

	0 mm/yr	0.62 mm/yr	1 mm/yr	1.5 mm/yr	2 mm/yr
RCP3-PD: 2050	97%	0%	0%	0%	0%
RCP8.5: 2050	100%	2%	1%	0%	0%
RCP3-PD: 2100	92%	0%	0%	0%	0%
RCP8.5: 2100	100%	86%	65%	43%	30%

Using the joint probabilities we produced for the RCP scenario runs, we can now calculate exceedance probabilities for various isolines of surface mass balance change by integrating over the samples that fall above a certain threshold (see Figure 7). Results for 0, 0.62, 1 and 2 mm SLR/yr are given in Table 5.

In the reference period 1960-1990, the SMB is estimated to be -0.62 mm/yr, a gross gain of the GRL ice sheet (that was historically balanced by an associated loss by dynamical processes), so that a 0.62 mm/yr change in SLR contribution computed here would lead to an absolute SMB of zero. A zero SMB is the point at which no gross mass gain of the GRL could occur, even under zero dynamical ice sheet losses. These calculations do not account for sea level rise due to changes in dynamical losses of the Greenland ice sheet. These lead to a net loss of ice mass, even at a SMB of zero, and could possibly lead to substantially higher changes in sea level rise as observations suggest (e.g. Van den Broeke et al. [2009]).
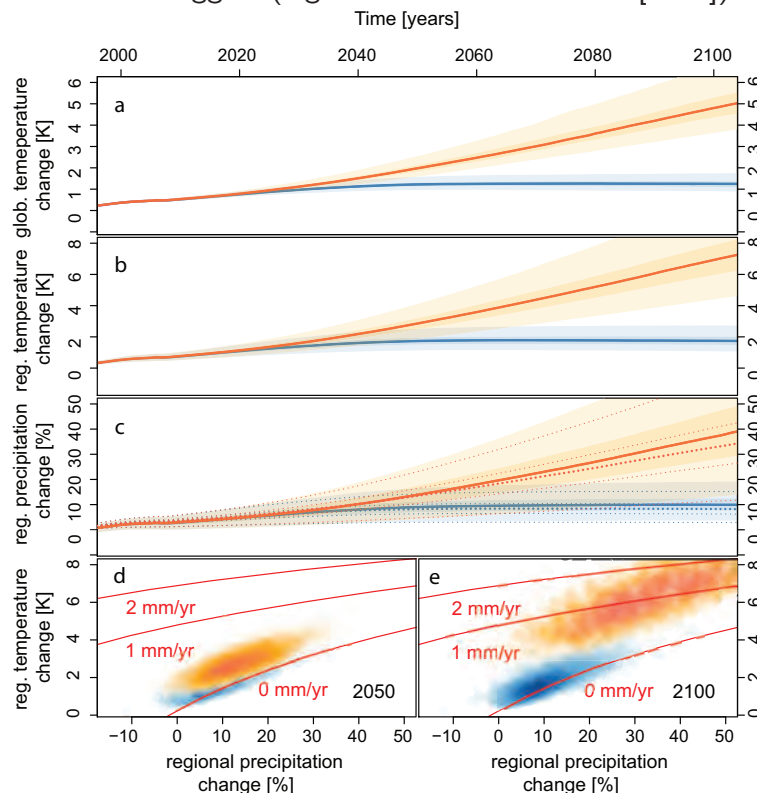
Figure 7: Regional temperature and precipitation changes for the Greenland area ($\overline{GRL}$) and the associated changes in the surface mass balance: a) Probabilistic projections of global mean temperature change based on the RCP3-PD (blue) and the RCP8.5 (orange) emission scenarios. Light shaded area mark the inner 80% of the uncertainty distribution and the dark shaded areas mark the inner 33%. b) Probabilistic projections of the associated mean change in regional temperatures. Dashed lines represent the associated estimates based on the basic model. c) Probabilistic projections of the associated mean change in regional precipitation. Dashed lines represent the associated estimates based on the basic model. c,d) bi-dimensional uncertainty distributions of regional temperature and precipitation changes for the year 2050 and the year 2100, respectively (Blue: RCP-3PD, Orange: RCP8.5). Red lines indicate isolines of associated changes in Greenland's surface mass balance in units of sea level rise per year [Gregory and Huybrechts, 2006]. All regional climate changes are calculated relative to the year 1975 adjusted to the reference period used by Gregory and Huybrechts [2006].

4. Limitations, Sensitivities and Outlook

This section highlights sensitivities, limitations and possible future extensions of the presented scaling approach. In particular, difficulties in interpreting our results are highlighted.

4.1. Limitations of the scaling approach

Coupling the uncertainty distributions of global mean temperature to the regional scaling coefficients can lead to an extrapolation of the available AOGCM simulations beyond the calibration range of the statistical model. Especially the RCP8.5 emission scenario leads to a sample of global mean temperature trajectories that goes beyond the range simulated by the CMIP3 AOGCMs. This hampers the estimation of exceedance probabilities especially for this high temperature range because new processes can come into play. The forthcoming CMIP5 ensemble will allow testing the validity of this extrapolation. Similarly, the results for the new lower scenario RCP3-PD will provide new insights into the validity of the scaling for the low scenarios, in which temperatures might peak in the course of the 21st century.

Estimation of the change in regional precipitation that is induced by tropospheric forcing is hampered by the high correlation of global mean temperature change and GHG forcing. Therefore some of the temperature induced changes might be attributed to the forcing component and vice versa. While our estimates are based on the relatively short stabilization periods available from the CMIP3 data the situation will improve when analyzing the RCP3-PD simulations planned for the CMIP5 project. This scenario will comprise a period of declining GHG forcings, thereby breaking the close correlation between temperature and forcing (see Figure 15 of the Appendix).

In addition, there will be simulations in which CO_2 is instantaneously quadrupled [Taylor et al., 2011]. These idealized CMIP5 runs will provide an ideal setting for separating the "fast" forcing induced effect on precipitation from the "long term" response to global mean temperature change.

Our approximation of the tropospheric GHG forcing is based on the assumption that the tropospheric forcing is proportional to the TOA forcing. While this is supported by Andrews et al. [2010] for CO_2 it needs further validation. Our approximation might be improved by future studies providing more information about the tropospheric fraction of the GHG forcing, particularly for non-CO_2 - GHGs.

Our study does not allow any statement about the validity of the AOGCM projections. It provides a kind of summary of their projections but does not weight the AOGCMs according to

implemented feedbacks processes, their representation of aerosol effects or the agreement with observations. For example, aerosol forcings were only partially implemented in most CMIP3 AOGCMs, and dynamic vegetation or sea ice models were not coupled in almost all cases. This might have a strong influence on regional projections.

Handling the inter-scenario variability as an unsystematic uncertainty component might be a limitation for some regions. In case of the temperature scaling coefficients the "commit" scenario seems to be most problematic (Figure 9 of Appendix C): The temperature scaling coefficients for this scenario shows relatively strong deviations that tend to be systematically (i.e. persistent over most of the AOGCMs) lower or higher than zero in some regions. This may be due to the stabilization character of the commitment run with changing land ocean warming gradients. The effect could also be caused by aerosols: In many regions the aerosol loading reaches a high level at the end of the 20th century. This high level is held constant for the commitment run providing relatively strong cooling under a relatively low GHG induced warming.

With respect to precipitation, the scaling coefficients related to global temperature in the ocean region are systematically smaller than zero for the "1pctto4x" scenario while systematically larger than zero for the "commit" scenario (Figure 10 of Appendix C). The reason for that is unclear but the effect might be due to inappropriate weightings when deriving of the tropospheric forcing for each GHG [Frieler et al., 2011].

4.2. Application of the bi-dimensional approach to subregions or seasons

Our approach is based on monthly data. Thus, instead of calculating annual averages it may easily be applied to seasonal averages. For example, it might be interesting to distinguish between winter and summer temperature over Greenland, where wintertime warming is stronger than summertime warming [Meehl et al., 2007]. In this setting, the inter-AOGCM (inter-scenario and inter-run) variations of the seasonal scaling coefficients might also be correlated across seasons. This can be handled by fitting a bi-dimensional random effects model where one component describes summertime temperature changes while the other one describes the winter temperature changes. In an analogous way it is also possible to obtain a bi-dimensional uncertainty distribution of temperature or precipitation scaling coefficients of neighboring regions. For instance, one component of the model could describe annual temperature changes in the Western subregion of Antarctica while the second describes temperature changes of the Eastern part. Even an extension to more than two dimensions is possible. A 12-dimensional

model could describe a complete annual cycle of scaling coefficients but may require some restrictions concerning the considered correlations structures to allow convergence of the fitting routine.

5. Conclusion

We introduced a new scaling approach to calculate probabilistic projections of regional temperature and precipitation changes. Unlike other studies – to our knowledge –, our method allows the separation of the inter-AOGCM, inter-scenario and inter-run variability of the scaling coefficients. Furthermore, estimates of the correlation between the uncertainty distributions of the temperature and precipitation scaling coefficients can be obtained. We provide estimates of all these components of variability calculated from the wide range of different AOGCMs and scenarios considered within the CMIP3 model intercomparison.

Our approach captures the possible correlations between the uncertainty distributions associated with the temperature and precipitation component. It is thus suitable for coupling with impact functions that depend on the bi-variate input. In particular it is possible to calculate the exceedance probabilities for different isolines in the two dimensional temperature-precipitation plane. In case of Greenland's surface mass balance where the effect of increasing temperatures can partly be balanced by increasing precipitation the strong correlation of both components of the uncertainty distribution leads to reduced probabilities of exceeding certain sea level rise isolines.

We provide samples of scaling coefficients and regional temperature and precipitation changes for 31 world regions including the whole land and ocean area in the online archive (www.pik-potsdam.de/~frieler/regional). As a very efficient way to calculate probabilistic projections of regional temperature and precipitation changes our results may for example be easily applied within other impact studies in preparation of the Working Group II contribution to the IPCC AR5 report.

6. Acknowledgements

A. Model code

Here we provide a schematic representation of the R-code used to fit the basic model (cf. equation (1)):

We start from two data frames temp.dat and prec.dat that contain six columns each. The first column contains the ten year averages of regional temperature changes ($\Delta T_{regional}$) in temp.dat and the regional changes of the precipitation data ($\Delta P_{regional}$) in prec.dat. In both cases this column is simply called "output". The second, third and forth columns are specify the model, scenario and run and are called "model", "scenario" and "run" . The fifth column contains the ten year averages of the global mean temperature changes, ΔT_{global}. Then the one dimensional models can be fitted by

$$\texttt{var.lme} =$$
$$\texttt{lme (output} \sim \Delta T_g - 1 \,|$$
$$\quad \texttt{random} = \texttt{list(model} =\sim \Delta T_g - 1,$$
$$\quad \texttt{scenario} =\sim \Delta T_g - 1,$$
$$\quad \texttt{run} =\sim \Delta T_g - 1),$$
$$\texttt{weights} = \texttt{varIdent(form} =\sim 1\,|\,\texttt{model}),$$
$$\texttt{data} = \texttt{var.dat})$$

where var = "temp" or var = "prec". The "weights" statements is used to estimate AOGCM specific residual variances. To fit the bivariate model the temperature and the precipitation data frames are combined:

$$\texttt{combined.dat} = \begin{pmatrix} \texttt{temp.dat} \\ \texttt{prec.dat} \end{pmatrix}.$$

We add a temperature indicator, i.e. an additional column called "t.ind" containing "1" for rows belonging to temp.dat and "0" for rows belonging to prec.dat. A precipitation indicator

"p.ind" is added analogously. Finally the bivariate model is fitted by:

$$\texttt{bivariate.model.lme} =$$
$$\texttt{lme (output} \sim \texttt{I}(\Delta T_g * \texttt{t.ind}) + \texttt{I}(\Delta T_g * \texttt{p.ind}) - 1,$$
$$\texttt{random} = \texttt{list (}$$
$$\texttt{model} = \sim \texttt{I}(\Delta T_g * \texttt{t.ind}) + \texttt{I}(\Delta T_g * \texttt{p.ind}) - 1,$$
$$\texttt{scenario} = \sim \texttt{I}(\Delta T_g * \texttt{t.ind}) + \texttt{I}(\Delta T_g * \texttt{p.ind}) - 1,$$
$$\texttt{run} = \sim \texttt{I}(\Delta T_g * \texttt{t.ind}) + \texttt{I}(\Delta T_g * \texttt{p.ind}) - 1),$$
$$\texttt{weights} = \texttt{varIdent(form} = \sim 1 \,|\, \texttt{model} * \texttt{t.ind},$$
$$\texttt{fixed} = \texttt{delta)},$$
$$\texttt{data} = \texttt{combined.dat)}$$

In this way the correlation of the temperature and the precipitation component of the *random effects* is estimated automatically. Assuming that e.g. the inter-run random effects were independent the model was modified by specifying

$$\texttt{run} = \texttt{pdDiag}(\sim \texttt{I}(\Delta T_g * \texttt{t.ind}) + \texttt{I}(\Delta T_g * \texttt{p.ind}) - 1)$$

in the "random" statement.

B. Residual diagnostics

To test the assumption of normally distributed residuals especially for the precipitation data we used the explorative Quantile-Quantile-Plot method. The different panels of Figure 8 were generated by the R commands

$$\texttt{qqnorm(temp.model.lme, resid(., type = "p")|model)}$$
$$\texttt{qqnorm(prec.model.lme, resid(., type = "p")|model)}.$$

Here, the quantiles of the standardized empirical residuals are compared to the theoretical quantiles of standard normal distribution. Data falling on the diagonal mean that the data nearly follows the theoretical distribution, in our case the standard normal distribution. For both variables and both considered regions that is the case (see Figure 8).
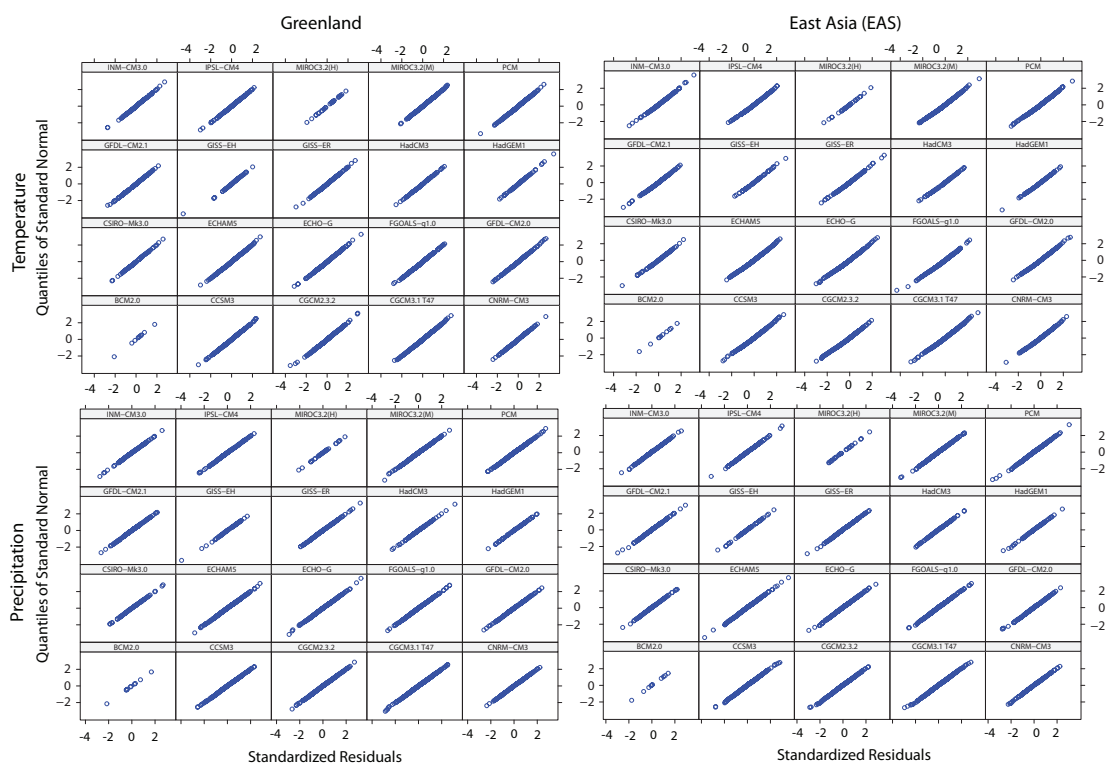
Figure 8: QQ-Plot of the standardized residuals for the Greenland region ($\overline{\text{GRL}}$) (panel (a) and (b)) and the East Asia region (panel (c) and (d)). Panel (a) and (c) refer to the temperature and panel (b) and (d) to the precipitation residuals. Data falling on the diagonal support the assumption of normally distributed residuals

C. Estimation of scenario specific random effects

Not the random effects $(r_i^{\text{mod}}, \tilde{r}_i^{\text{mod}})$, $(r_{i,j}^{\text{scen}}, \tilde{r}_{i,j}^{\text{scen}})$, and $(r_{i,j,k}^{\text{run}}, \tilde{r}_{i,j,k}^{\text{run}})$ themselves but only the components of their covariance matrixes are parameters for the considered random effects models. It is nevertheless possible to "estimate" their individual values as their Best Linear Unbiased Predictors (BLUPs) (see [Pinheiro and Bates, 2000], p. 71). Within the R-package nlme this is done by the ranef command that we separately applied to the temperature and precipitation component of the regional models to estimate the scenario specific random effects $(r_{i,j}^{\text{scen}}, \tilde{r}_{i,j}^{\text{scen}})$ for each AOGCM:

$$\mathtt{ranef(temp.lme, level = 2)}$$
$$\mathtt{ranef(prec.lme, level = 2)}.$$

In Figure 9 the temperature related estimates are plotted for each individual scenario to display whether there is a common scenario effect persistent over all AOGCMs. The same was done for the precipitation component in Figure 10 of the supplementary material.
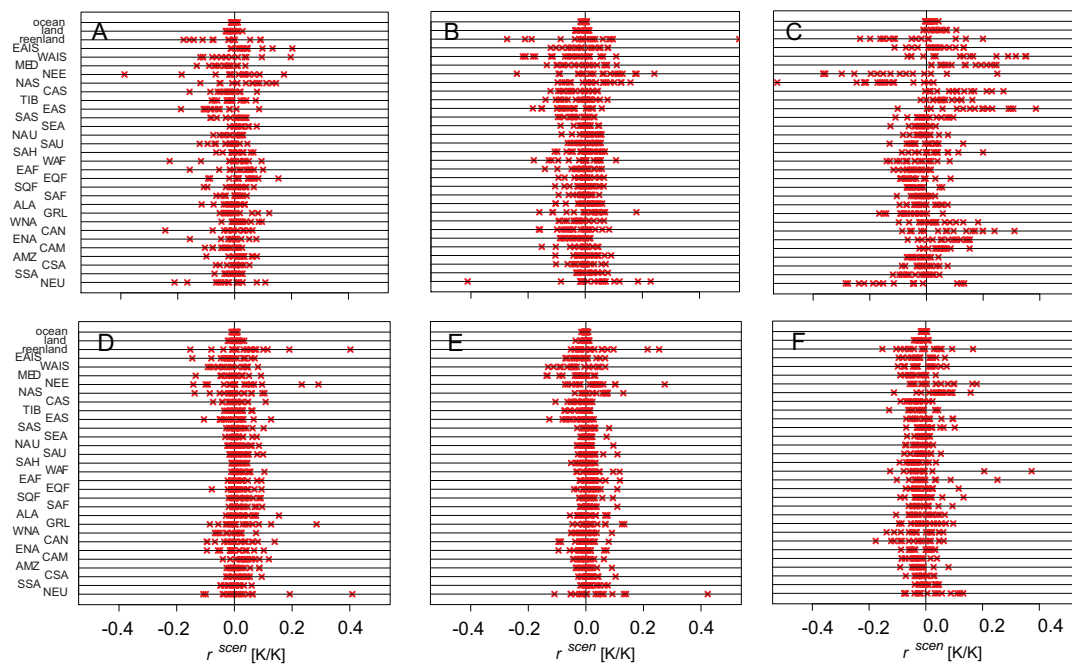
Figure 9: Scenario specific random effects associated with the regional temperature change per global mean temperature change (r^{scen} given in equation (2)) as estimated from the extended model versions. One cross represents the estimate associated with one specific AOGCM. Panels: (A) 1pctto4x, (B) 1pctto2, (C) commit, (D) sresb1, (E) sresa1b, (F) sresa2.
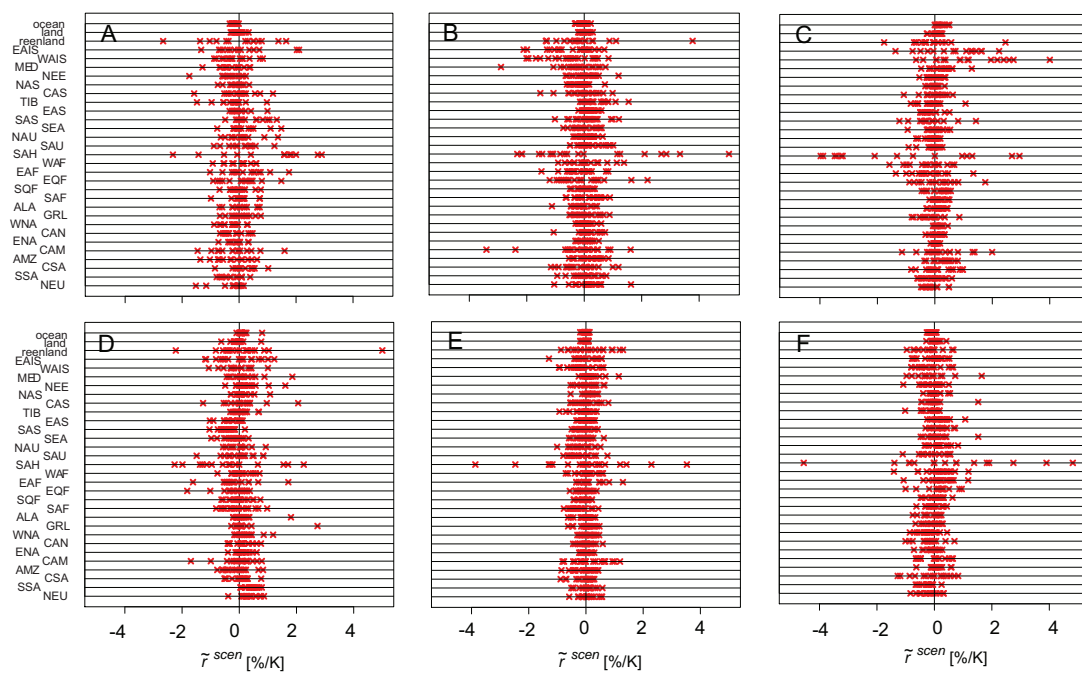
Figure 10: Scenario specific random effects associated with the regional precipitation change per global mean temperature change ($\tilde{r}^{\text{scen}}$ given in equation (2)) as estimated from the extended model versions. One cross represents the estimate associated with one specific AOGCM. Panels: (A) 1pctto4x, (B) 1pctto2, (C) commit, (D) sresb1, (E) sresa1b, (F) sresa2.

D. BC and SOx emissions

Figure 11 and 12 show the BC and SOx emissions for the future RCP3-PD and RCP8.5 scenario we used for the future projections. Data are given for the large scale emission regions we considered within the model fitting.
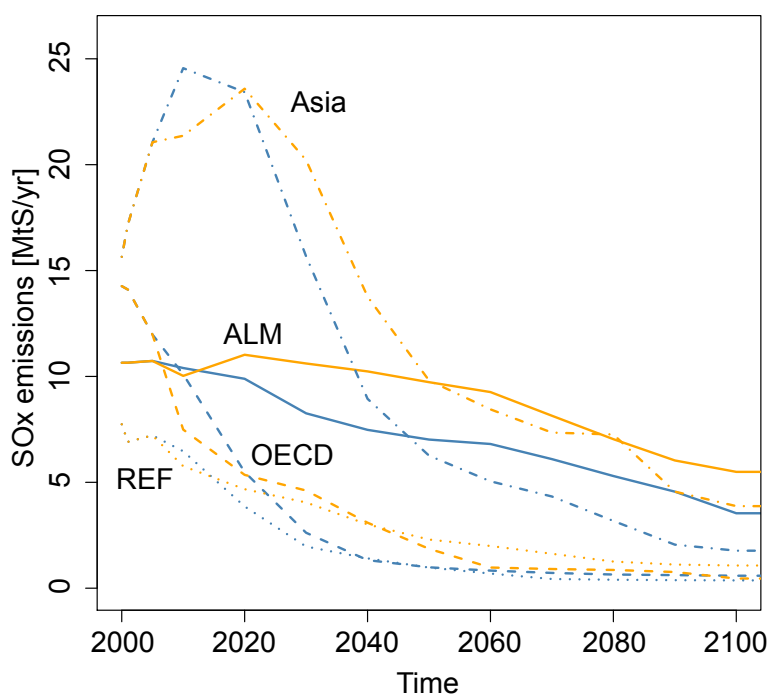
Figure 11: Regional SOx emissions [MtS/yr]. Orange: RCP8.5, Blue: RCP3-PD.
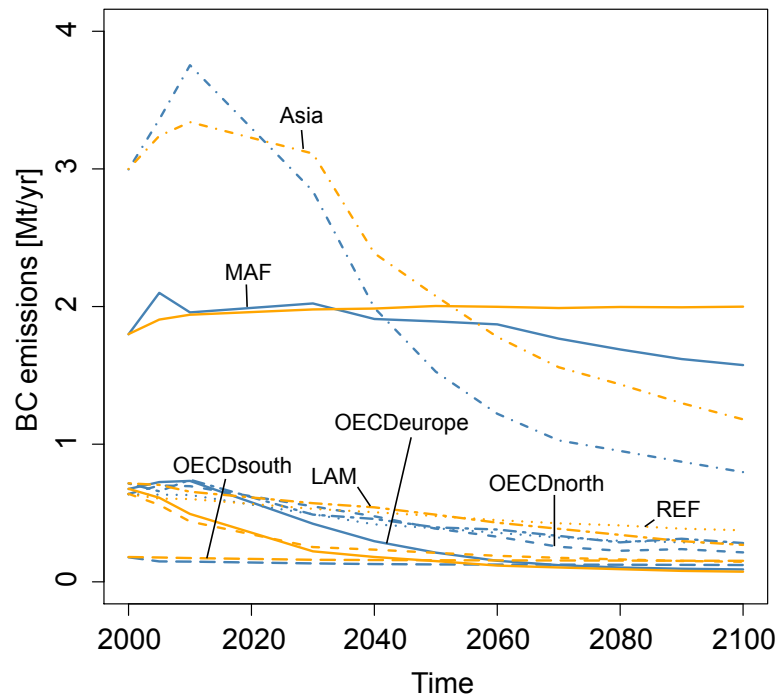
Figure 12: Regional Black Carbon emissions [Mt/yr]. Orange: RCP8.5, Blue: RCP3-PD.

E. Individual Contributions to precipitation changes

Figure 13 and 14 show the individual contributions of GHG forcing, BC and SOX emissions and global mean temperature change on precipitation changes over the $\overline{GRL}$ and the EAS region as estimated by the extended model (see Table 4 for the multi-model mean scaling coefficients). Median projections are based on the RCP3-PD and the RCP8.5 scenarios. For comparison we also show the median of the overall response as estimated on the basis of the extended model and the median response based on the basic statistical model.
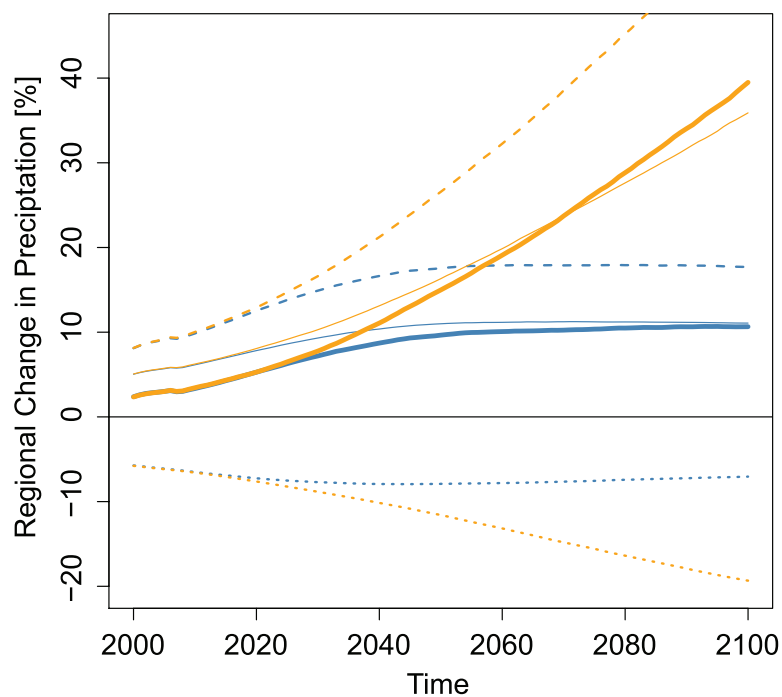
Figure 13: Individual contributions to regional precipitation change over Greenland. Blue lines represent results for the RCP3-PD scenario while results for the RCP8.5 scenario are marked in orange. Long-dashed-lines: Temperature induced changes as estimated from the extended model (see Table 4). Short dashed line: GHG induced change as estimated by the same statistical model. Thick solid line: Overall response given by the sum of both components. Thin solid line: Temperature induced change as estimated from the basic statistical model. All lines represent the medians of the associated probabilistic projections.
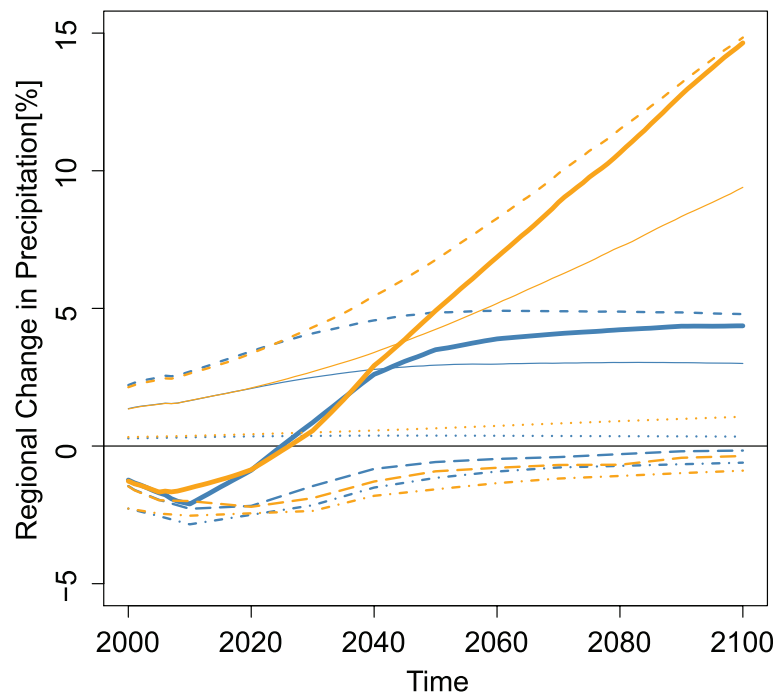
Figure 14: Individual contributions to regional precipitation change over East Asia (EAS). Blue lines represent results for the RCP3-PD scenario while results for the RCP8.5 scenario are marked in orange. Short-dashed-lines: Temperature induced changes as estimated from the extended model (see Table 4). Dotted line: GHG induced change as estimated by the same statistical model. Long-dashed line: contribution of sulfate aerosols. Dot-dashed lines: BC induced changes. Thick solid line: Overall response given by the sum of the four components. Thin solid line: Temperature induced change as estimated from the basic statistical model. All lines represent the medians of the associated probabilistic projections.
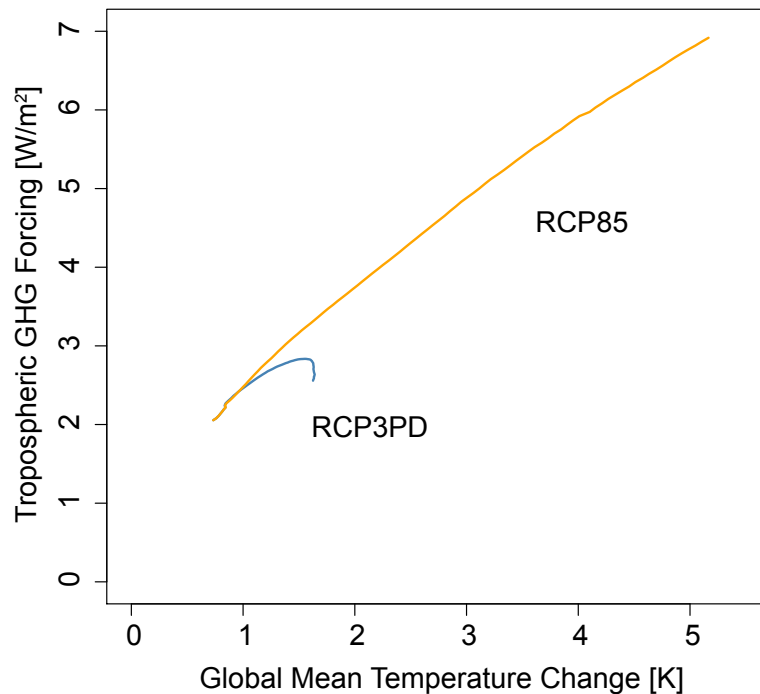
Figure 15: Relationship between global mean temperature change and our approximation of the tropospheric GHG forcing, see main text for details. Both the global mean temperature change and the tropospheric forcing are given by the median of their probabilistic projections provided by MAGGIC6 for the RCP3-PD (blue) and RCP8.5 (orange) scenario.

Literature

B.A. Albrecht. Aerosols, cloud microphysics, and fractional cloudiness. *Science*, 245(4923): 1227, 1989.

M.R. Allen and W.J. Ingram. Constraints on future changes in climate and the hydrologic cycle. *Nature*, 419(6903):224–232, 2002. ISSN 0028-0836.

M.R. Allen, D.J. Frame, C. Huntingford, C.D. Jones, J.A. Lowe, M. Meinshausen, and N. Meinshausen. Warming caused by cumulative carbon emissions towards the trillionth tonne. *Nature*, 458(7242):1163–1166, 2009. ISSN 0028-0836.

T. Andrews, P.M. Forster, O. Boucher, N. Bellouin, and A. Jones. Precipitation, radiative

forcing and global temperature change. *Geophysical Research Letters*, 37(14):L14701, 2010. ISSN 0094-8276.

Timothy Andrews, Piers M. Forster, and Jonathan M. Gregory. A surface energy perspective on climate change. *Journal of Climate*, 22(10):2557–2570, 2009. doi: $10.1175/2008JCLI2759.1$. URL http://journals.ametsoc.org/doi/abs/10.1175/2008JCLI2759.1.

Govindasamy Bala, K. Caldeira, and R. Nemani. Fast versus slow response in climate change: implications for the global hydrological cycle. *Climate Dynamics*, 35:423–434, 2010. ISSN 0930-7575. URL http://dx.doi.org/10.1007/s00382-009-0583-y. 10.1007/s00382-009-0583-y.

P. Brohan, JJ Kennedy, I. Harris, SFB Tett, and PD Jones. Uncertainty estimates in regional and global observed temperature changes: a new dataset from 1850. *J. Geophys. Res.*, 111 (D12), 2006.

P. M. Cox, R. A. Betts, M. Collins, P. P. Harris, C. Huntingford, and C. D. Jones. Amazonian forest dieback under climate-carbon cycle projections for the 21st century. *Theoretical and Applied Climatology*, 78:137–156, 2004. ISSN 0177-798X. URL http://dx.doi.org/10.1007/s00704-004-0049-4. 10.1007/s00704-004-0049-4.

S. Dessai, X. Lu, and M. Hulme. Limited sensitivity analysis of regional climate change probabilities for the 21st century. *Journal of Geophysical Research*, 110(D19):D19108, 2005. ISSN 0148-0227.

C.M. Domingues, J.A. Church, N.J. White, P.J. Gleckler, S.E. Wijffels, P.M. Barker, and J.R. Dunn. Improved estimates of upper-ocean warming and multi-decadal sea-level rise. *Nature*, 453(7198):1090–1093, 2008. ISSN 0028-0836.

B. Dong, J.M. Gregory, and R.T. Sutton. Understanding land-sea warming contrast in response to increasing greenhouse gases. Part I: Transient adjustment. *Journal of Climate*, 22(11): 3079–3097, 2009. ISSN 1520-0442.

P.M.F. Forster and K.E. Taylor. Climate forcings and climate sensitivities diagnosed from coupled climate model integrations. *Journal of Climate*, 19(23):6181–6194, 2006. ISSN 1520-0442.

P. Friedlingstein, P. Cox, R. Betts, L. Bopp, W. von Bloh, V. Brovkin, P. Cadule, S. Doney, M. Eby, I. Fung, G. Bala, J. John, C. Jones, F. Joos, T. Kato, M. Kawamiya, W. Knorr, K. Lindsay, H.D. Matthews, T. Raddatz, P. Rayner, C. Reick, E. Roeckner, K.-G. Schnitzler, R. Schnur, K. Strassmann, K. Weaver, C. Yoshikawa, and N. Zeng. Climate-carbon cycle

feedback analysis: Results from the c4mip model intercomparison. *Journal of Climate*, 19 (14):3337–3353, 2006.

K. Frieler, M. Meinshausen, T.S. von Deimling, T. Andrews, and P. Forster. Changes in global-mean precipitation in response to warming, greenhouse gas forcing and black carbon. *Geophysical Research Letters*, 38(4):L04702, 2011. ISSN 0094-8276.

F. Giorgi. A simple equation for regional climate change and associated uncertainty. *Journal of Climate*, 21(7):1589–1604, 2008. ISSN 1520-0442.

F. Giorgi and X. Bi. Updated regional precipitation and temperature changes for the 21st century from ensembles of recent AOGCM simulations. *Geophysical Research Letters*, 32 (21):L21715, 2005. ISSN 0094-8276.

JM Gregory and P. Huybrechts. Ice-sheet contributions to future sea-level change. *Philosophical Transactions of the Royal Society A: Mathematical, Physical and Engineering Sciences*, 364(1844):1709, 2006. ISSN 1364-503X.

M. Hulme, T.M.L. Wigley, E. Barrow, S. Raper, A. Centella, S. Smith, and A. Chipanshi. *Using a Climate Scenario Generator for Vulnerability and Adaptation Assessments: MAGICC and SCENGEN: Version 2.4 Workbook*. Climatic Research Unit Norwich, 2000. ISBN 0902170309.

C. Huntingford and P. M. Cox. An analogue model to derive additional climate change scenarios from existing GCM simulations. *Climate Dynamics*, 16:575–586, 2000.

A. Jones, J. Urban, D. P. Murtagh, P. Eriksson, S. Brohede, C. Haley, D. Degenstein, A. Bourassa, C. von Savigny, T. Sonkaew, A. Rozanov, H. Bovensmann, and J. Burrows. Evolution of stratospheric ozone and water vapour time series studied with satellite measurements. *Atmospheric Chemistry and Physics*, 9:6055–6075, 2009.

F.H. Lambert and M.J. Webb. Dependency of global mean precipitation on surface temperature. *Geophysical Research Letters*, 35(16):L16706, 2008. ISSN 0094-8276.

L.O. Mearns, M. Hulme, T.R. Carter, R. Leemans, M. Lal, P. Whetton, L. Hay, R. N. Jones, R. Katz, T. Kittel, J. Smith, and R. Wilby. *Climate Change 2001: The Scientific Basis. Contribution of Working Group I to the Third Assessment Report of the Intergovernmental Panel of Climate Change*. Cambridge University Press, 2001.

G. A. Meehl, T. F. Stocker, W. D. Collins, P. Friedlingstein, A. T. Gaye, J. M. Gregory, A. Kitoh, R. Knutti, J. M. Murphy, A. Noda, S. C. B. Raper, I. G. Watterson, A. J. Weaver, and Z.-C. Zhao. *Climate Change 2007: The Physical Science Basis. Contribution*

of Working Group I to the Fourth Assessment Report of the Intergovernmental Panel on Climate Change, chapter Global Climate Projections. Cambridge University Press, Cambridge, United Kingdom and New York, NY, USA, 2007.

M. Meinshausen, N. Meinshausen, W. Hare, S.C.B. Raper, K. Frieler, R. Knutti, D.J. Frame, and M.R. Allen. Greenhouse-gas emission targets for limiting global warming to 2 C. *Nature*, 458(7242):1158–1162, 2009. ISSN 0028-0836.

M. Meinshausen, SCB Raper, and TML Wigley. Emulating coupled atmosphere-ocean and carbon cycle models with a simpler model, MAGICC6–Part 1: Model description and calibration. *Atmos. Chem. Phys.*, 11:1417–1456, 2011.

J.F.B. Mitchell, TC Johns, M. Eagles, WJ Ingram, and RA Davis. Towards the construction of climate change scenarios. *Climatic Change*, 41(3):547–581, 1999. ISSN 0165-0009.

T.D. Mitchell. Pattern scaling: an examination of the accuracy of the technique for describing future climates. *Climatic Change*, 60(3):217–242, 2003. ISSN 0165-0009.

J.C. Pinheiro and D.M. Bates. *Mixed-effects models in S and S-PLUS*. Springer Verlag, 2000.

V. Ramanathan, P. J. Crutzen, J. T. Kiehl, and D. Rosenfeld. Aerosols, climate, and the hydrological cycle. *Science*, 294(5549):2119, 2001.

B. D. Santer, T. M. L. Wigley, M. E. Schlesinger, and J. F. B. Mitchell. Developing climate scenarios from equilibrium g.c.m. results. Technical Report Rep. 47, Max Planck institut für Meteorologie, Hamburg, 1990.

S. Solomon, G.K. Plattner, R. Knutti, and P. Friedlingstein. Irreversible climate change due to carbon dioxide emissions. *Proceedings of the National Academy of Sciences*, 106(6):1704, 2009.

DA Stainforth, T. Aina, C. Christensen, M. Collins, N. Faull, DJ Frame, JA Kettleborough, S. Knight, A. Martin, JM Murphy, et al. Uncertainty in predictions of the climate response to rising levels of greenhouse gases. *Nature*, 433(7024):403–406, 2005. ISSN 0028-0836.

K. E. Taylor, R. J. Stouffer, and G. A. Meehl. A summary of the cmip5 experiment design, 2011. URL http://cmip-pcmdi.llnl.gov/cmip5/docs/Taylor_CMIP5_design.pdf.

S. Twomey. The influence of pollution on the shortwave albedo of clouds. *Journal of the atmospheric sciences*, 34(7):1149–1152, 1977. ISSN 1520-0469.

M. Van den Broeke, J. Bamber, J. Ettema, E. Rignot, E. Schrama, W.J. Van de Berg,

E. Van Meijgaard, I. Velicogna, and B. Wouters. Partitioning recent Greenland mass loss. *Science*, 326(5955):984, 2009.

D.P. van Vuuren, J. Edmonds, M. Kainuma, K. Riahi, A. Thomson, K. Hibbard, G. C. Hurtt, T. Kram, V. Krey, J.-F. Lamarque, T. Matsui, M. Meinshausen, N. Nakicenovic, S. J. Smith, and S. K. Rose. The representative concentration pathways: An overview. *Climatic Change*, submitted.

I.G. Watterson. Calculation of probability density functions for temperature and precipitation change under global warming. *Journal of Geophysical Research*, 113(D12):D12106, 2008. ISSN 0148-0227.

T. M. L. Wigley and S. C. B. Raper. Interpretation of high projections for global-mean warming. *Science*, 293:451–454, 2001.

P. Wu, R. Wood, J. Ridley, and J. Lowe. Temporary acceleration of the hydrological cycle in response to a CO2 rampdown. *Geophysical Research Letters*, 37(12):L12705, 2010. ISSN 0094-8276.
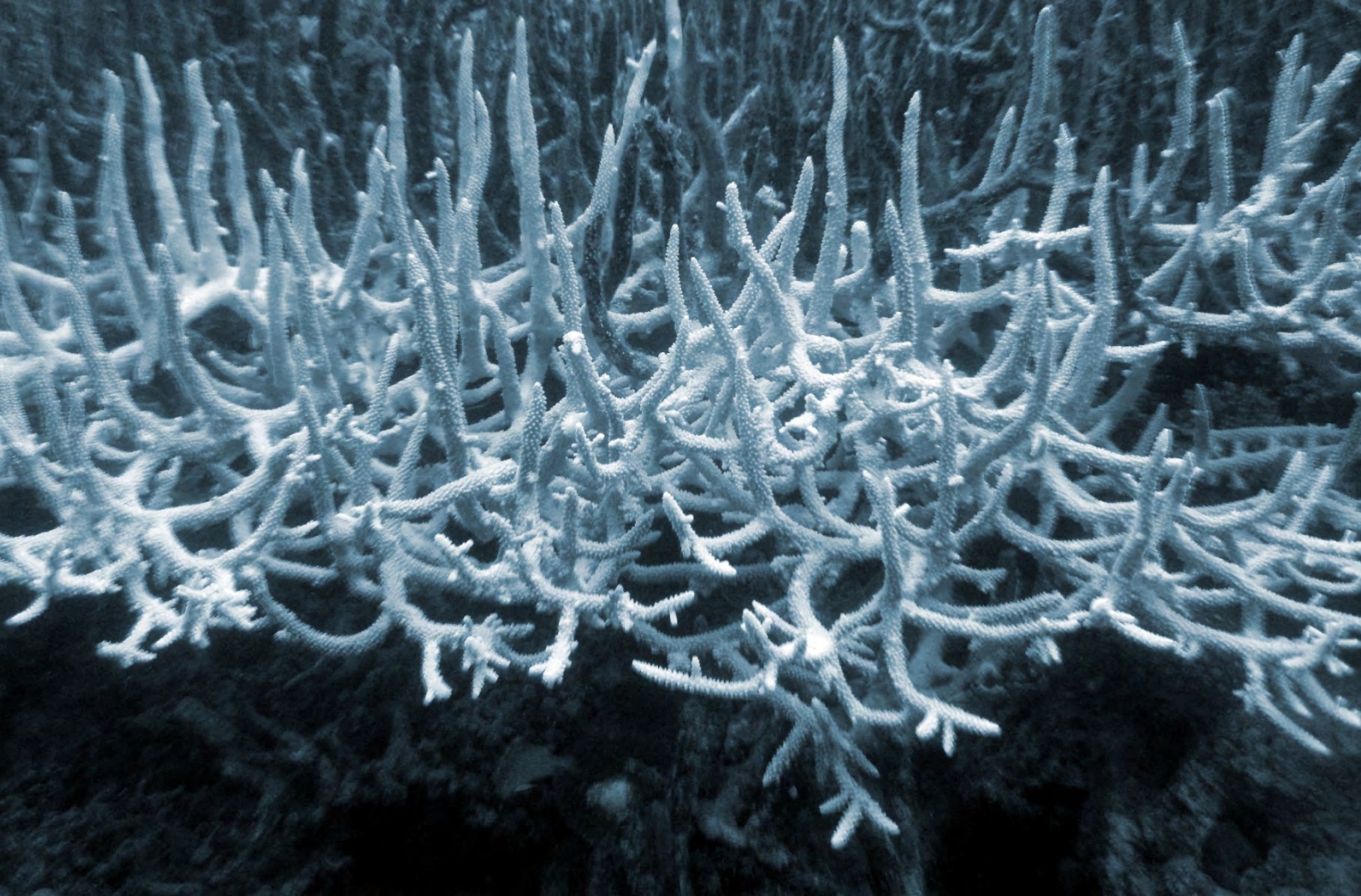
Chapter 4 Coral Reefs

Majority of Coral Reefs at Risk already below 1.5°C of Global Warming.

K. Frieler[1], M. Meinshausen*[1], A Golly[1], M. Mengel[1], K. van der Merwe[1], S. Donner[2], O. Hoegh-Guldberg[3]

[1] Earth System Analysis, Potsdam Institute for Climate Impact Research, Germany
[2] Department of Geography, University of British Columbia, Canada
[3] Global Change Institute, University of Queensland, Australia

This part of our UFOPLAN work was in preparation to be submitted to an international scientific journal, when this report was finalized.

Abstract

Coral reefs face an uncertain future due to ocean warming, with thermal adaptation and ocean acidification compounding the coral's heterogeneous response. While previous studies were confined to few General Circulation Models and single SRES scenarios we provide probabilistic projections of long-term coral reef degradation in terms of global mean temperature change. We show that preserving >10% of coral reefs worldwide would require limiting warming to below 1.5°C (AOGCM range: 1.3-1.8°C) relative to pre-industrial levels – under constant thermal tolerance. With aragonite saturation dependent thermal bleaching thresholds and without thermal adaptation, we project 86% (67-96%, 68% uncertainty range) of coral reefs to experience serious degradation by 2030 under the most optimistic of the new IPCC emissions scenarios, RCP3PD.

Analysis

Coral reef ecosystems provide habitat for over a million species. They are important to the socio-economic well-being of approximately 500 million people (*1*). Currently reef-building corals only persist within the narrow environmental conditions typical of the shallow, sunlit and alkaline waters of tropical coastal areas. The carbonate coral reef ecosystems that they build are only found in regions where temperatures exceed 18°C in winter and aragonite saturation states are greater than 3.3 Ω_{ara} (*2, 3*). The area occupied by coral dominated reefs has contracted steadily over the past several decades (*4*), with local stressors such as overfishing, pollution, disease, and declining coastal water quality being seen as major drivers of reef deterioration. In addition, coral reefs are sensitive to elevated sea temperatures (*5*) which can result in coral bleaching, a breakdown of the fundamental symbiosis between corals and the dinoflagellate symbionts residing in coral tissue.

Mass coral bleaching events were observed since the early 1980s and have affected reefs at scales that have often involved entire reef systems and regions (see e.g. (*6*) or (*7*)). Over 1997-98, mass coral bleaching affected coral reefs in almost every part of the world, with an estimated 16% of reef building corals dying following the exceptionally warm conditions of that year (*1*). While corals are able to re-establish themselves after mass bleaching events, in many cases it takes one to two decades for the ecosystem to return to the pre-bleaching state (*8*). An increase in the frequency and severity of mass coral bleaching could overwhelm the ability of coral reefs to recover between events. If this happens, coral-dominated reef ecosystems shift towards reef systems dominated by non-coral

organisms such as macro-algae. The corresponding reefs are lower in biodiversity, and provide less ecosystem services (*9*) than coral-dominated ecosystems (*10*).

Here, Degree Heating Months (DHM) are used as an indicator of thermal stress and associated bleaching events (*11*). In comparison to the Degree Heating Weeks (DHW) used for real time prediction of coral bleaching events (*12, 13*) the indicator it is based on projected monthly ocean surface temperatures. It sums the excess warming above the mean of maximal monthly temperatures (MMMmax) of the climatological 1980-1999 base period in a rolling 4-month window (*14*) (see SOM, section 2). To quantify the global extent of bleaching events we use a 0.5° x 0.5° map indicating 2160 geospatial locations of coral reefs worldwide from Reefbase (see www.reefbase.org) as adapted by Donner (*14*). DHM at each of these grid points were calculated after employing a simple linear downscaling of SST data to obtain temperature projections at the coral reef cells' locations. The downscaling/interpolation is based on the four closest AOGCM grid points to every coral reef cell, taking into account the AOGCM specific land-sea masks and resolutions (see SOM, section 1). The difference to an approach that merges satellite and AOGCM data at individual locations was found to be minor for the SRES scenarios (see SOM FigS 5).

A DHM total of 1°C*month was used as the best indicator for the lower bleaching threshold (DHW > 4°C*week) while a DHM value > 2°C*month was associated with an upper, or severe, bleaching threshold (DHW > 8°C*week) (*15*). These thresholds were derived from observed bleaching events on the reef level. They do not distinguish between species which might show distinct thresholds (*16*).

Based on this indicator we provide a comprehensive global bleaching analysis joining three major advances only partly considered in previous studies. Firstly, we calculate the fraction of coral reef cells at risk of high thermal stress in terms of global mean surface air temperature rather than the time period in a given emissions scenario. Thereby we take advantage of the close quasi scenario independent relationship between mean regional and global warming levels diagnosed from AOGCMs (*17, 18*). That also allows to derive an essentially scenario independent description of coral reef response to global warming levels. Secondly, to capture the uncertainty in projected regional sea surface temperatures (SST) we diagnose more than 32,000 model years from up to 7 scenarios (20th century, 3 SRES, the COMMIT and 2 idealized CO_2-only scenarios) and up to 5 ensemble members per scenario by 19 AOGCMs that provided output to the comprehensive multi-model CMIP3 archive (see SOM, section 1). This allows a more robust representation of uncertainty. Thirdly, we employ time-variable thermal thresholds to illustrate the effects of thermal adaptation and/or ocean acidification. On the reef level thermal adaptation may in particular include a shift to species with a higher thermal tolerance.

So far, bleaching indicators at different levels of global warming were also considered by (*19*) for the Caribbean region and two individual AOGCMs. The regional study by (*20*) also followed a multi-model approach but does not provide the linkage to global mean temperature changes. While the effect of thermal adaptation on projected bleaching frequencies was included in other analyses (*14, 20*) the possible effect of lower bleaching threshold due to ocean acidification was not considered yet.

Reef recovery from mass coral bleaching and mortality events varies widely but is usually very limited within the first five years (*8, 21*). Therefore, we assume that a recurrence frequency of 20%/yr is the maximum tolerable frequency (17) of recurrent severe thermal stress events. If that frequency surpasses 20%, lasting damages can be assumed to occur, henceforth referred to as "long-term degradation". AOGCM specific fraction of years with DHM values > 2°C*month within different global mean temperature bins were calculated over all available scenario runs (see SOM, section 2) and for each individual coral reef grid cell. Alternatively, "long-term degradation" might be assumed as soon as the temporal distance between two "DHM > 2 °C * month" events for a single reef cell is less than 5 years. Both approaches provide similar results as shown in Fig S3 (see SOM).

Figure 1 shows the frequency of exceeding DHM = 2°C*month at individual grid cells and in three different global mean temperature bins averaged over all AOGCMs. Across the individual coral reef cells there is some latitudinal variation of frequencies, with higher frequencies at lower latitudes. This might explain some of the heterogeneity of coral losses found by (*16*). However, at 1.5 °C global warming the average projected bleaching frequency is higher than 0.2%/year at all reef cells.
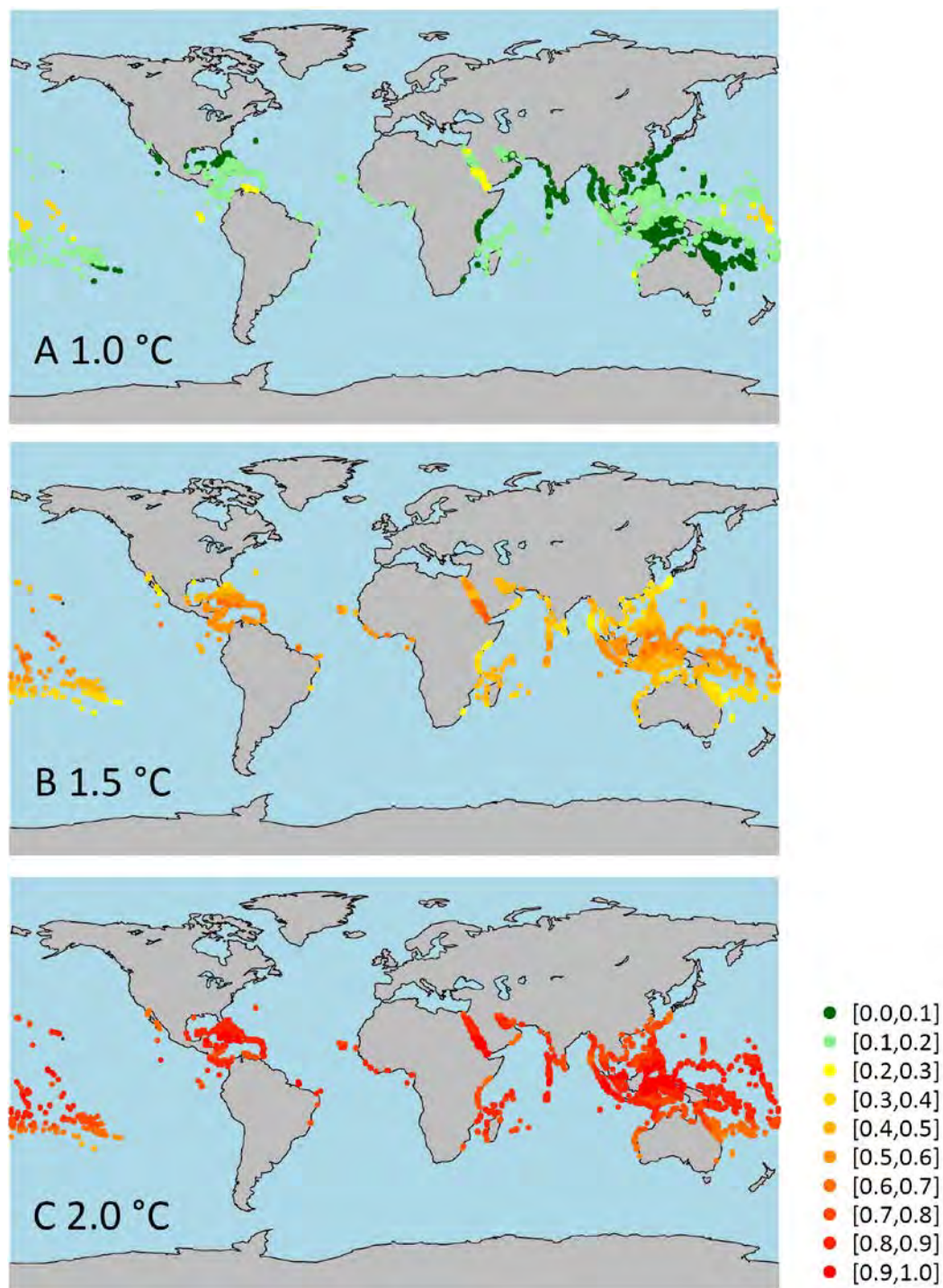
Fig 1 – Frequency of DHM>2°C*month events at different levels of global mean warming (A: 1.0 °C, B: 1.5 °C and C: 2.0°C). Color coding indicates the average of the 19 AOGCM specific frequencies calculated at each coral reef grid point. Green points mean frequencies below 0.2 and yellow to red points mean frequencies above that critical limit for long term degradation.

Figure2A shows AOGCM specific fractions of reef cells where frequent thermal stress might lead to long term degradation. It illustrates the increase of degradation in terms of global mean temperature change. The thick grey line represents the AOGCM average over the individual fractions. This ex-post average can be opposed to an ex-ante average where all AOGCMs simulations are treated as if they were ensemble members of a single AOGCM and the fraction of "affected reef cells" is based on that ensemble. Arguments for the ex-post averaging are given in SOM, section 5. Figure2B shows the AOGCM-mean fraction in terms of global mean temperature change and varying bleaching thresholds.

To put these numbers into perspective and to explore possible effects of thermal adaptation and ocean acidification on bleaching thresholds we project global-mean warming levels and CO2 concentrations probabilistically for the harmonized emissions of the Representative Concentration Pathways, RCPs, newly developed in the context of the IPCC-AR5 (see SOM, section 8). A Markov Chain Monte Carlo method was used to constrain parameters of our reduced complexity climate model with historical observations (22), and we emulate 9 carbon cycle models part of the C4MIP intercomparison (22, 23). Samples of the 2050 projections for the strong mitigation RCP-3PD scenario were displayed in the global mean temperature – bleaching threshold plane.

In the first case, we assume that the thermal tolerance of corals, in particular the 2°C*month DHM-threshold, is a good indicator for recently observed severe bleaching events and will continue to reflect the aggregate impact of heat extremes on corals in the future (white diamonds).

In the second case (white plus-symbols) we explore the extent to which thermal adaptation would have to occur to balance the challenges presented by warming oceans. Therefore, we also investigate a 'thermal adaptation' scenario, where the threshold for severe bleaching events would is assumed to increase linearly from 6°C*month to DHM levels of 6°C*month or more in 2100. This level of thermal stress is extremely rare over the past several decades; it exceeds the maximum reached during the 2005 Caribbean bleaching event (25) and is likely only ever reached in the Central Equatorial Pacific during warm ENSO events.

In the third case (white circles) we assume that in combination with the projected warming, ocean acidification may accelerate the degradation of coral reefs during the 21st century. Both experimental (24-26) and field observations (27-29) indicate that some but not all corals respond to ocean acidification and reduced aragonite saturation through reduced calcification rates. However, ocean acidification may also increase the sensitivity of reef building corals to thermal stress (30). To explore this possible effect in an 'aragonite-dependent' sensitivity experiment, we adapt the thermal threshold

based on the respective atmospheric CO_2-concentration in that year in order to account for ocean acidification (SOM, section 3). Only once the average tropical (30°S to 30°N) aragonite concentrations drop below the saturation level (Ω_{ara} <1), which is the moment when exposed coral skeletons start to dissolve in seawater, we assume a zero thermal threshold (Fig. S2). This translation is enabled by the fact that tropical surface aragonite saturation levels are, on a timescale of years to decades, in equilibrium with atmospheric CO_2-concentrations. Thus, we were able to closely emulate zonal ocean chemistry simulations (*31*) using a linear rational function (Fig. S1). In our Monte Carlo approach, we draw doublets from the joint distribution of global-mean temperature and CO_2-concentrations of our probabilistic RCP projections, translate the CO_2-concentrations to aragonite levels and apply the simplified aragonite-dependent thermal threshold. However, already at some point above the aragonite saturation level of 1, coral reef structures will not be able to counterbalance biological and physical erosion, which is necessary for carbonate accretion and the long-term existence of the coral reef. Thus, our aragonite-dependent threshold is optimistic.
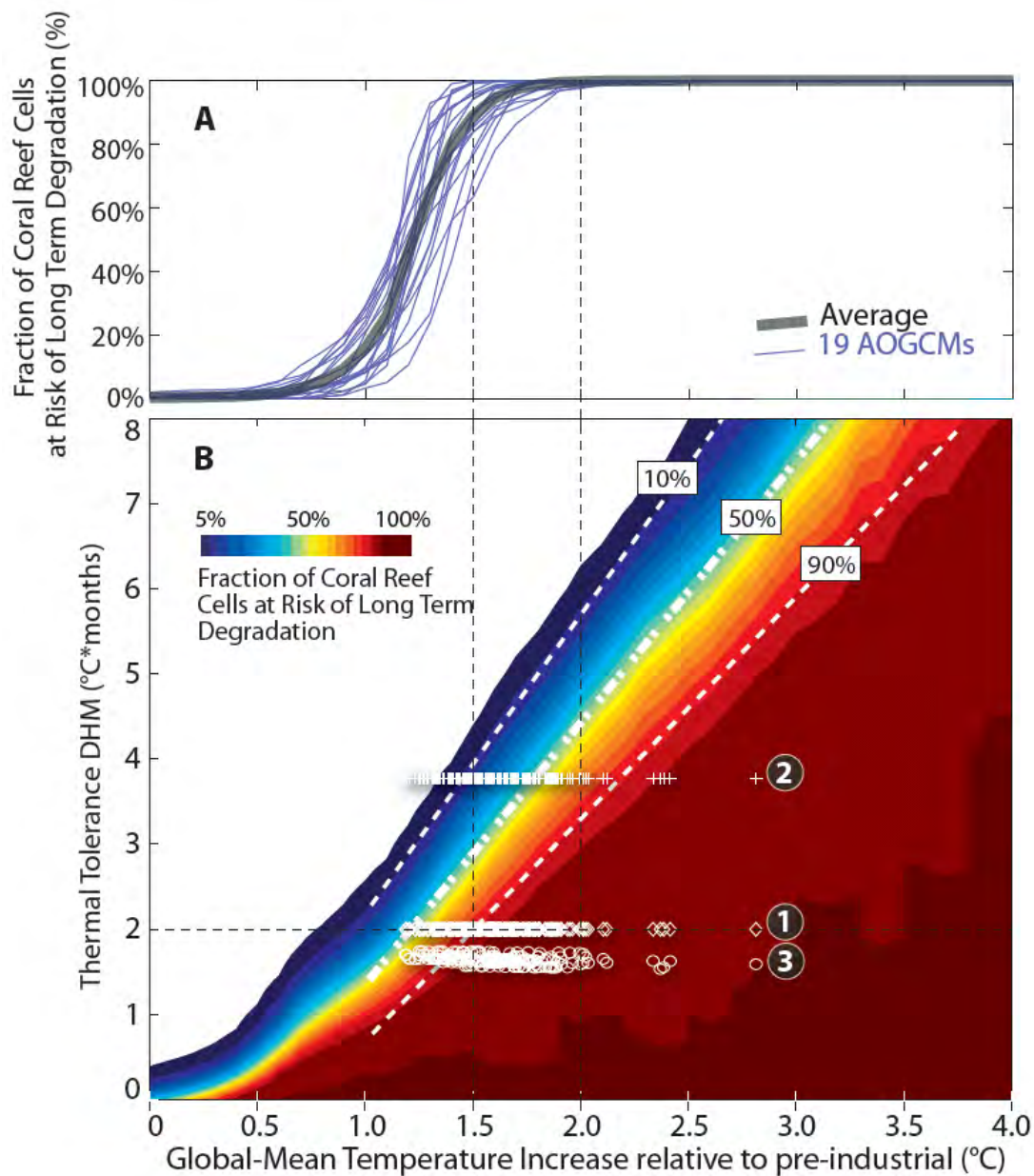
Fig. 1 (**A**) Corals at risk of long-term degradation for constant thermal threshold DHM=2 and individual AOGCMs. The average across 19 AOGCMs (thin blue lines) is shown as thick grey line, corresponding to the cross-section (dashed horizontal line) in panel B. (**B**) Fraction of world's coral reef cells (colored areas) at risk of long-term damage due to frequent (> 1 in 5 years) coral bleaching events, depending on global-mean temperature (x-axis) and assumed thermal threshold (y-axis). A constant DHM=2 thermal threshold is indicated by the horizontal dashed line. 200 random ensemble members for the 2050 climate state conditions under RCP3-PD with constant thermal threshold (white diamonds, black circled 1), thermal adaptation (white plus-symbols, black circled 2), and aragonite-dependent thresholds (white circles, black circled 3) are shown. Vertical dashed lines indicate global-mean temperature levels of 1.0C 1.5°C and <2.0°C, where panels C, D, and F show an estimate of the regional heterogeneity of the degradation. See text.

Figure 2A ahows that assuming no change in thermal tolerance (DHM>2°C*months) at a 2°C global-mean temperature rise, an upper limit agreed to in international climate policy negotiations (*32*), all current coral reef cells are projected to face environmental conditions that mean long-term ecological degradation. This result is remarkably robust across different AOGCMs, with the most optimistic indication being that 98% of coral reefs are subject to long term degradation (Table 1). Even at 1.5°C, an alternative international temperature goal to be reviewed by 2015 (*32*), our results suggest that around 89% (63-100%) of coral reef communities face environmental conditions unfavourable to their continued existence (Fig. 2A). With the current rate of warming (~0.2°C/decade), a 1°C warming above pre-industrial levels is going to be surpassed in the coming one or two decades (*2, 33*), which might already put 16% (3-29%) reef locations at risk.

Table 1. The fraction of reef cells at risk of long-term degradation for global-mean warming relative to pre-industrial levels (top rows). Shown is the average, as well as the full range across diagnosed AOGCMs for three different thermal thresholds, with DHM=2 being the default in this study. Corresponding global-mean temperatures are provided for specific levels of reef cell degradation (bottom rows).

Threshold	Global-mean surface temperatures rel. pre-industrial (°C)				
	1.0°C	1.25°C	1.5°C	1.75°C	2.0°C
DHM=1	88% (74-98%)	99% (91-100%)	100% (100-100%)	100% (100-100%)	100% (100-100%)
DHM=2	16% (3-29%)	55% (17-84%)	89% (63-100%)	98% (89-100%)	100% (98-100%)
DHM=3	3% (0-7%)	11% (0-27%)	43% (7-88%)	79% (54-97%)	94% (74-100%)
	Fraction at risk (% of coral reef cells)				
	10%	30%	50%	70%	90%
DHM=1	0.6K (0.4-0.7K)	0.7K (0.6-0.8K)	0.8K (0.7-0.9K)	0.9K (0.8-1.0K)	1.0K (0.9-1.2K)
DHM=2	0.9K (0.7-1.2K)	1.1K (1.0-1.3K)	1.2K (1.1-1.4K)	1.3K (1.2-1.5K)	1.5K (1.3-1.8K)
DHM=3	1.3K (1.1-1.5K)	1.4K (1.3-1.6K)	1.5K (1.4-1.7K)	1.7K (1.4-1.9K)	1.9K (1.5-2.3K)

Figure 2B shows a linear relationship between the required thermal tolerance (DHM), and global-mean temperature (ΔT) for a given fraction of reef cells (x) that is at risk of disappearance, so that $DHM(T,x) = y_0 + m\Delta T$ with the coefficients y_0 and m provided in Table 2 below. These coefficients were derived for our ex-post average results across 19 AOGCMs for global warming levels in excess of 1°C relative to pre-industrial levels. Above 1°C of global warming, a thermal adaptation of 3.5, 3.1 and 2.6 DHM per degree of global warming would be necessary to offset the increased thermal stress, so that no more than 10%, 50% or 90% of coral reef locations face the risk of long-term degradation, respectively (Fig 2B and SOM, Table S2).

Table 1. Regression results for the necessary thermal tolerance of corals (DHM) depending on the global-mean warming (ΔT) relative to pre-industrial levels and the fraction of reef cells that will be at risk of long-term degradation (x).

Fraction of Reef Cells at Risk of Disappearance *x*	Intercept y_0 (DHM)	Increase of thermal tolerance per degree of warming / slope *m* (DHM/°C)
10%	-1.3207	3.5052
50%	-1.7194	3.0711
90%	-1.9216	2.6074

For the lowest emission scenarios currently investigated by the Intergovernmental Panel on Climate Change (IPCC) in preparation for its Fifth Assessment Report (AR5), RCP3-PD, the projected global-mean temperatures by 2050 range approximately around 1.0°C up to 1.5°C relative to the 1980-1999 period, or 1.5°C to 2.0°C relative to pre-industrial. Half of the individual realisations of our historically constrained global-mean temperature projections for RCP3-PD for the year 2050 fall in the area with long-term damage to coral reefs in excess of 95% (SOM, section 7). The projected degradation is widespread despite the fact that RCP3-PD presents the strongest mitigation scenario currently investigated for the IPCC AR5. For higher RCP scenarios, it is only question of the time before the vast majority of the world's coral reefs face long-term degradation. By the end of this century, 100% of reef cells experience thermal stress (DHM>2°C*months) at sufficiently high frequency (>20%/year) – even under the most optimistic AOGCM case (Table S3) – to suggest long-term degradation from frequent coral bleaching events. Considering single SRES scenarios in order to allow for comparison with earlier studies, there is generally broad agreement (5,13,17).– although differences are revealed for individual scenarios, especially the COMMIT scenario (SOM Fig S6). We test whether the inclusion of spatially coarser AOGCMs (coarser than 1.5° longitudinal ocean resolution) might have biased the results of this study (SOM, Table S1). The global-mean temperature that corresponds to 50% of coral reefs being at risk of disappearance given a DHM>2°C*months thermal tolerance, is 1.23°C relative to pre-industrial levels in average across all 19 diagnosed AOGCMs. For the 9 lower or 10 higher resolution models, this average does not change noticeably, i.e. 1.22°C and 1.24°C, respectively, indicating that our choice to include a comprehensive set of 19 CMIP3 AOGCMs, irrespective of their ocean resolution, seems not to bias our results.

Analogously to the year 2050 projections of the RCP-3PD scenario the fraction of coral reef cells that might be subject to long term degradation can be projected for other years and RCP-scenarios (see Figure 3).
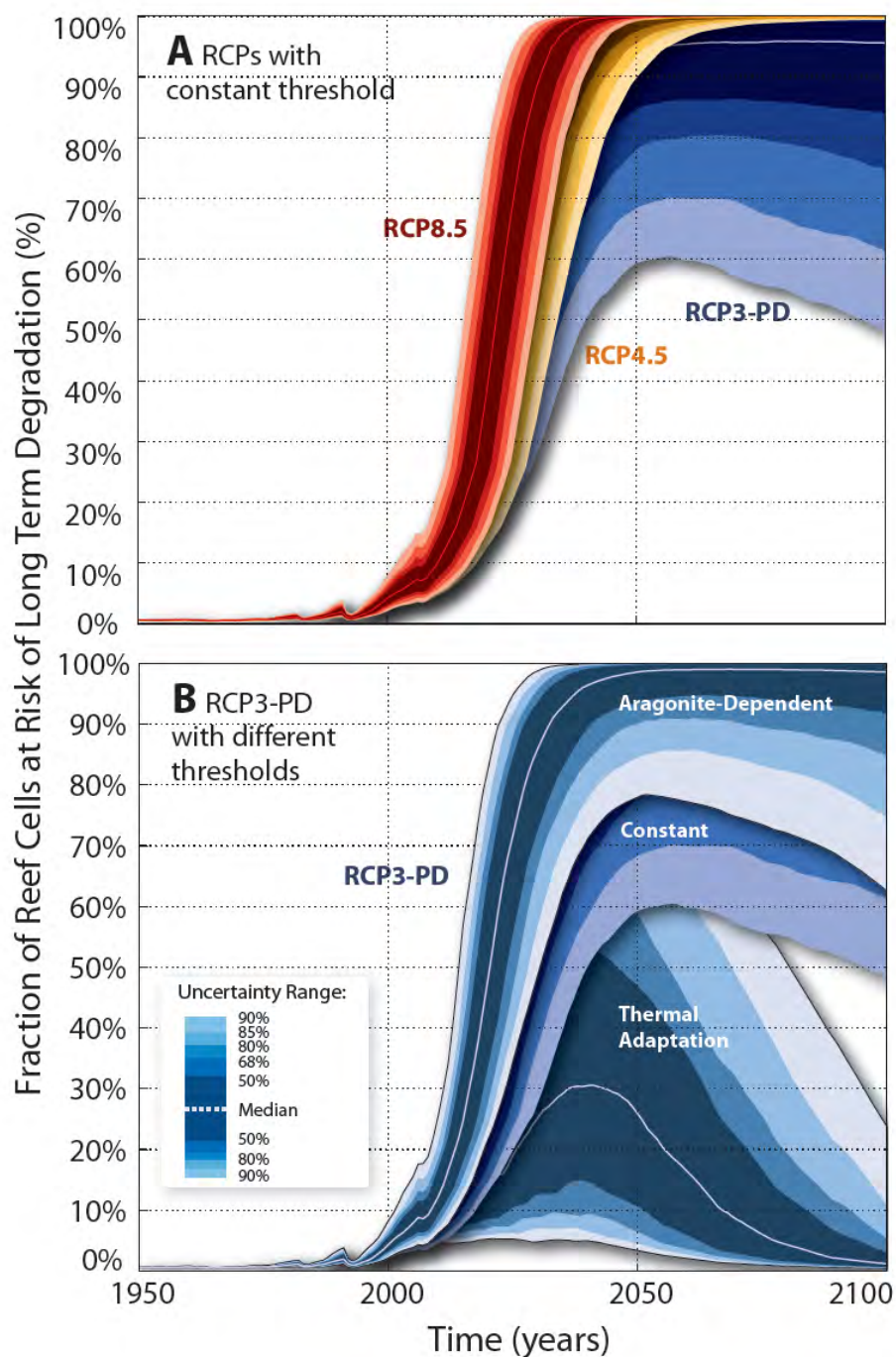
Fig. 2 Projected probabilistic fraction of world's coral reefs subject to long-term degaration under the Representative Concentration Pathways. (**A**) Default projection, assuming a constant thermal threshold DHM=2 and a five year return period as leading to the demise of coral reefs. (**B**) Under the scenario RCP3-PD, thermal adaptation (lower grey shaded areas), and aragonite-dependency (upper saturated blue shaded areas), decreases and increases the projected fraction of coral reef subject to long-term damages compared to the default constant thermal threshold, respectively (cf. Table 1). See expanded Fig S4 in SOM.

The thermal adaptation scenario results suggest that two-third of the world's coral reefs would survive conditions under RCP3-PD (Fig. 3B and SOM, Table S2). Declining temperatures would make 99% (95% to 99%, 68% uncertainty range) of the coral reefs cells suitable for the survival of corals again by the end of the 21st century. This thermal adaptation scenario is likely to be optimistic given the combination of other pressures that are causing the reduced ecological resilience of reef building corals, as well as the current downward trajectory of coral reef extent (e.g. (*4*)). There is little experimental or observational evidence for the rapid evolution of thermal tolerance in reef building corals, which tend to have long generation times (5-100 years) (2), although corals might profit from generation times of the symbionts that are orders of magnitude shorter. Previous paleontological studies highlighting the resilience of corals even under high CO2 concentrations and warming tend to explore conditions at equilibrium, over timescales of thousands of years, not decadal or centennial timescales (*16*). Thermal adaptation capacities are likely to differ strongly. The aggregate thermal tolerance for coral communities may increase as total coral cover and diversity declines, because selective coral morbidity and mortality during bleaching events may lead to survival of only bleaching-resistant or resilient growth forms and species, or of corals in specific thermal refuges.

In both cases of constant or aragonite-dependent thermal thresholds, the period that corals would have to "bridge" in unfavourable environments will be on the timescale of centuries, certainly beyond 2100 (see Fig. 3). New stable ecosystems, dominated by macro-algae, could further hinder any recovery (*10*). We did not investigate the multiple synergistic effects of changing environmental conditions on coral reef systems, like pollution, fishing or other climate-related variables such as cloudiness (*2, 34*). Effective conservation of coral reefs in the face of changing climate and ocean chemistry is likely to depend on our understanding how these other variables affect coral reef resilience. Furthermore, additional in-situ observations and laboratory studies will help refine our understanding about the aggregated likely effects of acidification and warming for individual coral reef ecosystems.

Globally, our results provide further evidence that coral reefs face an important near-term threat even in a very ambitious future emission mitigation scenario and under a global warming level of only 1.5 °C. The vast majority of coral reefs appear susceptible to extensive degradation within the next few decades (cf. *6, 14*). To protect at least 50% of the coral reef cells, global mean temperature change would have to be limited to 1.2°C (1.1-1.4°C) as long we do not assume a strong adaptation to thermal stress. At global warming levels of 2°C, there seems to be little doubt about the fate of coral reef ecosystems. And even with such mitigation efforts, the window of opportunity to save large fractions of coral reefs is small and quickly shrinking.

Acknowledgements

Author contributions

AG, KF and MMein contributed equally to this paper. KF and MMein designed the study. AG, KM, and MMen analyzed data with contributions by KF and MMein. MMein, KF, SD and OH-G wrote the paper.

References

1. C. Wilkinson, "Status of coral reefs of the world:2004" (Global coral reef monitoring network, 2004).
2. O. Hoegh-Guldberg *et al.*, *Science* **318**, 1737 (Dec 14, 2007).
3. J. A. Kleypas *et al.*, *Science* **284**, 118 (Apr 2, 1999).
4. J. F. Bruno, E. R. Selig, *PLoS ONE.* **2**, e711 (2007).
5. O. Hoegh-Guldberg, G. J. Smith, *J Exp Mar Biol Ecol* **129**, 279 (1989).
6. O. Hoegh-Guldberg, *Marine & Freshwater Research* **50**, 839 (1999).
7. C. M. Eakin, J. M. Lough, S. F. Heron, in *Coral Bleaching: Patterns, Processes, Causes and Consequences* M. J. H. van Oppen, J. M. Lough, Eds. (Springer Berlin, 2008) pp. 41 - 68.
8. A. Baker, P. W. Glynn, B. Riegl, *Estuarine Coastal and Shelf Science* **80**, 435 (2008).
9. F. Moberg, C. Folke, *Ecological Economics* **29**, 215 (1999).
10. P. J. Mumby, Hastings, A., Edwards, H. J., *Nature* **450** (2007).
11. O. Hoegh-Guldberg, paper presented at the Ninth International Coral Reef Symposium, October 23-27, 2000, Bali, Indonesia 2000.
12. G. Liu, W. J. Skirving, A. E. Strong, *Eos Transactions* **84**, 137 (2003).
13. G. Liu, A. E. Strong, W. J. Skirving, L. F. Arzayus, paper presented at the 10th International Coral Reef Symposium, June 28-July 2, 2004. , Okinawa, Japan 2006.
14. S. D. Donner, *PLoS ONE* **4** (Jun 3, 2009).
15. S. D. Donner, W. J. Skirving, C. M. Little, M. Oppenheimer, O. Hoegh-Guldberg, *Global Change Biology* **11**, 2251 (Dec, 2005).
16. J. M. Pandolfi, S. R. Connolly, D. J. Marshall, A. L. Cohen, *Science* **333**, 418 (2011).
17. K. Frieler, M. Meinshausen, N. Braun, B. Hare, (in preparation).
18. B. D. Santer, T. M. L. Wigley, M. E. Schlesinger, J. F. B. Mitchell, "Developing Climate Scenarios from Equilibrium GCM Results" *Tech. Report No. 47* (MPI, 1990).
19. M. C. Simpson *et al.*, in *United Nations Development Programme (UNDP), Barbados, West Indies*. (2009).
20. R. K. Hoeke, P. L. Jokiel, R. W. Buddemeier, R. E. Brainard, *PLoS ONE* **6** (2011).
21. O. Hoegh-Guldberg, R. J. Jones, *Marine Ecology Progress Series, 1999 ;0(0):0.* **183**, 73 (1999).
22. M. Meinshausen *et al.*, *Nature* **458**, 1158 (2009).
23. M. Meinshausen, S. C. B. Raper, T. M. L. Wigley, *Atmospheric Chemistry and Physics* **11**, 1417 (2011).
24. J. A. Kleypas, C. Langdon, in *Coral Reefs and Climate Change: Science and Management. AGU Monograph Series, Coastal and Estuarine Studies* J. Phinney, O. Hoegh-Guldberg, J. Kleypas, W. Skirving, A. E. Strong, Eds. (Geophys. Union, Washington DC, 2006), vol. 61, pp. 73-110.
25. C. Langdon, Atkinson, M.J., *J Geophys Res.* **110** (2005).
26. K. a. E. Schneider, J., *Limnology and Oceanography* **51**, 1284 (2006).
27. S. Ohde, van Woesik, R., *Okinawa, Bull. Mar. Sci.* **65**, 559 (1999).
28. J. Silverman, B. Lazar, L. Cao, K. Caldeira, J. Erez, *Geophysical Research Letters* **36** (Mar 13, 2009).
29. J. Silverman, B. Lazar, J. Erez, *Journal of Geophysical Research-Oceans* **112** (May 1, 2007).
30. K. R. N. Anthony, D. I. Kline, G. Diaz-Pulido, S. Dove, O. Hoegh-Guldberg, *Proceedings of the National Academy of Sciences of the United States of America* **105**, 17442 (Nov 11, 2008).

31.   K. Caldeira, M. E. Wickett, *J. Geophys. Res.* **110**, C09S04 (2005).
32.   UNFCCC. (United Nations Framework Convention on Climate Change, Cancun, Mexico, 2010).
33.   G. A. Meehl *et al.*, in *IPCC Fourth Assessment Report* IPCC, Ed. (Cambridge University Press, Cambridge, 2007).
34.   T. P. Hughes *et al.*, *Current Biology* **17**, 360 (Feb 20, 2007).

Supporting Material

Majority of Coral Reefs at Risk already below

1.5°C of Global Warming

K. Frieler[1], M. Meinshausen [1,2], A Golly[1], M. Mengel[1], K. van der Merwe[1], S. Donner[3], O. Hoegh-Guldberg[4]

[1] Earth System Analysis, Potsdam Institute for Climate Impact Research, Germany

[2] School of Earth Sciences, University of Melbourne, Australia

[3] Department of Geography, University of British Columbia, Canada

[4] Global Change Institute, University of Queensland, Australia; *Corresponding author: M. Meinshausen,

malte.meinshausen@pik-potsdam.de

1. AOGCM processing

Where available, we used up to 5 ensemble members for the full-forcing SRES IPCC B1, A2 and A1B, as well as commit scenarios (the latter keeps concentrations constant at year-2000 levels). In addition, we analyze as well the idealized CO_2-only scenarios 1pctto2x and 1pctto4x. This amounts to a total of 30'728 AOGCM model years being analyzed for this study regarding monthly grid-cell level ocean surface temperatures (tos) and annual average global-mean air surface temperatures (tas) (see Table S1). We omitted the analysis of individual coral reef cells for those AOGCMs, in which the land-sea mask revealed less than 4 of the 12 closest AOGCM grid points. Temperature anomalies against pre-industrial levels were calculated as temperature anomalies towards the 1980-1999 base period simulated by the AOGCMs plus the best-estimate observational value between 1850 and 1990 warming, i.e. 0.5°C, according to the HadCRUT3v dataset (*1*).

Table S1 - Diagnosed AOGCMs, their ocean resolution, coverage of reef locations, the respective scenarios, and total number of AOGCM model years used in this study.

AOGCM	Ocean Resolution	Covered reef cells	Analyzed Scenarios	Diagnosed simulation years	SST control run data available?
short ID	*Degree Lat x Degree Lon*	*number*	*scenario list*	*in years*	*yes/no*
cccma_cgcm3_1	(1.9 -2.3)x 1.9	2042	1pctto2x, 1pctto4x, 20c3m, commit, sresa1b, sresa2, sresb1	4239	yes
cnrm_cm3	1 x 2	2048	1pctto2x, 20c3m, commit, sresa1b, sresa2, sresb1	1341	no
gfdl_cm2_0	(0.3 - 1) x 1	2121	1pctto2x, 1pctto4x, 20c3m, commit, sresa1b, sresa2, sresb1	1492	yes
gfdl_cm2_1	(0.3 - 1) x 1	2121	1pctto2x, 1pctto4x, 20c3m, commit, sresa1b, sresa2, sresb1	1731	yes
giss_model_e_h	1 x 1	2037	1pctto2x, 20c3m, sresa1b	1141	yes
giss_model_e_r	(3-4) x 5	2160	1pctto2x, 1pctto4x, 20c3m, commit, sresa1b, sresa2, sresb1	2842	yes
iap_fgoals1_0_g	1 x 1	2149	1pctto2x, 20c3m, commit, sresa1b, sresb1	2349	no
inmcm3_0	2 x 2.5	2158	1pctto2x, 1pctto4x, 20c3m, commit, sresa1b, sresa2, sresb1	1330	yes
ipsl_cm4	1 x 2	2055	1pctto2x, 1pctto4x, 20c3m, commit, sresa1b, sresa2, sresb1	829	yes
miroc3_2_medres	(0.5 - 1.7)x 1.4	2094	1pctto2x, 1pctto4x, 20c3m, commit, sresa1b, sresa2, sresb1	2764	yes
mpi_echam5	1 x 1	2153	1pctto2x, 1pctto4x, 20c3m, sresa1b, sresa2, sresb1	1596	no
ukmo_hadcm3	1.3x1.3	2137	1pctto2x, 20c3m, commit, sresa1b, sresa2, sresb1	889	yes
ukmo_hadgem1	(0.3-1)x1	2105	1pctto2x, 1pctto4x, 20c3m, sresa1b, sresa2	852	yes
cccma_cgcm3_1_t63	(0.9-1.1) x 1.4	2016	20c3m, sresa1b, sresb1	644	yes
csiro_mk3_0	(0.9-1) x 1.9	2150	20c3m, commit, sresa1b, sresa2, sresb1,	1111	yes
giss_aom	3 x 4	2160	20c3m, sresa1b, sresb1,	692	yes
miub_echo_g	(0.5 -2.8)x2.8	2115	20c3m, commit, sresa1b, sresa2, sresb1	2001	yes
mri_cgcm2_3_2a	(0.5-2)x2.5	2160	20c3m, commit, sresa1b, sresa2, sresb1	2131	yes
ncar_ccsm3_0	(0.1-0.5)x1.1	2142	20c3m, commit, sresa2, sresb1	754	yes
Total		**2160**		**30728**	

2. Degree-Heating-Months (DHM) calculation

In contrast to the calculation of DHWs, in which periods of excessive warming are aggregated only if they exceed a 1°C threshold, we integrate excess monthly mean thermal anomalies without a threshold (threshold of 0°C), following Donner (*2*). Thus, monthly SST levels in excess of the site-specific MMMmax level are integrated over a 4 months rolling window. We conservatively used the MMMmax level as mean of the annual monthly maxima in the climatological period rather than the maximum of climatologically monthly means (MMM) (*3*). This results in slightly lower heat stress projections, particular in regions without a strong seasonality (see section 3).

The DHM value is assigned towards the end of the rolling window, and for each year, only the maximal DHM value is retained. We only account the DHM in the first year for areas in which the warmest months extend across the year border, as otherwise abnormally warm summer periods would be counted as two consecutive years with high DHMs. When we relate the DHM values to global-warming levels, we anormalize the global-mean surface air temperatures of AOGCM data with respect to the 1980-1999 average, following the IPCC AR4 practice (*4*). For relating warming to pre-industrial levels, we add 0.5°C, corresponding to the best-estimate observational temperature increase between 1860-1890 and 1980-1999 (*1*). With a rolling window of 0.5°C width on the global-warming axis, we compute the frequency of DHM>2°C*month events, with 100% indicating that DHM>2°C*month events are projected to occur in every year for that particular global warming level and location.

To illustrating our approach, Figure S1 shows temperature projections at a reef cell near Tuvalu (10.75°S, 180°E) under the SRES A1B scenario. Temperature changes provided by 19 AOGCMs are shown as differences to the AOGCM specific mean of monthly maxima (MMMmax) in the 1980-1999 base period. The associated annual DHM values are displayed in Fig. 1B. Panel C shows AOGCM specific fractions of years with DHM values greater than or equal to 2 degree months in comparison to the AOGCM specific number of years falling in the considered temperature bin.
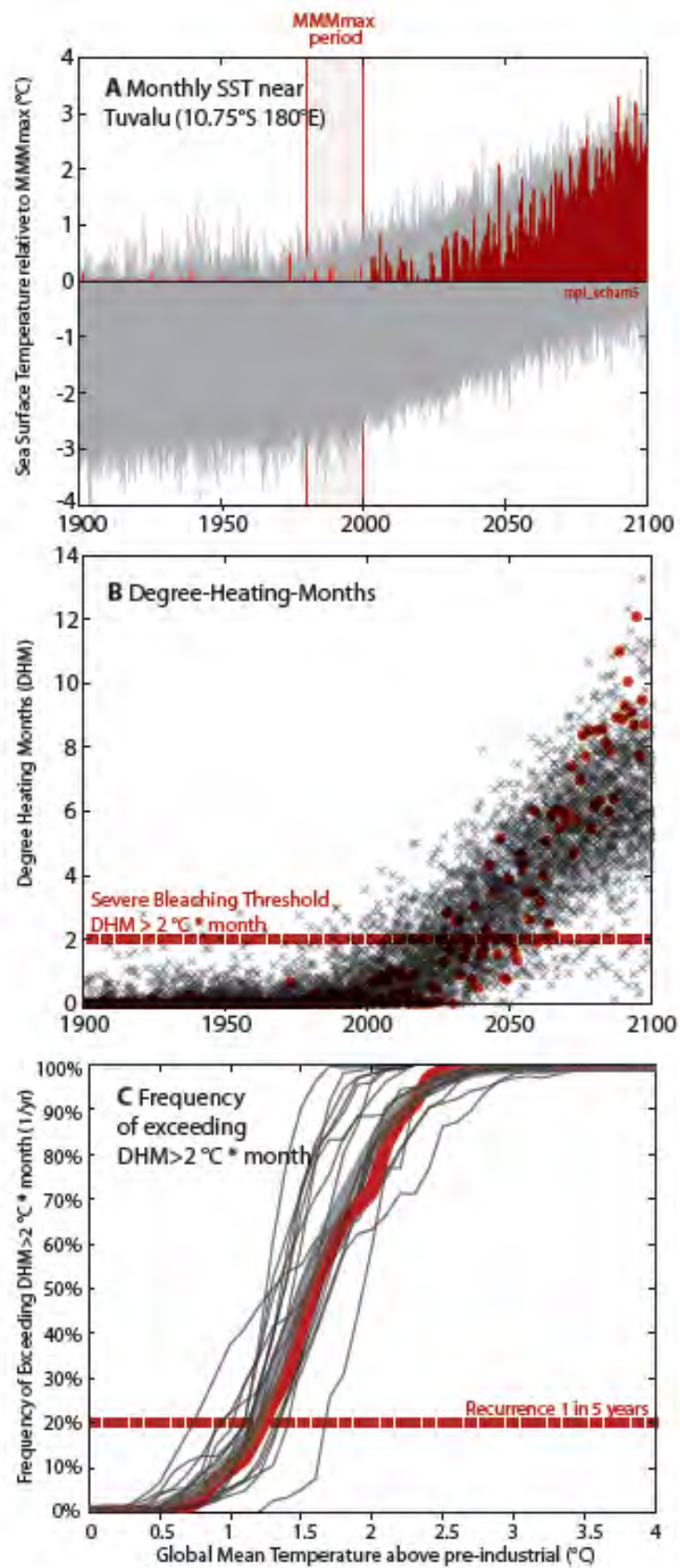
Fig. S1 (previous page) Heat stress projections at the example location of Tuvalu (10.75°S, 180°E), mpi_echam5 data shown in red while other AOGCM data are plotted in grey: (**A**) Downscaled monthly sea surface temperatures of 19 AOGCMs (grey lines) normalized relative to their maximum monthly mean (here, MMMmax) level over the 1980-1999 period, shown for scenario SRES A1B. (**B**) Derived Degree-Heating-Months for the same location. (**C**) The recurrence frequency of exceeding DHM≥2 in Tuvalu relative to the global-mean temperature levels. Shown are diagnostics for 19 individually analyzed AOGCMs and the ex-post AOGCM average (thick grey line).

Donner et al. (*2*) analysed the constraints of using coarse resolution data from coupled Atmosphere-Ocean General Circulation Models (AOGCMs) instead of high resolution satellite or using local in-situ measurements routinely applied for short term predictions of bleaching events. AOGCM data was found to be a suitable proxy for predicting thermal stress that can lead to mass coral bleaching at large spatial scales (e.g. 50 km x 50 km).

3. Maximal monthly means (MMMmax) Calculation

The MMM level is the baseline temperature level, above which the monthly temperature anomalies are counted towards the heat stress index DHM. This MMM level can be derived, inter alia, in two ways: Either as the maximum over the 12 climatological averages of monthly temperatures within the baseperiod (MMM), or as average across all warmest months in that baseperiod (MMMmax, (*3*)). In geographical areas with a strong seasonality, both approaches will yield the same MMM level. In areas without a strong seasonality, the MMMmax approach will yield higher MMM values and hence lower heat stress indicators. We adopt the second approach. Furthermore, we calculate a shifting MMMmax level over time in order to account for any drift in the corresponding control run experiment of the AOGCM. Hence, we calculate the site-specific MMMmax as the sum of a) the mean of maximal monthly temperatures in a 20 year rolling window of the corresponding pre-industrial control run, and b) the difference in the mean of maximal monthly temperatures over the 1980-1999 base period between the control and 20th century run. For 3 of the diagnosed 19 AOGCMs, control run surface ocean temperature data was not available. In these cases, zero drift has been assumed (Table S1). The applied MMM definition would not change the overall conclusions of our study, as evident from the results by Donner (*3, 5*) and shown for our diagnostic in Fig S6.

4. Aragonite-dependent thermal threshold

Rising atmospheric carbon dioxide has impacts on corals in addition to its effect on global temperature. Ocean acidification arises due to the increased flux of carbon dioxide into the world's oceans, where it reacts with water to produce a weak acid (carbonic acid) which lowers the pH of seawater and has other effects such as reducing the carbonate ion concentration. A steady decline in pH has been reported across the world's oceans (*6*). Ocean acidification by reducing aragonite concentrations is expected to reduce the growth of calcifying organisms such as reef-building corals (*7-9*). For relating projected atmospheric CO_2 concentrations to aragonite saturation levels in the tropical oceans, we matched earlier results by Caldeira and Wickett (*10*). Our derivation of the illustrative aragonite-dependent thermal tolerance threshold is indicated in Fig.S **1** below.

At the coral reef locations, current carbonate ion concentration are already substantially lower than at any time during the past 420'000 years (*11*). Current atmospheric CO_2 concentrations are 390ppm (*12*), which is more than 90ppm higher than the maxima of the concentrations over that time (180 – 300ppm) (*13*). Atmospheric CO_2 concentrations, and thereby ocean acidification, will even further increase in the future. Unabated anthropogenic CO_2 emissions from fossil fuel burning and landuse sources could lead to nearly 1000ppm by the end of the century (*14*) – following the RCP8.5 scenario (*15*). Even assuming strong mitigation as in the RCP3-PD scenario (*16*), CO_2 concentrations are projected to increase up to about 450 ppm CO_2 by the mid of the century, falling only slightly to 420 ppm by 2100 and close to 360ppm by 2300 (*14*).
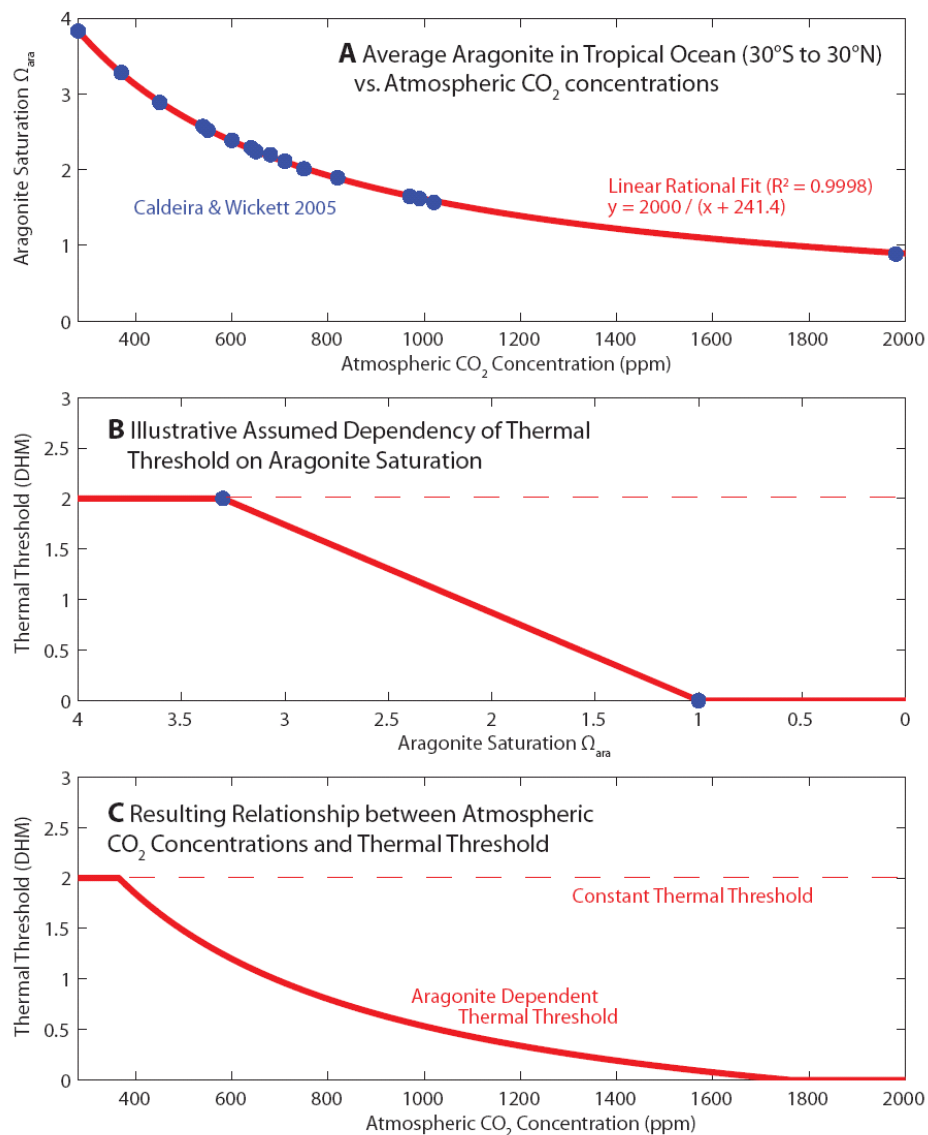
Fig.S2-The aragonite-dependent thermal tolerance. (A) Based on zonal simulations for the tropical ocean by Caldeira and Wickett (17) (their Figures 3 and 6) shown as blue dots, a linear rational fit was derived to relate tropical average aragonite saturation levels from various 2100 and 2300 scenario projections to atmospheric CO2 concentration (red line). (B) Assumed relation between coral's thermal tolerance and tropical average aragonite-levels, linearly decreasing from 3.3Ωara to zero thermal tolerance when aragonite supersaturation ceases (1Ωara). (C) As combination of (A) and (B), the resulting thermal tolerance threshold in relation to atmospheric CO2 concentrations decreases with higher concentrations (thick solid line), unlike the default assumption of a constant thermal threshold (thin dashed line).

5. Ex-post versus ex-ante averages

Diagnosing multi-model ensembles poses the problem of whether averaging (or weighted averaging) across models should be done early in the diagnostic process (e.g. treating all AOGCMs simulations as if they were ensemble members of a single AOGCM). Alternatively, the ultimate diagnostic (e.g. fraction of coral reefs expected to be subject to long term degradation) could first be produced for simulations of each AOGCM individually, with (weighted) averaging being performed at the end. The ex-ante aggregation of all regional warming patterns across different AOGCMs leads to an averaging of patterns, i.e., diminishing AOGCM-to-AOGCM differences across regions. This implies that the points in time (or on the global-mean temperature axis) of threshold crossings for the various coral reef cells become more similar. In other words, at the point when a certain fraction of the coral reefs are projected to face unfavourable conditions is going to be closer together in a multi-model analysis that aggregates ex-ante, rather than ex-post (cf. upper-right panel in FigS2 and Fig2B in main text). Similar to previous analysis regarding area fractions with certain precipitation trends (*18*), our analysis shows that the ex-ante aggregation of individual AOGCMs tends not to appropriately reflect the tails of the distributions found in the individual AOGCMs. Specifically, 5% of the reef cells are categorized in the ex-ante aggregation as too often (>20%) above the thermal threshold (DHM>2) at 0.7°C global-mean temperatures, while for the ex-post average across individual AOGCMs this warming level is lower, i.e., 0.5°C.

The ex-post average across all diagnosed AOGCMs results shown in Fig.2B of the main text is derived for each global-mean temperature bin by averaging all AOGCMs, of which at least 5 model years (with 5x12 monthly data points) were available per bin.
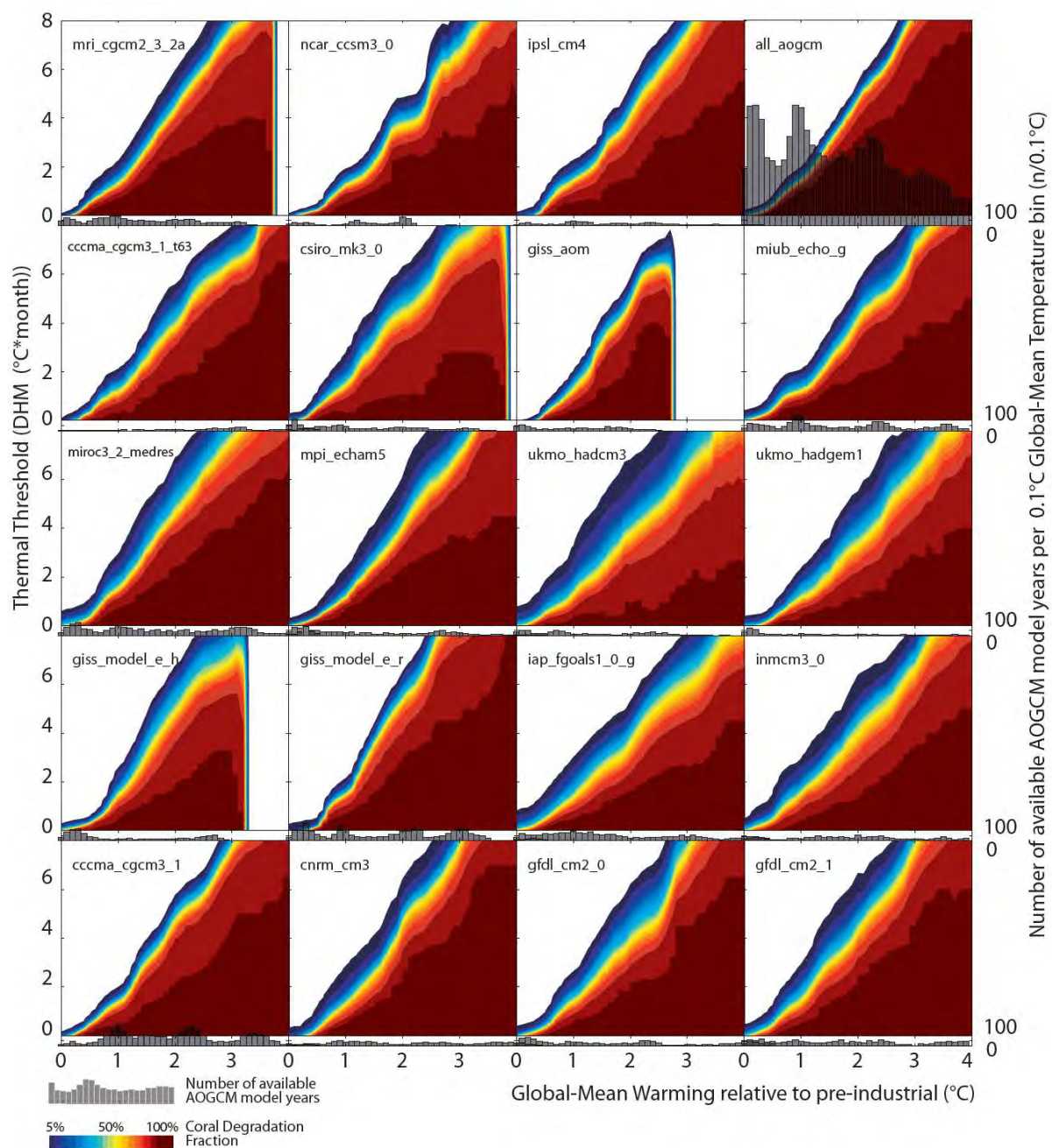
Fig.S 3. Fractions of coral reef cells that are expected to be subject to severe degradation in relation to global-mean temperature levels and the thermal tolerance in Degree Heating Months, derived from 19 AOGCMs. Red areas indicate that a fraction of up to 100%, blue areas of up to 50% of worldwide global reef cells (n = 2160) are at risk of long-term degradation. A threshold for the tolerable recurrence of DHM>2°C*month events is assumed to be 5 years. Grey histograms indicate the number of data points available from each AOGCM for each 0.1°C global-mean temperature interval (total 30'728 years, see Table S1). Aggregating all available AOGCM data points ex-ante, can lead to artificially lowered uncertainty in the coral reef degradation fractions (see top right panel 'all_aogcms'), compared to the average across all diagnosed AOGCMs (see Fig. 2B in main text).

6. Frequency of bleaching events versus recurrence time.

Long-term degradation is assumed to occur when bleaching frequencies are equal to 20%/yr or higher ("frequency based approach "). The choice of this critical threshold is based on the assumption that corals need at least five years to recover from severe bleaching events (*19, 20*). However, this assumption also allows for an alternative way of determining the events of long-term degradation: Coral reef cells might be classified as subject to long-term degradation as soon as two bleaching events occur with less than 5 years recovery time in between ("recurrency based approach"). In the "restoration case" there might be the possibility to recover even after these events as soon as there is no bleaching event within the following five years. In this situation the "old" episode is deleted from the memory and coral reef cells are classified as "healthy" again. In contrast, assuming no restoration means that coral reefs are classified as subject to long-term degradation as soon as the recurrence time of bleaching events is for the first time less than five years. Afterwards the cell does not lose that status any more. We analysed both cases and compared the outcome to our default definition (see Figure S4).
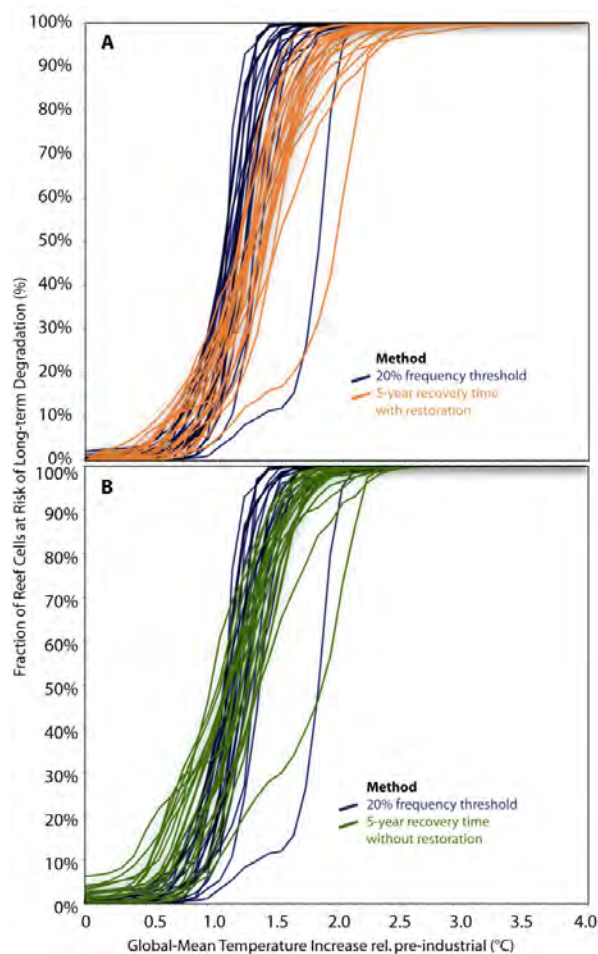
Fig.S 4. Fraction of reef cells at risk of long-term degradation. Blue lines in both panels describe the fraction of "affected" grid cells under the "frequency based" definition of long-term degradation events. Individual lines represent the results of individual AOGCMs. Alternatively, reefs cells are classified as 'long-term degraded' as soon as two bleaching events occur within less than five consecutive years. While the orange lines in panel A represent the results for the case where recovery is assumed to occur as soon as there are 5 years without bleaching, the green lines in panel B are calculated excluding recovery.

7. Ensemble projections of temperature and CO_2 concentrations.

In a probabilistic Monte Carlo approach, we project global mean temperatures based on the set of harmonized GHG and aerosol emissions that had been used to produce the harmonized RCP for use in the CMIP5 AOGCM intercomparison (*21*) – using the same carbon cycle climate model MAGICC6 (*22*).

Our carbon-cycle climate model MAGICC6 closely emulates 9 of the C4MIP (*23*) higher-complexity carbon cycle models. In combination with the historically constrained climate projections, we derive a 600-member ensemble of joint surface air temperature and CO_2 concentrations distributions from 1975 to 2300, equivalent to the probabilistic setting in ref. (*24*).

We use the historically constrained version of MAGICC, which provides, inter alia, joint distributions of surface air temperatures, and CO_2 concentrations, both of which are necessary to estimate probabilistic impact on corals.
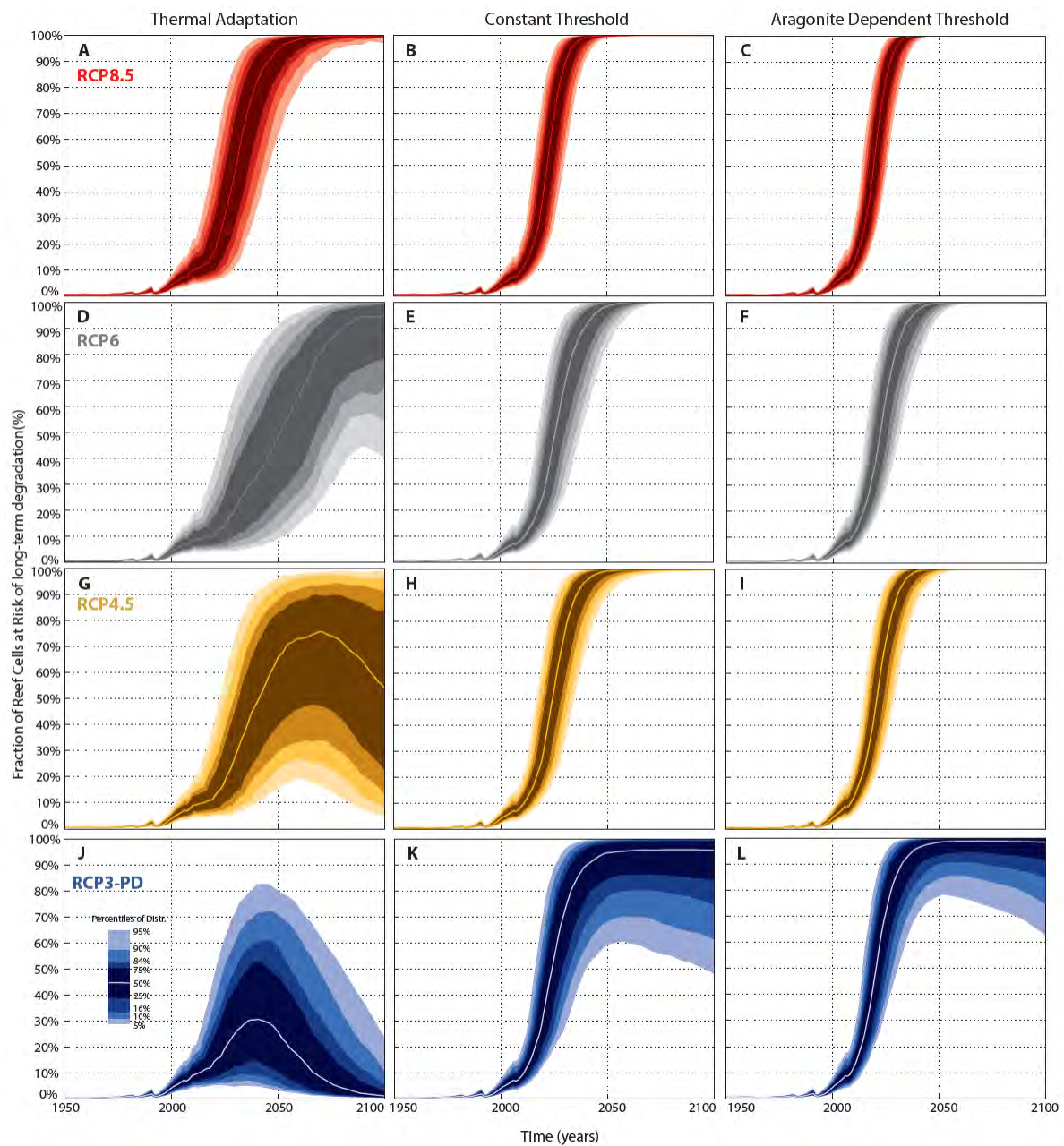
Fig.S 5. Fraction of reef cells at risk of long term degradation under the four Representative Concentration Pathways, RCP8.5 (**A-C**), RCP6 (**D-F**), RCP4.5 (**G-I**), and RCP3-PD (**J-L**) and three sensitivity cases for coral's thermal tolerance: thermal adaption (**A,D,G,J**), constant (**B,E,H,K**) and aragonite-dependent thermal tolerance (**C,F,I,L**). Expanded Figure 3 of main part.

TableS 2. Fractions of coral reef cells at risk of long term degradation under RCP scenarios. The thermal tolerance is either assumed constant (DHM>2 °C * month), linearly increasing over time (DHM>2°C*month in 2010 up to DHM>6°C*month in 2100), or dependent on the Aragonite-saturation level. Values are median percentage fractions of 2160 coral reef cells with 68% uncertainty ranges provided in brackets. In all three thermal threshold cases, the minimally necessary recovery period after a coral bleaching event is assumed to be 5 years in line with earlier studies (*3*).

Scenario	Thermal Tolerance	2020	2030	2040	2050	2100
	Constant	38 (20-60)	88 (68-96)	99 (96-100)	100 (100-100)	100 (100-100)
	Thermal adaptation	17 (8-34)	47 (21-74)	81 (52-94)	94 (80-99)	100 (99-100)
RCP85	Aragonite-dependent	55 (33-76)	96 (86-99)	100 (100-100)	100 (100-100)	100 (100-100)
	Constant	25 (15-47)	68 (42-86)	91 (72-98)	98 (91-100)	100 (100-100)
	Thermal adaptation	10 (6-22)	21 (8-44)	33 (12-62)	49 (19-78)	95 (67-99)
RCP6	Aragonite-dependent	39 (23-63)	83 (61-94)	97 (88-100)	100 (98-100)	100 (100-100)
	Constant	30 (16-51)	75 (50-90)	95 (84-99)	99 (96-100)	100 (100-100)
	Thermal adaptation	12 (7-26)	28 (11-53)	49 (21-78)	66 (30-88)	54 (14-91)
RCP45	Aragonite-dependent	45 (26-67)	88 (71-97)	99 (95-100)	100 (100-100)	100 (100-100)
	Constant	33 (18-55)	72 (46-89)	90 (68-97)	95 (78-99)	96 (75-99)
	Thermal adaptation	14 (7-29)	25 (9-50)	31 (9-60)	26 (7-58)	1 (1-5)
RCP3-PD	Aragonite-dependent	48 (28-70)	86 (67-96)	96 (84-100)	99 (90-100)	99 (85-100)

8. Comparison to Donner, 2009.

The most comprehensive study to date that investigated thermal stress in the 21st century and its potential effect on coral reefs based on AOGCM projections was undertaken by S. Donner (*2, 3*). Donner diagnosed the SRES and the COMMIT scenarios, as modelled by the GFDL CM2.0 and CM2.1 models (see FigS.6) – merged with recent satellite observations. Donner created a composite dataset starting from 1985-2000 satellite sea surface temperatures, extended by the AOGCM modelling data, so that the base period's seasonal and inter-monthly variability matched the satellite observations.

Using 11-year averaging windows, we compare below our diagnostics for the matching subset of 19 AOGCMs, i.e. GFDL CM2.0 and CM2.1, over the same 21st century time-span, using identical thresholds for tolerable thermal stress levels (DHM>2) and recurrence frequencies (1/5 years). We furthermore adapt our methodology to as well calculate maximum monthly means (MMM) to compare our data to a wider set of Donner 2009 results (see FigS 6A), in addition to our default MMMmax approach (cf. section 3 above).

We find generally close agreement between our interim diagnostics and the results of Donner (*3*), except for the commit run, which keeps 21st century concentrations constant (see Fig.S. 6A). Given that both SRES and the commit scenario start from the same 20th century runs (20c3m) and are generally similar up to 2010 or even 2020 (cf. Fig. SPM.5 in (*4*)), one would expect that derived fractions of reef cells were similar over that time-period. The main explanation for the difference is the definition of the year that the frequency of thermal stress events exceeded 20%. We reported the first year that the frequency of events (in the surrounding time window) reaches or exceeds 20%; Donner (*3*) used the year at which the recurrence frequency reaches and remains above 20%.Thus, although the warming is similar in the different scenarios through 2015 or 2020, it levels off after that in the commitment run, and most cells do not reach a sustained 20% frequency until the end of the century.
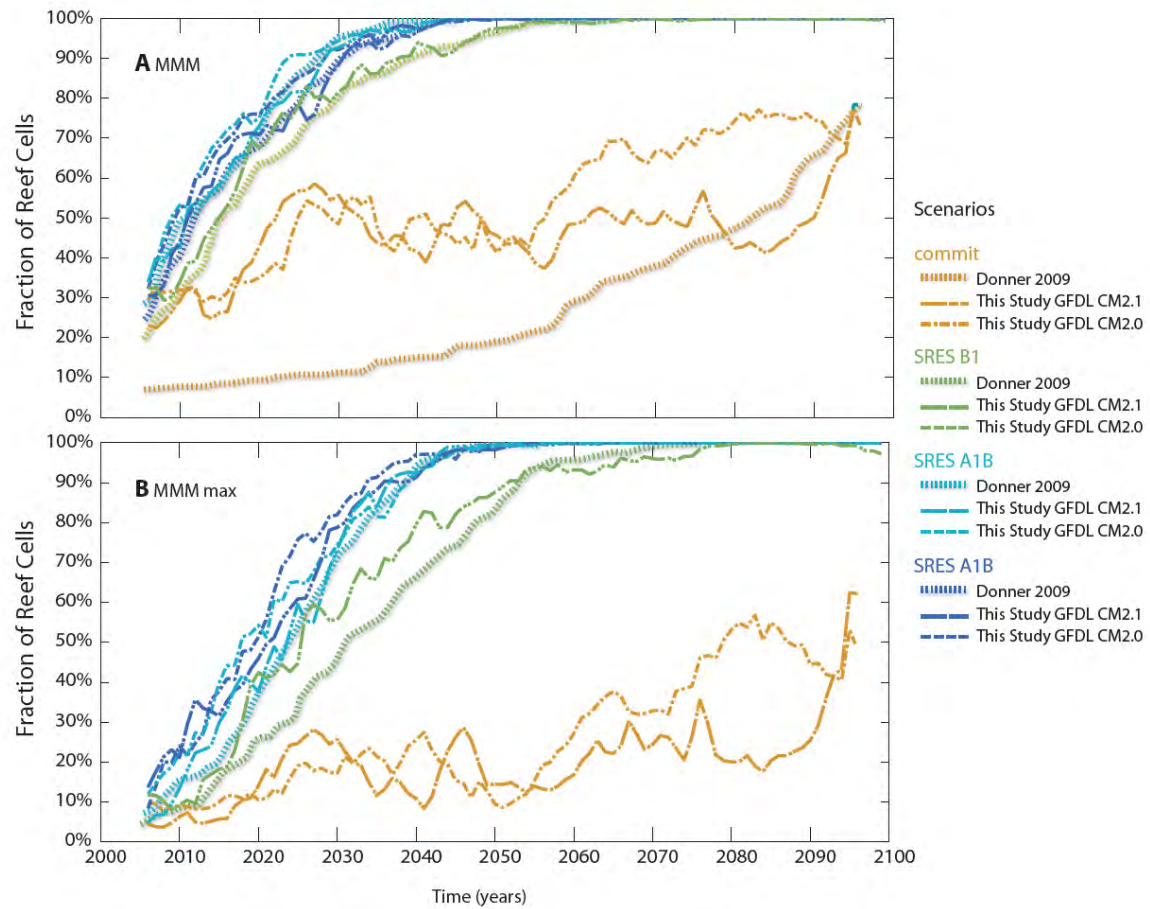
Fig.S 6. Comparison of our results with the findings by Donner (*3*) for the SRES B1, A1B and A1FI scenarios – both assuming a thermal threshold of DHM>2 and a threshold for the recurrence frequency of >20%. (**A**) Results for MMM approach and (**B**) the MMMmax approach used in this study (see text).

References

1.   P. Brohan, J. J. Kennedy, I. Harris, S. F. B. Tett, P. D. Jones, *Journal of Geophysical Research-Atmospheres* 111, D12106 (2006).

2.   S. D. Donner, W. J. Skirving, C. M. Little, M. Oppenheimer, O. Hoegh-Guldberg, *Global Change Biology* 11, 2251 (Dec, 2005).

3.   S. D. Donner, *Plos One* 4 (Jun 3, 2009).

4.   IPCC, IPCC, 2007: Climate Change 2007: The Physical Science Basis. Contribution of Working Group I to the Fourth Assessment Report of the Intergovernmental Panel on Climate Change [Solomon, S., D. Qin, M. Manning, Z. Chen, M. Marquis, K.B. Averyt, M.Tignor and H.L. Miller (eds.)]. Cambridge University Press, Cambridge, United Kingdom and New York, NY, USA. (Cambridge University Press, Cambridge, UK and New York, USA, 2007), pp. 994.

5.   S. D. Donner, T. R. Knutson, M. Oppenheimer, Proceedings of the National Academy of Sciences of the United States of America 104, 5483 (Mar 27, 2007).

6.   G. A. Meehl *et al.*, in *IPCC Fourth Assessment Report* IPCC, Ed. (Cambridge University Press, Cambridge, 2007).

7.   P. L. Jokiel *et al.*, *Coral Reefs* 27, 473 (Sep, 2008).

8.   J. A. Kleypas *et al.*, *Science* 284, 118 (Apr 2, 1999).

9.   J. Silverman, B. Lazar, L. Cao, K. Caldeira, J. Erez, *Geophysical Research Letters* 36 (Mar 13, 2009).

10.   K. Caldeira, M. E. Wickett, *Journal of Geophysical Research-Oceans* 110 (Sep 21, 2005).

11.   O. Hoegh-Guldberg *et al.*, *Science* 318, 1737 (Dec 14, 2007).

12.   P. Tans. (NOAA/ESRL, 2011).

13.   L. Augustin *et al.*, *Nature* 429, 623 (Jun 10, 2004).

14.   M. Meinshausen *et al.*, *Climatic Change* (submitted).

15.   K. Riahi, A. Gruebler, N. Nakicenovic, Technological Forecasting and Social Change (Special Issue: Greenhouse Gases - Integrated Assessment) 74, 887 (2007).

16.   D. van Vuuren *et al.*, *Climatic Change* 81, 119 (2007).

17.   K. Caldeira, M. E. Wickett, *J. Geophys. Res.* 110, C09S04 (2005).

18.   R. Knutti, R. Furrer, C. Tebaldi, J. Cermak, G. A. Meehl, *Journal of Climate* 23, 2739 (May, 2010).

19.   A. Baker, P. W. Glynn, B. Riegl, *Estuarine Coastal and Shelf Science* 80, 435 (2008).

20.	O. Hoegh-Guldberg, R. J. Jones, *Marine Ecology Progress Series, 1999 ;0(0):0.* 183, 73 (1999).

21.	D. P. van Vuuren *et al.*, *Climatic Change*, 1 (2011).

22.	M. Meinshausen, S. Raper, T. Wigley, *Atmos. Chem. Phys.* 11, 1417 (2011).

23.	P. Friedlingstein *et al.*, *Journal of Climate* 19, 3337 (July 2006, 2006).

24.	M. Meinshausen *et al.*, *Nature* 458, 1158 (2009).

Chapter 5 Permafrost

Estimating the permafrost-carbon feedback on global warming

T. Schneider von Deimling[1], M. Meinshausen[1], A. Levermann[1,2], V. Huber[1], K. Frieler[1], D. M. Lawrence[3], V. Brovkin[4,1]

[1] Potsdam Institute for Climate Impact Research, Potsdam, Germany

[2] Potsdam University, Potsdam, Germany

[3] Climate and Global Dynamics Division, National Center for Atmospheric Research, Boulder, Colorado, USA.

[4] Max Planck Institute for Meteorology, Hamburg, Germany

Abstract

Thawing of permafrost and the associated release of carbon constitutes a positive feedback in the climate system, elevating the effect of anthropogenic GHG emissions on global-mean temperatures. Multiple factors have hindered the quantification of this feedback, which was not included in the CMIP3 and C[4]MIP generation of AOGCMs and carbon cycle models. There are considerable uncertainties in the rate and extent of permafrost thaw, the hydrological and vegetation response to permafrost thaw, the decomposition timescales of freshly thawed organic material, the proportion of soil carbon that might be emitted as carbon dioxide via aerobic decomposition or as methane via anaerobic decomposition, and in the magnitude of the high latitude amplification of global warming that will drive permafrost degradation. Additionally, there are extensive and poorly characterized regional heterogeneities in soil properties, carbon content, and hydrology. Here, we couple a new permafrost module to a reduced complexity carbon-cycle climate model, which allows us to perform a large ensemble of simulations. The ensemble is designed to span the uncertainties listed above and thereby the results provide an estimate of the potential strength of the permafrost-carbon feedback. For the high CO_2 concentration scenario (RCP8.5), 12-52 PgC, or an extra 3-11% above projected net CO_2 emissions from land carbon cycle feedbacks, are released by 2100 (68% uncertainty range). This leads to an additional warming of 0.02-0.11°C. Though projected 21st century emissions are relatively modest, ongoing permafrost thaw and slow but steady soil carbon decomposition means that, by 2300, more than half of the potentially vulnerable permafrost carbon stock in the upper 3m of soil layer (600-1000PgC) could be released as CO_2, with an extra 1-3% being released as methane. Our results also suggest that mitigation action in line with the lower scenario RCP3-PD could contain Arctic temperature increase sufficiently that thawing of the permafrost area is limited to 15-30% and the permafrost-carbon induced temperature increase does not exceed 0.01-0.07°C by 2300.

1. Introduction

The climate response to anthropogenic greenhouse gas emissions is markedly influenced by internal earth system feedbacks. Carbon cycle feedbacks (Cramer, Bondeau et al. 2001; Friedlingstein, Cox et al. 2006; Sitch, Huntingford et al. 2008) are among the most prominent examples of such internal feedbacks, where an initial increase in temperature triggers a reaction from land biomass and soils that leads to carbon dioxide emissions, which in turn amplifies the warming. The strength of this carbon cycle – climate feedback (γ_L) is generally measured as cumulative carbon release (or reduced uptake) per degree of warming. This average land carbon sensitivity γ_L is +79PgC/°C across the C^4MIP generation of carbon cycle models (Friedlingstein, Cox et al. 2006) under the high SRES A2 scenario up to 2100. Additional release of carbon from thawed permafrost, referred to as "permafrost-carbon feedback" in the following, would add to this land carbon feedback. At present, the release of additional carbon to the atmosphere as carbon dioxide or methane due to the thawing of permafrost (Lawrence and Slater 2005) and the subsequent decomposition of the soil organic carbon is not typically represented in carbon cycle models. For example, none of the carbon cycle models participating in C^4MIP (Friedlingstein, Cox et al. 2006) included this feedback.

The carbon feedback from high latitude regions and its importance for the future climate is rather unconstrained, with uncertainties existing in the overall availability and quality of carbon stored in frozen soils, permafrost thawing rates, organic matter decomposition rates and, importantly, the relative proportion of anaerobic decomposition (resulting in CO_2 and CH_4 emissions) versus aerobic decomposition (resulting in CO_2 emissions only). However, the permafrost feedback uncertainties are basically "one-sided", i.e., the inclusion of the permafrost-carbon feedback will

most likely increase future climate impacts (or enhance the mitigation challenge). Although some feedbacks that dampen global warming might be triggered, such as vegetation growth induced by permafrost thaw and nutrients release, there is little reason to believe that the net effect of large-scale permafrost thaw would lower future temperature rise (McGuire, Chapin et al. 2006).

The potential magnitude of the permafrost-carbon feedback is substantial given that around thousand Petagram of organic carbon is stored in the upper 3 meters of permafrost soil alone(Schuur, Bockheim et al. 2008). The total carbon pool in permafrost areas is as high as 1672 PgC, if deeper Yedoma and Deltaic carbon deposits are included, 88% of which reside in perennially frozen ground, as estimated by a recent and updated meta-data analysis (Tarnocai, Canadell et al. 2009). These numbers can be put into perspective if one considers that the accumulated anthropogenic fossil fuel CO_2 emissions for the medium-low RCP4.5 scenario is 1000PgC over years 2000 to 2300 (Meinshausen, Smith et al. 2011) (cf. Fig. 3b in Meinshausen, Smith et al. 2011), and that supposed total (historical and future) anthropogenic emissions of 1000PgC would result in a most likely CO_2-induced warming of 2°C (Allen, Frame et al. 2009), and that the current atmospheric CO_2 content (389 ppm CO_2) is ~830 PgC.

The purpose of this study is to provide a first probabilistic estimate of the importance of the permafrost-carbon feedback for the global temperature rise. We investigate this question for the set of all four Representative Concentration Pathways (RCPs) (Moss, Edmonds et al. 2010; van Vuuren, Edmonds et al. 2011). For climatic consequences without permafrost feedback refer to (Schewe, Levermann et al.).

2. Modeling Approach

2.1 General Approach

This section provides an overview of the simulation setup, of our simplified permafrost module, and of the climate model used to run the different emission scenarios. Our study intends to provide a snapshot of the current scientific understanding by combining modeling results from the permafrost soil community with evidence from observational and simulation studies of soil microbial processes. Integrating a permafrost module into a reduced complexity carbon cycle climate model enables us to provide a first probabilistic estimate of the permafrost-carbon effects on global mean temperature projections. We chose this computationally efficient approach to investigate parameter uncertainties in a probabilistic framework over the century long timescales involved, here until 2300. Thus, our approach intends to synthesize and supplement, not to bypass, the highly resolved and process-based permafrost modeling endeavors.

2.2 Climate carbon-cycle model and simulation setup

For investigating the climatic effect of future carbon release from thawing permafrost soils we apply MAGICC6, the latest version of a reduced complexity carbon cycle climate model (see e.g. Wigley and Raper 2002), described in Meinshausen et al.(2009). MAGICC6's carbon cycle can closely emulate 10 high-complexity carbon cycle models that took part in C[4]MIP (Friedlingstein, Cox et al. 2006) with respect to their main carbon pools, fluxes and atmospheric CO_2 concentrations in no-feedback and with-feedback carbon cycle experiments. MAGICC also includes gas-cycle parameterizations for methane, including temperature and OH-dependent lifetimes (Ehhalt, Prather et al. 2001)

Emissions from the thawing of permafrost soils, however, have not been taken into account neither in C[4]MIP models nor in MAGICC6. Adding the carbon dioxide

and methane emissions from the permafrost module (described in the next section) to MAGICC's gas cycles, and feeding back the respective temperatures at each time step to the permafrost and carbon cycle module allows an integrated and internally consistent analysis.

Here, we use a probabilistic version of MAGICC6, which was calibrated to reflect historical observations of surface air temperatures and ocean heat uptake, as described in Meinshausen et al. (2009). We combine 600 equally likely drawings from the 82-dimensional joint probability distribution for this historically constrained climate model with random drawings of 9 sets of carbon cycle model parameters, as well as random drawings from uniform and independent distributions of 21 parameters in our permafrost module (see Table 1). Each of the 9 carbon cycle parameter sets contains 17 individual parameters to emulate one of the C^4MIP models, as described in Meinshausen et al., (2009), leaving out the one C^4MIP model that MAGICC6 is least capable of emulating, IPSL.

Table 1 – Default and sensitivity range parameters of the permafrost module. Sensitivity ranges are sampled from a uniform distribution between the stated minimal and maximal value.

Parameter Permafrost Module	Description	Unit	Default	Sensitivity Range
N	Number of zonal bands		50	50
T_{max}	Regional Arctic temperature anomaly threshold for "northernmost" zonal band	°C	10	[8 12]
T_{min}	Regional Arctic temperature anomaly threshold for "southernmost" zonal band	°C	0	0
β_{ms}	Annual Freezing or Thawing Rate of Mineral Soil Fraction	%/°C/yr	0.01	[0.005 0.015]
β_{peat}	Annual Freezing or Thawing Rate of Peatland Soil Fraction	%/°C/yr	0.005	[0.0025 0.0075]
α	Amplification of global warming over permafrost area rel. to global mean warming	°C/°C	1.6	[1.4 2]
Φ	Amplitude of Annual Temperature Cycle in upper soil	°C	5	[4 6]
$\tau_{ms,aer}$	Default turnovertime of aerobic mineral soil fraction at 10°C	yrs	40	[30 60]
λ_{an}	Q10 Temperature feedback norm factor for anaerobic decomposition rate	°C	309 (Q10 = 2.3)	[256 662] (Q10=[2 6])
λ_{aer}	Q10 Temperature feedback norm factor for aerobic decomposition rate	°C	309 (Q10 = 2.3)	[256 513] (Q10=[2 4])
m_T	Temperature sensitivity of the simplified soilwater parameterisation.	°C^{-1}	0.04	[0.04*0.8 0.04*1.2]
W_{offset}	An offset in the simplified soilwater parameterisation	Mass Fraction	0.2	[0.02*0.9 0.02*1.1]
W_{min}	The minimal soilwater content	Mass Fraction	0.2	[0.02*0.9 0.02*1.1]
$R_{peat/ms}$	Ratio of decomposition rate in peatland vs. mineral soil	Fraction	0.5	[0.3 0.7]
$R_{an/aer}$	Ratio of anaerobic vs. aerobic decomposition rate	Fraction	0.1	[1/40 1/7]
$A_{ms,an}$	Area fraction of mineral soil with anaerobic decomposition	Fraction	0.05	[0.01 0.1]
$A_{peat,an}$	Area fraction of peatand soil with anaerobic decomposition	Fraction	0.8	[0.7 0.9]
C_0	The total initial carbon pool	PgC	800	[600 1000]
R_{ms}	Fraction of total carbon that is in mineral soil	Fraction	0.8	[0.7 0.9]
φ	Distribution of total carbon content towards the "Southern" (1) or "Northern" Areas (-1) or uniformly equal distribution (0).		0	[-0.5 0.5]
χ	Fraction of methane oxidation on its transport to the atmosphere	Fraction	0.15	[0.1 0.2]

We do not prescribe the RCP8.5 GHGs concentrations, but calculate these dynamically using RCP8.5 emissions, so that added permafrost emissions will have an effect on CO_2 and CH_4 concentrations and simulated temperatures. Thus, we start our analysis from the harmonized set of greenhouse gas, aerosol and tropospheric ozone precursor RCP emissions, as they were used for creating the RCP GHG concentrations (and available here: http://www.pik-potsdam.de/~mmalte/rcps/).

In addition to our large ensemble simulations, we perform a single illustrative run with default parameter settings for our permafrost module in order to illustrate the dynamics over century long timescales. For this, we use MAGICC6 settings that are identical to those used for producing the RCP concentration scenarios (Frieler, Meinshausen et al.). Specifically, MAGICC's carbon cycle is calibrated towards the C^4MIP Bern2.5CC carbon cycle model, and the climate response parameters reflect a median projection across the CMIP3 AOGCMs. For the permafrost module, we assume default settings as listed in **Table 1** ("Default").

2.2 Permafrost Module

Here, we provide a conceptual overview of our simplified permafrost module and its main parameter assumptions (see **Table 1**), with the Appendix providing a detailed mathematical description. Our permafrost module compartmentalizes the organic carbon of permafrost regions into bins with a similar warming threshold, above which permafrost will start thawing. In our simplified framework, neglecting topology and local climate as well as soil conditions, we call these bins "zonal bands", given that - generally speaking - the Southernmost permafrost regions of the Northern Hemisphere are likely to start thawing first, and the Northernmost regions last. This spatio-temporal characteristic of permafrost thaw is also seen in process-based modeling studies of permafrost degradation (Zhuang, Melillo et al. 2006).

We assume the frozen carbon content that is potentially vulnerable to decomposition in the upper 3 meters in permafrost soils to be between 600 and

1000 PgC. Our assumption is somewhat lower than recent best-guess estimates of 1024 GtC of top 3m soil carbon content in the permafrost zone (Schuur, Bockheim et al. 2008; Tarnocai, Canadell et al. 2009), as we consider only the fraction of permafrost carbon in perennially frozen ground – which eventually might be released to the atmosphere. A smaller portion of the estimated 1000 Pg carbon pool will always reside in near-surface layers, with expected carbon densities approaching those of non-permafrost soils. By default, we assume this potentially vulnerable permafrost carbon content to be uniformly distributed into 50 zonal bands, while for our uncertainty-based projections (see section 3.2) we vary the carbon content across the latitudinal bands (see Appendix A1). We assume the "Southernmost" band to start thawing at any warming above pre-industrial levels ($T_{min} = 0°C$), and the "Northernmost" band starting to thaw at an Arctic warming above pre-industrial levels of 8-12°C (see Fig. 1). Several studies have suggested that strong degradation of the surface layers of permafrost soils may occur under such pronounced Arctic warming (Saito, Kimoto et al. 2007; Yi, Woo et al. 2007; Lawrence and Slater 2008; Zhang, Chen et al. 2008; Schaefer, Zhang et al.).

Our modeling approach is meant to describe gradual permafrost degradation resulting from progressive active layer thickening, but it does not explicitly account for permafrost degradation by talik formation, erosion or thermokarst development – processes also of importance to the fate of future permafrost.

We assume a range of 1.4 to 2.0 for polar amplification, i.e. the average increase of annual average surface air temperatures in the permafrost region relative to the global-mean increase. We base this on an analysis of CMIP3 AOGCM (Meehl, Covey et al. 2005) projections, that derives a central estimate of ~1.6 with a 2-sigma uncertainty of 0.2 (Frieler, Meinshausen et al.). Our upper end of the assumed uniform distribution considered here is slightly above the maximum value from AOGCMs to account for cases of strong future sea ice retreat, which may only partly be captured by the analyzed CMIP3 AOGCMs (Stroeve, Holland et al. 2007). Such a

strong retreat will increase polar temperature amplification in permafrost regions (Lawrence, Slater et al. 2008; Screen and Simmonds 2010). For the purpose of retrieving this polar amplification factor from the AOGCMs, the diagnosed permafrost region is here assumed as North-Eastern Europe (NEE), North-Asia/Siberia (NAS) and Alaska (ALA) following the region definitions of Giorgi et al. (2005).
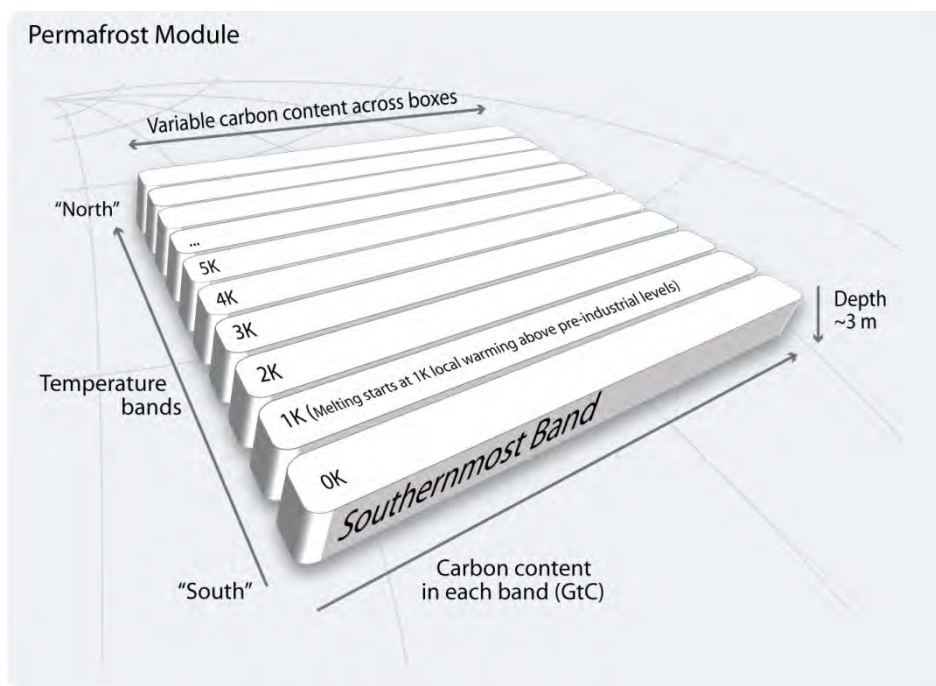
Figure 1 - Schematic overview of the simplified permafrost module with n zonal bands (default n=50) in which thawing starts at different global warming levels. The carbon content of the represented permafrost fractions (approximating upper 3m soil layer) can vary across the different zonal bands of equally spaced temperature intervals (default = 0.2K spacing), with the default being an initially uniform carbon content distribution. Each zonal band is further subdivided into four soil pools with differing thaw and decomposition characteristics: mineral and peatland soils, divided into aerobic and anaerobic fractions.

The two main soil types in permafrost regions – mineral and peatland soils – exhibit rather different properties of relevance to induced emissions (e.g. in terms of thermal soil conductivities or in terms of the ratio of aerobic vs. anaerobic soil conditions). By peatland soils here we understand soils with a high fraction of organic material (peat, litter) which are likely to turn into temporal wetlands when permafrost thaws. We thus subdivide the carbon in each zonal band into four pools: permafrost carbon stored in mineral and in peatland soils, each pool being subdivided into an aerobic and an anaerobic fraction. The largest carbon pool is characterized by physical properties of mineral soils and we assume that these soils contain 70-90% of the total permafrost carbon content (see R_{ms} in **Table 1**), given that an estimated 80% of carbon is stored in the upper 3m frozen mineral soils (Tarnocai, Canadell et al. 2009).

A key uncertainty is the fraction of carbon that might be decomposed under anaerobic conditions – resulting potentially in methane emissions to the atmosphere. Given the high warming potential of methane, the overall magnitude of the permafrost-carbon feedback will depend strongly on this fraction.

Based on Frolking et al. (2001) we assume an anaerobic fraction of 70% to 90% for peatland soils. Mineral soils are dominated by aerobic conditions with only a small fraction of carbon in anaerobic environments (90%-99% aerobic fraction assumed). Although there is large uncertainty, Arctic climate change could increase water-logged areas (and hence the anaerobic part of decomposition) due to increased precipitation and associated soil moisture increases as well as thermokarst lake and wetland formation as ice-rich permafrost soils thaw and subside. On the other hand, increased drainage could lead to the opposite effect, even under increased precipitation. In this study, we hence keep the anaerobic area fractions constant.

In the anaerobic areas, not all decomposed carbon will be emitted as methane. Only half of the decomposed carbon in the anaerobic pool is converted to methane, following the process of methagonesis (Khvorostyanov, Krinner et al. 2008). Furthermore, on its pathway through the soil layers to the atmosphere, a part of this methane is oxidized. Here, we assume oxidization rates of only 10%-20% (see χ in **Table 1**), as the majority of methane could be released via the fast pathways of ebullition and plant-mediated transport, therefore bypassing the oxic layer (Wagner, Liebner et al. 2009). Under these conditions, only a comparatively small fraction of methane is getting oxidized on its slow diffusive transport to the surface. Note however that the oxidization assumptions are subject to substantial uncertainty (Riley, Subin et al.). For example, Walter and Heimann (2000) point to the large uncertainty in plant-mediated transport, assuming a best-estimate of 50% oxidation of methane.

While we do not explicitly account for the timescale of CH_4 transport based on our assumption of the dominance of fast transport processes, we implicitly account for uncertainty in the timescale of CH_4 release to the atmosphere by considering a large spread in assumed anaerobic decomposition times (see below). Furthermore, by assuming that a fixed fraction of methane is oxidized on its way to the atmosphere, we neglect the direct temperature sensitivity of oxidation rates.

The soil thawing (and re-freezing) rates are assumed to be half as fast in peatland soil areas (0.0025 to 0.0075%/°C/yr) compared to those of mineral soils (0.005 to 0.015%/°C/yr) because of high thermal insulation of the peat organic matter and high ice content. As past decomposition has left carbon of low quality in the soils before incorporation into permafrost (Schuur, Bockheim et al. 2008), we assume a relatively slow decomposition time of carbon in both soil types compared to high turnover rates of freshly formed organic detritus. We tune the aerobic decomposition rate of the largest permafrost carbon stock, i.e. carbon in mineral soils, to correspond to a turnover time at 10°C of between 30 and 60 years, which is

comparable to the 33 year turnover timescale for the intermediate pool used in the Lunds-Potsdam-Jena dynamic vegetation model (Sitch et al. (2003)). The decomposition rate for aerobic conditions is much higher than for anaerobic conditions with modeling studies suggesting ratios of 10:1 to 40:1 (Frolking, Roulet et al. 2001). Incubation experiments tend to favor slightly smaller ratios (Scanlon and Moore 2000). Hence we assume a uniform range of 7:1 to 40:1. Both, oxic and anoxic decomposition rates in both soil types are adjusted depending on the soil temperatures. Our sampled parameter range corresponds to Q10 values between 2 and 4 for the aerobic and between 2 and 6 for the anaerobic decomposition, accounting for the large uncertainty in temperature sensitivity of soil carbon mobilization (Davidson and Janssens 2006). The large anaerobic Q10 range expresses the larger uncertainty in temperature sensitivity of anaerobic decomposition (cf. Walter, Edwards et al. 2007).

Additionally, we assume that oxic decomposition rates are dependent on soil moisture and implemented a simple soil moisture parameterization based on the annual cycle of soil temperature. The close link between soil temperature and soil moisture in our model is motivated by the fact that state-of-the-art climate models consistently show an increase in water availability (i.e. an increase in precipitation minus evaporation) in permafrost regions in a warmer climate (see Fig. 3.5 in Meehl 2007).

3. Results

3.1. Illustrative run with default parameter settings

To illustrate the dynamics of our simplified modeling framework, we first show results for a single illustrative experiment for the high RCP8.5 scenario and with default parameters (see Table 1). In our model, permafrost starts degrading at the same level of warming in mineral and peatland soils, though it takes longer for the heat anomaly to penetrate into the peatland soil (Fig. 2a,d). By 2050, only the southern latitudinal bands are subject to degradation, while by 2100 a large fraction of the surface permafrost pool is thawed. Degradation of the northernmost permafrost areas only starts in the second half of the 22nd century.

Given the slow timescale of decomposition, permafrost carbon is released only gradually after thawing the surface soils and continues for centuries. The largest contribution to carbon emission comes from the aerobic decomposition of organic material located in the mineral soil pool (Fig. 2b). The peak emissions resulting from aerobic decomposition of peatland carbon around 2150 is an order of magnitude smaller compared to those from aerobic decomposition from mineral soils (see Fig. 2b,e). This is because of the assumed 20:80 ratio of total peatland to mineral soil carbon, the slower thawing and decomposition rates of peatland soil compared to mineral soils, and the much higher anaerobic soil fraction in peatlands. Carbon release from the anaerobic pool describes the slowest timescale of permafrost dynamics due to the much lower decomposition rates in anaerobic compared to aerobic environments (a factor of ten difference for our default case). Carbon emissions due to aerobic decomposition fall again after peaks in the early 22nd century for the lower zonal bands, indicating depletion of available soil carbon stocks over the multi-centennial timeframe considered here (see Fig. 2b,e).
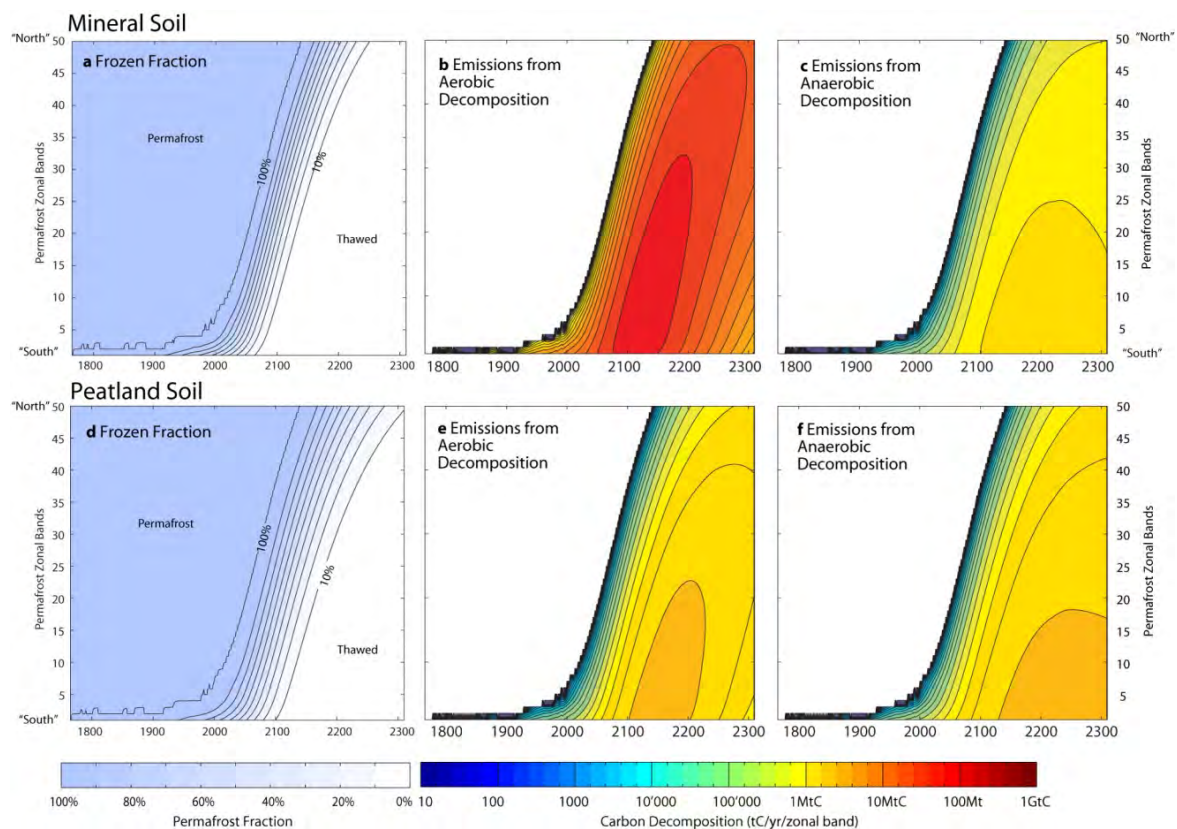
Figure 2 – Fraction of intact permafrost and carbon release in PgC/yr per zonal band from mineral soil (upper row) and peatland soil (lower row) via aerobic (b,e) and anaerobic (c,f) decomposition, respectively, under the RCP8.5 scenario and illustrative default settings (see text and Table 2). Starting in the "Southernmost" zonal band, the thawing of the parameterized 3m thick soil layer progresses northward to colder zonal bands (vertical axis) over time (horizontal axis) (see panel a,d), being followed by carbon releases.

Assuming that northern peatlands are complex, adaptive ecosystem (Belyea and Baird 2006) this carbon pool might prove to be less vulnerable to loss due to self-sustaining vegetation and hydrology feedbacks (Frolking, Talbot et al. 2011). We assume that he majority of this pool is subject to slow anaerobic decomposition, which is tantamount to assuming a larger resilience of peatland carbon to climate change.

3.2. Projections for RCPs including uncertainties

In the following, we go beyond a consideration of our default parameter scenario and discuss model outcomes in the probabilistic framework in which we account for uncertainty in parameters of the carbon-cycle climate model and in the permafrost module (see Table 1).

For the mitigation scenario RCP3-PD that limits global mean temperature changes to below 2°C, cumulative CO_2 emissions from permafrost are 4PgC (68% uncertainty range: 2-7PgC) by 2100 (Table 2). The analysis of RCP8.5, a scenario that implies extensive global warming reaching well above 10°C by 2150 (Fig. 3e), shows a pronounced degradation of near-surface permafrost (about 31-66% thaw, 68% uncertainty range) by 2100 and almost complete thawing by 2200. Modeling studies based on physical permafrost schemes consistently show pronounced permafrost degradation by 2100, but to strongly differing extents (Euskirchen, McGuire et al. 2006; Saito, Kimoto et al. 2007; Yi, Woo et al. 2007; Lawrence and Slater 2008; Zhang, Chen et al. 2008; Eliseev, Arzhanov et al. 2009; Schaefer, Zhang et al.). A direct comparison of permafrost degradation estimates is hindered given differences in forcing scenarios and in the definitions of permafrost degradation which are used in these studies. While our estimates of permafrost degradation fall within the range of these studies, we do not cover the upper estimates of rapid permafrost degradation as reported in (Lawrence, Slater et al. 2008) and (Schaefer, Zhang et al.). Therefore we consider our results as fairly   conservative with respect to the timing and extent of permafrost degradation.

Given that microbial activity strongly increases for temperatures above the freezing point (Monson, Lipson et al. 2006), large portions of soil carbon are subject to enhanced decomposition. Forcing our model with the high-emission scenario RCP8.5, permafrost-induced CO_2 emission rates start increasing after 2050 to about 1PgC yr^{-1} in 2100. This result is comparable to an extrapolated estimate based on net ecosystem carbon exchange measurements of permafrost patches, resulting in an emission estimate of 0.8 – 1.1 PgC yr^{-1} by 2100 (Schuur, Vogel et al. 2009) . The maximum of our projected emissions (median 3PgC yr^{-1}) is reached in the mid 22nd century (see Fig. 3c). The upper end of our 68% uncertainty range suggests CO_2 emission up to 5PgC yr^{-1}. CO_2 emissions resulting from the oxidation of permafrost-released methane and anaerobic CO_2 production in the soils contribute to these large emission rates, but to a much smaller extent than the aerobic CO_2 release (Fig. 3 b,e). Cumulative CO_2 emissions under RCP8.5 are 26PgC (12-52PgC) by 2100. By 2300, the majority of the permafrost carbon stock could be already released to the atmosphere, with cumulative CO_2 emissions being 529 PgC (362-705PgC) (Table 2).
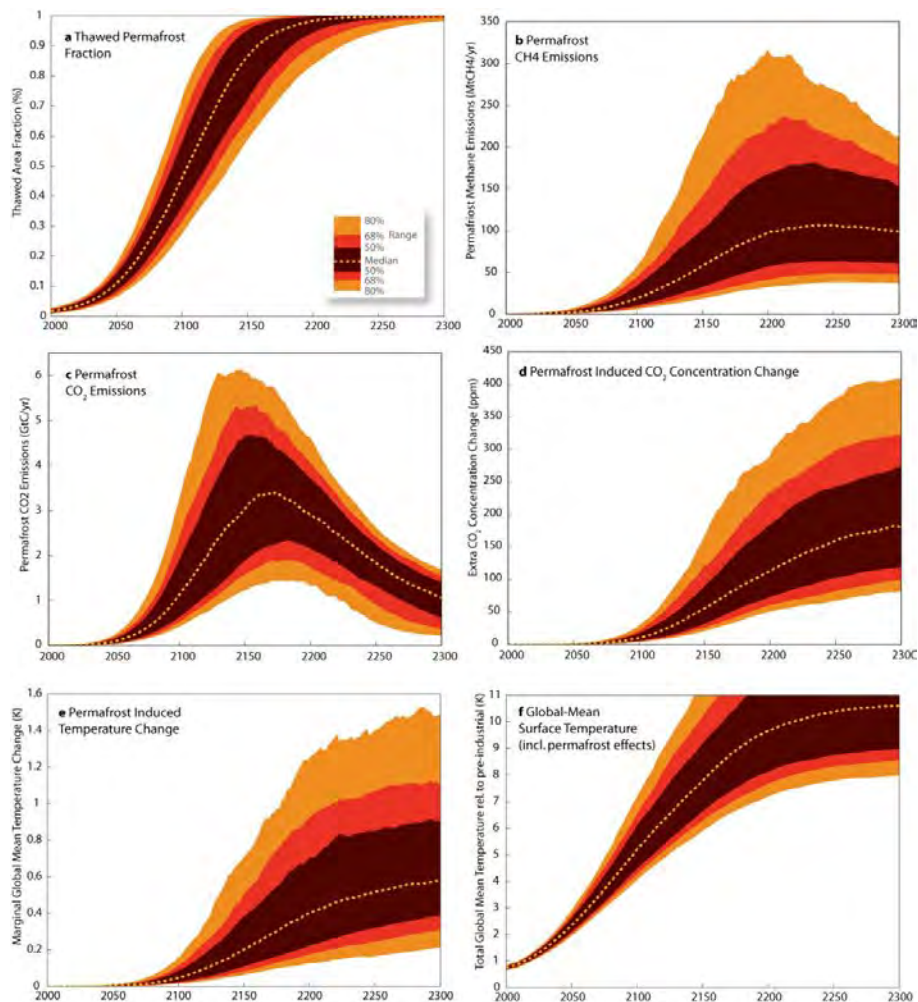
Figure 3 – This study's estimated ranges of thawed permafrost fraction (a), permafrost methane (b) and CO₂ emissions (c), permafrost induced CO₂ concentration (d) and temperature change (e), and the total anthropogenically induced global mean temperature anomaly (f). Results were obtained form an uncertainty analysis for the RCP8.5 scenario. The uncertainty ranges results from 600 member ensemble simulations, using a Monte Carlo sampling that combines the joint distribution of 82 climate model parameters, 9 sets of 17 carbon cycle parameters and 21 independently sampled parameters of our permafrost model (see text and Table 2).

Table 2 - Median (68%-range) estimates of permafrost characteristics under the four RCPs in year 2100, 2200 and 2300. The thawed permafrost area is provided, weighted in relation to the initial carbon pool distribution. Cumulative emissions of CO_2, CH_4 and the share of carbon that is released as methane are shown for cumulative emissions from pre-industrial times until the indicated year. Subsequent rows indicate additional CO_2 concentrations, CO_2 radiative forcing, CH_4 radiative forcing and global mean temperatures due to permafrost thawing above the background scenario. The permafrost carbon sensitivity γ_{LP} indicates the change in the permafrost carbon stock until that year, given relative to that year's global mean surface temperature.

RCP3-PD	2100	2200	2300
Thawed Permafrost (%)	15% (11-22%)	20% (15-29%)	21% (15-30%)
Cumulative CO_2 Emissions (PgC)	4 (2-7)	10 (5-19)	15 (8-29)
Cumulative CH_4 Emissions ($MtCH_4$)	155 (71-337)	469 (209-1032)	808 (355-1746)
Carbon released as Methane (%)	3% (1-6%)	3% (2-6%)	4% (2-7%)
Added CO_2 Concentration (ppm)	1 (1-2)	2 (1-5)	3 (2-6)
Delta CO_2 Radiative Forcing (W/m^2)	0.01 (0.01-0.03)	0.03 (0.02-0.07)	0.05 (0.02-0.09)
Delta CH_4 Radiative Forcing (W/m^2)	0 (0-0.01)	0 (0-0.01)	0 (0-0.01)
Delta Temperature (°C)	0.01 (0-0.02)	0.02 (0.01-0.05)	0.03 (0.01-0.07)
Permafrost Carbon Sensitivity γ_{LP} (PgC/°C)	2.4 (1.4-4)	7.4 (4.5-12)	13 (8-20.7)
RCP45			
Thawed Permafrost (%)	23% (16-33%)	38% (27-54%)	44% (32-63%)
Cumulative CO_2 Emissions (PgC)	8 (4-15)	32 (16-66)	60 (30-124)
Cumulative CH_4 Emissions ($MtCH_4$)	227 (101-506)	988 (438-2200)	2060 (877-4593)
Carbon released as Methane (%)	2% (1-4%)	2% (1-4%)	3% (1-4%)
Added CO_2 Concentration (ppm)	2 (1-5)	10 (4-22)	18 (8-39)
Delta CO_2 Radiative Forcing (W/m^2)	0.02 (0.01-0.05)	0.09 (0.04-0.2)	0.17 (0.08-0.34)
Delta CH_4 Radiative Forcing (W/m^2)	0.01 (0-0.01)	0.01 (0-0.02)	0.01 (0-0.02)
Delta Temperature (°C)	0.02 (0.01-0.04)	0.07 (0.03-0.16)	0.12 (0.05-0.29)
Permafrost Carbon Sensitivity γ_{LP} (PgC/°C)	2.9 (1.7-5)	11.2 (6.6-18.5)	20 (11.8-32.1)
RCP6			
Thawed Permafrost (%)	26% (18-38%)	57% (41-82%)	69% (50-96%)
Cumulative CO_2 Emissions (PgC)	9 (5-19)	68 (34-143)	138 (71-280)
Cumulative CH_4 Emissions ($MtCH_4$)	245 (110-548)	1647 (720-3884)	3776 (1652-9157)
Carbon released as Methane (%)	2% (1-4%)	2% (1-3%)	2% (1-4%)
Added CO_2 Concentration (ppm)	3 (2-7)	25 (11-55)	49 (22-103)
Delta CO_2 Radiative Forcing (W/m^2)	0.03 (0.01-0.05)	0.17 (0.08-0.34)	0.32 (0.16-0.62)
Delta CH_4 Radiative Forcing (W/m^2)	0.01 (0-0.02)	0.02 (0.01-0.05)	0.02 (0.01-0.05)
Delta Temperature (°C)	0.02 (0.01-0.05)	0.13 (0.06-0.33)	0.24 (0.11-0.6)
Permafrost Carbon Sensitivity γ_{LP} (PgC/°C)	2.8 (1.6-4.9)	16.1 (9.1-25.9)	29.6 (17.8-45.1)
RCP85			
Thawed Permafrost (%)	46% (31-66%)	98% (90-100%)	100% (99-100%)
Cumulative CO_2 Emissions (PgC)	26 (12-52)	320 (170-543)	529 (362-705)
Cumulative CH_4 Emissions ($MtCH_4$)	493 (212-1198)	6393 (2622-16571)	16964 (7440-41289)
Carbon released as Methane (%)	1% (1-3%)	2% (1-3%)	3% (1-5%)
Added CO_2 Concentration (ppm)	10 (4-22)	113 (59-239)	181 (98-331)
Delta CO_2 Radiative Forcing (W/m^2)	0.05 (0.02-0.11)	0.32 (0.18-0.57)	0.47 (0.28-0.73)
Delta CH_4 Radiative Forcing (W/m^2)	0.01 (0.01-0.03)	0.08 (0.03-0.17)	0.08 (0.03-0.14)
Delta Temperature (°C)	0.05 (0.02-0.11)	0.40 (0.17-0.94)	0.58 (0.3-1.15)
Permafrost Carbon Sensitivity γ_{LP} (PgC/°C)	5.1 (2.7-8.6)	32.1 (21.5-43.3)	46.9 (35.2-61)

Running a simple carbon-climate box model for the fossil-intensive A2 scenario, (Raupach, Canadell et al. 2008) estimate CO_2 release from thawing permafrost soils until 2100. This study does not account for different temporal dynamics of aerobic/anaerobic and mineral/peatland soil pools and assumes a rather fast time constant for the C release from thawed permafrost carbon. Their estimate of 80 ppm atmospheric CO_2 concentration change from permafrost carbon is above our high-end estimate in 2100 (22 ppm for the upper 68%-range, RCP8.5, see Table 2). A recent study by Schaefer et al. (2011) infers a cumulative carbon flux of 190 ± 64 Gt from thawed permafrost by 2200 based on the A1B scenario. Our simulation results based on the RCP6 scenario (describing a forcing of comparable magnitude) suggest median emissions until 2200 of 69 GtC, with maximum emission of 146 GtC for the 68% range (245 GtC for the 90% range). Key to the higher estimates of Schaefer et al. (2011) is their simulated fast permafrost degradation leading to 80-90% of permafrost carbon thaw before 2100 (while we infer an upper bound of 54% permafrost loss for the 90% uncertainty range by 2100, RCP6). Slow decomposition of anaerobic pools and slow degradation of peatland soils is not accounted for in their study. Much lower C emission is suggested by (Zhuang, Melillo et al. 2006) who applied a process-based emission model to infer an upper estimate of 17 Pg C resulting from permafrost thaw in the 21st century for their high emission scenario (being slightly larger than RCP8.5).

Our inferred methane emissions from anaerobic decomposition of permafrost carbon are rather small, accounting for approximately 1% to 3% of the total carbon release. Due to the higher radiative forcing efficiency of methane, this relatively low fractional release of methane is important with respect to the total temperature increase, with up to a third of the permafrost-induced forcing stemming from these methane releases under the high RCP8.5 scenario (cf. Table 2). Compared to current total anthropogenic methane emissions (roughly 300 MtCH$_4$ yr^{-1} in year 2000), permafrost-induced methane emissions can reach a similar magnitude by 2200 (median around 100MtCH$_4$ yr^{-1}, see Fig. 3Figure b), which corresponds to roughly a

factor of 3 to 10 increase of 20th century natural net methane emissions from the Arctic (McGuire, Anderson et al. 2009).

If the Siberian Yedoma complex were to thaw as analysed by one modeling study which factored in the heat release by microbial decomposition (Khvorostyanov, Ciais et al. 2008) – a process which we neglect in our considerations – permafrost CH_4 release rates are likely to strongly increase. Future methane emission up to 30,000 Tg CH_4 is estimated from a complete thawing of the Yedoma carbon pool alone, based on up-scaling of observational estimates from extensive hotspot methane ebullition over thermokarst lakes (Walter, Zimov et al. 2006; Walter, Smith et al. 2007).

Our global-mean temperature simulations of the RCP scenarios, once including the permafrost module and once excluding it, indicate that the median warming by 2100 is not substantially altered. If we accounted for rather high rates of permafrost thaw as modeled by (Lawrence, Slater et al. 2008) and (Schaefer, Zhang et al.) we expect to infer a non-negligible warming contribution by 2100 from permafrost carbon for the high anthropogenic emission scenarios. For the mitigation scenario RCP3-PD, permafrost-carbon feedbacks add negligibly to the warming. For the high RCP8.5 scenario, permafrost-carbon feedbacks can trigger additional global-mean temperature increase of about 0.05°C (0.02-0.11°C) by 2100, further increasing to 0.40°C (0.17-0.94°C) by 2200 and 0.58°C (0.30- 1.15°C) in 2300 (see Table 2 and Fig. 3f). The intermediate RCP scenarios imply intermediate permafrost feedbacks, roughly proportional to their radiative forcing levels (see Table 2).

3.3. Permafrost sensitivities

The permafrost carbon pool is diminished by 5.1PgC (2.7-8.6PgC) per degree of global warming under RCP8.5. This is the RCP scenario that is most closely comparable to the SRES A2 scenario, for which the C[4]MIP intercomparison has been undertaken. Hence, the total carbon sensitivity of, on average, 79PgC/°C with a

broad range from 20 to 177 PgC/°C across the C^{4}MIP models (Friedlingstein, Cox et al. 2006) could be slightly higher. When permafrost-carbon feedbacks are included, the average estimate would increase 6% (3% to 10%), shifting the best estimate of total land carbon sensitivity from 79PgC/°C by 2100 to above 84 PgC/°C.

Our results highlight the limitations of this indicator 'carbon pool sensitivity', given that cumulative carbon releases per degree of warming is not a scenario- or time- independent characteristic (Table 2). Until 2100, the permafrost-carbon sensitivity under the lower scenarios, RCP3-PD, RCP4.5 and RCP6 is only estimated to be half of that under RCP8.5. On longer timescales, the permafrost-carbon sensitivity increases substantially, 5 times under RCP3-PD until 2300 and approximately 10 times under the higher RCP6 and RCP8.5 (see Table 2).

4. Limitations

The robustness of our results crucially depends on our assumptions made for parameterizing physical and microbial processes which determine the magnitude and timing of carbon release from permafrost soils. By having generously varied model parameters to account for known uncertainties we have spanned a broad possible range of future permafrost evolution. Yet our simplified representation of complex permafrost thawing dynamics and subsequent carbon release has several important limitations.

Effects of snow cover changes, which either can amplify or dampen soil warming, are not accounted for explicitly in our model. While snow state changes are likely to have strongly impacted recent soil temperatures trends, its role of affecting soil temperatures beyond 2050 is expected to exert a much smaller weight as surface air warming becomes the dominant driver for permafrost degradation (Lawrence and Slater 2010).

Due to pronounced spatial inhomogenities in the soils and in local climatology, the "real world" change at specific permafrost sites will differ strongly from our simplified model which assumes that carbon is distributed homogeneously in each latitudinal band and is of the same quality (while carbon content is varied across latitudes). Highly site-specific permafrost thaw can result from site-specific soil and vegetation cover properties, such as a strong insulation effect exerted by an organic-rich surface or a thin peat layer, or the effect on soil thermal properties resulting from unfrozen water in the ground (Alexeev, Nicolsky et al. 2007; Nicolsky, Romanovsky et al. 2007) . Additionally, interaction of the C- and N-cycle (Canadell, Pataki et al. 2007) and various non-linear and complex ecosystem feedback loops

(Heimann and Reichstein 2008; Jorgenson, Romanovsky et al. 2010) can play an important role in the fate of permafrost carbon but are not considered here.

We focus our analysis on the top 3 meters of land permafrost soils where carbon densities are high and uncertainty about the rate of thaw of deep ground layers is not as important. For large warming anomalies on multi-centennial timescales, carbon release from deeper carbon reservoirs is likely. Of particular relevance is the potential degradation and emissions of highly labile carbon found in deeper layers of the Siberian Yedoma complex (Khvorostyanov, Ciais et al. 2008) and fluvial deposits (Tarnocai, Canadell et al. 2009), with a potential to further increase emissions from permafrost. Furthermore, large amounts of carbon are likely to be stored in sub-sea permafrost (Shakhova, Semiletov et al. 2010) and in methane hydrate deposits on continental margins (Archer, Buffett et al. 2009). We did not account for these additional carbon sources and therefore our high-end estimate of 1000 PgC of carbon being potentially vulnerable to future release is likely a conservative estimate.

A key question remains with respect to the impact of permafrost thaw on water table depth, which ultimately determines the fraction of carbon released as CO_2 or as methane. This aspect is considered an obvious gap in state-of-the-art Earth system models (O'Connor, Boucher et al. 2010). Thawing may lead to enhanced soil drainage (lowering of water table) while landscape collapse is likely to favor thermokarst lake or wetland formation, resulting in increased CH_4/CO_2 emission ratios. High rates of CH_4 release from newly forming thermokarst lakes indicate that this process might be a crucial contributor to future methane emission from permafrost soils (Walter, Edwards et al. 2007). Apart from this effect on hydrology, soil thermal properties are changed with enhanced permafrost thaw, although this dynamic is not considered in our study.

With future permafrost thaw and Arctic temperature rise, vegetation cover will respond to more favorable growing conditions, resulting in expected higher CO_2 sequestration in Arctic regions (Friedlingstein, Cox et al. 2006; Canadell, Pataki et al. 2007). Nutrients, released during the decomposition of organic material, could support new forest and biomass buildup. We do not explicitly account for the effect of increased CO_2 uptake by expansion of vegetation into thawed permafrost regions. From a radiative balance viewpoint, the carbon sequestration effect is likely to be compensated somewhat or in full by the lowering of albedo resulting from modified Arctic vegetation (Betts 2000; Matthews and Keith 2007). In case of very strong warming with a pronounced decrease in spring-time snow-cover this compensation will be less effective (a decrease in albedo feedback) – while increased transpiration from enhanced forest cover and the associated positive water vapor feedback might become more important (Swann, Fung et al. 2010).

Our results are limited by the realism of global-mean temperature projections: While our results cannot confidently project warmings of 10°C, which is above the upper end of the AOGCM calibration range of MAGICC6 (approximately 6°C), our results can be taken as an indication of the timing and potential magnitude of permafrost feedback effects. The results that we present here, i.e. that permafrost-carbon feedbacks are relevant at the global scale and will become increasingly important on longer time horizons, are based on highly simplified representations of permafrost and carbon-cycle climate dynamics. Similar studies using process-based models that are constrained by observations are urgently needed to better quantify permafrost-carbon and other permafrost feedbacks more robustly.

5. Conclusion

The inclusion of a highly simplified, dynamic permafrost module into the reduced complexity carbon-cycle climate model MAGICC has shown how permafrost carbon emissions could affect long-term projections of future temperature change. Our results underline the importance of analyzing long-term consequences of land carbon emissions beyond 2100. Studies focusing on short time horizons (e.g. Anisimov 2007) infer a rather small permafrost feedback, in line with our results, while climatic consequences of thawing permafrost soils become clearly apparent after 2100 for the medium and higher RCP scenarios. Even more pronounced than many other components of the Earth System, the permafrost feedback highlights the inert and slow response to human perturbations. Once unlocked under strong warming, thawing and decomposition of permafrost can release amounts of carbon until 2300 comparable to the historical anthropogenic emissions up to 2000 (approximately 440GtC, cf. Allen, Frame et al. 2009). Under the RCP8.5 scenarios – with cumulative permafrost CO_2 emissions of 362 PgC to 705 PgC – this permafrost-carbon feedback could add nearly half a degree warming (0.17-0.94°C) warming from 2200 onwards, albeit in a world that will already be dissimilar to the current one due to global-mean temperature levels near to and possibly in excess of 10°C. Our method is however not able to bound a worst-case scenario. For example, if there is extensive thermokarst formation (Walter, Zimov et al. 2006; Walter, Smith et al. 2007) or subsea permafrost degradation (Shakhova, Semiletov et al. 2010; Shakhova, Semiletov et al. 2010), substantial CH_4 emissions could result from thawing these high Arctic ecosystems.

For lower scenarios, e.g. the mitigation scenario RCP3-PD, our results suggest that future warming is unlikely to increase Arctic temperatures enough to release a

large fraction of the carbon stored in permafrost soils, although up to 22% could be thawed already by 2100. If strong mitigation of emissions is pursued, it seems still possible to prevent the release of large fractions of this permafrost carbon over the coming centuries.

6. Appendix Model Description

The following Appendix describes our simplified permafrost module and its parameterizations.

A.1 Initial carbon pool distribution.

Our default carbon distribution assumes equal amounts of carbon in each of the zonal bands. These zonal bands represent carbon stores liable to thawing at different warming thresholds. In order to capture the uncertainty that a larger or smaller fraction of the total permafrost carbon might be subject to thawing for comparatively low temperature increases, we introduced flexibility in the model regarding this initial carbon distribution along the 'North-South' axis. Depending on the input parameter φ, initial total carbon pool C_0 is distributed across our n zonal bands $C_{i,0}$ according to:

$$C_{i,0} = \begin{cases} \left(i\frac{|\varphi|}{n^2} + \frac{1-|\varphi|}{n}\right)\frac{1}{A_{tot}}C_0, & -1 \leq \varphi < 0 \\ \frac{1}{n}C_0, & \varphi = 0 \\ \left((n-i+1)\frac{|\varphi|}{n^2} + \frac{1-|\varphi|}{n}\right)\frac{1}{A_{tot}}C_0, & 0 < \varphi \leq 1 \end{cases}$$

(1)

with A_{tot} being the normalization constant, ensuring that the individual contributions add up to C_0 (surface area of the grey shaded region marked in Fig. A1), $\left(A_{tot} = 1 - \frac{|\varphi|}{2}\left(1 - \frac{1}{n}\right)\right)$. For the limit $\varphi=1$, the "northernmost" zonal band (i=n) will only contain the small fraction $1/(n^2 \ast A_{tot})$ of the total carbon pool, while the southernmost zonal band (i=1) will contain the largest fraction $1/(n \ast A_{tot})$ with linear increasing carbon pool fractions in between. Graphically, the carbon pool fraction distributions that can be set via the φ parameter can be represented by a horizontally striped trapeze, with the lower/upper parallel side approaching zero for φ being set at 1 or -1 (see Fig. A1). This initial carbon pool in each zonal band is

attributed to the mineral and peatland soil fractions using the parameters $R_{ms,\,south}$ for band $i=1$ and $R_{ms,\,north}$ for the "northernmost" band $i=n$, with linear interpolation for intermediate zonal bands.

A.2. The thawing threshold in each zonal band

A regional warming threshold ΔT_i^{thresh} is attributed to each zonal band for describing the latitudinal dependency of permafrost thaw. A minimum warming for thaw is required in the Southernmost band ($\Delta T_{\min}$), and a maximum warming threshold in the Northernmost band (ΔT_{max}). Thus, by linearly interpolating between the zonal bands, the warming threshold in zonal band i is defined as:

$$\Delta T_i^{thresh} = \Delta T_{min} + \frac{(i-1)(\Delta T_{max} - \Delta T_{min})}{n-1} \qquad (2).$$

Using this threshold, we calculate the maximum temperature reached during summer ($T_{i,t}^{summer}$) relative to the freezing point in each year t in each zonal band:

$$T_{i,t}^{summer} = \alpha\,\Delta T_{global,t} - \Delta T_i^{thresh} \qquad (3),$$

with $\Delta T_{global,t}$ being the global-mean, annual average temperature anomaly, α being the latitudinal amplification factor, i.e., the ratio at which permafrost regions are expected to warm relative to the global mean, assuming a linear relationship between regional and global warming (Santer, Wigley et al. 1990; Hewitt, Stouffer et al. 2003; Frieler and et al. in preparation). As soon as global temperature increase is high enough to raise permafrost summer temperatures above zero in a given latitudinal band, permafrost thaw is initiated and soil carbon in this band gets subject to decomposition.

We calculate the transformation from soil between the permafrost and non-permafrost area on an annual basis. The summer temperature in year t is simply multiplied with the thawing/refreezing rate β_x to calculate the thawing or re-refreezing fractional depth D_t^x of each zonal band, with $D_t^x = \beta_x T_{i,t}^{summer}$ (x denoting either 'ms' or 'peat' for the mineral or peatland soils). By choosing different settings for β_x, we account for the large uncertainty present in model simulations of permafrost thaw.

A.3. Decomposition rates and their sensitivities to soil moisture and temperature.

Oxic decomposition rates in peat and mineral soils are assumed to be dependent on two factors, i.e., soil moisture and soil temperature. In the following, we describe simple parametrizations of the soil moisture status and of the temperature dependency of decomposition to infer a formula for effective decomposition rates. For anoxic conditions, decomposition rates are a function of soil temperature only.

Using a simple sinusoidal function, we approximate the annual cycle of the effective soil temperature in each band *i*, to compute the monthly soil temperatures $T_{i,m}^{soil}$

$$T_{i,m}^{soil} = \frac{\Phi}{2} \sin \frac{\pi(m-1)}{11} - \frac{\Phi}{2} + T_{i,t}^{summer} \qquad (4),$$

with *m=1,…,12* denoting the 12 months of year t, and Φ the amplitude of the mean soil temperature cycle in the upper 3 meters (estimated as 4-6°C) (cf. Khvorostyanov, Ciais et al. 2008) .

Building on the monthly soil temperatures in each latitudinal band, we linearly approximate the temperature dependency of soil moisture $W_{i,m}^{soil}$ according to model results from a 4xCO$_2$ run of the LPJ model (Sitch, Smith et al. 2003):

$$W_{i,m}^{soil} = \begin{cases} W_{min}, & m_T T_{i,m}^{soil} + W_{off} \leq W_{min} \\ m_T T_{i,m}^{soil} + W_{off}, & m_T T_{i,m}^{soil} + W_{off} > W_{min} \end{cases} \tag{5},$$

with m_T determining the soil moisture temperature sensitivity (default of 0.04°C^{-1}). Following Wania et al. (2009), we describe the moisture modifier function $F(W)$ as:

$$F(W_{i,m}^{soil}) = \frac{1 - e^{-W_{i,m}^{soil}}}{1 - e^{-1}} \tag{6}.$$

The temperature dependence of autotrophic respiration is described by a modified Arrhenius equation (Lloyd and Taylor 1994; Sitch, Smith et al. 2003):

$$F(T_{i,m}^{soil}) = e^{\lambda\left(\frac{1}{56.02} - \frac{1}{T_{i,m}^{soil}+46.02}\right)} \tag{7},$$

with λ describing the activation energy and F(T=20°C) often being called the 'Q10' factor, representing the increase in the decomposition rate from 10°C to 20°C.

Using results from equations (6) and (7), the annual average decomposition rate $\theta_{t,i,aer}^{ms}$ for aerobic respiration in mineral soils is derived from the inverse turnover time $1/\tau_{aer}^{ms}$ and modulated by the soil temperature modifier $F(T)$ and the moisture modifier $F(W)$. The time- and zonal band dependent decomposition rate $\theta_{t,i,aer}^{ms}$ for the mineral soil type and aerobic decomposition segment is the annual average over monthly decomposition rates:

$$\theta_{t,i,aer}^{ms} = \frac{1}{\tau_{aer}^{ms}} F(T_{i,m}^{soil}) F(W_{i,m}^{soil}) \tag{8}.$$

The effective aerobic decomposition rates for peatland carbon pool fractions are assumed to be lower, proportional to $\theta_{t,i,aer}^{ms}$ using the proportionality factors $R_{peat/ms}$ (assumed range 0.3 to 0.7). Anaerobic decomposition is calculated by using equation (8) with a fixed soil moisture modifier ($F(W_{i,m}^{soil}) = 1$) and an aerobic to anaerobic proportionality factor $R_{an/aer}$ with a default value of 0.1.

A.4. Area of aerobic and anaerobic decomposition

The anaerobic area fraction A_{an}^x (for peatland or mineral soils) relates to the thawed permafrost area, so that the anaerobic area fraction $A{'}_{t,i,an}^x$ in relation to the total zonal band area (indicated by the hyphen) is given by

$$A{'}_{t,i,an}^x = A_{an}^x \left(1 - A{'}_{t,i,pf}^x\right) \tag{9},$$

with $A{'}_{t,i,pf}^x$ being the fraction of intact permafrost, starting at 100% at the beginning of the simulations and then decreasing as warming progresses.

Unlike in a spatially resolved high resolution permafrost model coupled to an AOGCM, our simplified structure does not permit to keep track of the carbon content of individual soil patches over time. Thus, for a change in the permanently frozen area fraction, an assumption is required of how much carbon is actually transferred between the respective carbon pools. We make a simplifying assumption of a uniformly distributed carbon density in each area type, anaerobic and aerobic, permafrost and non-permafrost. Ideally, a higher resolved model would keep track of individual patches or parts of the permafrost column. Thus, the change of the thawed anaerobic (z='an') or aerobic (z='aer') area $\Delta A{'}_{t,i,z}^x$ relative to the total zonal band area is given by the annual thawing rate D_t^x and the respective permafrost area $A{'}_{t,i,pf}^x$

$$\Delta A{'}_{t,i,z}^x = D_t^x A{'}_{t,i,pf}^x \tag{10}.$$

In parallel to the fractional areas, the respective carbon pools $C^x_{t,i,z}$ are updated, (i.e. the released carbon is subtracted from the pool) for both soil types x, i.e., peatland and mineral soil, each year t, zonal band i and the anaerobic and aerobic decomposition segments z.

A.5. Calculating emissions.

The carbon release can now be calculated using the decomposition rates derived in equation (8) above and the calculated amount of thawed carbon being available in the four soil pools (mineral and peatland soil, under aerobic and anaerobic conditions). Given that pools in MAGICC are generally end of year t/beginning of year $t+1$ quantities, and emissions the sum over year t, the carbon emissions from the aerobic and anaerobic carbon pools are derived as:

$$E^x_{t,i,z} = \theta^x_{t,i,z} C^x_{t,i,z} \tag{11}$$

Carbon emissions from aerobic decomposition occur in the form of carbon dioxide, and those from the anaerobic decomposition in the form of both methane and carbon dioxide. With half of the carbon in anaerobic areas being converted to CH_4 in the soil, a certain fraction χ of the latter half is assumed to be oxidized on its way through the upper soil layers, before reaching the atmosphere.
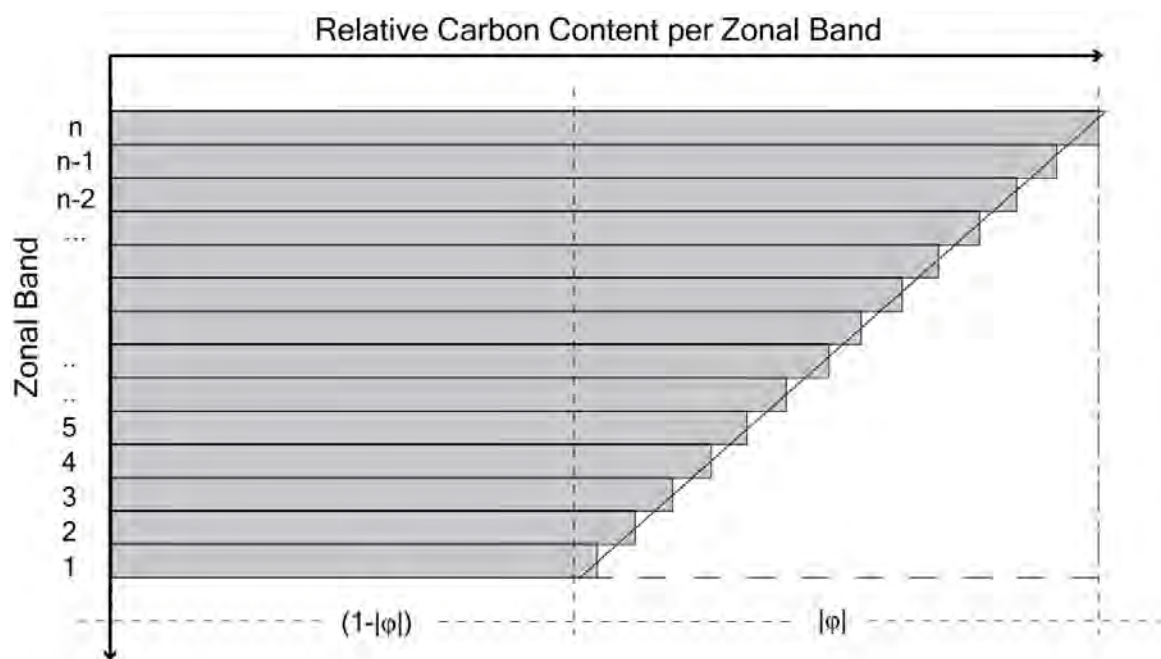
Figure A1 - Illustration of the simplified parameterisation to vary the north-south distribution of the initial carbon content C_0 across the n zonal bands with the parameter φ, here shown for a 'northward' bias ($-1<φ<0$). By default ($φ=0$), each zonal band is allocated the same share, $1/n\,C_0$.

7. Acknowledgements

8. References

Alexeev, V. A., D. J. Nicolsky, et al. (2007). "An evaluation of deep soil configurations in the CLM3 for improved representation of permafrost." Geophysical Research Letters **34**(9): -.

Allen, M. R., D. J. Frame, et al. (2009). "Warming caused by cumulative carbon emissions towards the trillionth tonne." Nature **458**(7242): 1163.

Allen, M. R., P. A. Stott, et al. (2000). "Quantifying the uncertainty in forecasts of anthropogenic climate change." Nature **407**: 617-620.

Andreae, M. O., C. D. Jones, et al. (2005). "Strong present-day aerosol cooling implies a hot future." Nature **435**(7046): 1187-1190.

Andrews, T., P. M. Forster, et al. (2009). "A Surface Energy Perspective on Climate Change." Journal of Climate **22**(10): 2557-2570.

Anisimov, O. A. (2007). "Potential feedback of thawing permafrost to the global climate system through methane emission." Environmental Research Letters **2**(4): 2-7.

Archer, D., B. Buffett, et al. (2009). "Ocean methane hydrates as a slow tipping point in the global carbon cycle." Proceedings of the National Academy of Sciences of the United States of America **106**(49): 20596-20601.

Belyea, L. R. and A. J. Baird (2006). BEYOND "THE LIMITS TO PEAT BOG GROWTH": CROSS-SCALE FEEDBACK IN PEATLAND DEVELOPMENT. **76:** 299-322.

Betts, R. A. (2000). "Offset of the potential carbon sink from boreal forestation by decreases in surface albedo." Nature **408**(6809): 187-190.

Canadell, J. G., D. E. Pataki, et al. (2007). Saturation of the Terrestrial Carbon Sink. Terrestrial Ecosystems in a Changing World, Springer Berlin Heidelberg**:** 59-78.

Cramer, W., A. Bondeau, et al. (2001). "Global response of terrestrial ecosystem structure and function to CO_2 and climate change: results from six dynamic global vegetation models." Global Change Biology **7**(4): 357-373.

Davidson, E. A. and I. A. Janssens (2006). "Temperature sensitivity of soil carbon decomposition and feedbacks to climate change." Nature **440**(7081): 165-173.

Ehhalt, D., M. J. Prather, et al. (2001). Atmospheric Chemistry and Greenhouse Gases. Climate Change 2001: The Scientific Basis. Cambridge, Cambridge University Press.

Eliseev, A. V., M. M. Arzhanov, et al. (2009). "Changes in climatic characteristics of Northern Hemisphere extratropical land in the 21st century: Assessments with the IAP RAS climate model." Izvestiya Atmospheric and Oceanic Physics **45**(3): 271-283.

Euskirchen, E. S., A. D. McGuire, et al. (2006). "Importance of recent shifts in soil thermal dynamics on growing season length, productivity, and carbon sequestration in terrestrial high-latitude ecosystems." Global Change Biology **12**(4): 731-750.

Friedlingstein, P., P. Cox, et al. (2006). "Climate–Carbon Cycle Feedback Analysis: Results from the C4MIP Model Intercomparison." Journal of Climate **19**(14): 3337-3353.

Friedlingstein, P., P. Cox, et al. (2006). "Climate-carbon cycle feedback analysis: Results from the (CMIP)-M-4 model intercomparison." Journal of Climate **19**(14): 3337-3353.

Frieler, K. and et al. (in preparation). "A scaling approach to probabilistic assessment of regional climate change."

Frieler, K., M. Meinshausen, et al. (2011). "A scaling approach to probabilistic assessment of regional climate change." submitted to Journal of Climate.

Frolking, S., N. T. Roulet, et al. (2001). "Modeling northern peatland decomposition and peat accumulation." Ecosystems **4**(5): 479-498.

Frolking, S., J. Talbot, et al. (2011). "Peatlands in the Earth's 21st century coupled climate-carbon system." submitted to Environmental Reviews.

Heimann, M. and M. Reichstein (2008). "Terrestrial ecosystem carbon dynamics and climate feedbacks." Nature **451**(7176): 289-292.

Hewitt, C. D., R. J. Stouffer, et al. (2003). "The effect of ocean dynamics in a coupled GCM simulation of the Last Glacial Maximum." Climate Dynamics **20**(2-3): 203-218.

Jorgenson, M. T., V. Romanovsky, et al. (2010). "Resilience and vulnerability of permafrost to climate change." Canadian Journal of Forest Research-Revue Canadienne De Recherche Forestiere **40**(7): 1219-1236.

Khvorostyanov, D. V., P. Ciais, et al. (2008). "Vulnerability of east Siberia's frozen carbon stores to future warming." Geophysical Research Letters **35**(10): -.

Khvorostyanov, D. V., G. Krinner, et al. (2008). "Vulnerability of permafrost carbon to global warming. Part I: model description and role of heat generated by organic matter decomposition." Tellus Series B-Chemical and Physical Meteorology **60**(2): 250-264.

Lawrence, D. M. and A. G. Slater (2005). "A projection of severe near-surface permafrost degradation during the 21st century." Geophysical Research Letters **32**(24): -.

Lawrence, D. M. and A. G. Slater (2008). "Incorporating organic soil into a global climate model." Climate Dynamics **30**(2-3): 145-160.

Lawrence, D. M. and A. G. Slater (2010). "The contribution of snow condition trends to future ground climate." Climate Dynamics **34**(7-8): 969-981.

Lawrence, D. M., A. G. Slater, et al. (2008). "Sensitivity of a model projection of near-surface permafrost degradation to soil column depth and representation of soil organic matter." Journal of Geophysical Research-Earth Surface **113**(F2): -.

Lawrence, D. M., A. G. Slater, et al. (2008). "Accelerated Arctic land warming and permafrost degradation during rapid sea ice loss." Geophysical Research Letters **35**(11): -.

Lloyd, J. and J. A. Taylor (1994). "On the Temperature-Dependence of Soil Respiration." Functional Ecology **8**(3): 315-323.

Matthews, H. D. and D. W. Keith (2007). "Carbon-cycle feedbacks increase the likelihood of a warmer future." Geophysical Research Letters **34**(9): -.

McGuire, A. D., L. G. Anderson, et al. (2009). "Sensitivity of the carbon cycle in the Arctic to climate change." Ecological Monographs **79**(4): 523-555.

McGuire, A. D., F. S. Chapin, et al. (2006). "Integrated Regional Changes in Arctic Climate Feedbacks: Implications for the Global Climate System*." Annual Review of Environment and Resources **31**(1): 61-91.

Meehl, G. A., C. Covey, et al. (2005). "Overview of the Coupled Model Intercomparison Project." Bulletin of the American Meteorological Society **86**(1): 89–93.

Meehl, G. A., T. F. Stocker, W. Collins, P. Friedlingstein, A. Gaye, J. M. Gregory, A. Kitoh, R. Knutti, J. Murphy, A. Noda, S. C. B. Raper, I. Watterson, A. Weaver and Z.-C. Zhao (2007). Chapter 10: Global Climate Projections. Cambridge, Cambridge University Press.

Meinshausen, M., S. J. Smith, et al. (2011). "The RCP Greenhouse Gas Concentrations and their Extension from 1765 to 2300." submitted to Climatic Change.

Monson, R. K., D. L. Lipson, et al. (2006). "Winter forest soil respiration controlled by climate and microbial community composition." Nature **439**(7077): 711-714.

Moss, R. H., J. A. Edmonds, et al. (2010). "The next generation of scenarios for climate change research and assessment." <u>Nature</u> **463**(7282): 747-756.

Nicolsky, D. J., V. E. Romanovsky, et al. (2007). "Improved modeling of permafrost dynamics in a GCM land-surface scheme." <u>Geophysical Research Letters</u> **34**(8): -.

O'Connor, F. M., O. Boucher, et al. (2010). "Possible role of wetlands, permafrost, and methane hydrates in the methane cycle under future climate change: A review." <u>Rev. Geophys.</u> **48**(4): RG4005.

Raupach, M., J. Canadell, et al. (2008). Observing a Vulnerable Carbon Cycle. <u>The Continental-Scale Greenhouse Gas Balance of Europe</u>, Springer New York. **203:** 5-32.

Riley, W. J., Z. M. Subin, et al. "Barriers to predicting changes in global terrestrial methane fluxes: analyses using CLM4Me, a methane biogeochemistry model integrated in CESM." <u>Biogeosciences Discuss.</u> **8**(1): 1733-1807.

Saito, K., M. Kimoto, et al. (2007). "Evaluating a high-resolution climate model: Simulated hydrothermal regimes in frozen ground regions and their change under the global warming scenario." <u>J. Geophys. Res.</u> **112**(F2): F02S11.

Santer, B. D., T. M. L. Wigley, et al. (1990). Developing Climate Scenarios from Equilibrium GCM Results. Hamburg, Germany, MPI.

Scanlon, D. and T. Moore (2000). "Carbon dioxide production from peatland soil profiles: The influence of temperature, oxic/anoxic conditions and substrate." <u>Soil Science</u> **165**(2): 153-160.

Schaefer, K., T. Zhang, et al. (2011). "Amount and timing of permafrost carbon release in response to climate warming." <u>Tellus B</u> **63**(2): 165-180.

Schewe, J., A. Levermann, et al. (2011). "Climate change under a scenario near 1.5 °C of global warming: monsoon intensification, ocean warming and steric sea level rise." <u>Earth Syst. Dynam.</u> **2**(1): 25.

Schuur, E. A. G., J. Bockheim, et al. (2008). "Vulnerability of permafrost carbon to climate change: Implications for the global carbon cycle." <u>Bioscience</u> **58**(8): 701-714.

Schuur, E. A. G., J. G. Vogel, et al. (2009). "The effect of permafrost thaw on old carbon release and net carbon exchange from tundra." <u>Nature</u> **459**(7246): 556-559.

Screen, J. A. and I. Simmonds (2010). "The central role of diminishing sea ice in recent Arctic temperature amplification." <u>Nature</u> **464**(7293): 1334-1337.

Shakhova, N., I. Semiletov, et al. (2010). "Methane from the East Siberian Arctic Shelf Response." <u>Science</u> **329**(5996): 1147-1148.

Shakhova, N., I. Semiletov, et al. (2010). "Extensive Methane Venting to the Atmosphere from Sediments of the East Siberian Arctic Shelf." <u>Science</u> **327**(5970): 1246-1250.

Sitch, S., C. Huntingford, et al. (2008). "Evaluation of the terrestrial carbon cycle, future plant geography and climate-carbon cycle feedbacks using five

Dynamic Global Vegetation Models (DGVMs)." Global Change Biology **14**(9): 2015-2039.

Sitch, S., B. Smith, et al. (2003). "Evaluation of ecosystem dynamics, plant geography and terrestrial carbon cycling in the LPJ dynamic global vegetation model." Global Change Biology **9**(2): 161-185.

Stroeve, J., M. M. Holland, et al. (2007). "Arctic sea ice decline: Faster than forecast." Geophys. Res. Lett. **34**(9): L09501.

Swann, A. L., I. Y. Fung, et al. (2010). "Changes in Arctic vegetation amplify high-latitude warming through the greenhouse effect." Proceedings of the National Academy of Sciences of the United States of America **107**(4): 1295-1300.

Tarnocai, C., J. G. Canadell, et al. (2009). "Soil organic carbon pools in the northern circumpolar permafrost region." Global Biogeochemical Cycles **23**: -.

van Vuuren, D. P., J. Edmonds, et al. (2011). "Representative Concentration Pathways: an overview." submitted to Climatic Change.

Wagner, D., S. Liebner, et al. (2009). Global Warming and Carbon Dynamics in Permafrost Soils: Methane Production and Oxidation. Permafrost Soils, Springer Berlin Heidelberg. **16:** 219-236.

Walter, K. M., M. E. Edwards, et al. (2007). "Thermokarst lakes as a source of atmospheric CH4 during the last deglaciation." Science **318**(5850): 633-636.

Walter, K. M., L. C. Smith, et al. (2007). "Methane bubbling from northern lakes: present and future contributions to the global methane budget." Philosophical Transactions of the Royal Society a-Mathematical Physical and Engineering Sciences **365**(1856): 1657-1676.

Walter, K. M., S. A. Zimov, et al. (2006). "Methane bubbling from Siberian thaw lakes as a positive feedback to climate warming." Nature **443**(7107): 71.

Wigley, T. M. L. and S. C. B. Raper (2002). "Reasons for larger warming projections in the IPCC Third Assessment Report." Journal of Climate **15**(20): 2945-2952.

Yi, S. H., M. K. Woo, et al. (2007). "Impacts of peat and vegetation on permafrost degradation under climate warming." Geophysical Research Letters **34**(16): -.

Zhang, Y., W. J. Chen, et al. (2008). "Transient projections of permafrost distribution in Canada during the 21st century under scenarios of climate change." Global and Planetary Change **60**(3-4): 443-456.

Zhuang, Q. L., J. M. Melillo, et al. (2006). "CO2 and CH4 exchanges between land ecosystems and the atmosphere in northern high latitudes over the 21st century." Geophysical Research Letters **33**(17): -.

Chapter 6 AMOC

Emulating Atlantic overturning strength for low emission scenarios: consequences for sea-level rise along the North American east coast

C. F. Schleussner[1,2], K. Frieler[1], M. Meinshausen[1], J. Yin[3], A. Levermann[1,2]

[1] Potsdam Institute for Climate Impact Research, Telegrafenberg A62, 14473 Potsdam, Germany

[2] Physics Institute, Potsdam University, Potsdam, Germany

[3] Department of Geosciences, The University of Arizona, Tucson, Arizona

Abstract

In order to provide probabilistic projections of the future evolution of the Atlantic Meridional Overturning Circulation (AMOC), we calibrated a simple Stommel-type box model to emulate the output of fully coupled three-dimensional atmosphere-ocean general circulation models (AOGCMs) of the Coupled Model Intercomparison Project (CMIP). Based on this calibration to idealised global warming scenarios with and without interactive atmosphere-ocean fluxes and freshwater perturbation simulations, we project the future evolution of the AMOC mean strength within the covered calibration range for the lower two Representative Concentration Pathways (RCPs) until 2100 obtained from MAGICC6. For RCP3-PD with a global mean temperature median below $1.0\,^{\circ}$C warming relative to the year 2000, we project an ensemble median weakening of up to 11% compared to 22% under RCP4.5 with a warming median up to $1.9\,^{\circ}$C over the 21st century. Additional Greenland melt water of 10 and $20\,$cm of global sea-level rise equivalent further weakens the AMOC by about 4.5 and 10%, respectively. By combining our outcome with a multi-model sea-level rise study we project a dynamic sea-level rise along the New York City coastline of $4\,$cm for the RCP3-PD and of $8\,$cm for the RCP4.5 scenario over the 21st century. We estimate the total steric and dynamic sea-level rise for New York City to be about $24\,$cm until 2100 for the RCP3-PD scenario, which can hold as a lower bound for sea-level rise projections in this region, as it does not include ice sheet and mountain glacier contributions.

Introduction

The assessment of future risks of climate change requires not only mean projections but more importantly an estimate of the associated uncertainty ranges. Thus, probabilistic projections of climate systems for specific emission pathways are of great interest for the scientific community as well as for policy makers. Complex coupled Atmospheric-Ocean General Circulation Models (AOGCMs) are generally too computationally intensive to provide such probabilistic assessments with large ensembles of runs. This gap can be filled by models of reduced complexity that are able to emulate complex model output.

In this study we present such a reduced complexity model for the Atlantic Meridional Overturning Circulation (AMOC). One key component of this circulation is the formation of deepwater in the Nordic Seas and in the sub-polar North Atlantic that can be substantially hindered by a surface freshening in these regions. Anomalous freshwater flux into the North Atlantic

has led to a shutdown of the circulation in a variety of coupled climate models (Rahmstorf et al., 2005). Furthermore, there is evidence that the AMOC has undergone abrupt changes during the last glacial period (McManus et al., 2004). A complete cessation of the circulation would cause strong cooling, reduced precipitation and substantial shifts of wind patterns in northern Europe (Vellinga and Wood, 2002, 2007; Laurian et al., 2009). Simulations further suggest that an AMOC collapse causes an increase of sea-level around European and North American coast lines by up to 1 m (Levermann et al., 2005; Landerer et al., 2007) and would have strong impacts on the ecosystem of the Atlantic Ocean (Schmittner, 2005). In the AR4 however, none of the participating models showed such an AMOC collapse in the 21st century, but all exhibited a weakening of the AMOC with a large ensemble spread (Meehl et al., 2007) ranging from almost no to a 50% reduction in volume flux. In view of this large uncertainty, an assessment of the impacts connected to a gradual decline of the AMOC in the 21st century appears to be rather difficult.

Probabilistic projections of the AMOC behaviour under global warming scenarios have been performed in a number of different modelling experiments of different complexities (e.g., Challenor et al., 2006; Collins et al., 2006), mainly focussing on the risk of an abrupt cessation of the AMOC (Challenor et al., 2010; Hargreaves et al., 2004) and using observational data for historical constraining of the model parameters (Urban and Keller, 2010; Knutti et al., 2003).

Here, we present a different approach towards a probabilistic assessment of the uncertainty in mean AMOC projections by integrating three qualitatively different multi-model AOGCM emulation experiments. First, a simple conceptual model is used to emulate AOGCM simulations that provide an ideal setting for stepwise constraining the model parameters. (Gregory et al., 2005; Stouffer et al., 2006). Then these calibrated emulators will be forced with probabilistic projections of the global mean surface air temperature from the reduced complexity carbon cycle-climate model MAGICC6 (Meinshausen et al., 2011a,b). The combination of the obtained AMOC mean weakening projections with results of a multi-model sea-level rise study by Yin et al. (2009) finally allows for probabilistic projections for the dynamical sea-level rise in the New York City region.

In the second section of this manuscript we will introduce the conceptual AMOC model used in this study. The calibration of this model to AOGCM output is detailed in Sect. 2. As shown in Sect. 3 we calibrated our conceptual model to the output of five different AOGCMs. Using this calibrated emulator model we present probabilistic projections of the AMOC mean behaviour under two Representative Concentration Pathway (RCP) emission scenarios RCP3-PD and RCP4.5 in Sect. 4. The influence of additional Greenland melting is investigated in

Sect. 5. Projections for the dynamical sea-level rise in the New York City region are presented in Sect. 6, before some conclusions are drawn in Sect. 8.

1 Model description

In order to capture the basic physical processes relevant for the future AMOC evolution we use the box model by Stommel (1961). It incorporates the linear relation between volume transport and meridional density difference $m \propto \Delta \rho$ that has been reported in a number of coarse resolution ocean simulations under very different forcing scenarios (e.g., Hughes and Weaver, 1994; Klinger and Marotzke, 1999; Griesel and Morales-Maqueda, 2006; Schewe and Levermann, 2010). The box model's simplicity further allows a calibration with a minimal number of free parameters. As we will show in Sect. 2, the simulation set designed for Gregory et al. (2005) and Stouffer et al. (2006) is very strongly related to the free parameters in the Stommel model and can thereby be used to constrain their values.

The Stommel model was used in a variety of studies investigating the stability of the AMOC (e.g., Rahmstorf, 1996; Dijkstra et al., 2004; Guan and Huang, 2008; Drijfhout et al., 2010) or combined socio-economical impacts (Zickfeld and Bruckner, 2008). It does however not account for driving mechanisms of the AMOC (Kuhlbrodt et al., 2007) such as Southern Ocean winds (Toggweiler and Samuels, 1998). This clearly limits the applicability of the model, since it was recently shown that pycnocline dynamics such as those introduced by Gnanadesikan (1999) are necessary to capture the full AMOC dynamics in a coarse resolution model (Levermann and Fürst, 2010). Here we argue that the box-model can nonetheless emulate mean AMOC behaviour far away from a possible threshold in capturing the first-order baroclinic response to surface heat- and freshwater flux anomalies especially for time scales up to the year 2100.

In our study we follow the emulation approach of Zickfeld et al. (2004), who applied a Stommel model as an emulator to an earth system model of intermediate complexity. In their study, however, they aimed to emulate especially the threshold behaviour of the AMOC and thus used long-term hysteresis experiments for their calibration. The model used in our study (Fig. 1) has two boxes, one northern box representing the deep convection regions in the North Atlantic north of 45° N and one comprising the tropical and southern Atlantic.

The meridional volume transport m between the two boxes is determined by

$$m = k \, [\beta \, \Delta \, S \, - \, \alpha \, \Delta \, T], \qquad (1)$$
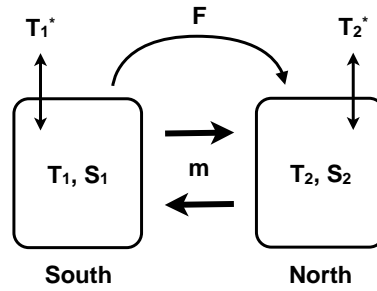
Figure 1: Schematic view of our conceptual two box model for the Atlantic Meridional Overturning Circulation.

where k is a proportionality constant, which we will use to tune the box model to different AOGCMs, $\Delta S = S_2 - S_1$ being the salinity difference and $\Delta T = T_2 - T_1$ being the temperature difference between the two boxes, $\alpha = 1.7 \times 10^{-4}\,\mathrm{K}^{-1}$ the thermal and $\beta = 8 \times 10^{-4}\,\mathrm{psu}^{-1}$ the haline expansion coefficient. Atmospheric forcing via a freshwater transport between the boxes and a temperature coupling with the surrounding is applied. This approach results in a set of four ordinary differential equations:

$$\dot{T}_1 = \frac{m}{V_1}\,(T_2 - T_1) + \lambda\,(T_1^* - T_1) \tag{2}$$

$$\dot{T}_2 = \frac{m}{V_2}\,(T_1 - T_2) + \lambda\,(T_2^* - T_2) \tag{3}$$

$$\dot{S}_1 = \frac{m}{V_1}\,(S_2 - S_1) + \frac{S_0\,F}{V_1} \tag{4}$$

$$\dot{S}_2 = \frac{m}{V_2}\,(S_1 - S_2) - \frac{S_0\,F}{V_2}, \tag{5}$$

where $S_0 = 35\,\mathrm{psu}$ is the reference salinity and V_1 and V_2 are the box volumes. T_1^* and T_2^* are reference temperatures in the absence of oceanic heat transport, representing the atmospheric thermal forcing onto the ocean, λ is the thermal coupling constant and F the a freshwater transport between the boxes, which incorporates both atmospheric moisture transport and oceanic eddy and gyre circulation transport.

Just considering temperature and salinity differences between the northern and the southern

box instead of absolute values, Eqs. (2)–(5) can be rewritten as

$$\Delta \dot{T} = -m\, V_{eff}\, \Delta T - \lambda\, \Delta T + \lambda\, \Delta T^* \tag{6}$$

$$\Delta \dot{S} = -m\, V_{eff}\, \Delta S - F\, S_0\, V_{eff}, \tag{7}$$

where V_{eff} is the effective volume $V_{eff} = \frac{V_1 + V_2}{V_1 V_2}$. Combining of Eqn. (6) and (7) with Eqn. (1) yields:

$$\Delta \dot{T} = k\alpha\, V_{eff}\, (\Delta T)^2 - k\beta\, V_{eff}\, \Delta T\, \Delta S \tag{8}$$
$$- \lambda\, \Delta T + \lambda\, \Delta T^*$$

$$\Delta \dot{S} = k\beta\, V_{eff}\, \Delta T\, \Delta S - k\alpha\, V_{eff}\, (\Delta S)^2 - F\, S_0\, V_{eff}. \tag{9}$$

As found for regional changes in surface air temperatures (e.g Mitchell, 2003; Giorgi, 2008), we assume that our reference temperature difference scales also linearly with δT_{glob}:

$$\delta\, (\Delta\, T^*) = \Delta\, T_0^* + p\, \delta\, T_{\mathrm{glob}}, \tag{10}$$

where p is the temperature forcing coefficient and ΔT_0^* the equilibrium temperature difference. Also we assume that the freshwater transport F into the northern box can be approximated linearly (Manabe and Stouffer, 1994; Rahmstorf and Ganopolski, 1999) by introducing a model specific hydrological sensitivity h:

$$\delta\, F = F_0 + h\, \delta\, T_{\mathrm{glob}}. \tag{11}$$

Thus, the temporal evolution of AMOC strength m is given as a function of global mean temperature change δT_{glob}. The equilibrium freshwater flux F_0 mainly influences the equilibrium overturning, which can ultimately be adjusted by the proportional constant k (compare Eq. 1). We therefore set F_0 for all models to 0.014 Sv according to Zickfeld et al. (2004). Thus, the number of adjustable parameters is limited to six: k, V_{eff}, λ, ΔT_0^*, p, and h. The calibration procedure of this parameters and the associated data sets are described in the following section.

2 Calibration data

In order to calibrate our conceptual model we used results from a related multi-model study on AMOC-stability presented in Gregory et al. (2005) and Stouffer et al. (2006). In the latter an artificial freshwater flux of 0.1 Sv is applied for 100 years in the Northern North Atlantic and the transient weakening of the AMOC as well the recovery is modelled for 200 years. This type of experiment with a temporal external forcing is particularly suitable to calibrate our emulation model to initial climate conditions by tuning k, V_{eff}, λ, and ΔT_0^*.

In Gregory et al. (2005) the transient impact of global warming on the AMOC is investigated. For this purpose, not only results of a 1% CO_2 quadrupling scenario are presented, but also the impacts of associated changes in heat flux and freshwater transport on the AMOC are investigated separately. Two additional transient experiments are performed in this study: one changing the atmospheric heat budget according to the warming scenario with freshwater fluxes prescribed to the control experiment and a second one which prescribes the freshwater fluxes as in the warming experiment but keeping CO_2 and thus the heat fluxes constant. The constant freshwater flux experiment is used here to determine AOGCM-specific temperature scaling coefficient p and the constant heat flux experiment to calibrate the hydrological sensitivity h. Finally, the fully combined transient run is used to validate our calibration as shown in Sect. 3.

Table 1: List of the emulated AOGCMs.

Model:	Institute	Reference
GFDL R30	Geophysical Fluid Dynamics Laboratory, USA	(Delworth et al., 2002)
MRI CGCM2.3	Meteorological Research Institute, Japan	(Yukimoto and Noda, 2002)
MPI/ECHAM5	Max Planck Institute for Meteorology, Germany	(Jungclaus et al., 2006a)
MIROC3.2	University of Tokyo, Japan	(Hasumi and Emori, 2004)
NCAR CCSM2.0	National Center for Atmospheric Research,USA	(Kiehl and Gent, 2004)

The five AOGCMs that participated in both multi-model studies and that we used for our emulation approach are listed in Table 1. Also the HadCM3 AOGCM by the Hadley Centre for Climate Prediction and Research participated in both studies, but this model shows a large overshoot of the AMOC strength after recovery from the freshwater perturbation in Stouffer et al. (2006). This overshoot is dominated by a convective release of subsurface heat as reported in Mignot et al. (2007). Such changes in convection and the associated vertical thermal structure in the ocean can not be captured by the Stommel model, which is why we excluded the HadCM3 model from this study.

3 Calibration of the conceptual model to AOGCM overturning behaviour

As referred to above, the equilibrium state of our simple model is determined by four parameters, k, V_{eff}, λ and ΔT_0^*. To calibrate this parameter-set to the AOGCM outputs, the same freshwater perturbation experiment performed with the AOGCMs (see data Sect. 2) was computed with our emulation model and the parameter-set was manually optimised to reproduce each AOGCM output (Table 2). The AOGCM output (thin lines) and our emulated paths (thick lines) are presented in Fig. 2a. Starting values were taken from Zickfeld et al. (2004). The atmospheric coupling parameter λ varies by more than one order of magnitude between the models (Table 2), which emphasises the dominant role of heat fluxes in the global warming experiments in line with Gregory et al. (2005). However, the parameter values k, V_{eff}, λ and ΔT_0^* do not allow for more than a qualitative interpretation.

Table 2: Results of the parameter optimisation. Values are given in: k [$10^{18}\,\mathrm{m}^3\,\mathrm{a}^{-1}$], V_{eff} [$10^{-17}\,\mathrm{m}^3$], λ dimensionless, ΔT_0^* [K], p dimensionless and h [$\mathrm{Sv}\,\mathrm{K}^{-1}$].

	GFDL	MRI	MPI	MIROC	NCAR
k	3.55	1	1.1	1.05	1.14
V_{eff}	7.2	6	5	6	4.2
λ	0.032	0.185	0.7	0.16	0.02
ΔT_0^*	-3.8	-4	-2.75	-4.3	-5.5
p	0.4	0.1	0.2	0.45	0.9
h	0.019	0.038	0.013	0.013	-0.003

After the calibration to the equilibrium response the temperature scaling coefficient p and the hydrological sensitivity h are determined. In Gregory et al. (2005) the haline and thermal contributions to the AMOC weakening were separated, which can be used to independently determine the two parameters (Table 2). The thermal case, a scenario with a compounded 1% per year increase in the CO_2 concentration with freshwater fluxes prescribed as in the control experiment, is shown in Fig. 2b. To determine the haline contribution the CO_2-concentration is held constant and the time-varying freshwater flux of the warming scenario is applied (Fig. 2c). Please note that the NCAR CCSM2.0 model shows a nearly constant atmospheric freshwater transport and has therefore a near-zero hydrological sensitivity, which is captured by our emulation.

To test our calibrated conceptual model we emulated a compounded 1% per year CO_2 concentration increase scenario and compared it with the reference experiment from Gregory et al.
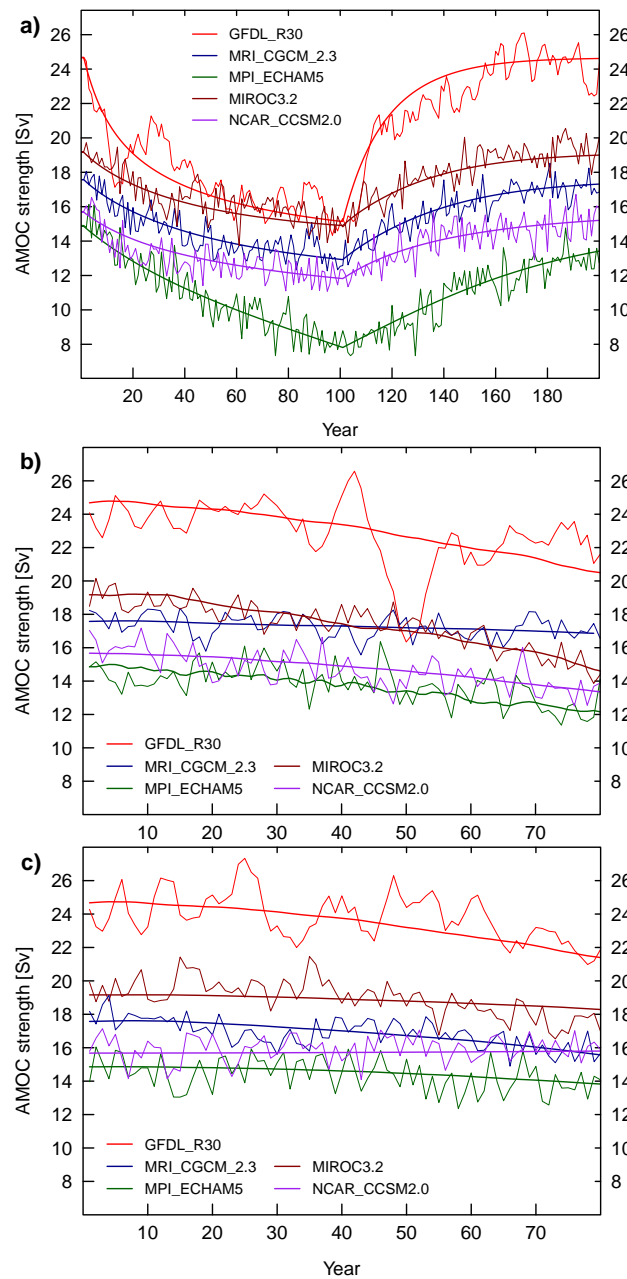
Figure 2: The results of the calibration procedure, the thin line represents the AOGCM output, the thick line the best fit results of our emulation. (**a**) The freshwater hosing experiment by Stouffer et al. (2006), where 0.1 Sv are artificial added in the Northern North Atlantic for 100 years starting in year 1. (**b**) The transient change in the AMOC strength as presented in Gregory et al. (2005) for a scenario with a compounded 1% per year increase in the CO_2 concentration, while the freshwater fluxes are kept constant. (**c**) The same scenario as in (**b**), but with constant CO_2-concentrations, whereas the freshwater fluxes of the full transient scenario are applied.

(2005). As it is shown in Fig. 3 our calibrated model outcome (thick line) is able to reproduce the AOGCM outcome (thin line) over the given time scale that corresponds to a warming below 3 °C in all models. We will use this calibrated emulation model in the next section to emulate low emission scenarios. This can be considered as an interpolation – we will not extrapolate to high emission scenarios, since these are not reached in the simulations used for the calibration and will push the system closer or beyond to the Stommel threshold. The Stommel equilibrium threshold is about 3 °C warming for our model ensemble.
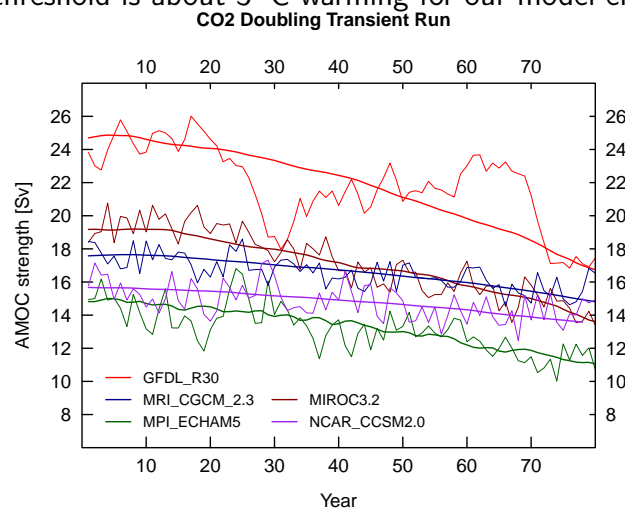
Figure 3: Comparison of the calibrated model outcome (thick line) with the AOGCM reference data for the 1% CO_2 increase scenario from Gregory et al. (2005) (thin line). Our emulation outcome reproduces the weakening trend of all five AOGCMs.

As shown in Fig. 3 AMOC behaviour differs strongly across the different emulated AOGCMs. The equilibrium AMOC strength ranges from 15 Sv for the MPI/ECHAM5 model to 25 Sv for GFDL R30 and also the transient response under the applied forcing differs significantly. Again the difference is highest between the GFDL R30 model and the MPI/ECHAM5: the first shows a strong weakening during the forcing period and a rapid recovery afterwards, whereas the latter shows a much slower recovery that is not fully completed within the 100 years time period. The uncertainty associated with single emulation parameters of the different models is much smaller than the inter AOGCM spread. Thus, we account for the major parametric uncertainty component when assuming all five emulator configurations obtained here as equally likely representations of the AMOC.

4 Emulating the overturning under global warming scenarios

In order to project the mean AMOC behaviour under global warming we combine each calibrated conceptual model (representing the AMOC behaviour of different AOGCMs) with the probabilistic temperature evolutions as obtained from an historically constrained MAGICC6 version (Meinshausen et al., 2009) for future RCP scenarios.
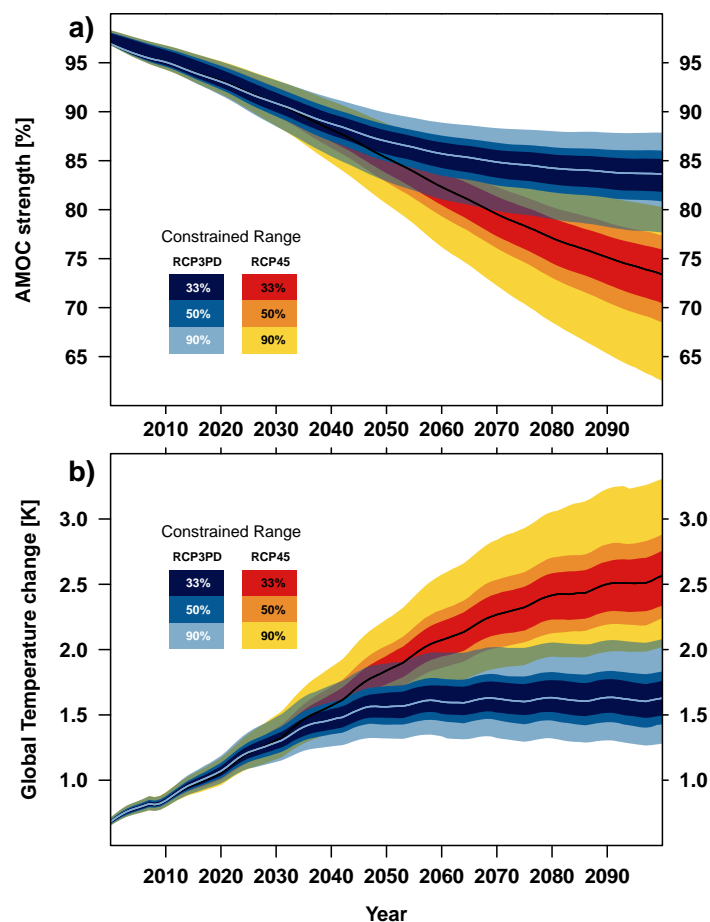

Figure 4: Probabilistic future projections for the RCP3-PD and RCP4.5 scenario relative to the year 2000. **(a)** AMOC **(b)** Corresponding global mean temperature obtained from the MAGICC6 model emulating IPCC AR-4 models.

More specifically, we use 600 random drawings out of a 82-dimensional joint parameter distribution, randomly combined with 10 emulations of C4MIP carbon cycle response characteristics (Friedlingstein et al., 2006), to project global-mean temperatures. Results for the harmonised

emissions scenarios of RCP3-PD and RCP4.5 are shown in Fig. 4b. We then combine each of the 600 realisations with each of our five models leading to 3000 different AMOC mean pathways that are considered equally likely. In order to stay within the calibrated range of temperature and freshwater changes, we performed projections only for these low scenarios RCP3-PD and RCP4.5.

Even though the thermal and haline contributions are very different between the five different models (compare the temperature scaling coefficient p and the hydrological sensitivity h in Table 2), the relative AMOC reduction under global warming is similar. For the RCP3-PD scenario the ensemble median (Fig. 4a blue curve) shows a median weakening of about 11% with respect to the year 2000 with a 50% constrained range between 9 and 14%. Note that this constrained range comprises the uncertainty in the temperature projections and also the ensemble spread. The RCP4.5 scenario results in a stronger weakening of about 22% in the five model ensemble (Fig. 4b red curve) with a 50% constrained range between 18 and 24%. The inter AOGCM spread for the RCP4.5 scenario is about 6 % (compare Fig. S1) , which is the major uncertainty component compared to the uncertainty of the individual model parameters. Our results are in very good agreement with a historical constrained Bayesian model study by Urban and Keller (2010), where a weakening of 17% is projected for a 21st century warming of 1.5 K.

5 Accounting for meltwater influx from Greenland

The AOGCM simulations of the CO_2 quadrupling scenario used for calibration do not account for possible melt water runoff from Greenland, but since we calibrated our model with absolute freshwater fluxes (see the calibration Sect. 3), we can now additionally investigate the effect of Greenland melting on the AMOC within the calibrated range of our model. The amount of Greenland meltwater runoff is one of the major sources of uncertainty e.g. in projections of global sea-level rise until 2100 (Gregory and Huybrechts, 2006). In particular the role of outlet glacier melting remains unclear. Recent findings suggest a strong acceleration of this melting in Southern Greenland (e.g. Rignot et al., 2010, and references therein). Pfeffer et al. (2008) assessed the maximum ice discharge from Greenland through kinematic constraints. In their assessment the total Greenland contribution by 2100 is projected to be 16.5 cm for low-range sea-level rise (SLR) scenarios, for which they assume a doubling in the Greenland outlet glacier velocities within the next decade. Graversen et al. (2010) found 17 cm to be an upper bound using a dynamical ice-sheet model. Given these estimates we applied an additional freshwater

forcing corresponding to a contribution of Greenland to global sea-level rise by 2100 of 10, 16.5 and 20 cm. Following Rahmstorf and Ganopolski (1999) we assumed a linear increase in the meltwater flux with global mean temperature change, which results in maximum freshwater fluxes of 14 mSv, 23 mSv and 28 mSv for the different SLR-contributions between 2090 and 2100.

Figure 5 shows the probabilistic projected ensemble medians for the RCP3-PD (left) and RCP4.5 (right) emission scenarios and the different Greenland freshwater forcings. The additional weakening with regard to the control run (red curve) is similar for both emission scenarios (4% and 9% for RCP3-PD and 4.5% and 10% for RCP4.5 and 10 and 20 cm, respectively), even though the absolute AMOC weakening is much stronger in the RCP4.5 scenario. Similar experiments have been performed by (Jungclaus et al., 2006b), who found an additional AMOC weakening of 5% by 2100 for the A1B emission scenario and 10 cm SLR contribution in the MPI/ECHAM5 AOGCM.
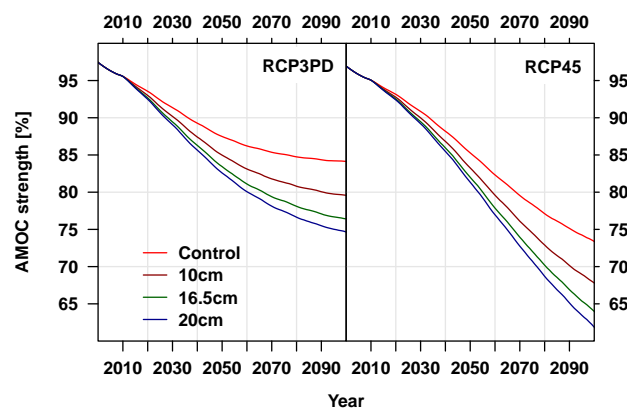
Figure 5: Projections of the probabilistic ensemble median AMOC-reduction for different Greenland meltwater influx scenarios for the RCP3-PD (left) and the RCP4.5 (right) emission pathway. Additional freshwater forcings correspond to 10, 16.5 and 20 cm Greenland contribution to global SLR by 2100.

We would like to highlight the conceptual nature of our experiment. In reality the Greenland meltwater flux is not uniformly applied over the whole northern North Atlantic and therefore the interaction with horizontal circulations can not be neglected as it has been also emphasised in Jungclaus et al. (2006b). Recent findings even suggest that the sub-polar gyre in the North Atlantic shows strong nonlinear behaviour with regard to regional freshwater forcings (Levermann and Born, 2007), probably influencing the AMOC behaviour (Montoya et al., 2010).

6 Projections of dynamic sea-level rise along the east coast of North America

Associated with an AMOC weakening are major changes in the sea-level patterns in the Atlantic, particularly a distinct rise in the North Atlantic (Levermann et al., 2005). While dynamic sea-level rise (SLR) is not spatially uniform and and might be even negative in the sub-polar gyre region (Landerer et al., 2007), it is robustly projected to be especially pronounced at the north-eastern coast of North America over an ensemble of the 12 AR4 models that perform best reproducing present-day sea-level (Yin et al., 2010). The linear dependence of the dynamic sea-level rise (DSLR) in the New York City region on the AMOC weakening as applied here was reported by Yin et al. (2009). The CMIP-3 model ensemble analysed by Yin et al. (2009) and associated linear regression results are shown in Table 3. The slopes of the different models scatter around 2 cm DSLR per Sv AMOC weakening, which compares well to observational data (Bingham and Hughes, 2009).

Table 3: Results of a linear regression of DSLR vs. AMOC weakening ($y = ax + b$) for a AR4 model ensemble derived from SRES A1B scenario runs and for the grid-point closest to NYC from (Yin et al., 2009)

	a [cm/Sv]	b [cm]
GFDL CM2.1	1.68 ± 0.08	3.30 ± 0.56
MIROC MEDRES	2.81 ± 0.14	1.95 ± 0.62
MPI ECHAM5	2.74 ± 0.26	2.63 ± 0.65
IPSL CM4	2.58 ± 0.15	2.32 ± 0.67
MIROC HIRES	1.45 ± 0.21	4.01 ± 0.59

To account for the uncertainty of the linear regression parameters shown in Table 3, we randomly picked a value out of a Gaussian distribution with a standard deviation of the parameter uncertainty and combined it for each of the five models with our 3000 AMOC representations. Thus, we provide probabilistic projections of the mean dynamic sea-level rise in the New York City region (Fig. 6).

While Greenland melting will have significant effect on global sea-level, its impact on regional sea-level along the North American east coast has been shown to be small due to gravitational and rotational adjustments (Mitrovica et al., 2001; Kopp et al., 2010). Thus, Fig. 6 represents an estimate of the full sea-level change in the area due to non-tectonic effects excluding contributions from Antarctica. We find a median DSLR of 4 cm for the RCP3-PD and 8 cm for the RCP4.5 scenario with a 50% confined range of 2.8 to 5.7 and 5 to 11 cm, respectively.

While the initial spread of $\pm$ 0.5 cm reflects the uncertainty of the offset parameter b, the 2100 ranges are dominated by the inter-AOGCM spread with AOGCM specific parameter uncertainties being of minor importance. For the higher SRES A1B scenario Yin et al. (2009) report an AMOC slow-down of 41% for the GFDL CM2.1 and a multi-model median dynamic sea-level rise of about 20 cm.
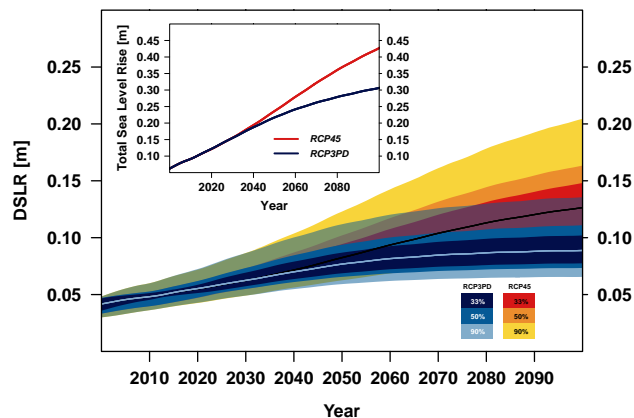

Figure 6: Probabilistic projections of the mean dynamic sea-level rise at the New York City coastline for the RCP3-PD (blue) and the RCP4.5 (orange) emission pathway until 2100. We project a median dynamic sea-level rise of 4 cm for the RCP3-PD and 8 cm for the RCP4.5 scenario. Inlay: Estimates of the steric and dynamic sea-level rise at the New York City coastline by combining our projections with simulations for the global steric sea-level rise by Schewe et al. (2010).

7 Conclusions

In this paper we expanded the idea of emulating complex model output by computationally efficient models of low complexity to the Atlantic Meridional Overturning Circulation and its behaviour under moderate global warming. In a conceptual approach we used a Stommel model for the AMOC consisting only of two boxes and a simple atmospheric coupling. The transient model behaviour can be calibrated by a set of six parameters including hydrological sensitivity and a temperature scaling coefficient to account for changes in the atmospheric forcing in terms of global mean temperature change. We calibrated different versions of our conceptual model to represent the outcome of five AOGCMs that participated in the multi-model studies by Stouffer et al. (2006) and Gregory et al. (2005) and performed probabilistic projections of the AMOC slow-down by 2100 using probabilistic projections of the global mean temperature

change for the RCP3-PD and the RCP4.5 emission pathways obtained by MAGICC6. In the five model ensemble median the AMOC weakened by 11% for the RCP3-PD and by 22% for the RCP4.5 scenario.

The calibration of our emulation model to AOGCM data was successful for the documented range until 2100 and low emission scenarios. However, there are numerous limitations of our simple model. Since we assumed a purely density driven AMOC with a volume transport that scales linearly with the density gradient between the boxes, the Stommel box model shows a bistability with regard to freshwater forcing and strong nonlinear behaviour close to the bifurcation point that can not be identified in the AOGCM output data.

The conceptual model omits low latitude upwelling and southern ocean winds as important drivers of the AMOC (Toggweiler and Samuels, 1995). Including them leads to a much more complex dependence of the meridional volume transport on the density gradient (Levermann and Fürst, 2010), but could help to extend our approach also to high emission – high warming scenarios (Fürst and Levermann , 2012). This model limitation does not effect the results presented in this work, since all projections performed are interpolations inside the calibration range.

Our calibration to absolute freshwater fluxes allowed us to investigate the impact of meltwater fluxes from Greenland on the AMOC, an aspect not included in the reference AOGCM experiments. We performed probabilistic projections for three different freshwater forcings that would correspond to 10, 16.5 and 20 cm Greenland contribution to SLR by 2100 and found additional reductions of the AMOC strength of 4, 7.5 and 9% for the RCP3-PD scenario and slightly higher for the RCP4.5. Being aware of the limitations of these projections that do not account for the dynamics of the horizontal circulation in the North Atlantic, they can nevertheless hold as a first estimate of the effect of Greenland melting on the AMOC until the end of the century.

Using a multi-model sea-level rise study by Yin et al. (2009), we were able to extend our probabilistic projections to investigate the impact of the AMOC slow-down on the dynamic sea-level rise in the New York City region as an example of an impact assessment. We find 4 cm of dynamic sea-level rise for the RCP3-PD and 8 cm for the RCP4.5 scenario. This probabilistic projection of dynamic sea-level rise is an example for the potential of a modular approach in climate system projections within the limits of interpolation. Simulations performed with a climate model of intermediate complexity show a global steric sea-level rise in the 21st century of about 20 cm for the RCP3-PD and 28 cm for the RCP4.5 emission pathway with regard to the year 2000 (Schewe et al., 2010), which is close to the upper 95% percentile provided in

IPCC AR4 for the similar SRES B1 scenario (Meehl et al., 2007). These numbers combine to a dynamic and steric sea-level rise of 24 and 36 cm in the New York City region (Fig. 6, inlay).

Remarkably, the combined steric and dynamic sea-level rise decelerates already in the 21st century for the lowest emission pathway RCP3-PD (compare Fig. 6, inlay), which is consistent with the evolution of the global mean temperature that reaches its maximum around 2060 (Fig. 4b). Nevertheless, sea-level responds slowly to global warming and continues to rise until the 23rd century for this emission pathway (Schewe et al., 2010).

In summary, we presented a probabilistic assessment of the future AMOC behaviour using a calibrated conceptual model and global mean temperature data for the RCP3-PD and RCP4.5 emission scenarios. Additionally, we extended our modular approach to investigate the influence of Greenland meltwater fluxes on the AMOC and to project dynamic sea-level rise in the New York City region. Our finding of 24 cm combined dynamic and steric sea-level rise for the RCP3-PD emission pathway can be interpreted as a lower bound for the total sea-level rise at the New York City coastline until 2100.

8 Acknowledgements

Literature

Bingham, R. J. and Hughes, C. W.: Signature of the Atlantic meridional overturning circulation in sea level along the east coast of North America, Geophys. Res. Lett., 36, L02603, doi:10.1029/2008GL036215, 2009.

Challenor, P.G. and Hankin, R.K.S. and Marsh, R.: Towards the probability of rapid climate change, Avoiding dangerous climate change,55–63,2006.

Challenor, P. and McNeall, D. and Gattiker, J.:Assessing the probability of rare climate events, The Oxford handbook of applied Bayesian analysis, Oxford Univ Pr,403–430,2010.

Collins, M. and Booth, B.B.B. and Harris, G.R. and Murphy, J.M. and Sexton, D.M.H. and Webb, M.J.: Towards quantifying uncertainty in transient climate change, Clim. Dyn., 27, 2, 127–147, 2006.

Delworth, T., Stouffer, R., Dixon, K., Spelman, M., Knutson, T., Broccoli, A., Kushner, P., and Wetherald, R.: Review of simulations of climate variability and change with the GFDL R30 coupled climate model, Clim. Dynam., 19, 555–574, 2002.

Dijkstra, H., Raa, L., and Weijer, W.: A systematic approach to determine thresholds of the ocean's Thermohaline circulation, Tellus A, 56, 362–370, 2004.

Drijfhout, S. S., Weber, S. L., and van der Swaluw, E.: The stability of the MOC as diagnosed from model projections for pre-industrial, present and future climates, Clim. Dynam., in press, doi:10.1007/s00382-010-0930-z, 2010.

Friedlingstein, P., Cox, P., Betts, R., Bopp, L., von Bloh, W., Brovkin, V., Cadule, P., Doney, S., Eby, M., Fung, I., Bala, G., John, J., Jones, C., Joos, F., Kato, T., Kawamiya, M., Knorr, W., Lindsay, K., Matthews, H., Raddatz, T., Rayner, P., Reick, C., Roeckner, E., Schnitzler, K.-G., Schnur, R., Strassmann, K., Weaver, K., Yoshikawa, C., and Zeng, N.: Climate Carbon Cycle Feedback Analysis: Results from the C4MIP Model Intercomparison, J. Climate, 19, 3337–3353, 2006.

Fürst, J., Levermann, A.: A minimal model for wind- and mixing-driven overturning - threshold behaviour for both driving mechanisms, Clim. Dynam., 37, online first, 2012.

Giorgi, F.: A simple equation for regional climate change and associated uncertainty, J. Climate, 21, 1589–1604, 2008.

Gnanadesikan, A.: A simple predictive model for the structure of the oceanic pycnocline, Science, 283, 2077–2079, 1999.

Graversen, R. G., Drijfhout, S., Hazeleger, W., Wal, R., Bintanja, R., and Helsen, M.: Greenland's contribution to global sea-level rise by the end of the 21st century, Clim. Dynam., in press, doi:10.1007/s00382-010-0918-8, 2010.

Gregory, J. M. and Huybrechts, P.: Ice-sheet contributions to future sea-level change, Philos. T. Roy. Soc. A, 364, 1709–1731, 2006.

Gregory, J. M., Dixon, K. W., Stouffer, R. J., Weaver, A. J., Driesschaert, E., Eby, M., Fichefet, T., Hasumi, H., Hu, A., Jungclaus, J. H., Kamenkovich, I. V., Levermann, A., Montoya, M., Murakami, S., Nawrath, S., Oka, A., Sokolov, A. P., and Thorpe, R. B.: A model intercomparison of changes in the Atlantic thermohaline circulation in response to increasing atmo-

spheric CO$_2$ concentration, Geophys. Res. Lett., 32, L12703, doi:10.1029/2005GL023209, 2005.

Griesel, A. and Morales-Maqueda, M. A.: The relation of meridional pressure gradients to North Atlantic Deep Water volume transport in an OGCM, Clim. Dynam., 26, 781–799, 2006.

Guan, Y. P. and Huang, R. X.: Stommel's Box Model of Thermocline Circulation Revisited – The Role of Mechanical Energy Supporting Mixing and the Wind-Driven Gyration, J. Phys. Oceanogr., 38, 909–917, 2008.

Hasumi, H. and Emori, S.: K-1 coupled model (MIROC) description, Center for Climate System Research, University of Tokyo, K-1 Tech. Rep., 1, 34, 2004.

Hargreaves, JC and Annan, JD and Edwards, NR and Marsh, R.: An efficient climate forecasting method using an intermediate complexity Earth System Model and the ensemble Kalman filter, Cim. Dyn, 23, 7, 745–760, 2004

Hughes, T. M. C. and Weaver, A. J.: Multiple Equilibria of an Asymmetric Two-Basin Ocean Model, J. Phys. Oceanogr., 24, 619–637, 1994.

Jungclaus, J. H., Botzet, M., Haak, H., Marotzke, J., Mikolajewicz, U., Roeckner, E., Keenly-side, N., Latif, M., and Luo, J. J.: Ocean circulation and tropical variability in the coupled model ECHAM5/MPI-OM, J. Climate, 19, 3952–3972, 2006a.

Jungclaus, J. H., Haak, H., Esch, M., Roeckner, E., and Marotzke, J.: Will Greenland melting halt the thermohaline circulation?, Geophys. Res. Lett., 33, L17708, doi:10.1029/2006GL026815, 2006b.

Kiehl, J. and Gent, P.: The community climate system model, version 2, J. Climate, 17, 3666–3682, 2004.

Klinger, B. A. and Marotzke, J.: Behavior of Double-Hemisphere Thermohaline Flows in a Single Basin, J. Phys. Oceanogr., 29, 382–399, 1999.

Knutti, R. and Stocker, TF and Joos, F. and Plattner, G.K.:Probabilistic climate change projections using neural networks, Clim. Dyn.,21,3,257-272,2003.

Kopp, R. E., Mitrovica, J. X., Griffies, S. M., Yin, J., Hay, C. C., and Stouffer, R. J.: The impact of Greenland melt on local sea levels: a partially coupled analysis of dynamic and static equilibrium effects in idealized water-hosing experiments, Climatic Change, 103, 619–625, 2010.

Kuhlbrodt, T., Griesel, A., Montoya, M., Levermann, A., Hofmann, M., and Rahmstorf, S.: On the driving processes of the Atlantic meridional overturning circulation, Rev. Geophys., 45, RG2001, doi:10.1029/2004RG000166, 2007.

Landerer, F. W., Jungclaus, J. H., and Marotzke, J.: Regional Dynamic and Steric Sea Level Change in Response to the IPCC-A1B Scenario, J. Phys. Oceanogr., 37, 296–312, 2007.

Laurian, A., Drijfhout, S. S., Hazeleger, W., and Hurk, B.: Response of the Western European climate to a collapse of the thermohaline circulation, Clim. Dynam., 34, 689–697, 2009.

Levermann, A. and Born, A.: Bistability of the subpolar gyre in a coarse resolution climate model, Geophys. Res. Lett., 34, L24605, doi:10.1029/2007GL031732, 2007.

Levermann, A. and Fürst, J.: Atlantic pycnocline theory scrutinized using a coupled climate model, Geophys. Res. Lett., 37, L14602, doi:10.1029/2010GL044180, 2010.

Levermann, A., Griesel, A., Hofmann, M., Montoya, M., and Rahmstorf, S.: Dynamic sea level changes following changes in the thermohaline circulation, Clim. Dynam., 24, 347–354, 2005.

Manabe, S. and Stouffer, R. J.: Multiple-century response of a coupled ocean-atmosphere mocel to an increase of atmospheric carbon dioxide, J. Climate, 7, 5–23, 1994.

McManus, J. F., Francois, R., Gherardi, J. M., Keigwin, L. D., and Brown-Leger, S.: Collapse and rapid resumption of Atlantic meridional circulation linked to deglacial climate changes, Nature, 428, 834–837, 2004.

Meehl, G. A., Stocker, T. F., Collins, W. D., Friedlingstein, P., Gaye, A. T., Gregory, J. M., Kitoh, A., Knutti, R., Murphy, J. M., Noda, A., Raper, S. C. B., Watterson, I. G., Weaver, A. J., and Zhao, Z.-C.: Climate Change 2007: The Physical Science Basis, Contribution of Working Group I to the Fourth Assessment Report of the Intergovernmental Panel on Climate Change, chap. Global Climate Projections, Cambridge University Press, Cambridge, UK and New York, NY, USA, 2007.

Meinshausen, M., Raper, S. C. B., and Wigley, T. M. L.: Emulating coupled atmosphere-ocean and carbon cycle models with a simpler model, MAGICC6: Part I - Model Description and Calibration, Atmos. Chem. Phys., 11, 1417,2011

Meinshausen, M., Raper, S. C. B., and Wigley, T. M. L.: Emulating coupled atmosphere-ocean and carbon cycle models with a simpler model, MAGICC6: Part 2 - Applications, Atmos. Chem. Phys., 11, 1457,2011

Meinshausen, M., Meinshausen, N., Hare, W., Raper, S. C. B., Frieler, K., Knutti, R., Frame, D. J., and Allen, M. R.: Greenhouse-gas emission targets for limiting global warming to 2 °C, Nature, 458, 1158–1162, 2009.

Mignot, J., Ganopolski, A., and Levermann, A.: Atlantic subsurface temperatures: response to a shut-down of the overturning circulation and consequences for its recovery, J. Climate, 20, 4884–4898, 2007.

Mitchell, T.: Pattern scaling: an examination of the accuracy of the technique for describing future climates, Climatic Change, 60, 217–242, 2003.

Mitrovica, J. X., Tamisiea, M. E., Davis, J. L., and Milne, G. A.: Recent mass balance of polar ice sheets inferred from patterns of global sea-level change, Nature, 409, 1026–1029, 2001.

Montoya, M., Born, A., and Levermann, A.: Reversed North Atlantic gyre dynamics in present and glacial climates, Clim. Dynam., in press, doi:10.1007/s00382-009-0729-y, 2010.

Pfeffer, W. T., Harper, J. T., and O'Neel, S.: Kinematic Constraints on Glacier Contributions to 21st-Century Sea-Level Rise, Science, 321, 1340–1343, 2008.

Rahmstorf, S.: On the freshwater forcing and transport of the Atlantic thermohaline circulation, Clim. Dynam., 12, 799–811, 1996.

Rahmstorf, S. and Ganopolski, A.: Long-term global warming scenarios computed with an efficient coupled climate model, Climatic Change, 43, 353, 1999.

Rahmstorf, S., Crucifix, M., Ganopolski, A., Goosse, H., Kamenkovich, I., Knutti, R., Lohmann, G., Marsh, B., Mysak, L. A., Wang, Z., and Weaver, A.: Thermohaline circulation hysteresis: A model intercomparison, Geophys. Res. Lett., 32, L23605, doi:10.1029/2005GL023655, 2005.

Rignot, E., Koppes, M., and Velicogna, I.: Rapid submarine melting of the calving faces of West Greenland glaciers, Nat. Geosci., 3, 187–191, 2010.

Schewe, J. and Levermann, A.: The role of meridional density differences for a wind-driven overturning circulation, Clim. Dynam., 34, 547–556, 2010.

Schewe, J., Levermann, A., and Meinshausen, M.: Climate change under a scenario near 1.5 °C of global warming: monsoon intensification, ocean warming and steric sea level rise, Earth System Dynamics 2, 25-35, 2011

Schmittner, A.: Decline of the marine ecosystem caused by a reduction in the Atlantic overturning circulation, Nature, 434, 628–633, 2005.

Stommel, H.: Thermohaline convection with two stable regimes of flow, Tellus, 13, 224–230, 1961.

Stouffer, R. J., Yin, J., Gregory, J. M., Dixon, K. W., Spelman, M. J., Hurlin, W., Weaver, A. J., Eby, M., Flato, G. M., Hasumi, H., Hu, A., Jungclaus, J. H., Kamenkovich, I. V., Levermann, A., Montoya, M., Murakami, S., Nawrath, S., Oka, A., Peltier, W. R., Robitaille, D. Y., Sokolov, A. P., Vettoretti, G., and Weber, S. L.: Investigating the Causes of the Response of the Thermohaline Circulation to Past and Future Climate Changes, J. Climate, 19, 1365–1387, 2006.

Toggweiler, J. R. and Samuels, B.: Effect of Drake Passage on the global thermohaline circulation, Deep-Sea Res., 42, 477–500, 1995.

Toggweiler, J. R. and Samuels, B.: On the ocean's large scale circulation in the limit of no vertical mixing, J. Phys. Oceanogr., 28, 1832–1852, 1998.

Urban, N.M. and Keller, K.: Probabilistic hindcasts and projections of the coupled climate, carbon cycle, and Atlantic meridional overturning circulation system: A Bayesian fusion of century-scale observations with a simple model, Tellus A, 62, 737–750, 2010

Vellinga, M. and Wood, R. A.: Global climatic impacts of a collapse of the Atlantic Thermohaline Circulation, Climatic Change, 54, 251–267, 2002.

Vellinga, M. and Wood, R. A.: Impacts of thermohaline circulation shutdown in the twenty-first century, Climatic Change, 91, 43–63, 2007.

Wigley, T. M. L. and Raper, S. C. B.: Interpretation of high projections for global-mean warming, Science, 293, 451–454, 2001.

Yin, J., Schlesinger, M. E., and Stouffer, R. J.: Model projections of rapid sea-level rise on the northeast coast of the United States, Nat. Geosci., 2, 262–266, 2009.

Yin, J., Griffies, S., and Stouffer, R. J.: Spatial Variability of Sea Level Rise in Twenty-First Century Projections, J. Climate, 23, 4585–4607, 2010.

Yukimoto, S. and Noda, A.: Improvements of the Meteorological Research Institute global ocean-atmosphere coupled GCM (MRI-CGCM2) and its climate sensitivity, CGER's Supercomputer Activity Rep., Vol. 10, National Institute for Environmental Studies, Tsukuba, Japan, 37–44, 2002.

Zickfeld, K. and Bruckner, T.: Reducing the risk of Atlantic thermohaline circulation collapse: sensitivity analysis of emissions corridors, Climatic Change, 91, 291–315, 2008.

Zickfeld, K., Slawig, T., and Rahmstorf, S.: A low-order model for the response of the Atlantic thermohaline circulation to climate change, Ocean Dynam., 54, 8–26, 2004.

Chapter 7 Greenland

Surface Mass Balance Changes
in Greenland and their Probability

N. Braun [1,2,3]   [1] PRIMAP Research Group, Earth System Analysis, Potsdam Institute for Climate Impact Research e.V.

[2] Technical University Berlin

[3] currently at Ecofys GmbH, Germany

Abstract

Quantification of uncertainties in future global climate projections is crucial for the development of emission mitigation and adaptation polices. Although the last report of the Intergovernmental Panel on Climate Change (IPCC) rated the calculated changes as likely there are uncertainties which have to be quantified. The probabilistic assessment of the projections is one possibility to do so. In this thesis, the approach was combined with two existing surface-mass balance (SMB) models and applied to determine the level and the probability of exceeding the 'Tipping Point' of the Greenland ice-sheet (GIS). In case the whole ice sheet would disappear completely, the global sea level would rise between 6 to 7 m. For a global temperature change of 4°C it is very likely (100%) that the 'Tipping Point' would be exceeded and a starts an irreversible ablation process. It is very likely that these 4°C will be exceeded until the end of this century if the current CO_2 emission would be tripled. And with a probability of 40% (for surface mass-balance modell 1) to 73% (for surface mass-balance modell 2) for doubling the current emissions. Changes in dynamics of the Ice-Sheets (e.g. mass losses through iceberg discharges) were not considered and would modify these results. The losses through the dynamic effects are estimated to be as high as the current mass loss through surface mass-balance.

Zusammenfassung

Für politische Entscheidungsträger ist oft die Information über die Klimaveränderung und den modllierten regionalen Auswirkungen alleine nicht hilfreich. Auch wenn der letzte Bericht des Intergovernmental Panel on Climate Change (IPCC) die dort berechneten zukünftige Temperatur Änderungen als sehr warscheinlich einstuft gibt es Unsicherheiten die quantifiziert werden müssen. Die Warscheinlichkeitstheoretische Bewertung der Veränderungen ist eine seit diesem Bericht gängige Methode dafür. In dieser Arbeit wurde diese Methode mit zwei Massenbilanzmodellen angewandt um die Höhe und Warscheinlichkeit eines Kipp-Punktes für das grönländische Eisschild zu ermitteln. Ein vollständiges Abschmelzen des Grönländischen Eisschilds würde zu einem globalen Meeresspiegelanstieg von 6 bis 7 m führen. Bei einer globalen Temperaturänderung von $4°C$ ist es sehr warscheinlich das der Kipp-Punkt erreicht wird und ein Abschmelzprozess in Gang gesetzt wird der sich in Zukunft weiter beschleunigen wird. Diese $4°C$ werden mit einer 100%igen Warscheinlichkeit noch in diesem Jahrhundert erreicht, wenn die momentanen Emissionen verdreifacht werden. Und mit einer Warscheinlichkeit von 40% (Modell 1) bis 73% (Modell 2) bei einer Verdopplung der aktuellen Emissionen. Bei diesen Berechnungen sind die Verluste durch dynamische Veränderungen des Eisschildes (z.B. Masseverluste durch das Ablösen von Eisbergen) noch gar nicht einberechnet, die fast nochmal das Doppelte ausmachen können.

1. Climate of Greenland

The Greenland Ice Sheet (GIS) belongs to the arctic climate region. This climate is defined by a low amount or absence of sunlight in winter and long days during summer, with significant spatial and temporal variation. Therefore the Arctic is a collection of regional climates with different ecological and physical climatic characteristics (Berner et al., 2005).

Greenland has a population of 57600 people; most of them living in the South. Despite the small number of inhabitants, Greenland has a crucial role in the world's climate. The Greenland cryosphere, the GIS, covers an area about 80%, more precisely $1.7 * 10^6\ km^2$. The ice surface reaches its greatest altitude on two north-south connected domes, or saddles. The southern dome reaches almost 3000 metres at latitudes 63° - 65°N; the northern dome reaches about 3290 metres at about latitude 72°N. The peaks of both domes are displaced to the East of the centre line of Greenland. The average thickness is around 1600 metres, with a total volume of ca. $3 * 10^6\ km^3$, which is equivalent to a sea-level rise of about 7.3 m (Bamber and Payne, 2004).

Another feature of the region around Greenland is the North Atlantic Drift[1], a northern continuation of the Gulf Stream. This circulation plays a major role in heat transport to the northern latitudes and is mainly driven by density differences.

The highest surface water densities are reached in cold regions; this causes convective mixing and sinking of deep water (Rahmstorf et al., 2005). This kind of circulation can be found in the South of Greenland with the Gulf Stream and regions of the North Atlantic deep water production to the East and West (see Figure 1) (Bamber and Payne, 2004).

According to the IPCC AR4 (Solomon et al., 2007), over the past few decades (see as well Figure 2), the average temperatures in the Arctic have risen at almost twice the rate as temperatures in the rest of the world. These climatic trends are projected to rise during this and upcoming centuries if the current greenhouse gas emission levels are rising.

For the arctic region it is projected, that there will be an additional warming of about 4 to 7°C over the next 100 years (ACIA, 2004). A warmer climate in the arctic region on and around Greenland implies a whole chain of consequences, both locally and worldwide:

- A melting of highly reflective arctic snow (around 80%) and ice reveals darker land and ocean surfaces, increasing absorption of the sun's heat and further warming of the planet.

---

[1]Thermohaline Circulation

Figure 1: This figure of Atlantic currents shows warmer surface currents (red) and cold north Atlantic Deep Water (NADW, blue). The thermohaline circulation heats the North Atlantic and Northern Europe. It extends right up to the Greenland and Norwegian Seas, pushing back the winter sea ice margin. (Source: Rahmstorf, S., Risk of sea-change in the Atlantic. Nature, 1997. 388: p. 825-826.)

- Increases of freshwater fluxes, due to acceleration of melting processes because of a warmer climate, could weakening the Thermohaline Circulation (THC) (Rahmstorf et al., 2005) and raise the global sea level.

- The biodiversity will be perturbed, especially by changing of sea-ice and eliminating of important breeding and feeding places

1.1. Local climate in Greenland

Ice-Core data taken from the summit of the GIS indicate that Greenland temperatures and accumulation rate changes can increase significantly over periods of a few years to decades (Alley et al., 1993). There are differences between climate in the North, South, East and West, due to the geography and the North Atlantic Drift.

The North Atlantic Drift gives the Southwest coast of Greenland a warmer climate and heavy rainfalls. Above the ice sheet, temperatures are generally substantially lower than on the margins and the coasts of Greenland. The lowest average annual temperatures, of -31°C, occur on the North-central part of the North dome, and average temperatures at the summit of the South dome are about -20°C. The temperatures can also be high, with average July temperatures of up to 5 and 6°C (Ohmura, 1997) in the South and on the coast, they can
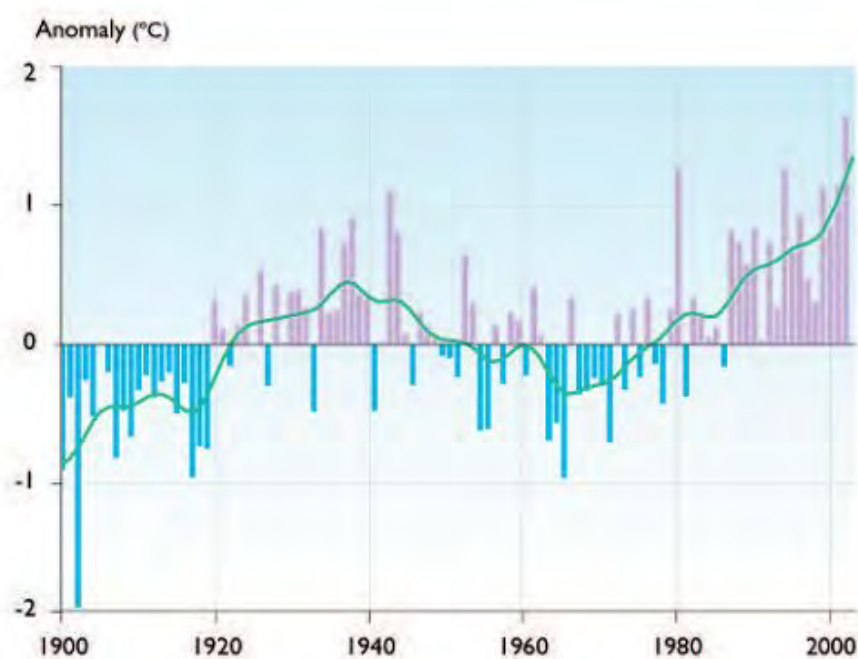
Figure 2: Annual anomalies of land-surface air temperature in the Arctic (60° to 90° N) using the GHCN dataset. Anomalies are calculated relative to the 1961 to 1990. The smoothed curve was created using a 21 point binomial filter, which approximates a 10 year running mean (ACIA, 2004).

lead to a widespread summer melting. The monthly average temperatures from 1973 to 2005 (Figure 3) for West coast and whole GIS, shows a rising trend. The data from 82 stations are provided by the National Climatic Data Center (NCDC [2]).
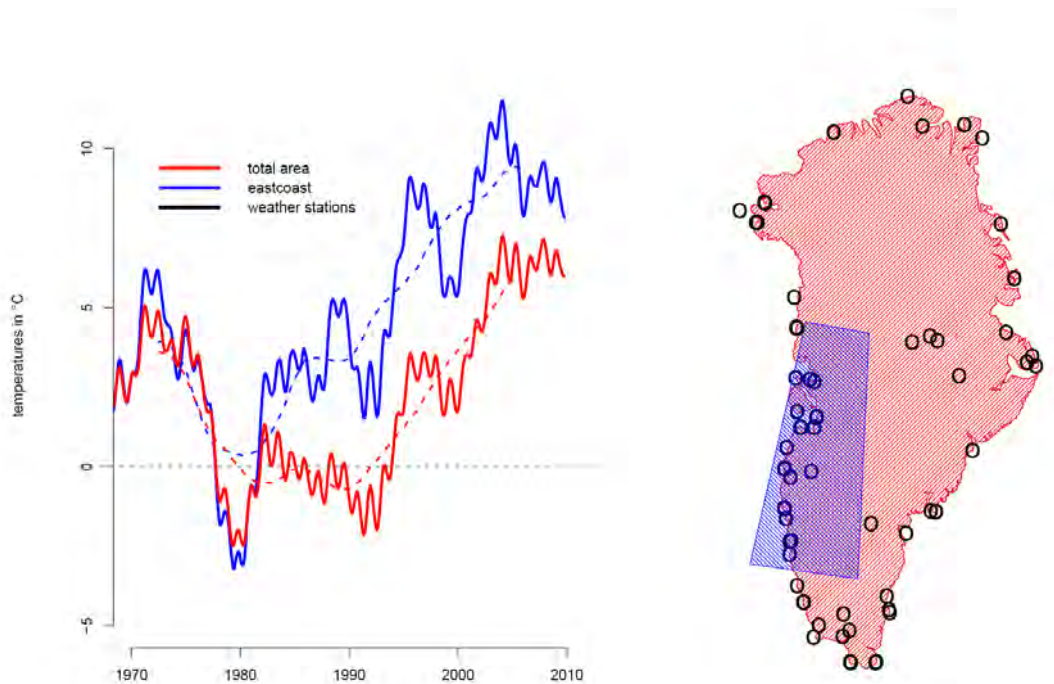
Figure 3: Comparison of West and total area Temperatures in Greenland. The dotted line is a 21-point binomial filtered curve which approximates monthly averages. On the right side, the map of Greenland shows the positions of all weather stations (black circles) considered for the calculation and the selected region on the West coast (own calculation, based on data from NCDC).

The consequences of the West coast climate are an earlier widespread summer melting with high accumulation rates and faster glaciers. One of the fastest moving glaciers is situated on the West coast, the Jacobshavn. This glacier (Figure 4) is flowing at its terminus at speeds of around 20 meters per day and have thinned by tens of meters per year during the last 5 to 15 years (Thomas et al., 2003).

Warming in Greenland is influenced by the sea-ice retreat. This has a strong effect in winter by replacing the cold surface by open ocean. In summer, the melting sea-ice will prevent sea surface temperatures from rising far above freezing point. Therefore the summer warming is less than the annual average, particularly on the coasts (Gregory and Huybrechts, 2006). The

---

[2]National Climatic Data Center ;http://www.ncdc.noaa.gov/oa/ncdc.html

trend in Figure 3 would turn to higher temperatures for the whole ice-sheet as for *Region 1*.

1.2. Precipitation Change

The general trend of precipitation over Greenland is a decrease of precipitation from South to North from about 2500 mm per year in the Southeast to less then 150 mm/y in the Northeast of Greenland. The moisture in the South is mainly determined by the Icelandic low and the resulting onshore flow (Huybrechts and Miller, 2005). Ohmura et al. (1999) gives an estimate for the average annual precipitation of about $297\ mm/y$. As a very typical feature for the arctic climate region, the precipitation rates over Greenland are relatively small. In fact, today's rates of precipitation are so small that the ice sheet would not exist today, if it would not already have existed and if its accumulation area would not be so large (Ohmura et al., 1999).
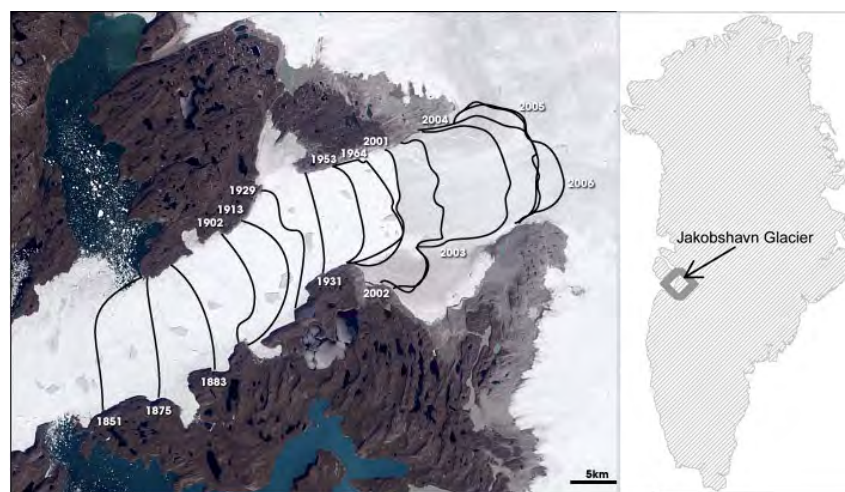

Figure 4: Retreating calving front of the Jacobshavn Isbrae glacier in Greenland from 1851-2006 (Source: NASA).

2. Modelling the Surface Mass Balance

To calculate the Surface Mass Balance (SMB) in Greenland, it is important to understand the physical and general features of ice sheets and glaciers. This chapter gives an overview of the relevant processes and scientific background for modelling the SMB. Additionally two methods for modelling future SMB changes will be introduced.

2.1. Defining surface mass balance (SMB)

The term 'mass balance' can be used in two ways with different meanings. The local or net surface mass balance (SMB) describes a specific point of the glaciers and is the sum of accumulation (the positive contribution to SMB) and ablation (the negative SMB change).

The SMB may be positive or negative depending on whether accumulation or ablation is dominating. However, the results of the SMB does not say anything about the local change of ice thickness or the local change of mass in a vertical column through the glacier. This is because the SMB may be compensated for, or even be overruled by mass input/loss due to a gradient of the horizontal flux (Hagen and Reeh, 2004).

The dominant process causing accumulation in Greenland is the snow fall; in lower parts of the GIS melt followed by runoff of the melt water is the dominant ablation process.

Other important processes are, evaporation (change from liquid to gas), condensation (change from gas to liquid), sublimation (change from gas to solid and vice versa), removal and deposition of snow by avalanches and wind and rain water that does not run off (capable to refreeze). In higher parts of the GIS sublimation forms the dominant contribution to ablation. All these processes are important for the scientific description of the dynamics of glaciers but because of limited computing capacity can not be considered in modelling in full detail.

In the following chapters the SMB is expressed in Gt/y (km^3/y) or (the most common unit) in mm water equivalent (mmWe). In many cases the interesting quantity is the change in mass over a year (annual SMB) the unit is mm/y (Greuell and Genthon, 2004).

The 'total mass balance' is defined as the total change in mass in a vertical column of glacier materials during an undefined period of time. Hence, the SMB is balanced by the ice discharge term. The main ice discharge losses in Greenland are resulting from calving of icebergs. This constitutes roughly 45 - 90% of the mass loss from the Greenland and Antarctic ice sheets. Iceberg calving accounts for the major mass loss from land-ice masses in the world, but

unfortunately, is still the term of the mass balance equation with the largest uncertainty.

2.2. The mathematical description of SMB

According to Hagen and Reeh (2004) the SMB at a point of a glacier is expressed by the following equation:

$$\partial H/\partial t = b_s + b_b - F[H(\partial u_s/\partial x + \partial v_s/\partial y) + u_s \partial H/\partial x] \tag{1}$$

where H = ice thickness, t = time, b_s and b_b are specific mass balances at the surface and bottom, u_s and v_s = horizontal components of the surface velocity (u_s is the description of flow) and $F = \overline{u}/u_s$ ($\overline{u}$ = depth-averaged velocity). The ice flow is assumed to be in x-direction. The total mass change of the glacier or the region of a glacier can be expressed by integrating either the local or specific mass balance over the total area of the glacier and subtracting the loss through possible vertical boundary surface such as calving fronts.

$$\Delta V = M_a - M_m - M_c \pm M_b \tag{2}$$

where ΔV = ice volume, M_a = the annual surface accumulation, M_m = the annual loss by glacial surface runoff, M_c = the annual loss by calving of icebergs, and M_b = the annual balance at the bottom (melting of freeze-on of ice). $M_a - M_m$ describes the SMB (Greuell and Genthon, 2004). Because of large uncertainties in the ice-discharge the only term considered in most models is the SMB term. Even the two models discussed in this thesis are dealing with the SMB term only.

2.3. Measurement of the Surface Mass Balance

The total mass balance and SMB as expressed in Equation 2 can be determined by three different methods: 1.) by direct measurement of the change in volume by monitoring surface elevation change (for the total mass balance) 2.) by the budget method, by which each term on the right hand side of the mass balance equation is determined separately (for both total mass balance and SMB) and the 3.) by the changes in gravity (e. g. GRACE project, is valid for the total mass balance).

The *direct measurement* contains different time and cost intensive methods. There is the traditional surveying method, where marked points on the glacier are surveyed from fix-points

outside the glaciers. The angles and distances are measured and thus point positions can be calculated. Although this method is time-consuming it can give very precise data. The cartographic method compares topographic maps from different years, e. g. digital elevation models. The size of errors depends on the accuracy of the maps derived from the geodetic network and the quality of aerial photos.

The cartographic method is more useful for monitoring long-term changes and spatial distribution of changes. Airborne measurements using laser ranging or radar sensors are applied in most studies. The so called 'Altimetry' methods contains furthermore satellite-borne lasers (Albertz, 2000). To the group of direct measurement belongs some more methods, like GPS tracking or the combined measurement of vertical velocity and snow accumulation ('coffee-can method') (Hagen and Reeh, 2004).

The second group is the *budget method*, that include measurement of the individual components of the total mass balance and the SMB. Particularly for determining the SMB, the budget method is an important approach. Changes in total mass balances can be a result of the individual components such as melting or accumulation rates, therefore it is necessary to observe these components. A large number of methods is used for the measurement: stake reading, index method, oxygen isotopes, automatic registration and radar. Every method is specialized on an individual component. The results of these measurements can be found in the database of the World Glacier Monitoring Service (WGMS).

The two important terms for determining the SMB are accumulation and ablation rates. Both terms are crucial for subsequently modelling of SMB changes. A wide range of measurement techniques is available for this purpose. *Stake reading* is a traditional method in mass balance monitoring. This method is based on a dense array of point measurements on the surface, of stakes drilled into the ice. This stake net can be used for winter snow accumulation and for summer ablation measurements. Additionally density measurements through snow pits or shallow cores are carried out. An example for an ablation stake is shown in Figure 5. Snow accumulation pattern can be obtained by snow probing. The results of the measured ablation and accumulation rates are drawn as equal balances as contour lines and then integrated on the whole glacier area. For large areas like the GIS it is very difficult to cover the entire area by traditional stake measurements, therefore it is better to use spot measurements, also known as *index method*. One possibility to make a representative measurement is to use a balance/elevation integration in which a single line of poles is placed from the lower to the highest part of the glacier. In each altitude the accumulation and ablation is measured by the traditional stake method (Hubbard and Glasser, 2005).

The determination of the density is an important issue for the mass balance and is required to transform snow accumulation depths into comparable water equivalent units. For lower depths (as density informations from the previous year for example) snow pits are applied where a known volume of sample is weighed are applied. Snow/firn[3] cores are taken for deeper density profiles (Mayer and Oerter, 2006).
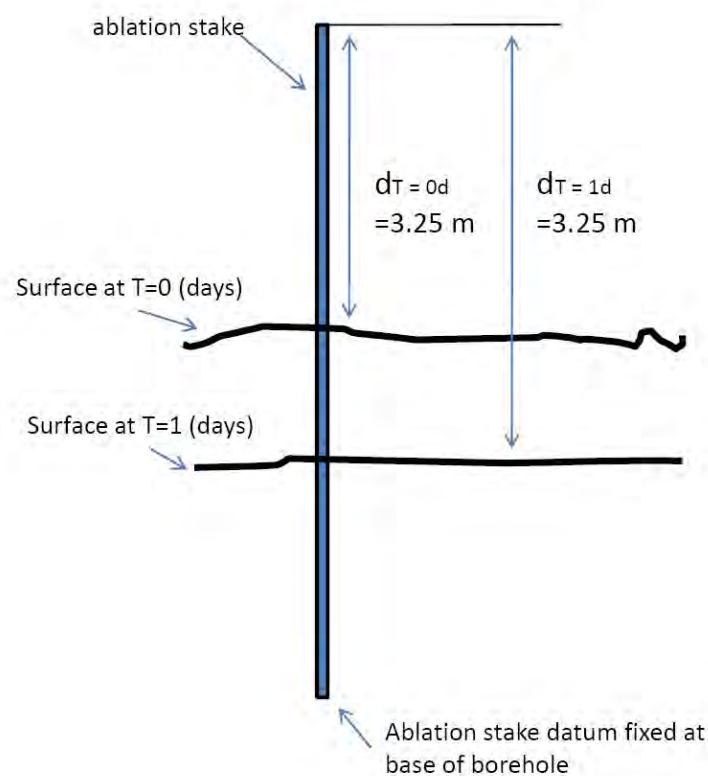

Figure 5: Example of the use of ablation stakes for measure lowering of ice or snow. Time period = (T=1 to T=0) = 1 day ; net ablation ($d_{T=1}$ to $d_{T=0} = 3.32 - 3.25\ m = 0.07\ m$; ablation rate = net ablation/time period = $0.07/1 = 0.07\ m/day$ (illustration taken from Hubbard and Glasser (2005)).

The third method is the measurement of changes in *gravity*. Since its launch in March 2002, the NASA German Aero space Center Gravity Recovery and Climate Experiment (GRACE) has been providing measurements of Earth's gravity field at roughly monthly intervals. The gravity field variations reflect changes in terrestrial water storage, snow/ice mass of polar ice

---

[3]old snow which has gone through multiple refreeze cycles

sheets, and mountain glaciers. The data are very steady and can be delivered regularly. There is a range of studies such as from (Chen et al., 2006) and (Velicogna and Wahr, 2005) using these data (Hagen and Reeh, 2004). Some results of these studies for the total mass balance are reported in Table 1.

2.4. Current estimations for total mass balance and Surface Mass Balance

The IPCC AR4 projected that the GIS is likely to lose mass because the increasing run-off is expected to exceed the precipitation increase in a warmer climate. IPCC AR4 did not expand on the individual model estimates or mass balance components (Meehl et al., 2007). There is a whole lot of literature for estimating the surface mass balance in Greenland, Table 1 gives a short overview about the different estimations and calculations from different authors and time periods.

Most of them are addressing Greenland's total mass balance, and some of them (Janssens and Huybrechts, 2000; Box et al., 2006, 2004; Church et al., 2001; Reeh et al., 1999; Fettweis, 2007) additionally provide numbers for run-off and SMB. Since most results of them have measured or modelled mass loss for the total mass balance, Zwally et al. (2005) and Hanna et al. (2005) have determined mass gain. The lowest bounds of the total mass balance are $-227 \pm 33 \ Gt/y$ (sea level contribution of $0.62 \pm 0.09 \ mm/y$) for the period of 2002 to 2006 (Velicogna and Wahr, 2005), $-204 \pm 37 \ Gt/y$ (sea level contribution of $0.56 \pm 0.10 \ mm/y$) for 2005 (Rignot and Kanagaratnam, 2006) and $-219 \pm 21 \ Gt/y$ (sea level contribution of $0.60 \pm 0.06 \ mm/y$) for 2002-2005 (Chen et al., 2006). The highest range for the total mass balance is $71 \pm 96 \ Gt/y$ for 1991 to 2000 (Box et al., 2004). The SMB ranges from $155 \pm 138 \ Gt/y$ for 1988-2004 (Box et al., 2006) to $281 \ Gt/y$ for 1979-2005 (Fettweis, 2007).

Figure 6 summarizes all estimations from Table 1 of the ice-sheet total mass balance for Greenland. Following Thomas et al. (2006), each box provides a horizontal extension of the observation period covered by a mass-balance estimate, and vertical extension from the estimated mass balance minus the stated uncertainty to the estimated mass balance plus the stated uncertainty. The different applied methodologies for the estimations are marked with different colours. This figure highlights a clear trend to the lower bounds. Nevertheless, these obvious trends include errors associated with the different techniques and large ranges of uncertainties (Alley et al., 2007). In addition to it, there is no standard approach within the techniques for measuring the total mass balance. Moreover, these mostly observation-based

studies are not representative for long-term variations, they are limited to the time period of the observation. In order to improve predictions of future behavior of the GIS it is necessary to better examine its current state and variability. Modelling the SMB are a useful possibility to get results that are not limited in time and space, especially when they validated by observation data (Hanna et al., 2005).
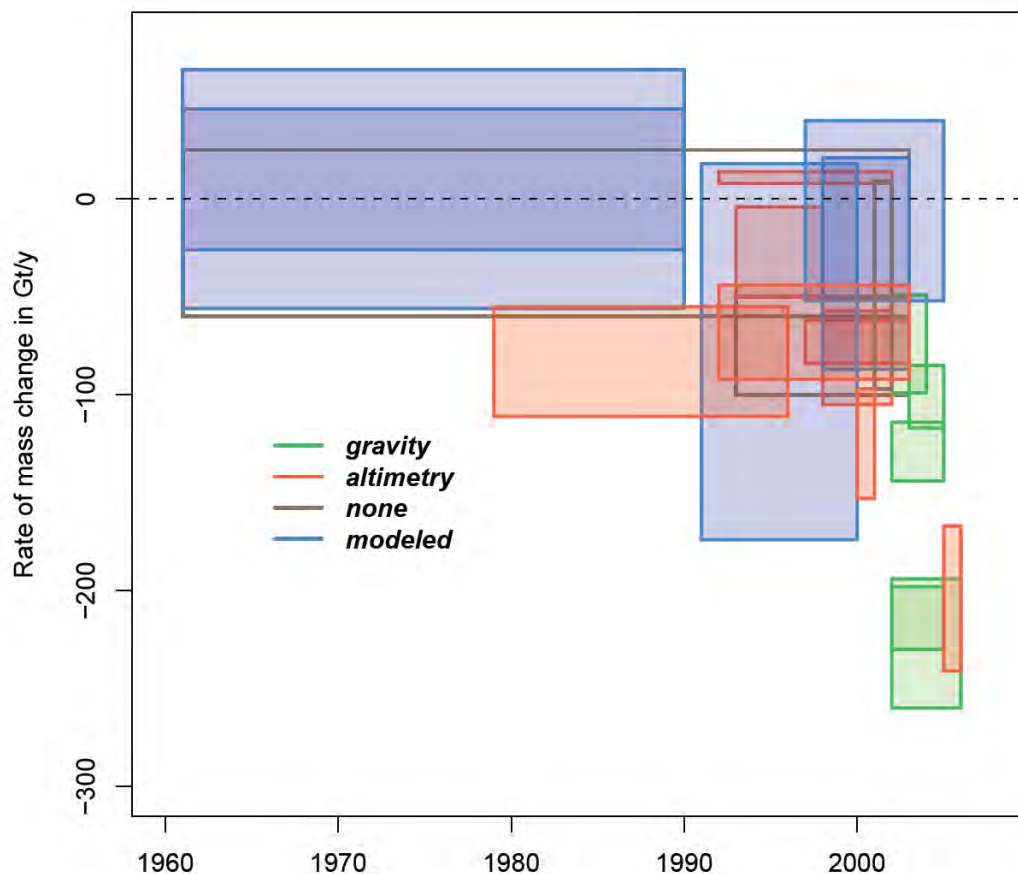

Figure 6: Different estimates of the rate of Greenland's mass change from literature. Following Thomas et al. (2006), the time span over which observation applies is indicated by the horizontal extent of the boxes. The vertical extent describes the uncertainty range (mean+uncertainty) and (mean-uncertainty).

Table 1: Overview about different estimations of SMB components in literature.

Reference	Time period	Mass balance Gt/y	Runoff Gt/y	SMB Gt/y	Ice discharge Gt/y	Method
(Chen et al., 2006)	04/2002-11/2005	-219 ± 21				gravity
(Lemke et al., 2007)	1961-2003	$+25$ to -60				
	1993-3003	-50 to -100				
(Krabill et al., 2000)	1993/4-1998/9	-46				altimetry
(Krabill et al., 2004)	1997-2003	-73 ± 11				altimetry
(Thomas et al., 2006)	1993-1998	-4 to -50				altimetry
	1998/9-2004	-57 to -105				altimetry
(Zwally et al., 2005)	1992-2002	11 ± 3				altimetry
(Luthcke et al., 2006)	2003-2005	-101 ± 16				gravity
(Velicogna and Wahr, 2006)	2002-2006	-227 ± 33				gravity
(Velicogna and Wahr, 2005)	2002-2004	-74 ± 25				gravity
(Janssens and Huybrechts, 2000)	1961-1990	-5 ± 51	281	262 ± 39		modelled
(Hanna et al., 2005)	1998-2003	-33 ± 54	383 ± 34	231 ± 49		modeled
	1961-1990	20 ± 46	240 ± 24			

continued from Table 1

Reference	Time period	Mass balance Gt/y	Runoff Gt/y	SMB Gt/y	Ice discharge Gt/y	Method
(Box et al., 2006)	1988-2004	−91	339 ±60	155 ±138		modelled
(Box et al., 2004)	1991-2000	71 ±96	268	176		modelled
(Church et al., 2001)	1961-1990	−44 ±53	297 ±32	225 ±41	235 ±3	
(Reeh et al., 1999)	2001	0	276	271	239	
(Fettweis, 2007)	1979-2005	−6.5 ±46	277	281		modelled
(Rignot and Kanagaratnam, 2006)	1996	−83 ±28				altimetry
	2000	−125 ±28				
	2005	−204 ±37				
(Johannessen et al., 2005)	1992-2003	−68 ±24				altimetry
(Ramillien et al., 2006)	2002-2005	−129 ±15				gravity

2.5. Modelling future Surface Mass Balance changes

To make predictions for the future behavior of the GIS mass changes, modelling the SMB is a crucial tool. The types of models can be distinguished between three categories: *general circulation models*: those take into account changes in the atmospheric circulation, which are particularly useful for calculating accumulation; *parameterized models*, such as surface energy balance models and degree-day models that are particularly useful for sensitivity calculations focussing in ablation resulting from climate changes and *boundary layer models* which can be used for local studies for ablation and yield information on relevant processes (Van de Wal, 2004). For the purpose of this thesis, the following section is focussing on the parameterized models. The last part of this section introduces two approaches by two different authors for calculating future trends in SMB changes.

Surface energy balance models

The name of the model suggests how this model works - at its simplest, the model attempts to account for all energy coming in and all energy going out of some system, in this case the Earth. For modelling ice-sheets these models compute each of the relevant energy fluxes between the atmosphere and the surface of the glaciers. The models are forced by meteorological measurements and observations (e. g. near surface temperature, near surface humidity, radiative fluxes, cloud amount and precipitation which renders these models difficult, but also more precise than the following approach - the degree-day approach (Hagen and Reeh, 2004).

Degree-Day Method

A simpler method for modelling the ablation, is the degree-day approach, which basically uses the equation:

$$N = \beta * T_{pdd} \tag{3}$$

where N is the predicted ablation, β is the degree-day factor (in mm water equivalent per day per Kelvin) and T_{pdd} is the sum of all positive daily mean temperatures (in °C) over the period of interest. β is a constant, which must be determined by the means of field data of N and T_{pdd}. Hence, the basic assumption is that ablation is linearly related to the sum of positive degree-days over the year. Though this method is not as correct as the energy balance model, it is nevertheless applied in a large number of studies.

However, the simple and cheaper way to calculate the SMB is the degree-day method: the computation of SMB is much cheaper and just a few physical issues must be considered. In most energy balance models it is necessary to specify values for variables such as extra-terrestrial irradiance, wind speed, humidity and cloud amount. The effect of all these physical issues are all aggregated into the degree-day factor (Greuell and Genthon, 2004). A disadvantage of the degree-day model is that it can only be used to calculate the sensitivity of the mass balance to variations of the temperature. Known temporal and spatial variations in variables other than temperature cannot be considered, too. Additionally, problems occur when T is measured around the melting point. Depending on the radiation balance, the threshold between melt and no melt maybe above or below 0°C. A solution of this problem is provided by some authors (e. g. Braithwaite (1995)), through introducing an intercept (β_0) into Equation 3

$$N = \beta_0 + \beta * T_{pdd} \tag{4}$$

The positive degree-day (PDD) method needs a mean daily temperature as input. Therefore it needs parameterization of temperature changes. For the GIS this can be parameterized as a function of elevation and latitude. The basis for this can be a compilation of all available monthly and annual temperatures data e.g. from AOGCMs. The positive degree-day sum is calculated based on the monthly temperature distribution in space and time. The ablation is evaluated by assigning degree-day factors for snow and ice. For monthly mean temperature this would mean for average temperatures T<0, ablation would be zero (Van de Wal, 2004).

Surface Mass Balance modelling according to (Fettweis et al., 2008)

The approach of Fettweis et al. (2008) can be divided in two parts: The first part contains the estimation of the SMB by using a coupled atmosphere-snow Regional Climate Model (MAR[4]) and simulating the SMB changes over a 37-year period (1970-2006). The second part contains a statistical approach for the estimation of SMB in relation to annual precipitation and summer temperature changes.

The regional climate model MAR is coupled to the 1-D Surface Atmospheric Transfer scheme SISVAT (Soil Ice Snow Vegetation Atmosphere Transfer). SISVAT consists of two separate modules, the soil-vegetation module and the snow-ice module. The snow-ice module is a multi-layered energy balance one-dimensional snow-ice model and determines the exchanges between the sea ice, the ice sheet surface, the snow covered tundra, and the atmosphere.

---

[4]Modele Atmospherique Regional

That means, that this method follows the surface energy balance approach (Fettweis, 2007). Since the details of estimation of SMB through MAR are not so relevant for this thesis the following section is focussing more on the second part (the statistical approach for modelling future SMB changes) of the calculations.

With help of a 37-year simulation (1970-2006) performed by MAR they found out that 97% of the inter-annual variability of the modelled SMB can be explained by summer (June, July, August) temperature and annual precipitation anomalies (Fettweis et al., 2008). The results of MAR SMB estimations are applied in the multiple regression Equation 5. Δ SMB is driven by GIS annual precipitation minus the GIS meltwater run-off variability(can be approximated by the 3 m above ground summer temperature),

$$\Delta SMB \cong a\ \Delta T_{jja} + b\ \Delta P_{yr} \qquad (5)$$

where a (in mm/K) and b (in mm/%) are constant parameters, which can be derived by solving the multiple regression. The temperature and precipitation changes are taken from those regions where the correlation with the SMB is the highest. Therefore the West coast, *R*egion 1, was chosen for the temperature anomalies and *R*egion 2, centred on the summit, for the precipitation changes (see Figure 7).

Fettweis et al. (2008) found, that these boundaries do not have significant impacts on the results. For the MAR model $a = -63.3 \pm 6$ and $b = 64.8 \pm 6$. Hence, they calculated a and b for other datasets (such as CRU[5],ECMWF[6],GHCN[7],NCEP[8] and UDEL[9]) following Equation 5 over the time period 1970-1999 and found also high correlation coefficients. In addition, the ratios $k = a/b$ are calculated, too. For normalized and de-trended time series they found a ratio around k = -1 (k = -1.5 and k = -0.75 respectively). In the following calculations in this thesis we use k = -1. According to the future SMB changes, it is assumed that all these calculations are still valid in near future. Furthermore, Fettweis et al. (2008) made assumptions concerning the dependence of the SMB on the temperature and precipitation anomaly, which should be the same for future projections as in 1970-1999. The selected two regions are representative for the whole ice-sheet for the entire period. The parameters a and b are constant for each AOGCM and the entire time period. Fettweis (2007) used as the base period 1970-1999 and the data from model outputs from the 'Climate of the 20th century

---

[5]Climate Research Unit TS 2.1 ,http://www.cru.uea.ac.uk
[6]ECMWF (Re)-Analysis,http://www.ecmwf.int
[7]Global Histo. Climato. Network 2,http://lwf.ncdc.noaa.gov/
[8]NCEP/NCAR Reanalysis 1,http://www.cdc.noaa.gov
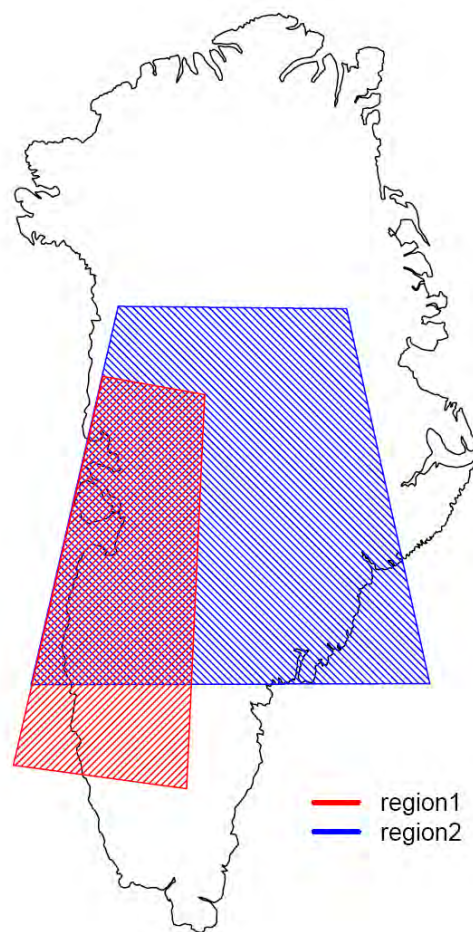[9]Arctic Land-Surface TS 1.01,http://climate.geog.udel.edu

Figure 7: The two regions defined by the paper of (Fettweis et al., 2008) for METHOD 2. *R*egion 1 for summer temperature changes and *R*egion 2 for annual precipitation changes (own illustration).

experiment'(20C3M). In a first step, the data from 20C3M experiment for precipitation for *R*egion 2 and summer temperatures for *R*egion 1 are detrended (to minimize the dependence on the reference period) and normalized followed by the calculation of the mean over the period of 1970 to 1999.

In a second step, the parameters a and b parameter for every AOGCM are calculated for a fixed k = -1. Concerning SMB results from MAR (explained above) time series, they use the standard deviation for SMB of around $100\ km^3/y$ for calculating these parameters. For $k = \frac{a}{b}$ is,

$$\sqrt{\frac{1}{29}\sum_{i=1970}^{1999}(aT_i + bP_i)^2} = a\sqrt{\frac{1}{29}\sum_{i=1970}^{1999}\left(T_i + \frac{1}{k}P_i\right)^2} = 100\ km^3/y \qquad (6)$$

where k = -1, b can be determined. The last step possibly is the calculation of the future changes of SMB. Hence, the mean 1970-1999 temperatures ($\overline{T_{base}}$) (resp.precipitation($\overline{P_{base}}$)) from the 20C3M experiment is subtracted from the projected (SRES A1B) local temperatures (T_x) (resp.precipitation(P_x)), which are divided by the normalization factor that was used for the normalization to provide this equation:

$$\Delta SMB = a\frac{T_x - \overline{T_{base}}}{stdev(T_{base})} + b\frac{P_x - \overline{P_{base}}}{stdev(P_{base})} \qquad (7)$$

In this thesis data for temperature change (base period and future projection) are taken from the output of MAGICC6.0 (see chapter 4.2) and converted into local AOGCM specific temperature and precipitation changes by the pattern scaling approach as described in chapter 4.3. The data for precipitation change are taken from the Program for Climate Model Diagnosis and Intercomparison (PCMDI; http: www-pcmdi.llnl.gov) and converted into mm. The approach of Fettweis (2007) as described above, is labelled as 'METHOD 2' in the following chapters.

Surface Mass Balance modelling according to (Gregory and Huybrechts, 2006)

Gregory and Huybrechts (2006) used for the estimation of future SMB changes the modelling approach of (Janssens and Huybrechts, 2000). This model uses the integrated sum of expected positive degree days, based on yearly averages of temperature, and different degree-day factors (DDFs) for snow and ice to calculate surface melt and the following runoff. The assumptions

is made that runoff occurs when melt exceeds a certain fraction of precipitation; hence surface temperature and precipitation are the important inputs to this type of model. As a result, the sensitivity of runoff is found to be $+0.35$ mm $°C^{-1}$ of the sea level change per year. The total runoff per year for the second half of the twentieth century is estimated to be 280 km^3/y. Following this methodology, for a range of $\overline{\Delta T}$ and $\overline{\Delta P}$ the SMB as a contribution to global-average sea level in mm/y are calculated and from this they subtract the mass balance computed from observed climatology. The results are plotted in a mass-balance perturbation table (see Figure 8). The conversion of Gt/y into mm/y is performed by using the formula $\rho = 1000\ kg/m^3$ for the density of water and by using $A_0 = 3.62 \times 10^{14}\ m^2$ for the area of the ocean.
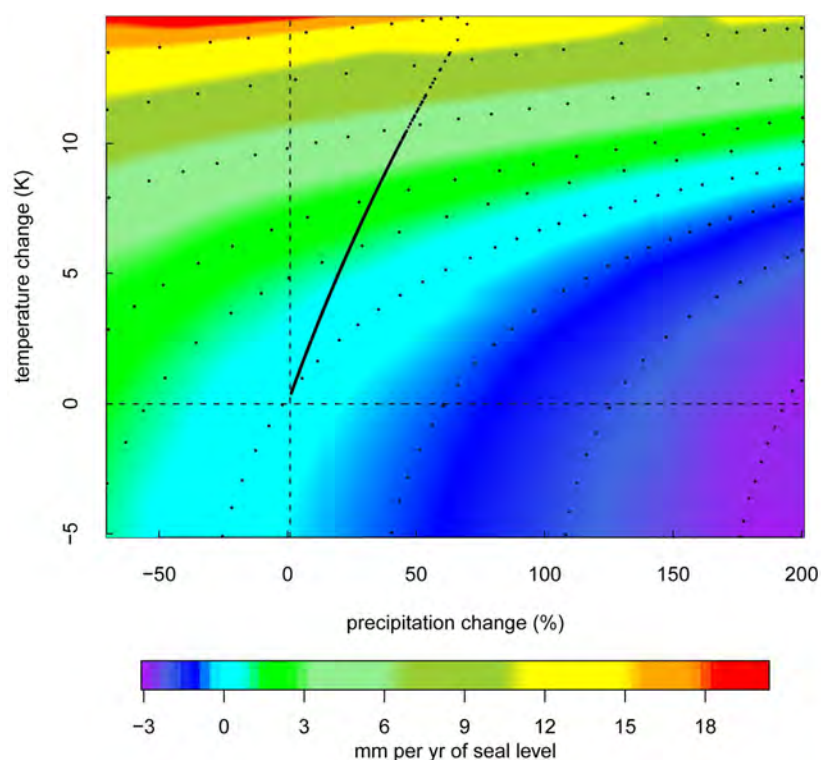

Figure 8: Ice-sheet mass-balance perturbation expressed as sea-level equivalent. The black dots exemplarily stand for the regional temperature and precipitation changes for one scenario (Gregory and Huybrechts, 2006).

Between the discrete set of values of $(\overline{\Delta P}/\overline{\Delta P_0}, \overline{\Delta T})$ a bilinear interpolation is applied. Given $\overline{\Delta P}$ and $\overline{\Delta T}$ from AOGCMs [10] can be obtained by looking up the appropriate value in the table. An increasing precipitation leads to a negative sea level contribution, because of higher accu-

---

[10] Atmosphere-Ocean General Circulation Model

mulation rates. Increasing temperatures lead to a positive contribution, because of accelerated melting rates.

(Gregory and Huybrechts, 2006) uses three scenarios and 18 AOGCMs for the future calculations. Unlike Fettweis et al. (2008), temperature and precipitation change are applied for the entire area up to the coast. For the 21st century up to 2100 the sea level rise per year stays below 1 mm/y (see Figure 9).
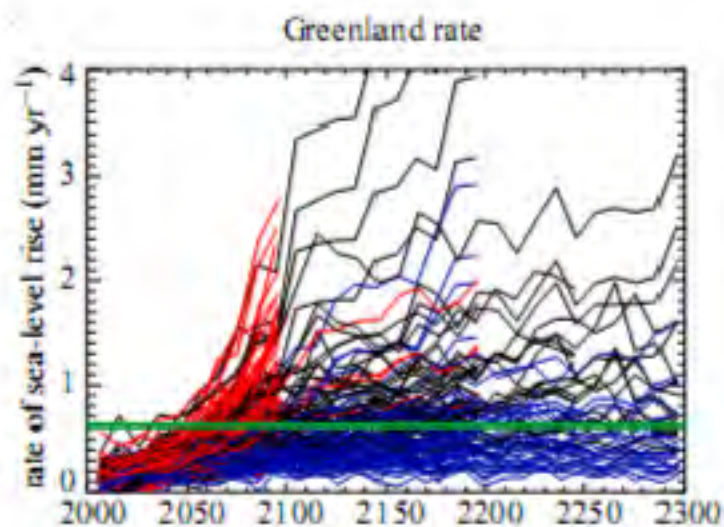

Figure 9: Rates of contribution to sea level (mm/y) from 2000 to 2300. The different line colours indicate different scenarios. (black= A1B, red=A2 and blue=B1; the horizontal green line stands for the magnitude of the present-day surface mass balance of the GIS (Gregory and Huybrechts, 2006).

The calculations in thesis use the perturbation-table from the paper (Gregory and Huybrechts, 2006) on page 1717 for estimating the future changes in SMB. The future precipitation (in %) and temperature changes (in °C) are taken from the MAGICC6.0 outputs. Unlike as in the paper the base period is refering to (Fettweis et al., 2008) (1970-1999). The approach as described above, is labelled as 'METHOD 1' in the following chapters.

3. Tipping Points

In current discussions the term 'Tipping Point' seems to be more and more an important issues to measure impacts on climate change. But what exactly is a 'Tipping Point'? There are some definitions to be found in literature and newspapers, something like: 'the levels at which the momentum for change becomes unstoppable.'(Times Magazine) or from a sociological point of view (Malcom Gledwell) 'the moment of critical mass, the threshold, the boiling point'. In chemistry it is the point, when one drop decides whether the substance is alkaline or acid. Concerning the world's climate a definition was made by the 'Committee on Abrupt Climate Change' and also cited in the AR4 of IPCC: 'Technically, an abrupt climate change occurs when the climate system is forced to cross some threshold, triggering a transition to a new state at a rate determined by the climate system itself and faster than the cause.' (The National Research Council, 2002)

3.1. Defining the tipping point for Greenland Ice Sheet

The tipping point for the GIS is defined as the point, when the SMB will be permanent negative i.e. the ice sheet will be eliminated and leads to a global sea level rise of 7.3 m. Even if this process is estimated to take centuries, there are still lots of uncertainties around this point. The question of dynamics and the influence of accelerating the ablation, like changes in mass balance through iceberg discharge is still not answered yet. A warmer climate in the arctic takes a whole chain of accelerating processes within. Snow and ice melting in summer but also increasing evaporation above the ocean, lead to higher moisture transport inland and increasing precipitation combined with warming suggests a simultaneous increase in summer rain occurrence, which accelerate the summer snow melting (Fettweis, 2007).

In recent studies the ablation process due to temperature changes is defined as the main accountable parameter (Lenton et al., 2008). Therefore it is expected that for this parameter a critical threshold exists. The last IPCC AR4 put the threshold for the permanent negative SMB in Greenland at $1.9°C$ to $4.6°C$ global warming (above preindustrial), which clearly can be exceeded during this century.

Gregory and Huybrechts (2006) gives a similar estimation at about $3°C$ global temperature change. In contrast to this, (Bamber et al., 2009) compared a simple temperature index model used in IPCC AR4 with one that includes a complete description of the energy balance at the surface and snow metamorphism and found due to the more complex model with different

sensitivities a much higher critical threshold at about 6° C: twice as much as the previous estimates. The differences in these estimations of the tipping point for Greenland have their origin in the lack of knowledge about the dynamics and the resulting acceleration of ablation and ice-discharge.
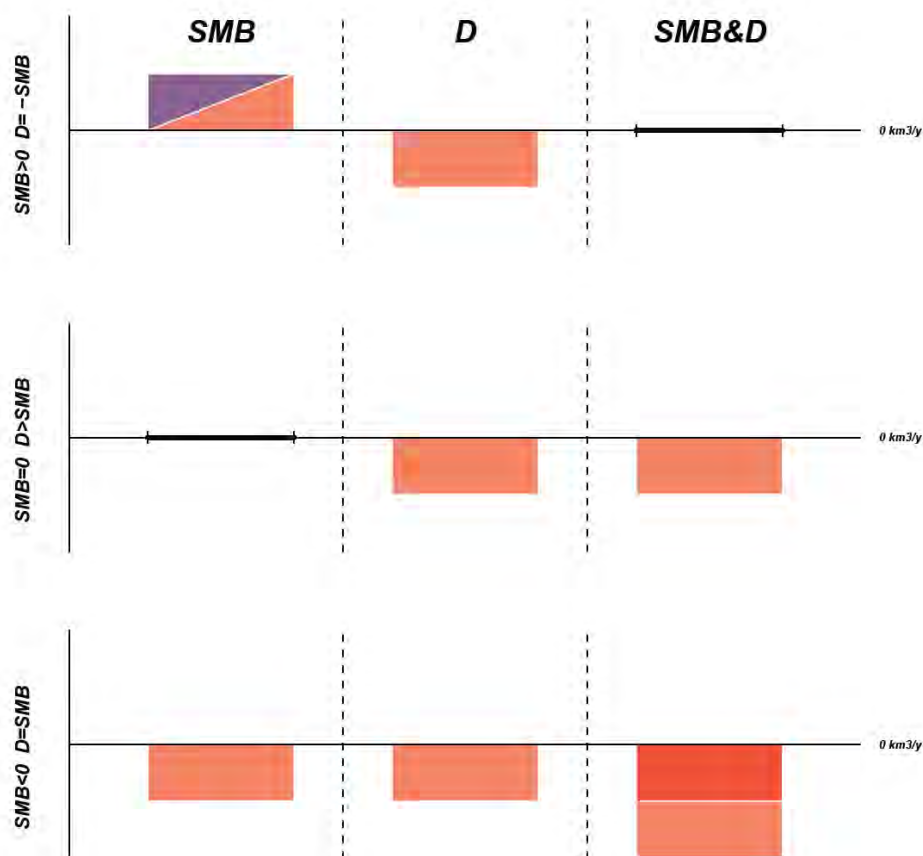

Figure 10: The Surface Mass Balance (SMB) is subject of permanent changes and is balanced by accumulation (blue) and ablation (red). Ablation and discharge of ice (D) are the main drivers of mass loss (as described in Chapter 3). As long as the SMB is positive and the mass of the uncertain term D = discharge is equal or smaller to the SMB, the total mass balance will be balanced at 0 km^3/y per year (upper plot). Although the ice-discharge term D is uncertain, this term will never take the value of zero. Therefore, if the SMB is taking the value of zero, the total mass balance will be negative (shown in the middle). Thus, a lot of dynamic processes will be accelerated and the process can be assumed to become irreversible. The SMB will reach this point if the current estimated SMB ($225 \pm 41\ km^3/y$) will change to zero ($\Delta SMB = -SMB_0$). The third case in the lower plot shows the assumption of negative SMB and ice-discharge (own illustration).

The easiest way to find this critical threshold for SMB is to define the threshold for SMB being permanent negative at $\Delta SMB = -SMB_0$. If the surface mass balance (SMB) is positive and there is no ice discharge (D), the ice sheet would expand until reaching the sea. If the SMB reaches zero, the ice sheet must retrieve from the coast to reduce D to zero. If the SMB becomes negative the ablation process will be accelerated until the entire ice-sheet is eliminated. Therefore SMB = 0 is taken as an threshold for the tipping point. This point will be reached, if the calculated change from the SMB balance models is equal to the mass balance in a unperturbed/current climate (see also Figure 10).

For the following calculations the $\Delta SMB = -SMB_0$ is defined at a value of $SMB_0 = 0.62\ mm/y = 225 \pm\ 41 km^3/y$, according to an estimation made by Church et al. (2001). This value was also used in different literatures and models, for example in the model of Gregory and Huybrechts (2006). Another estimation was issued by (Fettweis et al., 2008) for the period 1970-1999 at 350 Gt/y that is equivalent to 0.96 mm/y.

4. From climate data to probability of the Greenland Ice Sheet tipping point

The forecast of the climate change, caused by carrying tonnes of CO_2 in the atmosphere, comes along with a lot of uncertainties. These uncertainties arises from two principal causes: (1) internal and external natural climate variability; (2) incomplete understanding of Earth system processes and their imperfect representation in climate models (e.g. AOGCMs).

These uncertainties gives a wide range of interpretation in all political directions and views. Another problem is that these uncertainties are a major problem for those planning to adapt to a changing climate. Adapting to a smaller change than the one that is actually occurring (or one of the wrong sign) leads to expensive impacts and endanger lives, yet adapting to a larger change (or, again, one of the wrong sign), leads to wasting money (Murphy et al., 2009; Pittock et al., 2001). For this reason there is a need for a scientific quantification of the uncertainties. The probabilistic estimation, also called: *probabilistic projections* of the occurrence of an impact or a temperature range, was adopted by IPCC for the first time in the AR4. Current efforts in producing probabilistic projections of climate change concentrate on quantifying uncertainty in simulating climate response to given emissions scenarios. For climate policy, this needs not to be an issue, since climate change projections based on given emissions scenarios may allow an informed choice to be made on emissions policy (Murphy et al., 2009; Pittock et al., 2001). Of course there are several different methods to make the probabilistic estimations. In this thesis the approach of the probabilistic assessment is following the method of the 'PRIMAP'[11]group from the Potsdam Institute of climate impact research, as outlined below.

4.1. Overview of the calculation steps

The processing chain for calculating the risk of climate impacts is outlined in Figure 11. In a first step atmospheric concentrations and global mean temperatures are calculated for different emission scenarios using the MAGICC6.0 climate model. A pattern scaling module is used to scale global temperature to regional temperature and precipitation changes while retaining the global to regional relationship from the original AOGCM. These regional climate change distributions are then integrated with climate impact response functions parameterized from individual studies, diagnosing risk exceedance probabilities for a variety of climatic impacts.

---

[11]Potsdam Real-Time Integrated Model for probabilistic Assessment of emission Paths,www.primap.org
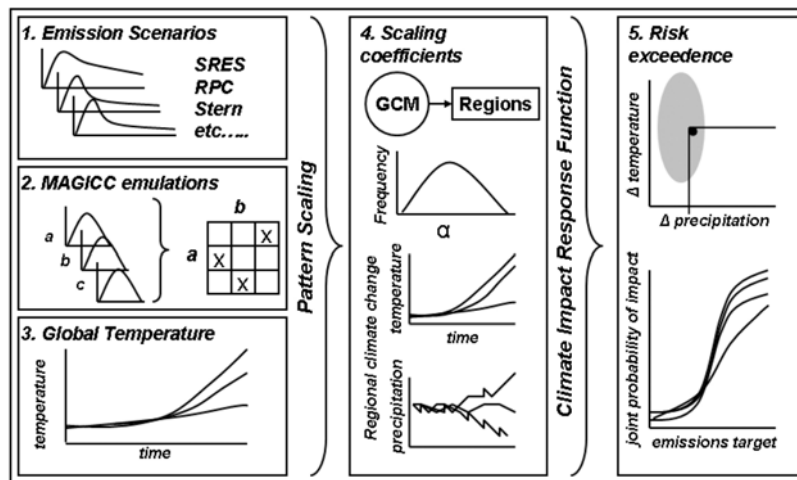
Figure 11: The process of calculation the climate impact risk as used in the PRIMAP group. (Poulter,pers.communication)

4.2. MAGICC6.0

The following description is taken from (Frieler et al.2009). MAGICC6.0 is a reduced complexity coupled carbon cycle climate model (Meinshausen et al., 2008). Its reduced complexity makes it highly efficient still being able to closely emulate more complex carbon cycle models (C4MIP), and global climate models (CMIP3), respectively (Meinshausen et al., 2008). Since it is a coupled carbon-cycle climate model, it allows to simulating the cause effect chain from emissions via the carbon cycle to atmospheric concentrations of CO_2 and other greenhouse gases (GHG) to the associated radiative forcing and resulting changes in global mean temperature. Recently, MAGICC6.0 was used in the context of a Bayesian Monte Carlo analysis to provide probabilistic projection of global mean temperature changes associated with different emission scenarios (Meinshausen et al., 2009). Therefore the most relevant input forcing parameters were constrained to the current level of knowledge reflected by the IPCC AR4 and more recent literature. In addition, the model was constrained by observational data as series of hemispheric land/ocean temperatures and ocean heat uptake. For all scenarios, MAGICC6.0 was run with 600 parameter set combinations to produce a time series of global temperature change. Figure 12 shows the temperature changes for the three selected scenarios A1B, A1F1 and halved-by-2050 (for 1900 - 2100). The distribution of the uncertainty increases with time. Furthermore, the various ranges are represented in the figure. The median, as the middle of

the distribution: half the scores are above the median and half are below the median, then the area in which 50 % , 80 % and 99 % of the values are located. The median is taken because it is less sensitive to extreme scores than the mean and this makes it a better measure than the mean for highly skewed distributions.
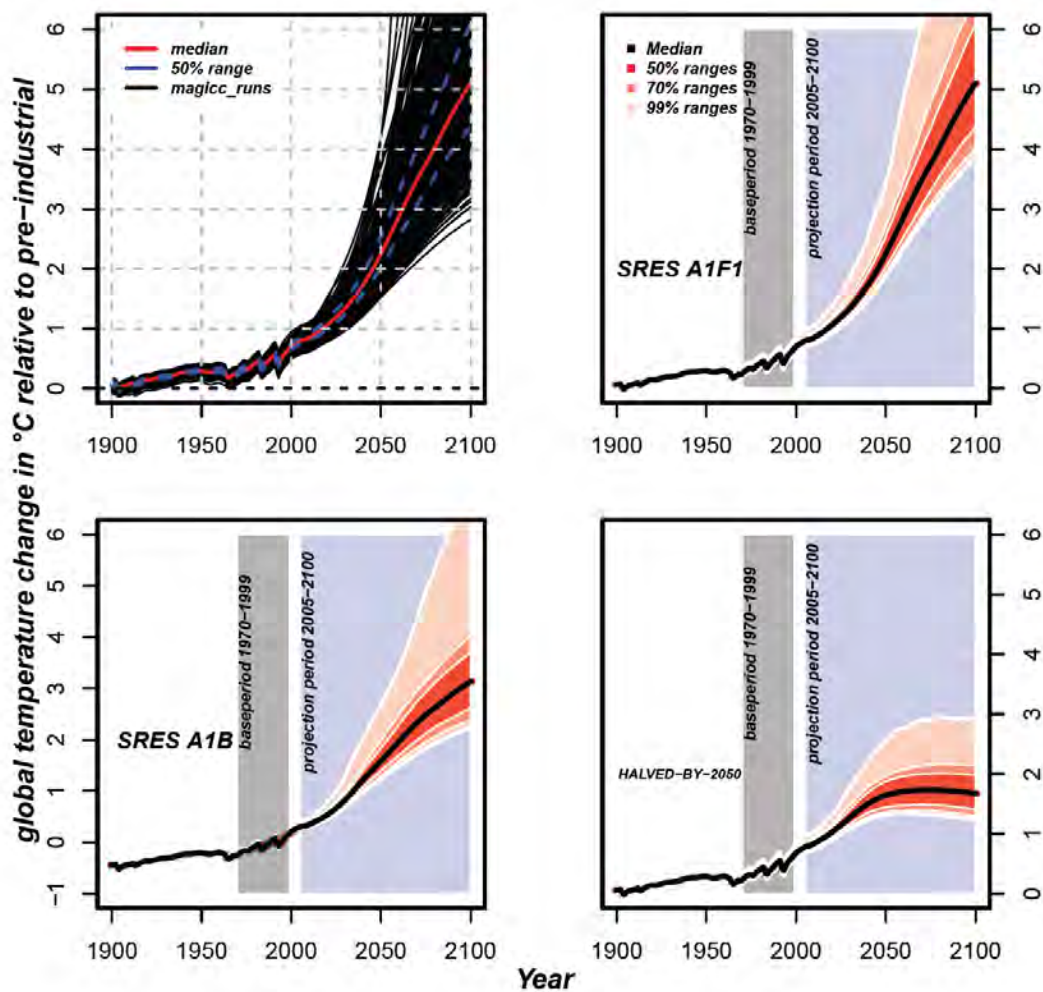

Figure 12: Time series of the MAGICC6.0 outputs for SRES A1F1,A1B and h50 Scenarios. The interquartile ranges are 50% = 75th and 25th percentile, 70% = 85th and 15th percentile and 99% = 1st and 99th percentile. Outliers larger than the 99% range are not included in this figure (own illustration).

4.3. Pattern Scaling

The approach for the upcoming calculations follows, a method developed by Frieler. This method especially focuses on the quantification of the uncertainty of coefficients resulting the scaling of global temperature to regional temperature and precipitation changes while retaining the global to regional relationship from the original AOGCMs.

In order to calculate the probability of a certain regional impact on a specific region, an approach was developed by Frieler, to scale global to regional temperatures and precipitation values without loosing the uncertainty distribution.

Based on the whole set of AR4 AOGCM simulations Frieler (pers.communication) developed a new statistical scaling methodology providing ensemble projections of regional climate change. The method utilizes the AOGCM based linear relation between global mean temperature changes and regionally averaged changes in temperature and precipitation.

In a first step, the regional means for the impact region (in this case: Greenland) were calculated for the data from the latest set of AOGCM simulations performed in the support of the IPCC AR4, and stored at the Program for Climate Model Diagnosis and Intercomparison (PCMDI; http: www-pcmdi.llnl.gov). Frieler used all available scenario runs, i.e. the idealized runs ('1pctto2x' and '1pctto4x') assuming increasing carbon dioxide concentrations of 1% per year up to doubling and quadrupling, respectively, the 20th century run ('20c3m'), the commitment run ('commit') keeping green house gas concentrations constant at 2000s level, and the SRES scenarios ('sresb1', 'sresa2', and 'sresa1b'). Figure 13 shows regional changes in ten year averages of summer temperature ($\Delta \overline{T}_{regional}$) plotted against global mean temperature change ($\Delta \overline{T}_{global}$) for Region 1(see section 2.5). And Figure 14 shows changes in ten year averages of log transformed annual precipitation ($\Delta \overline{log(P_{regional})}$) for Region 2 (see section 2.5) plotted against global mean temperature change ($\Delta \overline{T}_{global}$). The results for the whole Greenland area are shown in Figure 15 (for regional temperature change) and Figure 16 (for regional precipitation change).

Precipitation data were log-transformed, to get normally distributed data. The changes (Δ) were calculated with respect to the control runs[13] associated with the considered runs.

Two approaches were developed: the basic parametric approach and the non-parametric approach. In the first case one single model is fit to all available AOGCM data allowing the scaling coefficients to vary from AOGCM to AOGCM where the variability is normally distributed. In

---

[13]Control runs are long integrations where the model input forcing (solar irradiance, sulfates, ozone, greenhouse gases) are held constant and are not allowed to evolve with time.
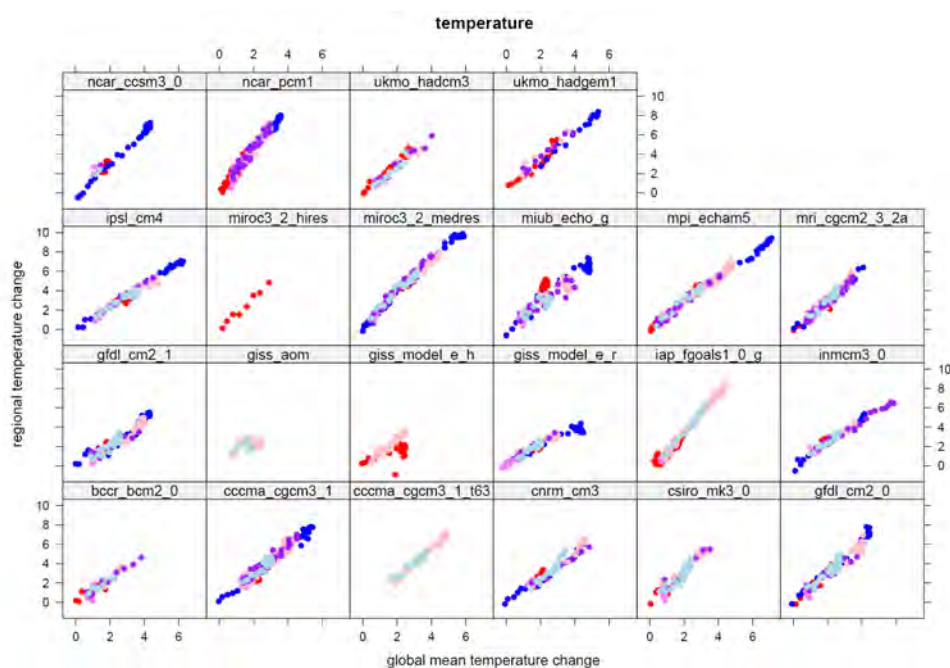
Figure 13: Scatter-plot for regional temperature change in relation to global temperature change for *R*egion 1. The data for 21 AOGCMs for 7 scenarios (if available) (marked by different colours of the dots) taken from PCMDI[12], regionally weighted and plotted against global temperature change. It should be highlighted that the correlation for GISS-AOM and GISS-EH is low and for MIROC3.2 Hires just one scenario has been available (Frieler in prep).
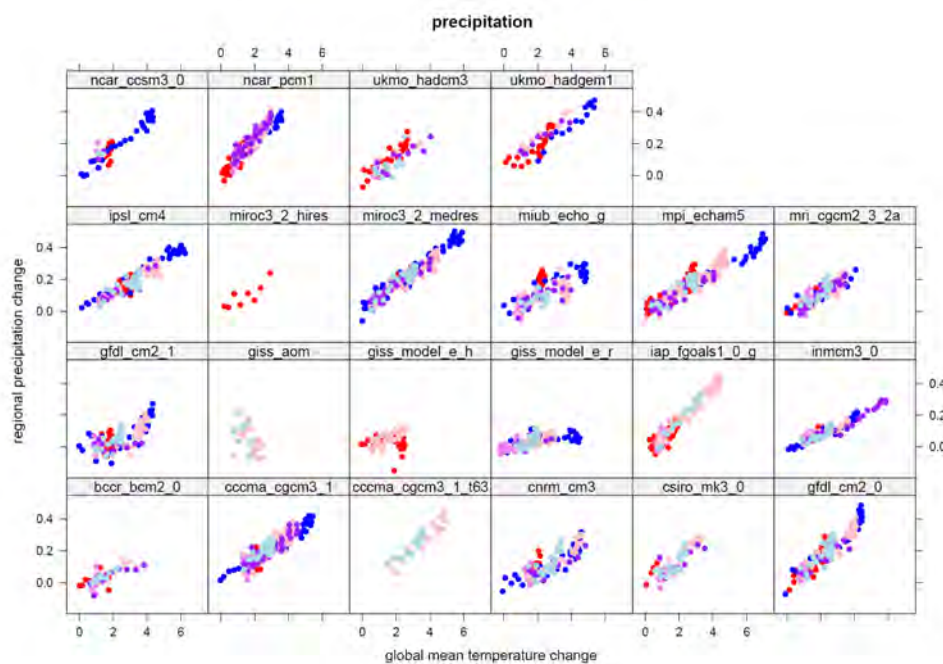
Figure 14: Scatter-plot for regional annual precipitation change in relation to global temperature change for Region 2. The data for 21 AOGCMs for 7 scenarios (if available) (marked by different colourrs of the dots) taken from PCMDI, regional weighted and plotted against global temperature change. It should be highlighted that the correlation for GISS-AOM, GISS-EH and GISS-ER is low and for MIROC3.2 Hires just one scenario has been available. (Frieler in prep)
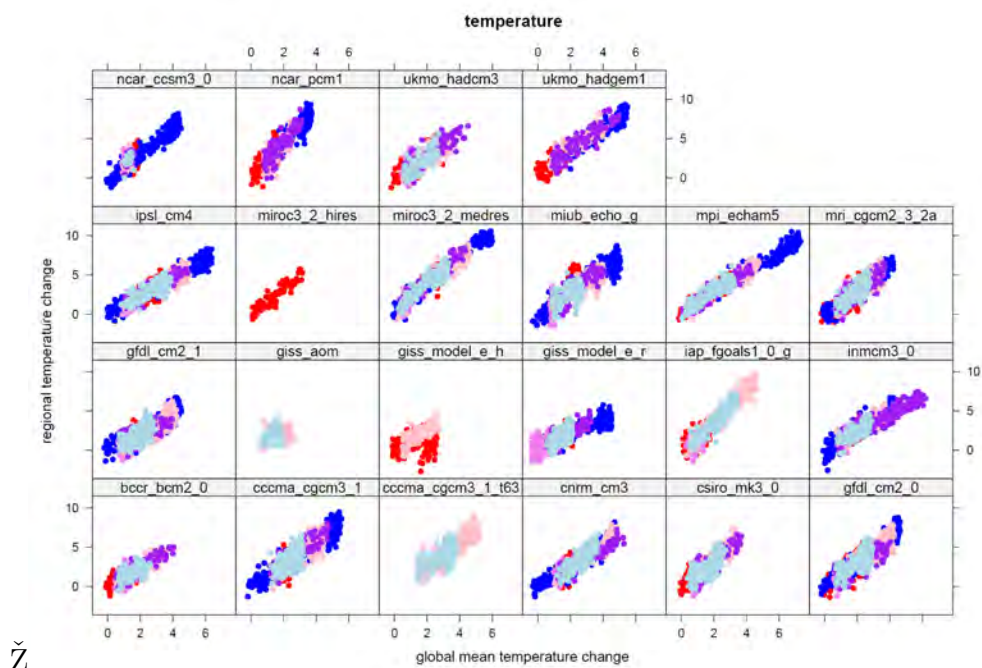
Ž

Figure 15: Scatter-plot for regional temperature change in relation to global temperature change for the whole GIS. The data for 21 AOGCMs for 7 scenarios (if available) (marked by different colours of the dots) taken from PCMDI, regional weighted and plotted against global temperature change. It should be highlighted that the correlation for GISS-AOM, GISS-EH and GISS-ER is low and for MIROC3.2 Hires just one scenario has been available (Frieler in prep).
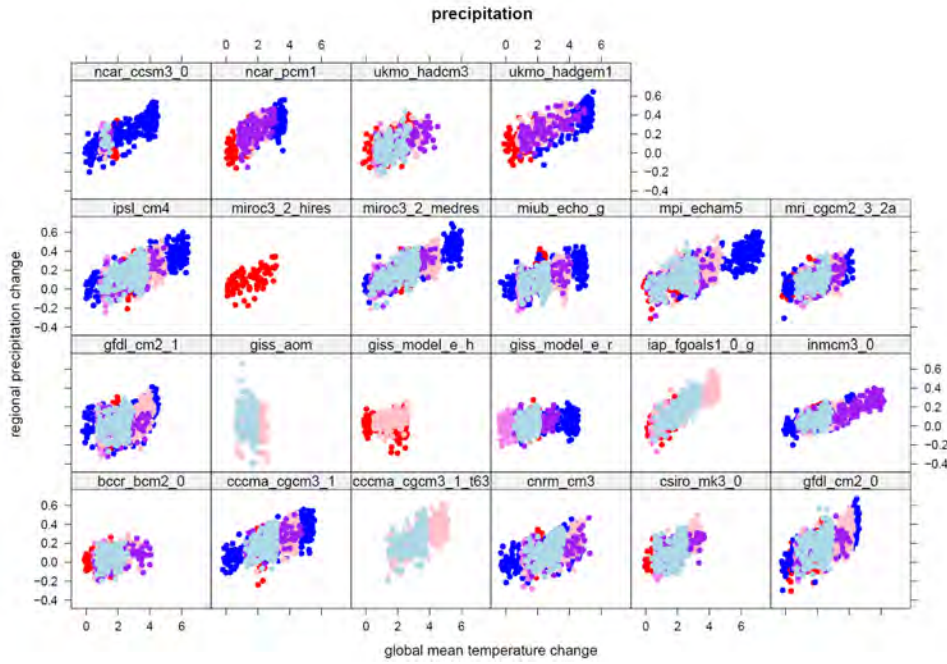
Figure 16: Scatter-plot for regional annual precipitation change in relation to global temperature change for the whole GIS. More Details see caption of Figure 14 (Frieler in prep).

the latter case one individual statistical model is fit to the results of each AOGCM. In this way the normality assumption for the inter-AOGCM variability of the scaling coefficients is avoided. The determination of the coefficients and their inter AOGCM, inter scenario and inter run variabilities (so called 'random effects') requires the application of a multi-level model. This is a statistical models of parameters that vary at more than one level. The basic parametric random effects model that was fitted to the data is expressed by the following equation:

$$
\begin{pmatrix} \Delta T_{regional} \\ \Delta log(P_{regional}) \end{pmatrix}_{i,j,k} = \begin{pmatrix} c + r_i^{mod} + r_{i,j}^{scen} + r_{i,j,k}^{run} \\ \tilde{c}_{i,j,k} + \tilde{r}_i^{mod} + \tilde{r}_{i,j}^{scen} + \tilde{r}_{i,j,k}^{run} \end{pmatrix} * \Delta T_{global} + \begin{pmatrix} \epsilon_{i,j,k} \\ \tilde{\epsilon}_{i,j,k} \end{pmatrix} \qquad (8)
$$

where $(c, \tilde{c})$ are the scaling coefficients for temperature and precipitation, that are subject to random variations, the inter-AOGCM variability , the inter-scenario variability and the run-to-run differences. ϵ describes the residual variability not explained by the scaling approach. Similar to the usual linear regression these residuals are assumed to be normally distributed.

For the calculation of the SMB in Greenland, following the two models described in chapter 2.5, the non-parametric approach was applied for both and the parametric approach was applied on the SMB model following METHOD 1. For each SMB model and each AOGCM

normal distributions of the scaling coefficients were sampled 2000 times to give a full representation of the scaling coefficient uncertainty. The METHOD 2 uses regional temperature data from Region 1 (see Section 2.5) and for precipitation change the climate data for Region 2. Therefore the correlation was calculated between the two regions. The resulting distribution of all coefficients is shown in Figure 17. For the parametric approach, the scaling coefficients are calculated for the entire area of Greenland whereas for the non-parametric approach coefficients are calculated for all AOGCMs (see Table 4 in Chapter 4.5) and both SMB projection approaches (see Section 2.5).

Figure 17 is picturing the coefficients for three example AOGCMs following the parametric and non-parametric approach. The parametric approach was applied for data of the whole GIS and shows a broad distribution. For the non-parametric approach the distributions for the models' CGCM3.1' and 'UKMO-HadCM3' for both regions are wider than for the total area, but it shows similar patterns to Figures 13, 14, 15 and 16. The model 'GISS-EH' shows a broad distribution in both cases what can be attributed to the low correlation between local and global temperature/precipitation change as shown in Figures 13, 14, 15 and 16.
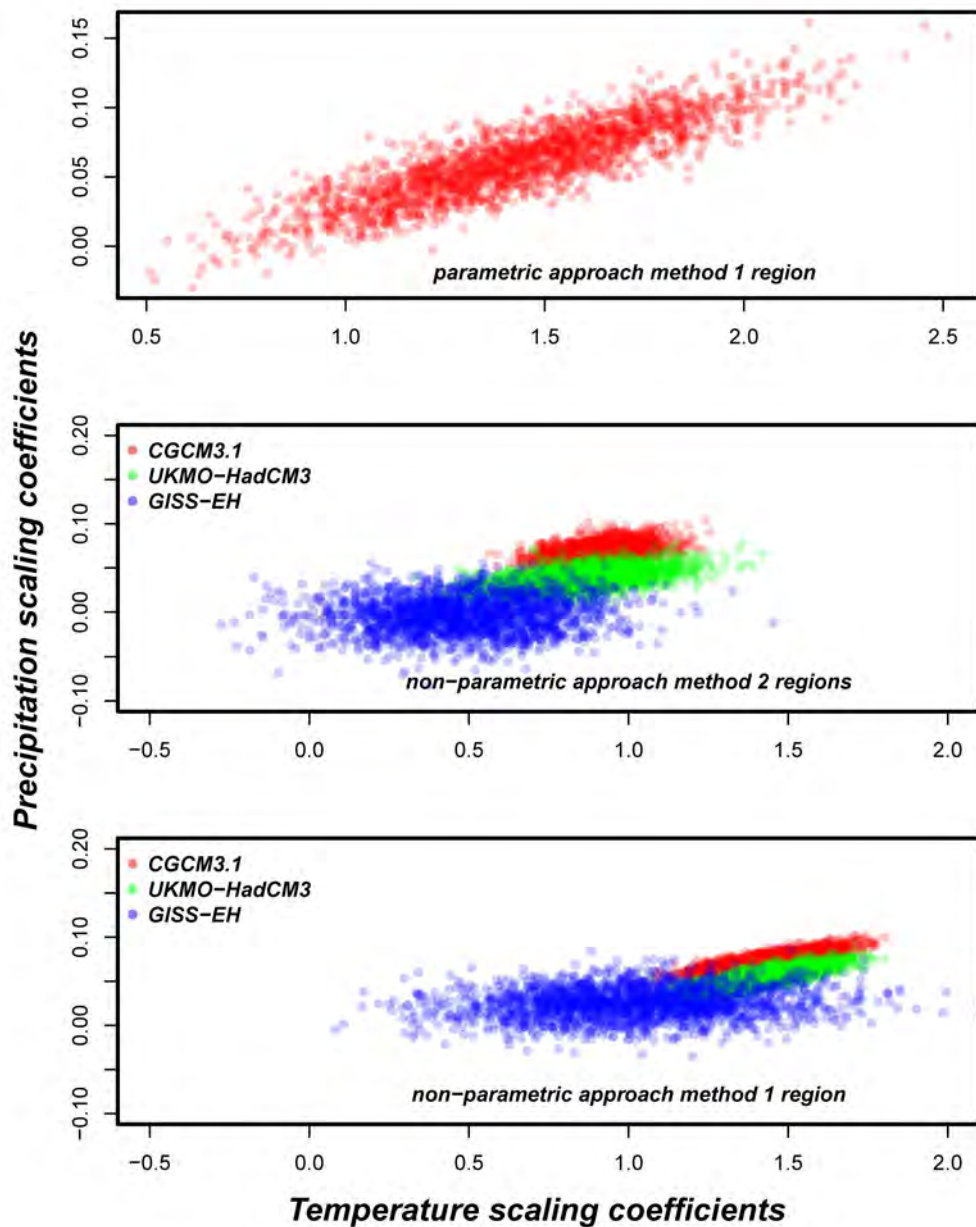
Figure 17: Scatter-plot of scaling coefficients for precipitation and temperature change. The upper plot shows the distribution of coefficients following the parametric approach for the whole GIS. The middle shows the non-parametric approach coefficients for *R*egion 1 (temperature change) and 2 (precipitation change). The bottom shows the coefficients for non-parametric approach for the whole GIS (own illustration).

4.4. Scenarios

The scenarios used in this thesis have two sources: The so called 'SRES' scenarios have their origin in the 'Special Report on Emissions Scenarios' (Nakicenovic and Swart, 2005). These scenarios were used to make projections in the Third and Fourth Assessment Report of the IPCC. They follow a variety of assumptions for future demographic, economic and technological development. In SRES there is a definition of four different scenario families with own storylines (Nakicenovic and Swart, 2005). The titles of the storylines (Nakicenovic and Swart, 2005) have been kept simple: A1, A2, B1 and B2.

- The A1 storyline and scenario family describes a future world of very rapid economic growth, global population that peaks in mid-century and declines thereafter, and the rapid introduction of new and more efficient technologies. Major underlying themes are convergence among regions, capacity building and increased cultural and social interactions, with a substantial reduction in regional differences in per capita income. The A1 scenario family develops into three groups that describe alternative directions of technological change in the energy system. The three A1 groups are distinguished by their technological emphasis: fossil intensive (A1FI), non-fossil energy sources (A1T), or a balance across all sources (A1B)

- The A2 storyline and scenario family describes a very heterogeneous world. The underlying theme is self-reliance and preservation of local identities. Fertility patterns across regions converge very slowly, which results in high population growth. Economic development is primarily regionally oriented and per capita economic growth and technological changes are more fragmented and slower than in other story lines.

- The B1 storyline and scenario family describes a convergent world with the same low population growth as in the A1 storyline, but with rapid changes in economic structures towards a service and information economy, with reductions in material intensity, and the introduction of clean and resource-efficient technologies. The emphasis is on global solutions to economic, social, and environmental sustainability, including improved equity, but without additional climate initiatives.

- The B2 storyline and scenario family describes a world in which the emphasis is on local solutions to economic, social, and environmental sustainability. It is a world with moderate population growth, intermediate levels of economic development, and less rapid and more diverse technological change than in the B1 and A1 story lines. While the scenario is also oriented towards environmental protection and social equity, it focuses

on local and regional levels.

Figure 18 illustrates the four scenario 'families'. In reality, the four scenario families share a space of a much higher dimensionality given the numerous assumptions needed to define any given scenario in a particular modelling approach. In this schematic diagram it is illustrated that the scenarios build on the main driving forces of GHG[14] emissions. Each scenario family is based on a common specification of some of the main driving forces.
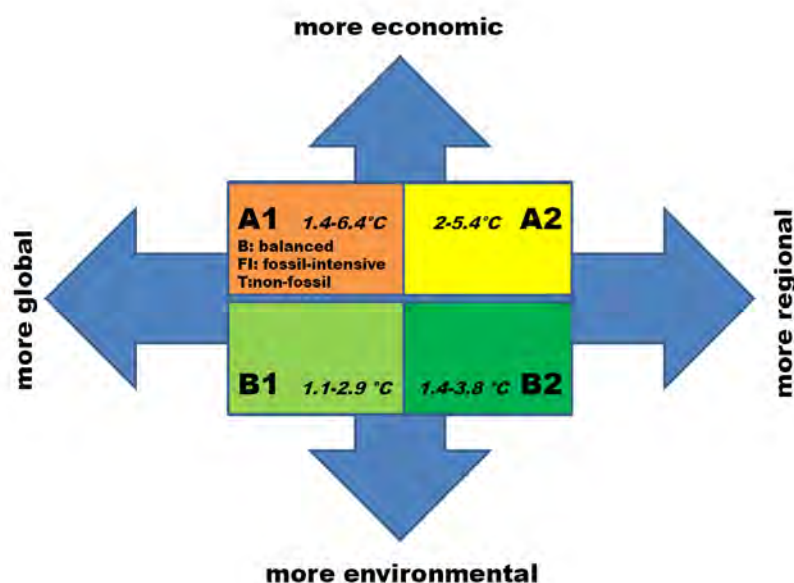

Figure 18: Four SRES families and the main driving forces (IPCC, 2007).

The calculations in this thesis are considering one of the families with two different model variances. A1B has a balanced emphasis on all energy sources and will be stabilizing at 720 ppm CO_2 in 2100. A1FI has an emphasis on fossil-fuels and will be stabilizing at 920 ppm CO_2 in 2100. The A1B scenario is also used for the SMB projection in (Fettweis et al., 2008) and (Gregory and Huybrechts, 2006), hence it makes sense to use it for the following calculations.

The third scenario assumes that CO_2 emissions are halved by 2050 compared to 1990 (Meinshausen et al., 2009). In this scenario the peak global mean temperature is around 2°C by the 2nd half of the 21st century. During the ongoing climate negotiations over one hundred countries have adopted this '2°C target'. In order to get a more likely chance of staying below 2°C, emissions would have to be reduced even below this target. A maximum of 1000 billion tonnes of CO_2 from 2000 to 2050 may be emitted into the atmosphere if the probability of

---

[14]Greenhouse gas

staying below 2°C shall not exceed 75% (Meinshausen et al., 2009). Around one third of this has already been emitted between 2000 und 2009.

4.5. AOGCM-Atmosphere-Ocean General Circulation Model

The AOGCMs belong to the group of General Circulation Models (GCM). GCMs are mathematical models of the general circulation of a planetary atmosphere coupled to an ocean and based on the Navier-Stokes equations on a rotating sphere with thermodynamic terms for various energy sources (i.e. radiation and latent heat) (Meehl et al., 2007).

The AOGCMs represent the pinnacle of complexity in climate models and incorporate as many processes as possible. They belong to the tools that provide regional projections of future climate change. However, they are still under development. Calculations in this thesis are based on the use of output from the AOGCMs in Table 4.

Table 4: Twenty-two AOGCMs from the IPCC AR4 used in this thesis.

Model	Source
CCSM3	National Center for Atmospheric Research, USA
CGCM3.1(T47)	Canadian Centre for Climate Modelling and Analysis, Canada
CNRM-CM3	Météo-France/Centre National de Recherches Météorologiques, France
CSIRO-MK3.0	Commonwealth Scientific and Industrial Research
ECHAM5-MPI-OM	Max Planck Institute for Meteorology, Germany
FGOALS-G1.0	National Key Laboratory of Numerical Modeling for Atmospheric Sciences and Geophysical Fluid Dynamics /Institute of Atmospheric Physics, China
GFDL-CM2.0	US Department of Commerce/National Oceanic and Atmospheric Administration
GFDL-CM2.1	/Geophysical Fluid Dynamics Laboratory, USA
GISS-AOM	National Aeronautics and Space Administration /Goddard Institute for Space Studies, USA
GISS-EH and ER	National Aeronautics and Space Administration /Goddard Institute for Space Studies, USA
INM-CM3.0	Institute for Numerical Mathematics, Russia
IPSL-CM4	Institut Pierre Simon Laplace, France
MIROC3.2(hires) and (medres)	Center for Climate System Research, National Institute for Environmental Studies, and Frontier Research Center for Global Change, Japan
MRI-CGCM2.3.2	Meteorological Research Institute, Japan
PCM	National Center for Atmospheric Research, USA
UKMO-HadCM3 and HadGEM1	Hadley Centre for Climate Prediction and Research/Met Office, UK

4.6. Probability calculations

The probability discussed and examined here is not the absolute probability of climate changing by some very exact value. This is impossible because - in contrast to other natural sciences - it is impossible to make experiments to prove these results. Hence, the probability is defined as the probability of the change in projected climate being greater or lower than the climate

at which the impact occurs using the Cumulative Distribution Function (CDF). For every real number x, the CDF of X is given by

$$x \mapsto F_X(x) = \mathrm{P}(X \leq x). \qquad (9)$$

The right-hand side represents the probability that the random variable X takes on a value less than or equal to x (Freedman et al., 2007). To define possible thresholds, a calculation of the probabilities exceeding a temperature threshold in, say 2050 or 2100 for the three scenarios was carried out (relative probability). In a first step the 2000 sampled coefficients were multiplied with a range of global temperature steps. The relative frequency for each scenario and year was determined for each temperature step. The second step contains the application of the same temperature steps as in step one on the impact response functions (for METHOD 2 this is Equation 7 in Chapter 3 and for METHOD 1 this is the perturbation table as shown in Figure 8). Using these results for a range of thresholds a calculation of the probabilities was carried out. The results are describing the CDF. The probability of exceeding a certain threshold for a individual scenario and year was determined by multiplying the results (CDF and relative probability) of each temperature step and summed up.

5. Future Changes in Surface Mass Balance

The objective of this chapter is the presentation of the final results according to the two methods explained in previous chapters. The results for both calculation methods are determined over the period of 2005-2100 for all 22 AOGCMS and the three scenarios. The first part of this section outlines the results for the temporal evolution of temperature, precipitation and sea level changes through SMB variances. The second part contains the calculation and discussion of the probabilities of exceeding a certain threshold of sea level rise per year.

5.1. Precipitation and Temperature between 2005 and 2100

Since temperature changes are responsible for the main ablation process of ice sheets, they play a major role in the calculation of the SMB. For METHOD 1, temperature changes refer to the entire area of Greenland and for METHOD 2 they refer to *R*egion 1 (as described in Chapter 2.5). The regional temperatures ($\Delta T_{regional}$) are determined by the pattern scaling approach through multiplication of global temperatures (ΔT_{global}) taken from MAGICC6.0 with the scaling coefficients (c) (see Equation 10). For METHOD 2, temperatures referring to *R*egion 1 are summer (June, July, August) temperatures and for METHOD 1 annual temperature changes are applied.

$$\Delta T_{regional} = c * \Delta T_{global} \tag{10}$$

Precipitation plays an important role in the accumulation of ice mass. Approximately 600 km^3 of precipitation reaches the surface of the ice sheet each year. Nearly 100 km^3 is lost by wind and sublimation[15] (Box et al., 2004). The regional precipitation change ($\Delta P_{regional}/P_0$) is calculated according to the pattern scaling approach as well. However, it must be considered that the coefficients for precipitation have been determined on a log scale.

$$\Delta P_{regional}/P_0 = \exp(c * \Delta T_{global}) \tag{11}$$

Figure 19 exemplary shows the results for both method/regions, all AOGCMs and the scenario A1B (for A1F1 and H50 see appendix A Figures 35 and 36). This figure highlights the fact that rising temperatures lead to higher precipitation changes, based on a correlation determined in the pattern scaling.

---

[15]change from gas to solid and vice versa

For all three scenarios the temperature changes for the entire area (METHOD 1) are higher than the ones that are calculated for the *R*egion 1 (METHOD 2). The range of the individual AOGCMs is for temperature changes almost the same, whereas the ranges for precipitation changes are differing between the two methods. In METHOD 2 (*R*egion 2), the range of the models is greater than in METHOD 1 due to outliers like the results of GISS-EH or GFDL-CM2.1. The correlation between global mean temperature and regional precipitation change for these two models is very low in comparison to other models (see also Chapter 4.3). The Figures 35 and 36 shows precipitation changes for scenario A1F1 and H50 (see Appendix).

In 2100, the median for both regions calculated from all AOGCMs differ by a temperature of 1.87 ° C. This difference can be ascribed to the characteristics of the different regions as described in chapter 2.5. The higher temperatures imply (because of the scaling coefficients), higher precipitation changes for METHOD 2 (in 2100 the differences are 8.14 %). The other two scenarios following the same patterns with different higher or lower median values.

Figure 20 displays an overview about all three scenarios and their medians. The largest temperature increase for 2100 is recorded in scenario A1F1, followed by A1B and the lowest scenario H50. In scenario H50 temperatures are rising up to 2050, and then remain stable up to 2100 at a certain value.(METHOD 2 at 1.12 °C and METHOD 1 at 1.86°C). In the beginning of the 21st century the scenario A1B shows that the temperatures for both methods/regions are rising in the same rate as H50 and A1F1. As from 2040 temperatures are rising at a higher rate than in scenario H50 but are lower than in A1F1. For precipitation changes, the pattern is the same as for temperature changes. All results generated for the year 2100 are given in Table 5. Compared to the results from Fettweis et al. (2008) the temperatures have all higher values (for A1B in 2100 by 2.4 °C), whereas the precipitation changes are almost remain constant (for A1B in 2100 by 17%).
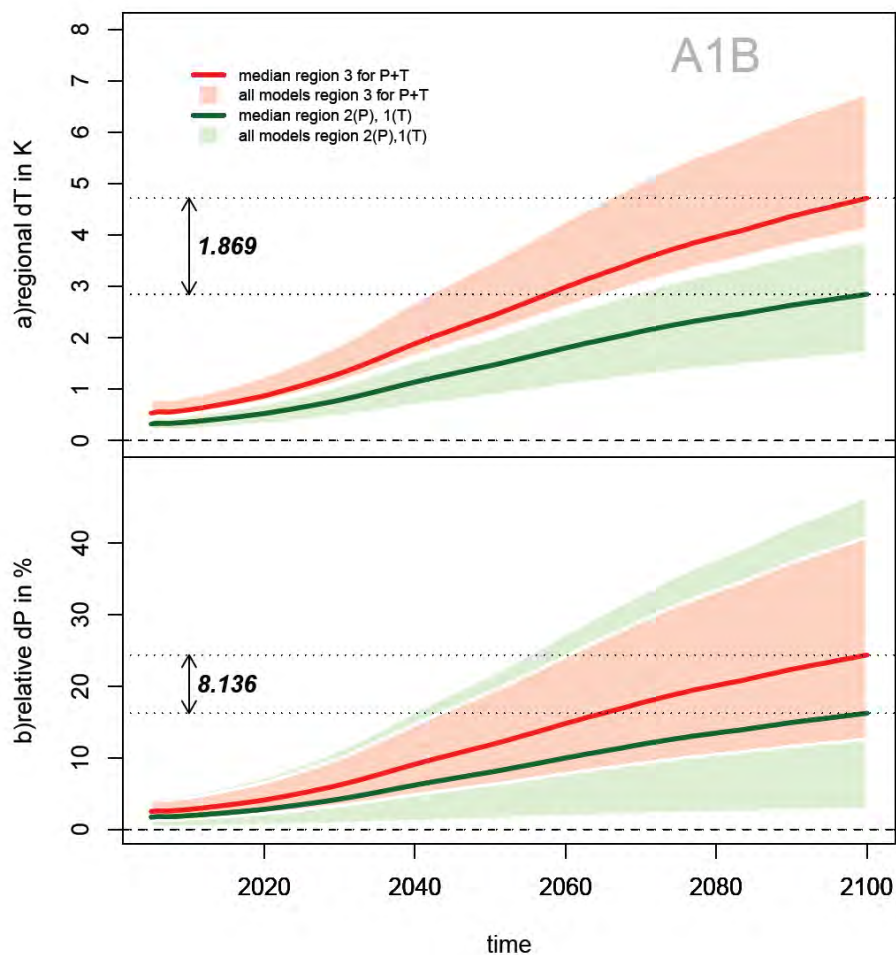
Figure 19: Precipitation and temperature change over the period 2005 to 2100 in SRES A1B. Upper panel: regional temperature changes. Solid lines represent the medians of the multi-AOGCM sample while the shaded areas represent the inter-AOGCM spread. Red: Projected changes in annual mean temperature for the whole Greenland area (labelled as region 3) as used in METHOD 1. Green: Projected changes in summer-JJA-temperatures over *R*egion 1 as used in METHOD 2. Lower panel: regional changes in annual precipitation. Solid lines represent the medians of the multi-AOGCM sample and shaded areas represent the inter-AOGCM spread of the projections. Red: Results for the whole ice sheet as used in METHOD 1. Green: Results for *R*egion 2 as used in METHOD 2.
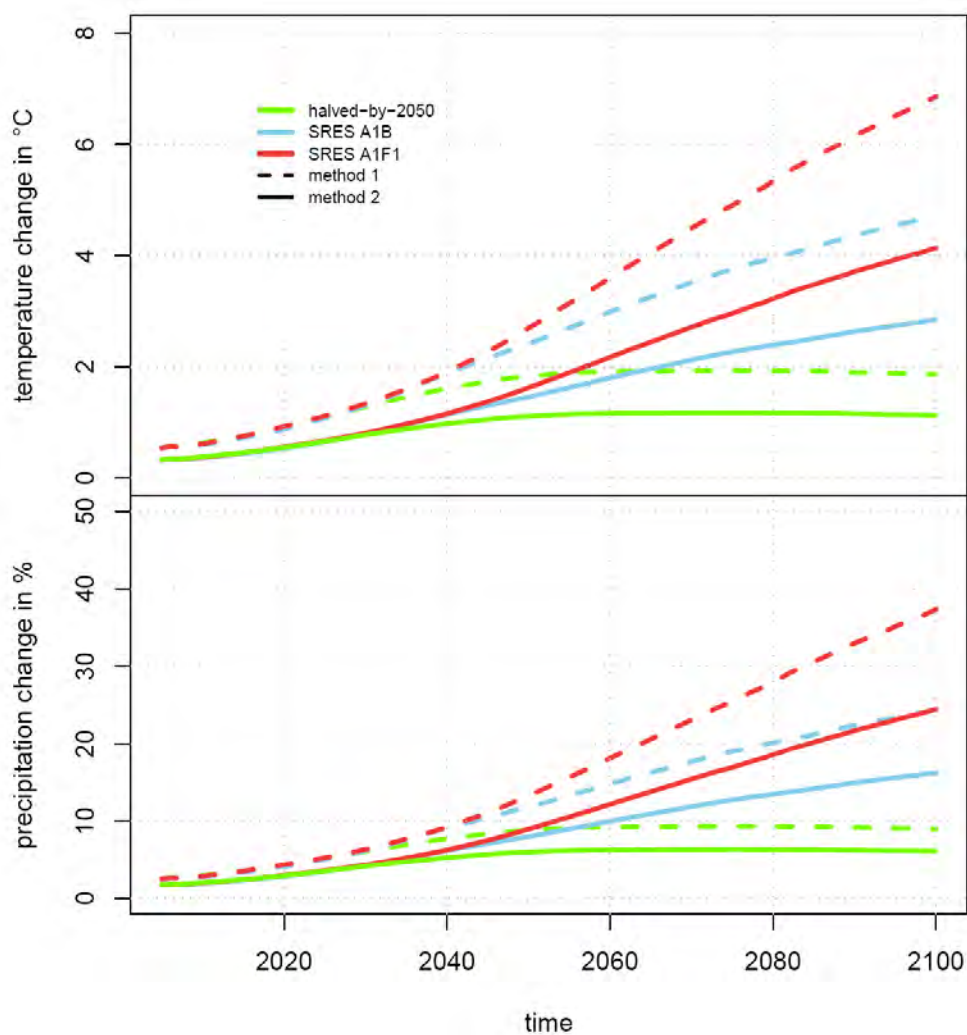
Figure 20: Time series of local temperature/precipitation medians projected by AOGCMs listed in Table 4 for the scenarios A1B, A1F1, H50 for both methods. The dotted lines represent METHOD 1 and solid lines METHOD 2 (own illustration).

Table 5: Overview of results for local precipitation and temperature changes in 2100. Temperatures are measured in °C and precipitation in %.

		METHOD 2			METHOD 1		
		A1B	A1F1	H50	A1B	A1F1	H50
ΔT	median	2.84	4.14	1.12	4.71	6.86	1.86
in °C	mean	2.82	4.11	1.11	4.73	6.88	1.87
	stdev	0.75	1.09	0.29	0.97	1.41	0.38
	min	1.37	2	0.54	1.9	2.76	0.75
	max	3.95	5.75	1.56	6.98	10.15	2.75
$\Delta P/P_0$	Median	16.22	24.45	6.11	24.35	37.33	8.99
in %	Mean	16.56	25.47	6.09	23.57	36.36	8.63
	stdev	12.97	20.43	4.64	10.05	16.02	3.53
	Min	-5.16	-7.42	-2.07	2.15	3.14	0.84
	Max	49.56	79.64	17.22	41.23	65.27	14.60

5.2. Sea level rise resulting from Surface Mass Balance changes between 2005 and 2100

The current SMB of Greenland is estimated to be approximately 225 Gt/y (204 km^3/y) (Church et al., 2001). That leads to a total mass balance (SMB minus ice discharge (D)) of -14 Gt/y (if the ice-discharge term is D = 239 Gt/y[16]) referring to Table 1.

Even if ice discharge is an important issue for calculating mass balances, there are large uncertainties about the dynamics that can not be included in the models. Therefore the SMB is the quantity which is considered here.

To convert the SMB to a sea level equivalent, the SMB is divided by the entire surface of oceans A= $3.62 * 10^{14}$ m^2 and the density of water d = 1000 kg/m^2. This conversion leads to a current amount of SMB, equivalent to 0.62 mm/y SLR.

Despite the higher temperatures that were calculated for METHOD 2, the increase in the SLR

---

[16]Reeh et al. (1999)

is less than in METHOD 1(see Figure 21). This difference can be explained by the different approaches and assumptions made in both methods. Since for example the sea level rises in a linear mode with temperature and precipitation in METHOD 2, in METHOD 1 this relation is a non-linear one (see Figure 22). Furthermore the sensitivities (ablation per degree temperature change) do show remarkable differences.
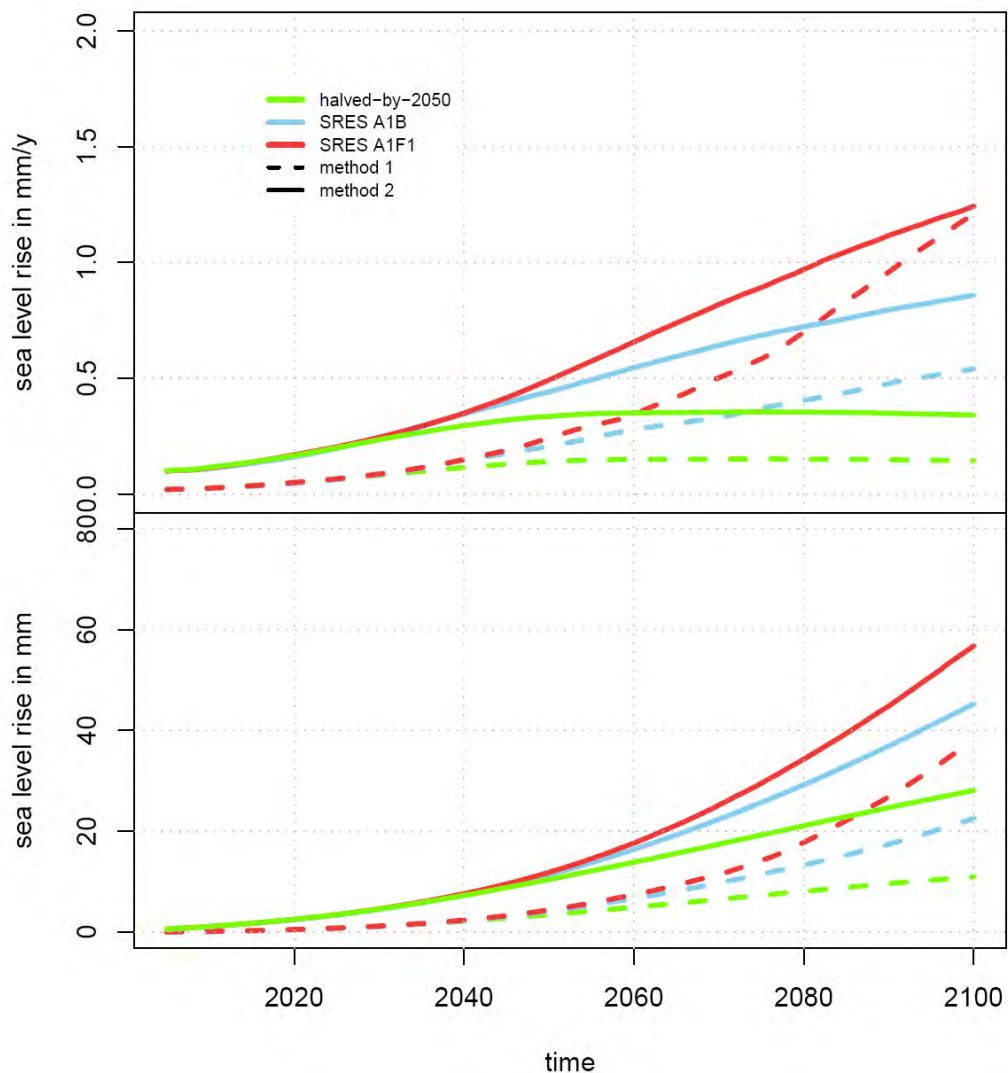

Figure 21: Time series of median changes in SLR [mm] and SLR per year [mm/yr] based on the multi-AOGCM sample of regional climate projections for the period from 2005 to 2100 (the individual AOGCMs are listed in Table 4). Color coding indicates the scenario: blue = A1B, red = A1F1, green = H50. The dotted lines represent results from METHOD 1 and solid lines represent results from METHOD 2 (own illustration).

The non-linear relation in METHOD 1, can be explained by refreezing processes which were

taken into account in this model. Figure 22 is a plot of the SLR for the AOGCM model 'UKMO-HadCM3' against temperature and precipitation changes.
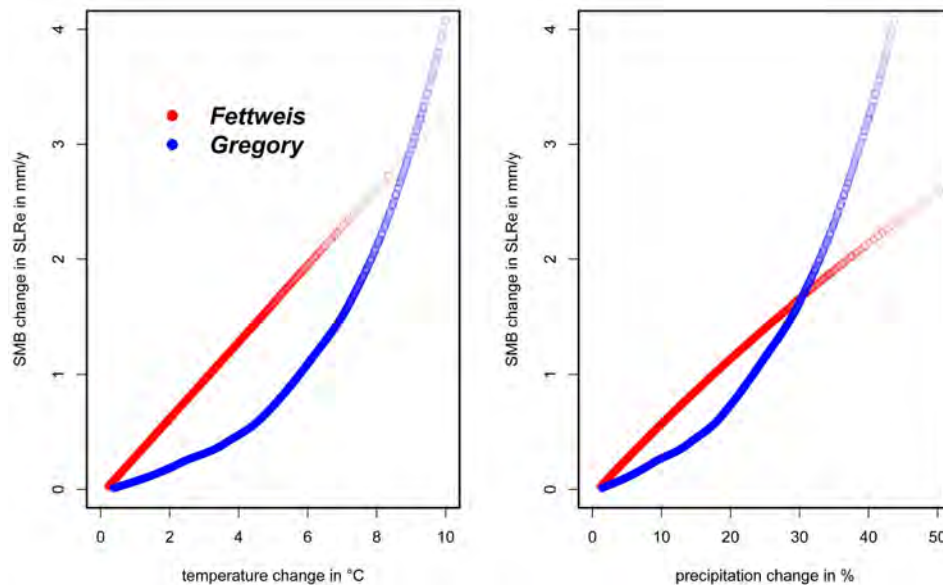

Figure 22: The relation between temperature/precipitation change and SLR per year. Labeled in blue: the results of(Gregory and Huybrechts, 2006) alias METHOD 1 and in red: of (Fettweis et al., 2008) alias METHOD 2.

The results (see Table 6) for the A1B scenario in METHOD 1 are in the range of the respective results from Gregory and Huybrechts (2006). According to the data from Fettweis et al. (2008) the results for METHOD 2 have got all higher values compared to the results of Fettweis et al. (2008).

One main reason for this difference can be a different assumption concerning the radiative forcing in the MAGICC outputs. If all yearly data are summed up, the result for the highest emission scenario (A1F1) in 2100 is 41.43 mm ± 17.11 mm for METHOD 1 and 53.52 mm $\pm$ 17.33 mm for METHOD 2. Even for the lowest scenario (H50) a SLR can be detected. For METHOD 1 the SLR in 2100 is within the range of 10.46 ± 4.34 mm and for METHOD 2 it is 26.67 ± 8.60 mm. This fact points out, that a SLR is not avoidable anymore, even if the emission will be halved by 2050.

The projections in the AR4 estimate a global sea level rise between 0.21 to 0.48 m for the A1B scenario and for the A1F1 0.26 to 0.59 m in 2090-2099 (relative to 1980-1999). The largest share comes from thermal expansion and glaciers. The calculated projections for Greenland would be a share around 20 % for the lowest bound of the AR4 estimation (0.21 m). In

comparison to the period 1993-2003 with around 8 % the share will be doubled until 2100. According to METHOD 2 the tipping point, $0.62\ mm/y$, will be exceeded for the scenarios A1B and A1F1 in 2100. In METHOD 1 only the high fossil scenario A1F1 is exceeding this threshold in 2100.

Table 6: Overview of results for SLR and SMB change for all scenarios from 2005 to 2100. 'stdev' stands for the standard deviation.

		METHOD 1			METHOD 2		
		A1B	A1F1	H50	A1B	A1F1	H50
$\Delta SMB\ in\ km^3/y$	Mean	-239.48	-571.37	-54.15	-291.99	-420.2	-116.87
	Median	-215.42	-502.34	-56.77	-309.8	-448.46	-123.12
	stdev	94.95	282.57	21.8	94.64	136.93	37.72
	Min	-517.16	-1531.72	-99.56	-473.09	-686.43	-187.48
	Max	-79.32	-129.57	-22.17	-136.2	-197.12	-54.15
$\Delta SLR\ in\ mm/y$	Mean	0.59	1.25	0.14	0.81	1.16	0.32
	Median	0.54	1.21	0.14	0.86	1.24	0.34
	stdev	0.23	0.45	0.06	0.26	0.38	0.1
	Min	0.2	0.33	0.06	0.38	0.55	0.15
	Max	1.23	2.22	0.25	1.31	1.9	0.52
$\Delta SLR\ in\ mm$	Mean	23.86	41.43	10.46	42.83	53.52	26.67
	Median	22.6	38.2	10.97	45.26	56.72	28.08
	stdev	8.86	17.11	4.34	13.85	17.33	8.6
	Min	8.77	12.46	4.18	19.9	24.94	12.35
	Max	46.33	94.09	19.69	69.02	86.58	42.75

Table 7 shows the results of the sensitivities for the GIS. These sensitivities are determined by dividing the calculated change in SLR (in 2100) by the calculated temperature change of the same year. It is notable that the temperature sensitivities vary for the different scenarios, while the differences in the precipitation sensitivities are very small.

This can again be attributed to the non-linear ablation process through temperature change. In the AR4 the results for the temperature sensitivities of individual AOGCMS (e.g. UKMO HadCM3) are within a range of 0.04 to 0.23 mm $y^-1\ ^{\circ}C^-1$ and for a bundle of 18 AOGCMS are 0.11 mm $y^-1\ ^{\circ}C^-1$. The results of Gregory and Huybrechts (2006) are in this range, since the sensitivities of Fettweis et al. (2008) are above the estimations made in AR4.

Table 7: Sensitivities for precipitation and temperature. The mean was calculated for the period from 2005-2100. The non-linear behavior of the model leads to the different sensitivities in METHOD 1 for each scenario.

		A1B	A1F1	H50
$\Delta SLRy_{mean}/\Delta T_{mean}$	METHOD 2	0.30	0.30	0.30
in $mm/y\ °C^{-1}$	METHOD 1	0.08	0.09	0.07
$\Delta SLRy_{mean}/\Delta P_{mean}$	METHOD 2	0.05	0.05	0.05
in $mm/y\ \%^{-1}$	METHOD 1	0.016	0.018	0.014

5.3. Probability

In order to determine the likelihood of the above results, particularly the probability of exceeding the tipping point in both models, the probabilities for a certain impact on a particular scenario are calculated.

The first step includes determination of the the probability of exceeding a certain global temperature. Figure 23 and Figure 24 shows the distribution of local temperatures and precipitation for 4 degrees global temperatures change in a two-dimensional histogram. For METHOD 2, one example AOGCM was selected (UKMO-HadCM3) and the associated 2000 scaling coefficient multiplied by 4. For METHOD 1 the 2000 coefficients sampled for the parametric approach were multiplied by 4. For METHOD 1, the impact isolines were added to the plot that, exemplify the thresholds. The calculation of the fraction of sample points lying above a certain threshold allows estimating the probability of exceeding certain limits of SLR due to global warming. Hence, the probability of exceeding the 1 mm/y threshold for METHOD 1 is 39.3% for METHOD 2 54.25%. The wider distribution of the values in METHOD 1 is due to the scaling coefficients calculated according to the parametric approach (see Chapter 4.3, Figure 17).
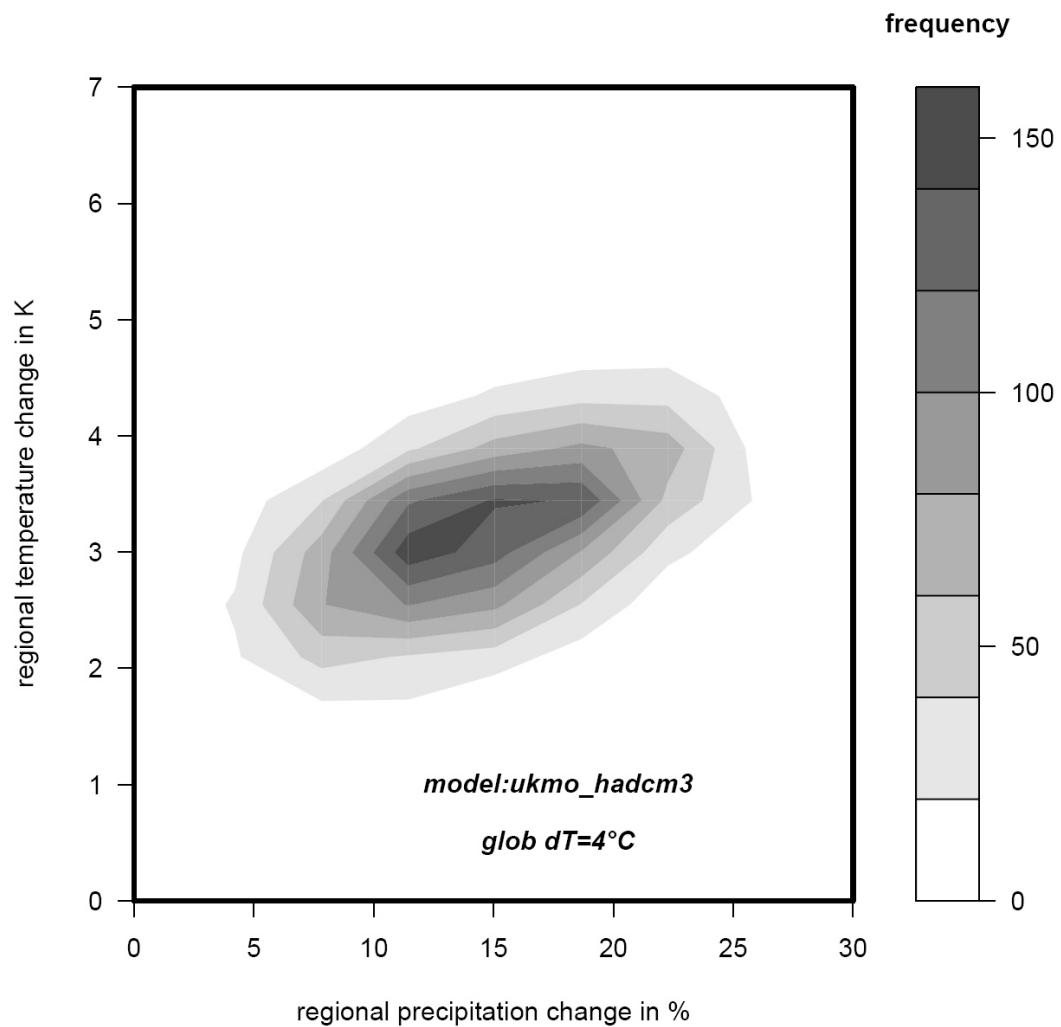
Figure 23: Two-dimensional histogram for four degrees global temperature change and the effect on local temperature and precipitation distributions for METHOD 2. The coefficients are calculated according to the non-parametric approach (see Chapter 4.3). The frequency on the right side of the plot indicate the absolute frequency (own illustration).
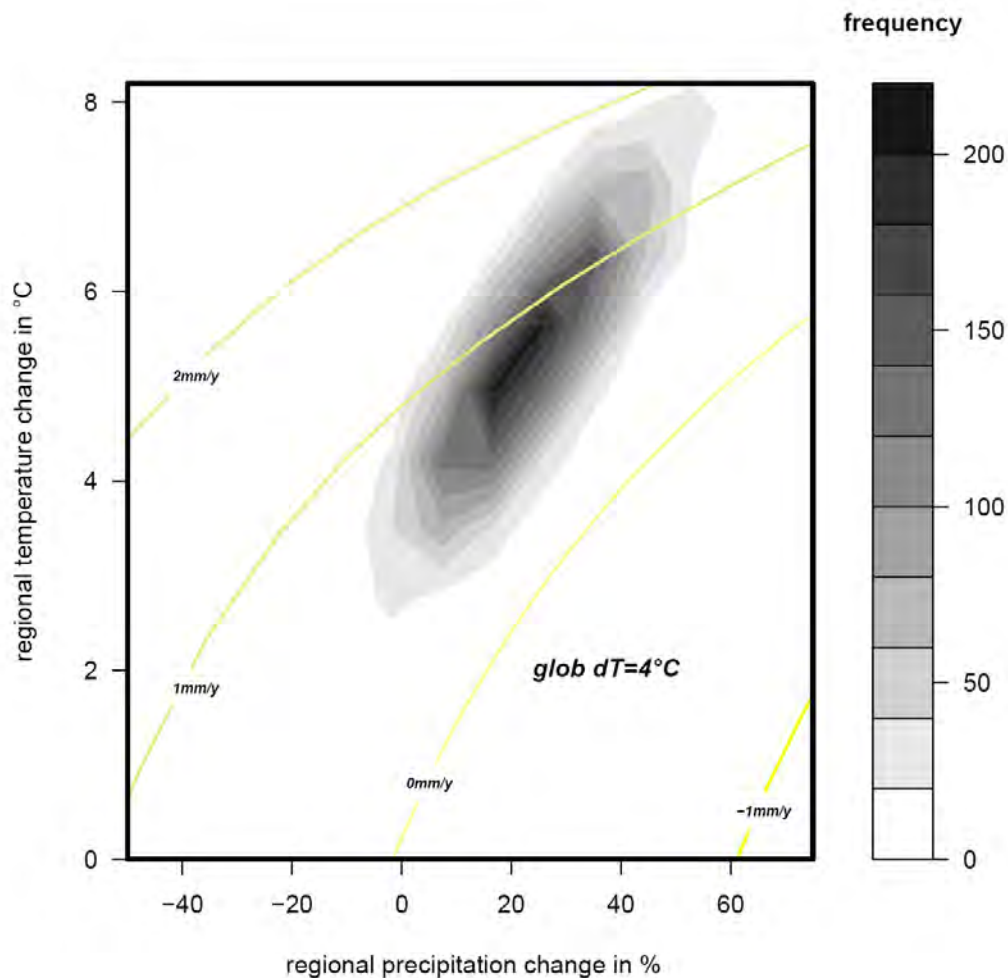
Figure 24: Two-dimensional histogram for four degrees global temperature change and the effect on local temperature and precipitation distributions for METHOD 1. The coefficients are calculated according to the parametric approach (see Chapter 4.3). The frequency on the right side indicate the absolute frequency (own illustration).

In order to obtain a time-independent cumulative distribution function (CDF), it was necessary to calculate the probabilities for a range of global temperatures (here: from 0 to $7°C$, in $0.1°C$ steps) and regional impacts (SLR 0 mm, 0.62 mm, 1 mm, 2 mm, 3 mm all per year) for both methods. These curves increase with rising temperatures. In addition, a calculation of global temperature densities for the three scenarios for two dates (2050, 2100) was carried out. The density curves and approximation curves of the density curves are shown in Figure 25. The ranges for 2050 compared to 2100 are in all three scenarios more concentrated around one
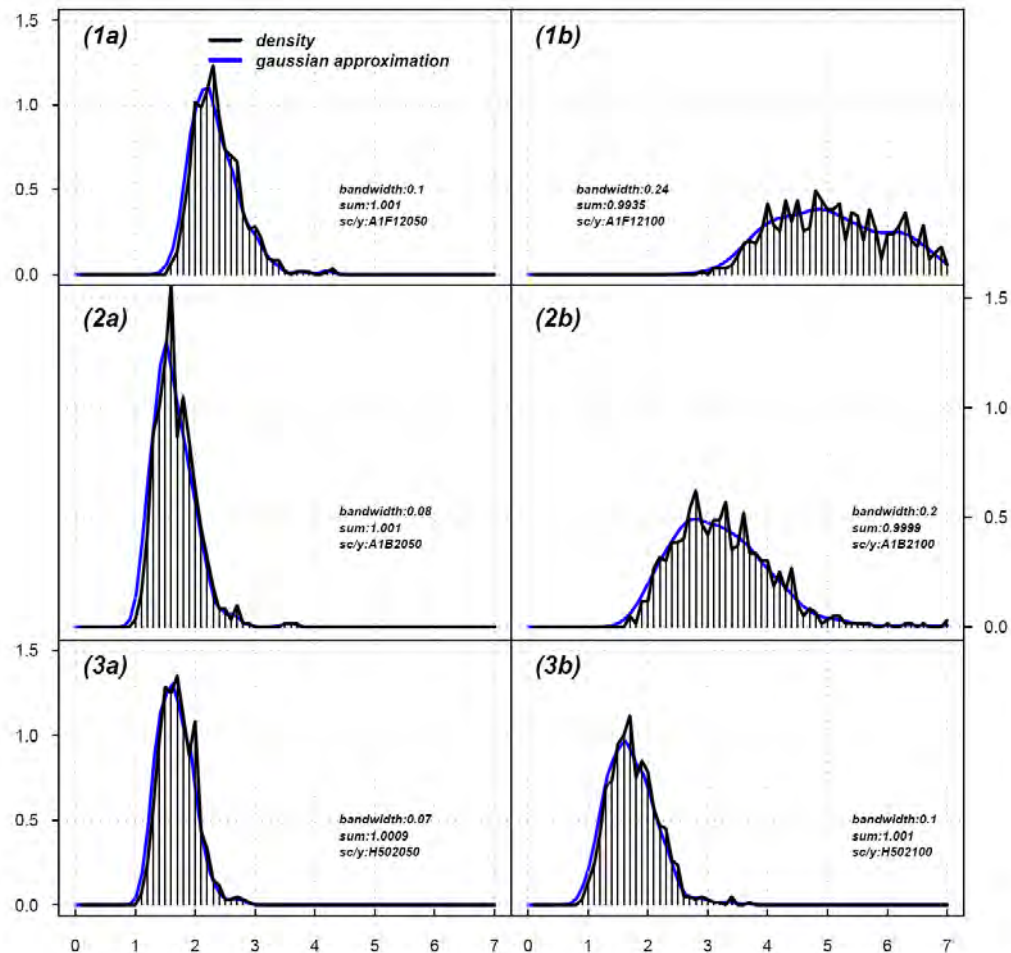
median area.

Figure 25: Density of data in 2050 and 2100 for SRES A1B, A1F1 and H50. In 1a), 2a) and 3a) the curves for 2050 are more concentrated around a median area than in 1b), 2b) and 3b) for 2100. Therefore the uncertainty for temperature change in 2100 is larger. The integrated sum under the density curves must be 1 (own illustration).

A combination of the CDF and the density curves are illustrated in the Figures 26 and 27. In order to get the probabilities for exceeding a certain impact for an individual scenario and year, the relative frequencies are multiplied by the CDF values.

Figure 26 shows the results of the parametric approach for METHOD 1, the appropriate results of probability calculations can be found in Table 8.

The peaks of the density curves for 2050 are concentrated around the lower values of global temperature changes, than the peaks of the CDF function (excl. 0 mm/y). Hence, the results

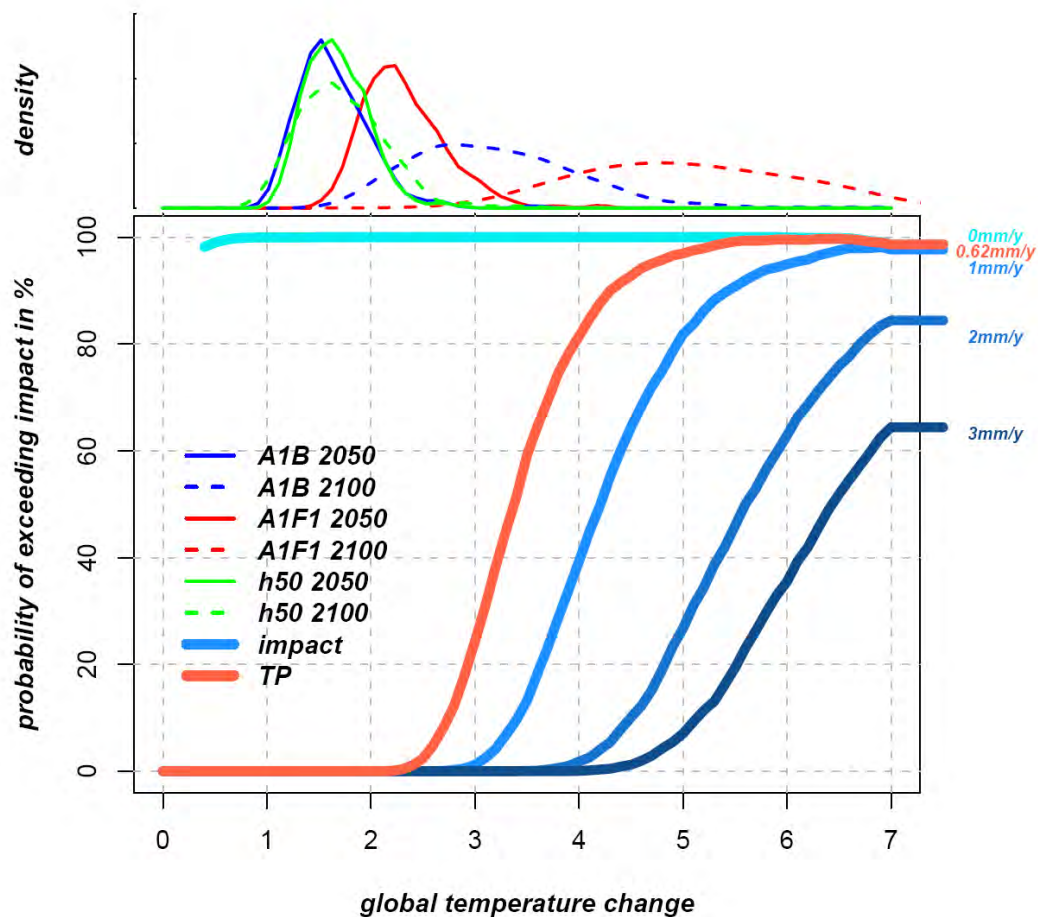for the calculations of probabilities are around 0% for 2050.

Figure 26: CDF and density function according to the parametric approach for METHOD 1. The density functions for 2050 and 2100 of Figure 25 are added on the top of the plot. Every line in the lower part indicate the probabilities for one of the five cases in 0.1°C steps of global temperature change. The cases are 0 mm/y, 0.62 mm/y (tipping point), 1 mm/y, 2 mm/y and 3mm/y. Zero mm per year is exceeded at 100% for all global temperature changes (own illustration).

Table 8: Results of probability calculations of exceeding a certain slr/y following the parametric approach for METHOD 1.

scenario	year	0mm/y	1mm/y	2mm/y	3mm/y	Tipping Point (0.62 mm/y)
A1B	2050	100%	0%	0%	0%	0%
	2100	100%	16.28%	2.3%	1%	40.33%
A1F1	2050	100%	1%	0%	0%	5.61%
	2100	100%	73.16%	32.86%	16.65%	92.40%
H50	2050	100%	0%	0%	0%	0%
	2100	100%	0%	0%	0%	0%

The parametric approach was only applicable to METHOD 1, therefore the following calculations refer to the non-parametric approach. In order to compare both methods, the calculation of the probabilities for one single AOGCM was carried out, and in a further step - for the range of all AOGCMs. Figure 27 shows the impact probabilities for the UKMO-HadCM3 AOGCM. The results (see Table 9) for this AOGCM are close to the results of the parametric approach.
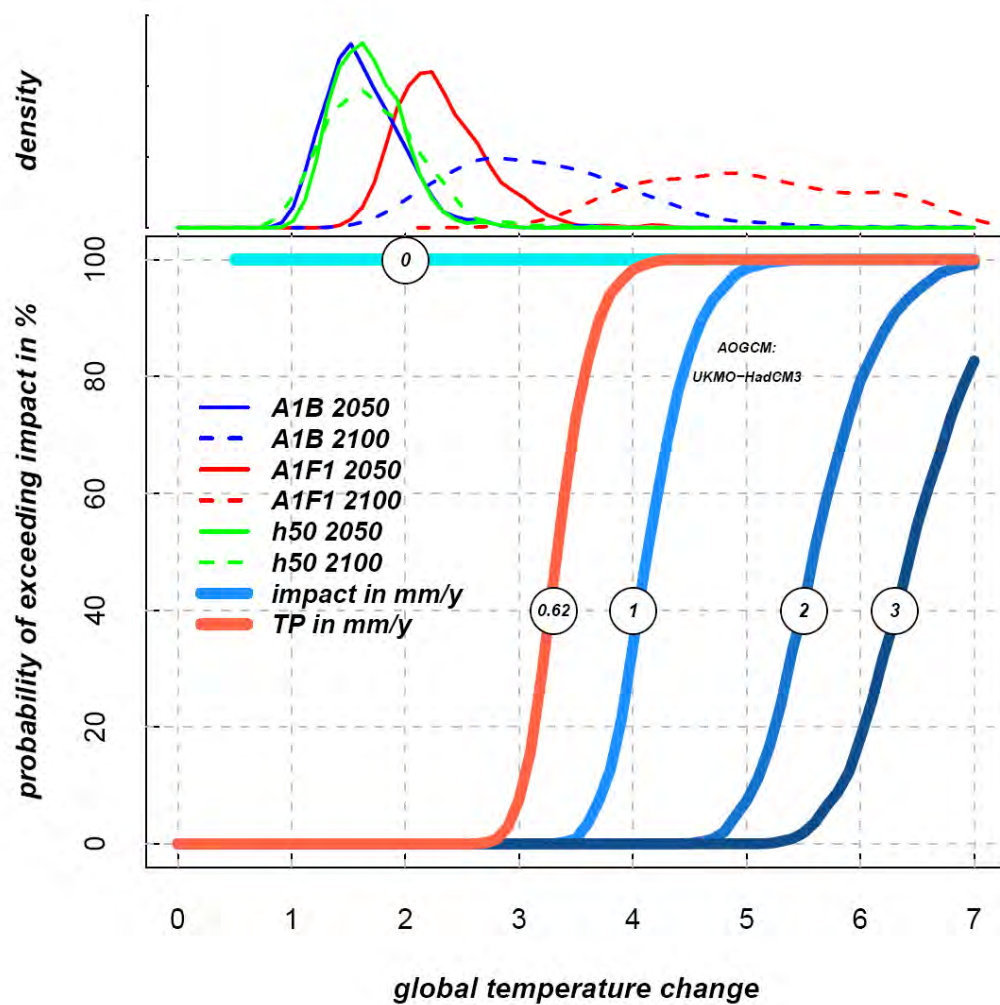
Figure 27: CDF and density function for non-parametric approach according to METHOD 1 for the AOGCM: UKMO-HadCM3. Every line in the lower part indicate the calculated probabilities for one of the five cases in 0.1°C steps of global temperature change. For example: the probability of exceeding the tipping point (0.62 mm/y, labeled in red) at a global temperature change of 3.2°C is 50% (own illustration).

Table 9: Results of probability calculations of exceeding a certain slr/y following the non-parametric approach for AOGCM: UKMO-HadCM3 for METHOD 1.

scenario	year	0 mm/y	1 mm/y	2 mm/y	3 mm/y	Tipping Point (0.62 mm/y)
A1B	2050	100%	0%	0%	0%	0%
	2100	100%	14.19%	1.48%	0%	41.52%
A1F1	2050	100%	0%	0%	0%	2.92%
	2100	100%	80.77%	30.85%	11.01%	97.7%
H50	2050	100%	0%	0%	0%	0%
	2100	100%	0%	0%	0%	0%

The probability for each AOGCM varies because of different assumptions and physical bases of the AOGCMs. Therefore a calculation of CDF for each of the 22 AOGCMs (see Chapter 4.5) was carried out and the minimum, maximum, median, 25th and 75th percentile were detected. The results for the individual CDFs of the AOGCMs are given in the appendix (Figure 37 and Figure 38). For METHOD 1, two outliers are excluded from the CDF ranges: the models GISS-EH and PCM. The GISS-EH is one of the models given in Chapter 4.3 in Figure 15, that shows just a low correlation between global temperature and local temperature change.

Figure 28 shows the results of the probabilities for the different cases (min, max, med, 25, 75). The results for the tipping point indicate that for H50 in both years, no or very low probabilities of exceeding the tipping point are determined. This is also the case for A1B in 2050.

For scenario A1F1 the probability of exceeding the tipping point reaches a maximum of 24 %. For 2100 an exceedance of the tipping point is in all cases very likely (almost 100 %). A bit lower, but likely is the exceedence of the tipping point in A1B by a maximum of 75.85 % (see Table 10).
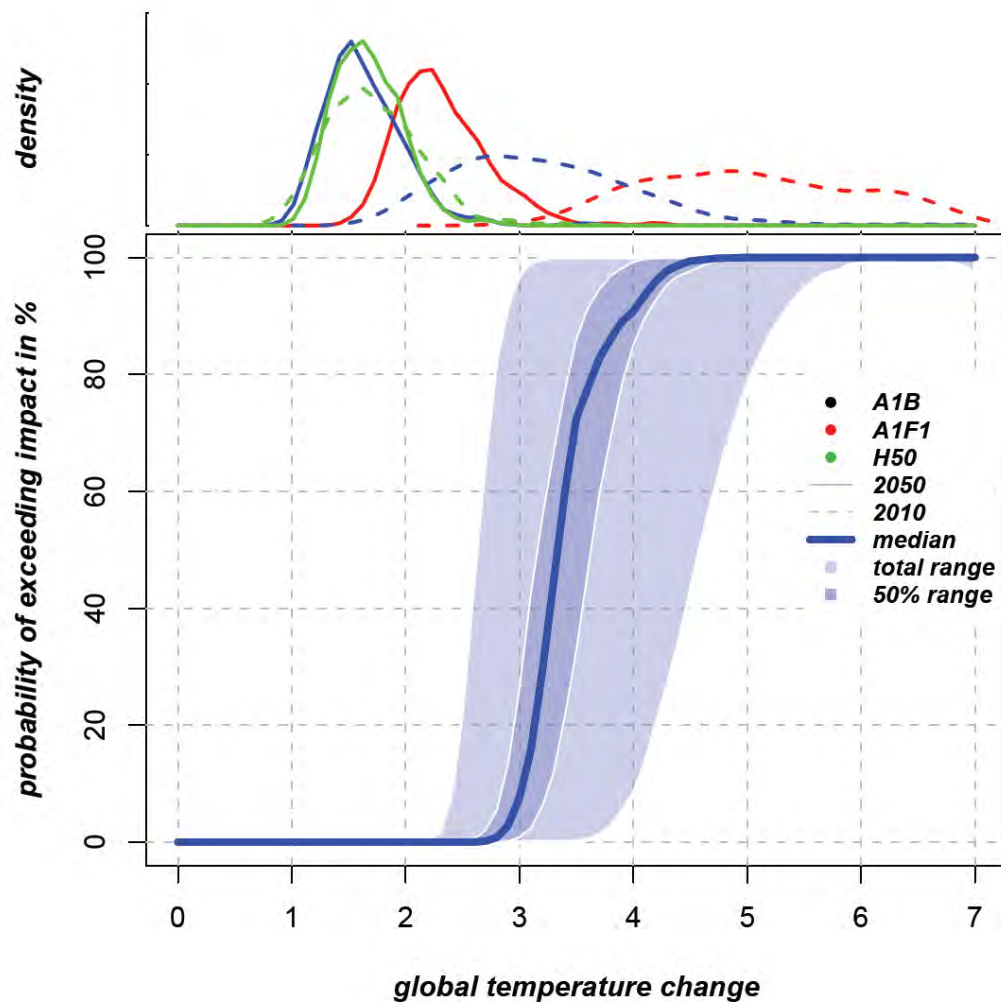
Figure 28: CDF and density function for non-parametric approach according to METHOD 1 for all AOGCMs (excl. GISS-EH and PCM) referring to the exceedance of the tipping point 0.62 mm/y. The area labeled in lightblue shows the range of all AOGCMs (excluding the outliers). The tipping point will be exceeded with a probability of 50 % in a range from 2.7 to 4.6°C global temperature change. The median (bold blue line) of the exceedance probabilities is equal to 50% at 3.2°C global warming (own illustration).

Table 10: Results for probabilities of exceeding 0.62 mm/y SLR for non-parametric approach according to METHOD 1 (all AOGCMs).

scenario	year	Min	Max	Median	25%	75%
A1B	2050	0%	1.9%	0%	0%	0%
	2100	7.36%	75.85%	40.0%	29.37%	48.96%
A1F1	2050	0%	24.38%	2.87%	1.30%	5.27%
	2100	64.64%	99.98%	96.38%	93.11%	98.65%
H50	2050	0%	1.13%	0%	0%	0%
	2100	0%	3.46%	0%	0%	0%

Probabilities for method 2

In this section the calculation of the probabilities for METHOD 2 is carried out. As already described in Chapter 5.2 the values for the sensitivities are much higher compared to METHOD 1. Therefore the expected probabilities for METHOD 2 must be higher than in METHOD 1.
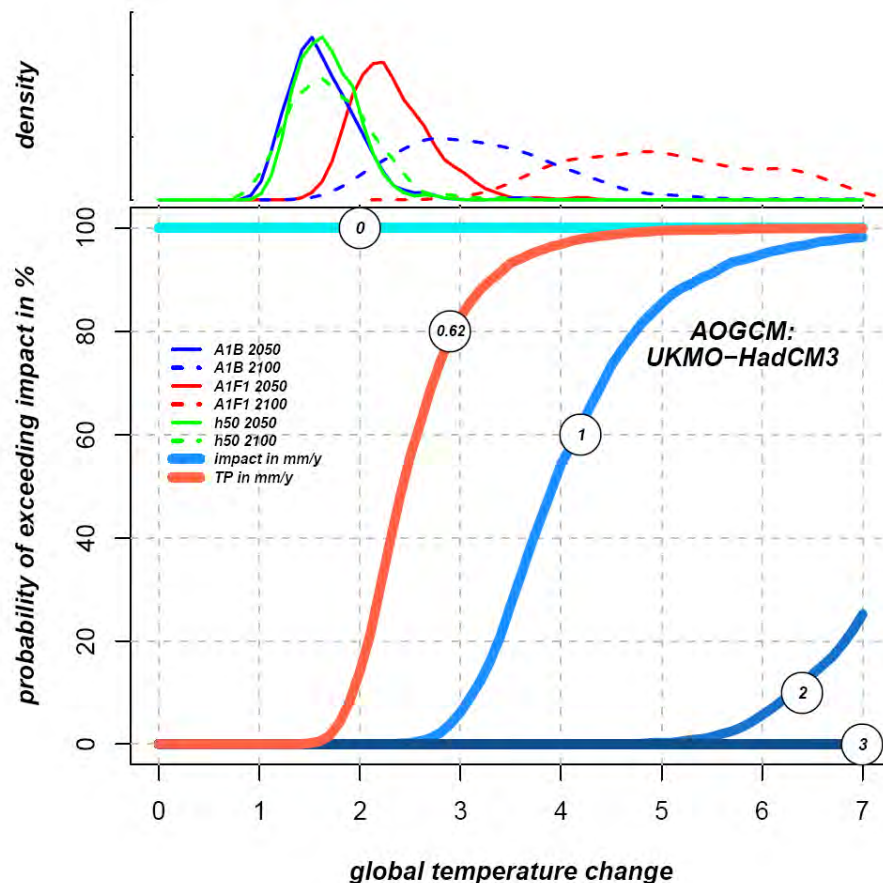

Figure 29: CDF and density function for non-parametric approach according to METHOD 2 for the AOGCM: UKMO-HadCM3. Every line in the lower part indicate the calculated probabilities for one of the five cases in 0.1°C steps of global temperature change. For example: the probability of exceeding the tipping point (0.62 mm/y, labeled in red) at a global temperature change of 2.4°C is 50% (own illustration).

Figure 29 shows the probabilities of exceeding a certain SLR for the UKMO-HadCM3. As already detected for the METHOD 1, the 0 mm/y threshold will be exceeded in all cases. The tipping point will be exceeded in 2050 for A1F1 by 42.4 % probability, in 2100 for A1B by 77.4 % and for A1F1 by 98.6% (see Table 11). The scenario H50 has also a much higher probability of exceeding the tipping point in the year 2100 measuring 11.9 % compared to the

model for METHOD 1.

Table 11: This table shows the results for the probability of exceeding a certain SLR per year according to the non-parametric approach. The selected AOGCM is UKMO-HadCM3 and are calculated for METHOD 2.

scenario	year	0mm/y	1mm/y	2mm/y	3mm/y	Tipping Point(0.62mm/y)
A1B	2050	100%	0%	0%	0%	7.44%
	2100	100%	22.98%	0%	0%	77.38%
A1F1	2050	100%	1.73%	0%	0%	42.37%
	2100	100%	78.47%	15.29%	0%	98.62%
H50	2050	100%	0%	0%	0%	7.28%
	2100	100%	0%	0%	0%	11.85%

As calculated for METHOD 1, the CDF for the different cases of the tipping point are calculated for METHOD 2 as well. The AOGCM: GISS-EH occurs as an outlier like in METHOD 1 and is excluded from the following calculations. The results of METHOD 2 indicate higher probabilities compared to the values of METHOD 1.

In 2050, the probability in all three scenarios for the maximal case, is already above 70 %. In 2100 the maximum, median, 25 % and 75 % quartile cases are all above the 75 % to 99.88% mark (in the maximum case). In the scenario A1F1, for all cases, even in the minimal case, it is very likely that the tipping point will be exceeded. Even in the scenario H50 for the maximum case, there is an 76 % probability of exceeding the tipping point.
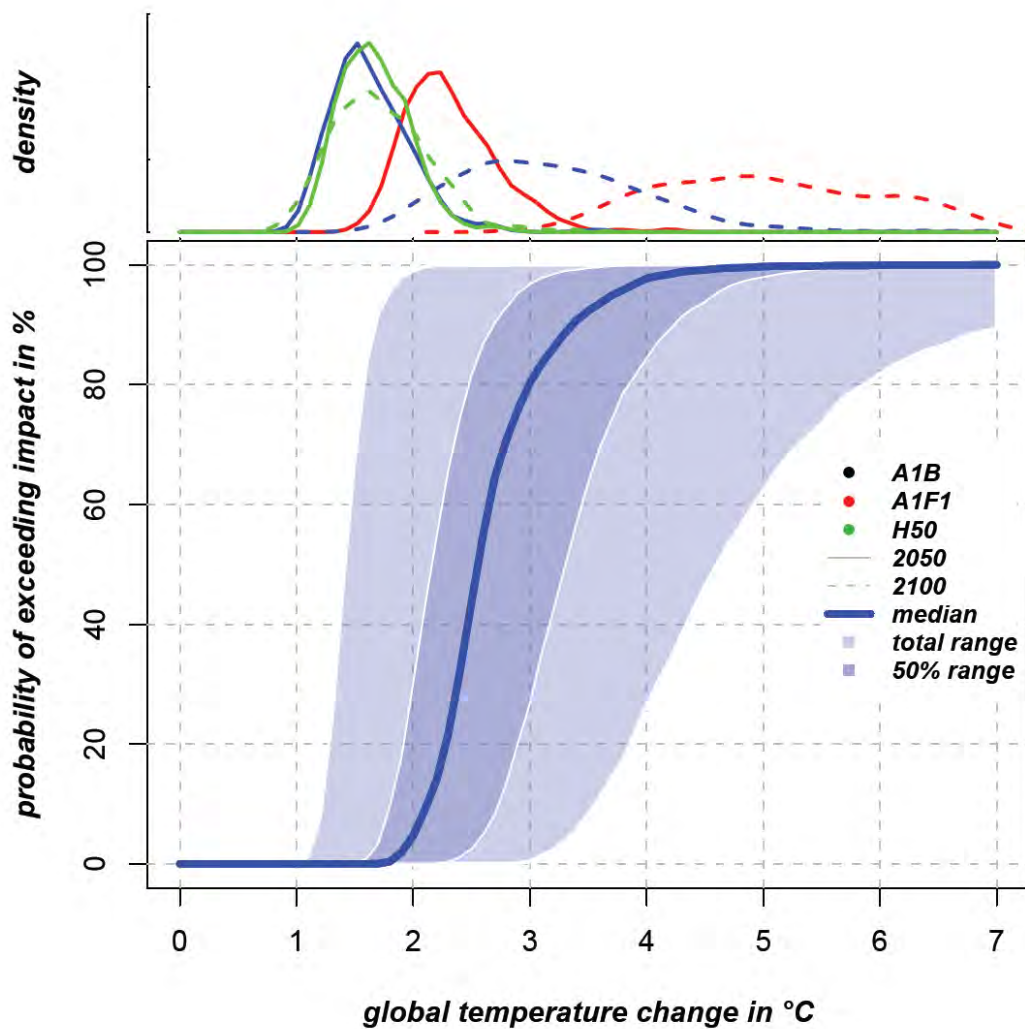
Figure 30: CDF and density function for non-parametric approach according to METHOD 2 for all AOGCMs (excl.GISS-EH) referring to the exceedance of the tipping point 0.62 mm/y. The area labeled in lightblue shows the range of all AOGCMs (excluding the outliers). The tipping point will be exceeded by 50 % in a range from 1.4 to 4.6°C global temperature change. The median (labeled in black) indicate the median probablities for exceeding the tipping point. In this example the 50 % mark will be exceeded at 2.6°C (own illustration).

Table 12: Results for probabilities of exceeding 0.62 mm/y for the non-parametric approach according to METHOD 2 (all AOGCMs).

scenario	year	Min	Max	Median	25%	75%
A1B	2050	0%	74.42%	3.92%	0%	13.05%
	2100	11.27%	99.88%	73.49%	42.60%	89.65%
A1F1	2050	0%	99.33%	32.24%	6.07%	62.36%
	2100	58.28%	100%	98.83%	93.62%	100%
H50	2050	0%	76.76%	3.30%	0%	13.52%
	2100	0%	79.70%	6.95%	0%	19.89%

Both models in a glance

In order to compare both models, in Figure 31 all results from both methods for the tipping point are plotted together. The results for METHOD 2 are in all cases and scenarios higher than the results from METHOD 1. Most of the values for the H50 and A1B 2050 scenario can be found in the lower bound close to zero for both years (2050, 2100). The results for the A1B scenario in 2100 are spread on the whole scale but most of the higher values belong to the results of METHOD 2. The scenario with the highest likelihood is the A1F1 scenario, where all values are located above the 50 % mark and actually most of them close to 100 %. The critical temperature threshold is obtained to be 4 degrees, because in all CDF curves this threshold leads to an exceeding of the tipping point ($0.62mm/y$) above 60%.
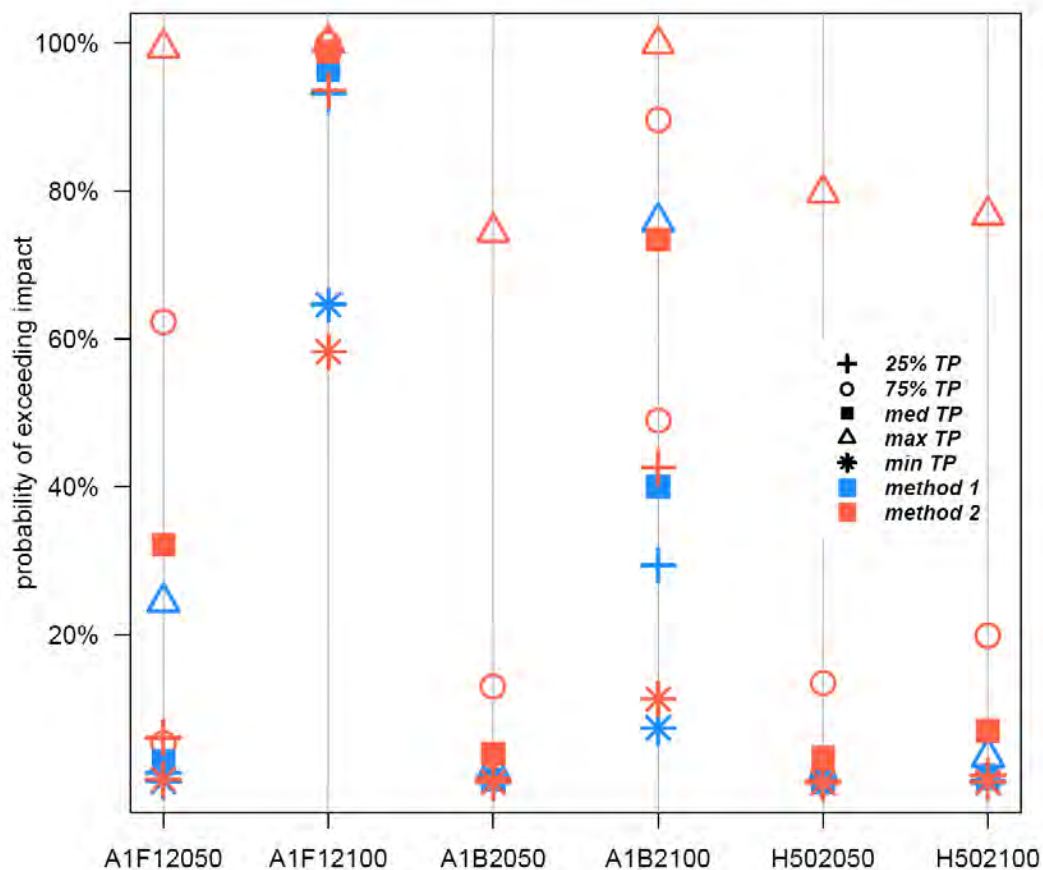
Figure 31: Overview of the results for both methods according to the probability of exceeding the tipping point. The symbols show the different cases, Minimum, Median, Maximum, 25% and 75%. Colored in blue are the results referring to METHOD 1 and in red METHOD 2.

5.4. Limitations

The two SMB methods being compared in this thesis show that there are remarkable differences in sensitivity, time-series and probabilities. Therefore it is difficult to compare the results. This fact might have technical reasons: 1.) errors in the calculations through different assumptions as were made in the source papers (Gregory and Huybrechts, 2006; Fettweis et al., 2008); 2.) use of different source data; 3.) use of a different base-period (instead of 1961-1990 the period 1970-1999 is used for METHOD 1 but this made only a slight difference).

6. Conclusion and Outlook

The key findings of this thesis are based on two existing surface-mass balance modelling methods for future predictions of sea-level rise. These two methods were applied on the MAGICC6.0 climate model and are combined with a pattern scaling approach for calculating regional temperature and precipitation changes. The main focus of this scaling approach is an improvement of the assessment of uncertainty in climate data. By combining cumulative density and relative density it is possible to calculate the probability for exceeding a certain impact. The selected impact here was the ablation of the GIS and the resulting contribution to the global sea level rise in 2050 and 2100. The critical temperature threshold and the appropriate probability for a permanent negative SMB were found by modelling the SMB (accumulation minus ablation).

Employing the use of METHOD 1 according to Gregory and Huybrechts (2006) it was possible to apply the parametric approach (pattern scaling) for determining local temperatures and precipitation changes. The results of this method lead to a tipping point of 4.5 °C global temperature change which will result in 92% probability of exceeding the critical threshold of 0.62 mm/y sea-level rise (relative to present day). This threshold can be reached if the fossil fuel intensive emission pathway, the A1F1 with a stabilizing of 920 ppm CO_2 (current emission 385[17] ppm) in 2100 will be implemented in global climate policies.

For the non-parametric approach the UKMO-HadCM3 AOGCM reaches 100% probability of exceeding the threshold at already 3.5 °C in both methods. Concerning METHOD 1 this is likely even for the midrange scenario A1B in 2100 (41.5 % probability) and for the scenario A1F1 by 97.7%. The higher sensivity determined in METHOD 2 (Fettweis et al., 2008) leads to a value of 77.4% for A1B (it is stabilizing at 720 ppm CO_2 in 2100). This means that even if we could obtain less than double the current CO_2 emissions, an exceedance of the critical threshold (tipping point) would not longer be avoidable. A median from all AOGCMs in both methods leads to a tipping point of 4 °C global temperature change.

The results for the two SMB models show large differences in the probabilities. The reasons for that are different assumptions already made in the two SMB models as for example re-freezing of melt water are not taken into account in the model according to Fettweis et al. (2008), METHOD 2. Even though, this approach uses a surface energy balance model, the influence of the simplification for calculating future predictions, play an important role and could influence the sensitivity (as shown in Table 7). On the other hand, the use of different

---

[17]National Oceanic and Atmospheric Administration (NOAA),
    http://www.noaanews.noaa.gov/stories2008/20080423methane.html

regions (METHOD 1, the whole area and METHOD 2, Region 1 and 2) for the calculations imply differences in temperature and precipitation data.

Changes in dynamics were not considered which would modify the results obtained. Mass-loss through ice-discharge is almost balanced by the current SMB (Church et al., 2001) that would lead to a zero total mass balance. However, observations from the last 20-30 years reveal a negative total mass balance (see section 2.4 Table 1). The mass-loss through ice-discharge could raise the probability of exceeding the critical threshold even in the next 20 years despite following the low emission scenarios of H50. But these dynamic trends are uncertain and up till now it is difficult to include them in a mass balance model.

However, further research could be carried out to include the assumptions of dynamics in the calculations e. g. as a fixed term. Although the GIS is expected to disappear earlier and faster than the Antarctic ice sheet they have to be regarded together. The most serious concerns arise from the Western part of the Antarctic ice-sheet, where a mass-loss from ice-shelves followed by ice-streams has been noted during the last decade (Rignot and Kanagaratnam, 2006). On the other hand, current estimations display a negative contribution to the rise of global sea level through the whole antarctic ice-sheet (Gregory and Huybrechts, 2006).

ACIA (2004). Impacts of a Warming Arctic-Arctic Climate Impact Assessment. *Impacts of a Warming Arctic-Arctic Climate Impact Assessment: Arctic Climate Impact Assessment 1*, 144.

Albertz, J. (2000). *Einführung in die Fernerkundung Grundlagen der Interpretation von Luft- und Satellitenbildern*. Wiss. Buchges.

Alley, R., M. Spencer, and S. Anandakrishnan (2007). Ice-sheet mass balance: assessment, attribution and prognosis. *Annals of Glaciology 46*, 1–7.

Alley, R. B., D. A. Meese, C. A. Shuman, A. J. Gow, K. C. Taylor, P. M. Grootes, J. W. C. White, M. Ram, E. D. Waddington, P. A. Mayewski, and G. A. Zielinski (1993, April). Abrupt increase in greenland snow accumulation at the end of the younger dryas event. *Nature 362*(6420), 527–529.

Bamber, J. and A. Payne (Eds.) (2004). *Mass Balance of the Cryosphere - Observations and Modelling of Contemporary and Future Changes*. Cambridge University Press.

Bamber, J., E. Steig, and D. Dahl-Jensen (2009). What is the tipping point for the greenland ice sheet? *IOP Conference Series: Earth and Environmental Science 6*(6), 062007 (1pp).

Berner, J., C. Symon, L. Arris, O. Heal, Arctic, National, and United (2005). *Arctic climate impact assessment*. Cambridge University Press.

Box, J., D. Bromwich, and L. Bai (2004). Greenland ice sheet surface mass balance 1991–2000: Application of Polar MM5 mesoscale model and in situ data. *J. Geophys. Res 109*(D16).

Box, J., D. Bromwich, B. Veenhuis, L. Bai, J. Stroeve, J. Rogers, K. Steffen, T. Haran, and S. Wang (2006). Greenland ice sheet surface mass balance variability (1988–2004) from calibrated Polar MM5 output. *Journal of Climate 19*(12), 2783–2800.

Braithwaite, R. (1995). Aerodynamic stability and turbulent sensible-heat flux over a melting ice surface, the Greenland ice sheet. *Journal of Glaciology 41*(139), 562–571.

Chen, J. L., C. R. Wilson, and B. D. Tapley (2006, September). Satellite gravity measurements confirm accelerated melting of greenland ice sheet. *Science 313*(5795), 1958–1960.

Church, J.A .and Gregory, J., P. Huybrechts, M. Kuhn, K. Lambeck, M. Nhuan, D. Qin, and P. Woodworth (2001). Changes in sea level in climate change 2001: The scientific basis. *Contribution of Working Group I to the Third Assessment Report of the Intergovernmental Panel on Climate Change [Houghton J.T. et al]*, 639–693.

Fettweis, X. (2007). Reconstruction of the 1979 to 2006 greenland ice sheet surface mass balance using the regional climate model mar. *The Cryosphere 1*, 21–40.

Fettweis, X., E. Hanna, P. Huybrechts, H. Gallee, and M. Erpicum (2008). Estimation of the greenland ice sheet surface mass balance for the 20th and 21st century. *The Cryosphere 2*, 117–129.

Freedman, D., R. Purves, and R. Pisani (2007, 2). *Statistics, 4th Edition* (4th ed.). W.W. Norton & Co.

Gregory, J. and P. Huybrechts (2006, May). Ice-sheet contributions to future sea-level change. *Philosophical Transactions of the Royal Society 364*, 1709–1731.

Greuell, W. and C. Genthon (2004). *Mass Balance of the Cryosphere*, Chapter Chapter 5 'Modelling land-ice surface mass balance', pp. 117–168. Cambridge University Press.

Hagen, J. and N. Reeh (2004). *Mass Balance of the Cryosphere*, Chapter Chapter 2.'In situ measurement techniques:land-ice', pp. 23–41. Cambridge University Press.

Hanna, E., P. Huybrechts, I. Janssens, J. Cappelen, K. Steffen, and A. Stephens (2005). Runoff and mass balance of the Greenland ice sheet: 1958–2003. *J. Geophys. Res 110*, D13108.

Hubbard, B. and N. Glasser (2005). *Field techniques in glaciology and glacial geomorphology*. Wiley.

Huybrechts, P. and H. Miller (2005). *13 Flow and balance of the polar ice sheets*, Chapter 13, pp. 1–13. Springer.

IPCC (2007, July). *Climate Change 2007 - The Physical Science Basis: Working Group I Contribution to the Fourth Assessment Report of the IPCC (Climate Change 2007)*. Cambridge University Press.

Janssens, I. and P. Huybrechts (January 2000). The treatment of meltwater retention in mass-balance parameterizations of the greenland ice sheet. *Annals of Glaciology 31*, 133–140(8).

Johannessen, O. M., K. Khvorostovsky, M. W. Miles, and L. P. Bobylev (2005, November). Recent ice-sheet growth in the interior of greenland. *Science 310*(5750), 1013–1016.

Krabill, W., W. Abdalati, E. Frederick, S. Manizade, C. Martin, J. Sonntag, R. Swift, R. Thomas, W. Wright, and J. Yungel (2000, July). Greenland ice sheet: High-elevation balance and peripheral thinning. *Science 289*(5478), 428–430.

Krabill, W., E. Hanna, P. Huybrechts, W. Abdalati, J. Cappelen, B. Csatho, E. Frederick,

S. Manizade, C. Martin, J. Sonntag, et al. (2004). Greenland ice sheet: increased coastal thinning. *Geophys. Res. Lett 31*, L24402.

Lemke, P., J. Ren, R. Alley, I. Allison, J. Carrasco, G. Flato, Y. Fujii, G. Kaser, P. Mote, R. Thomas, et al. (2007). Observations: changes in snow, ice and frozen ground. *Titel: Climate change -*, 337–383.

Lenton, T. M., H. Held, E. Kriegler, J. W. Hall, W. Lucht, S. Rahmstorf, and H. J. Schellnhuber (2008, February). Tipping elements in the earth's climate system. *Proceedings of the National Academy of Sciences 105*(6), 1786–1793.

Luthcke, S. B., H. J. Zwally, W. Abdalati, D. D. Rowlands, R. D. Ray, R. S. Nerem, F. G. Lemoine, J. J. McCarthy, and D. S. Chinn (2006, November). Recent greenland ice mass loss by drainage system from satellite gravity observations. *Science 314*(5803), 1286–1289.

Mayer, C. and H. Oerter (2006). *Warnsignale aus den Polarregionen*, Chapter 2.6 Die Massenbilanzen des Antarktischen und Grönländischen Inlandeises und der Charakter ihrer Veränderungen., pp. 92–96. Lozan,J.L., Grassl,H., Hubberten,H.-W., Hupfer,P., Karbe,L., Piepenburg,D.

Meehl, G., T. Stocker, W. Collins, P. Friedlingstein, A. Gaye, J. Gregory, A. Kitoh, R. Knutti, J. Murphy, A. Noda, S. C. Raper, I. Watterson, A. Weaver, and Z.-C. Zhao (2007). *In:Climate Change 2007: the physical science basis: contribution of Working Group I to the Fourth Assessment Report of the Intergovernmental Panel on Climate Change*, Chapter 10.Global Climate Projections, pp. 748–840. Cambridge University Press.

Meinshausen, M., , and S. C. T. M. L. W. Raper (2008). Emulating ipcc ar4 atmosphereocean and carbon cycle models for projecting global-mean, hemispheric and land/ocean temperatures: Magicc 6.0. *Atmos. Chem. Phys. Discuss 8*, 6153–6272.

Meinshausen, M., N. Meinshausen, W. Hare, S. C. B. Raper, K. Frieler, R. Knutti, D. J. Frame, and M. R. Allen (2009, April). Greenhouse-gas emission targets for limiting global warming to 2 degrees. *Nature 458*(7242), 1158–1162.

Murphy, J., D. Sexton, G. Jenkins, P. Boorman, B. Booth, R. Brown, C.C.and Clark, M. Collins, G. Harris, E. Kendon, R. Betts, S. Brown, T. P. Howard, K. A. Humphrey, M. P. McCarthy, R. E. McDonald, A. Stephens, C. Wallace, R. Warren, R. Wilby, and R. A. Wood (2009). *UK Climate Projections Science Report: Climate change projections.* Met Offce Hadley Centre, Exeter.

Nakicenovic, N. and R. Swart (2005). Special report on emissions scenarios. *Cambridge University Press. 598 1*, 598.

Ohmura, A. (1997). New temperature distribution maps for Greenland. *Zeitschrift für Gletscherkunde und Glazialgeologie 23*(1), 1–45.

Ohmura, A., P. Calanca, M. Wild, and M. Anklin (1999). Precipitation, accumulation and mass balance of the Greenland ice sheet. With 5 figures. *Zeitschrift fur Gletscherkunde und Glazialgeologie 35*(1), 1–20.

Pittock, A. B., R. N. Jones, and C. D. Mitchell (2001, September). Probabilities will help us plan for climate change. *Nature 413*(6853), 249–249.

Rahmstorf, S., M. Crucifix, A. Ganopolski, H. Goosse, I. Kamenkovich, R. Knutti, G. Lohmann, R. Marsh, L. Mysak, Z. Wang, et al. (2005). Thermohaline circulation hysteresis: A model intercomparison. *Geophys. Res. Lett 32*, L23605.

Ramillien, G., A. Lombard, A. Cazenave, E. Ivins, M. Llubes, F. Remy, and R. Biancale (2006). Interannual variations of the mass balance of the Antarctica and Greenland ice sheets from GRACE. *Global and Planetary Change 53*(3), 198–208.

Reeh, N., C. Mayer, H. Miller, H. H. Thomsen, and A. Weidick (1999). Present and past climate control on fjord glaciations in greenland: Implications for ird-deposition in the sea. *Geophys. Res. Lett. 26*, –.

Rignot, E. and P. Kanagaratnam (2006, February). Changes in the velocity structure of the greenland ice sheet. *Science 311*(5763), 986–990.

Solomon, S., D. Qin, M. Manning, M. Marquis, K. Averyt, M. Tignor, H. Miller, and Z. Chen (2007). *Climate change 2007: the physical science basis; Contribution of Working Group I to the fourth Assessment Report of the Intergovenmental Panel on Climate Change*. Cambridge Univ. Press.

The National Research Council (2002). Abrupt climate change: Inevitable surprises. Technical report, The National Research Council.

Thomas, R., W. Abdalati, E. Frederick, W. Krabill, S. Manizade, and K. Steffen (2003). Investigation OF Surface Melting AND Dynamic Thinning ON Jakobshavns Isbrae, Greenland. In *Program for Arctic Regional Climate Assessment (PARCA) Greenland Science and Planning Meeting January 14-15, 2003 Byrd Polar Research Center The Ohio State University*, pp. 38.

Thomas, R., E. Frederick, W. Krabill, S. Manizade, and C. Martin (2006). Progressive increase in ice loss from Greenland. *Geophys. Res. Lett 33*(10), L10503.

Van de Wal, R. (2004). *Mass Balance of the Cryosphere*, Chapter 11."'Greenland:modelling"', pp. 437–456. Cambridge University Press.

Velicogna, I. and J. Wahr (2005). Greenland mass balance from GRACE. *Geophys. Res. Lett 32*, L18505.

Velicogna, I. and J. Wahr (2006, September). Acceleration of greenland ice mass loss in spring 2004. *Nature 443*(7109), 329–331.

Zwally, H., M. Giovinetto, J. Li, H. Cornejo, M. Beckley, A. Brenner, J. Saba, and D. Yi (2005). Mass changes of the Greenland and Antarctic ice sheets and shelves and contributions to sea-level rise: 1992-2002. *Journal of Glaciology 51*(175), 509.

A. Scenario specific time-series for precipitation, temperature and sea-level rise
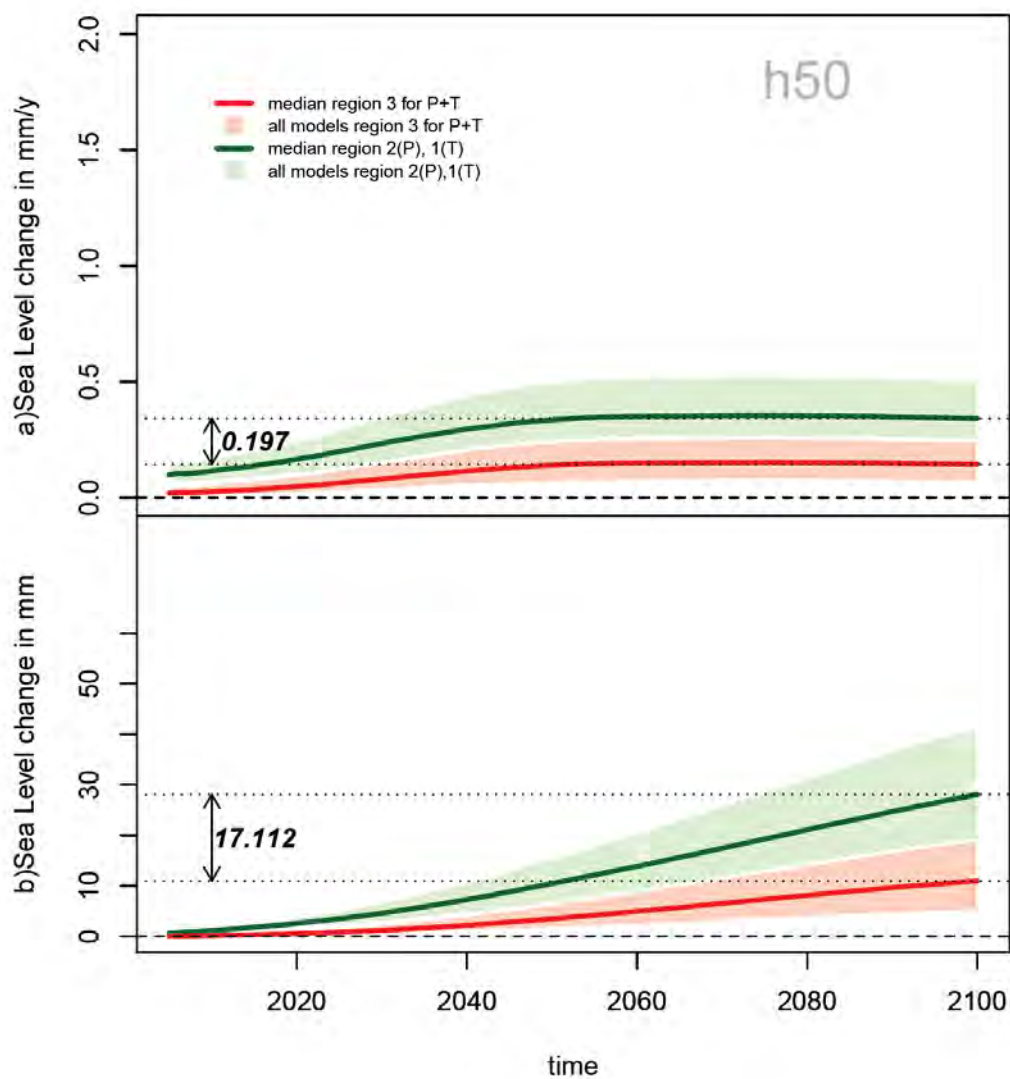

Figure 32: Sea Level change over the period 2005 to 2100 in scenario H50, a.) the Sea Level change in mm/y for METHOD 1 relating to the whole area of GIS(labelled as region 3) and for METHOD 2 relating to *R*egion 1 and b.) is the total Sea Level change until 2100 for both methods. Labeled in light green is the range of all medians of the 22 AOGCMs for METHOD 2, labeled in red is METHOD 1. The bold numbers indicate the resulting differences between the two methods in 2100.
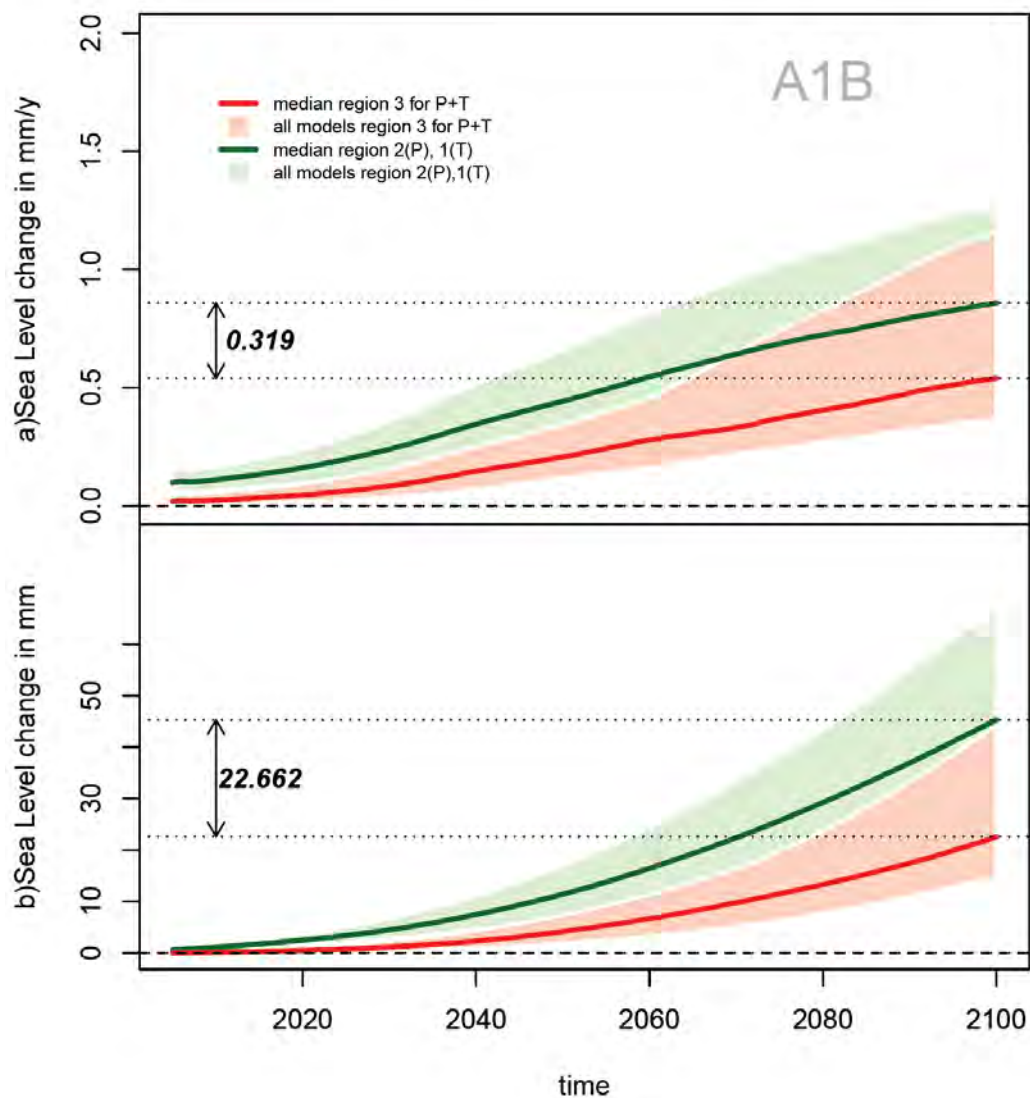
Figure 33: Sea Level change over the period 2005 to 2100 in scenario A1B, a.) the Sea Level change in mm/y for METHOD 1 relating to the whole area of GIS(labelled as region 3) and for METHOD 2 relating to *R*egion 1 and b.) is the total Sea Level change until 2100 for both methods. Labeled in light green is the range of all medians of the 22 AOGCMs for METHOD 2, labeled in red is METHOD 1. The bold numbers indicate the resulting differences between the two methods in 2100.
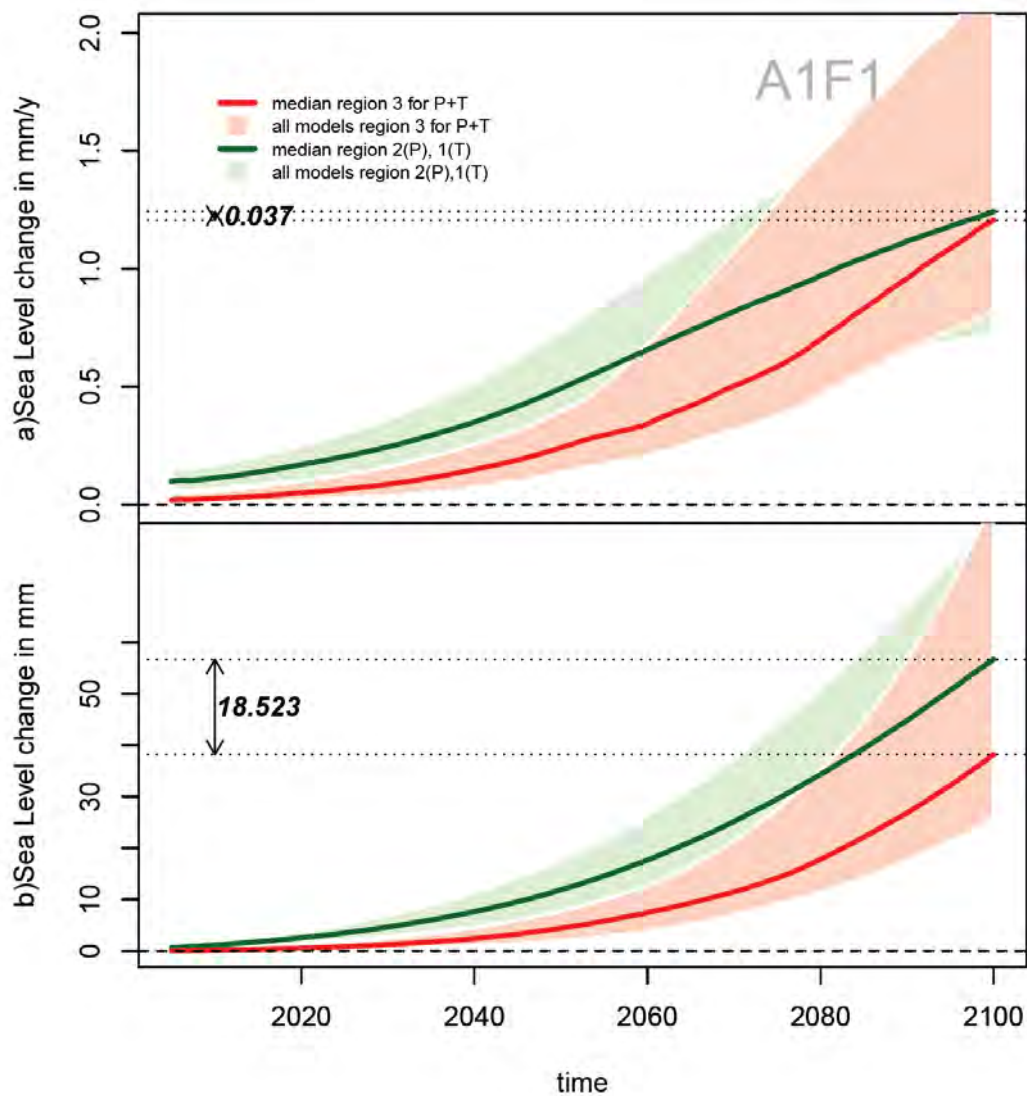
Figure 34: Sea Level change over the period 2005 to 2100 in scenario A1F1, a.) the Sea Level change in mm/y for METHOD 1 relating to the whole area of GIS(labelled as region 3) and for METHOD 2 relating to Region 1 and b.) is the total Sea Level change until 2100 for both methods. Labeled in light green is the range of all medians of the 22 AOGCMs for METHOD 2, labeled in red is METHOD 1. The bold numbers indicate the resulting differences between the two methods in 2100.
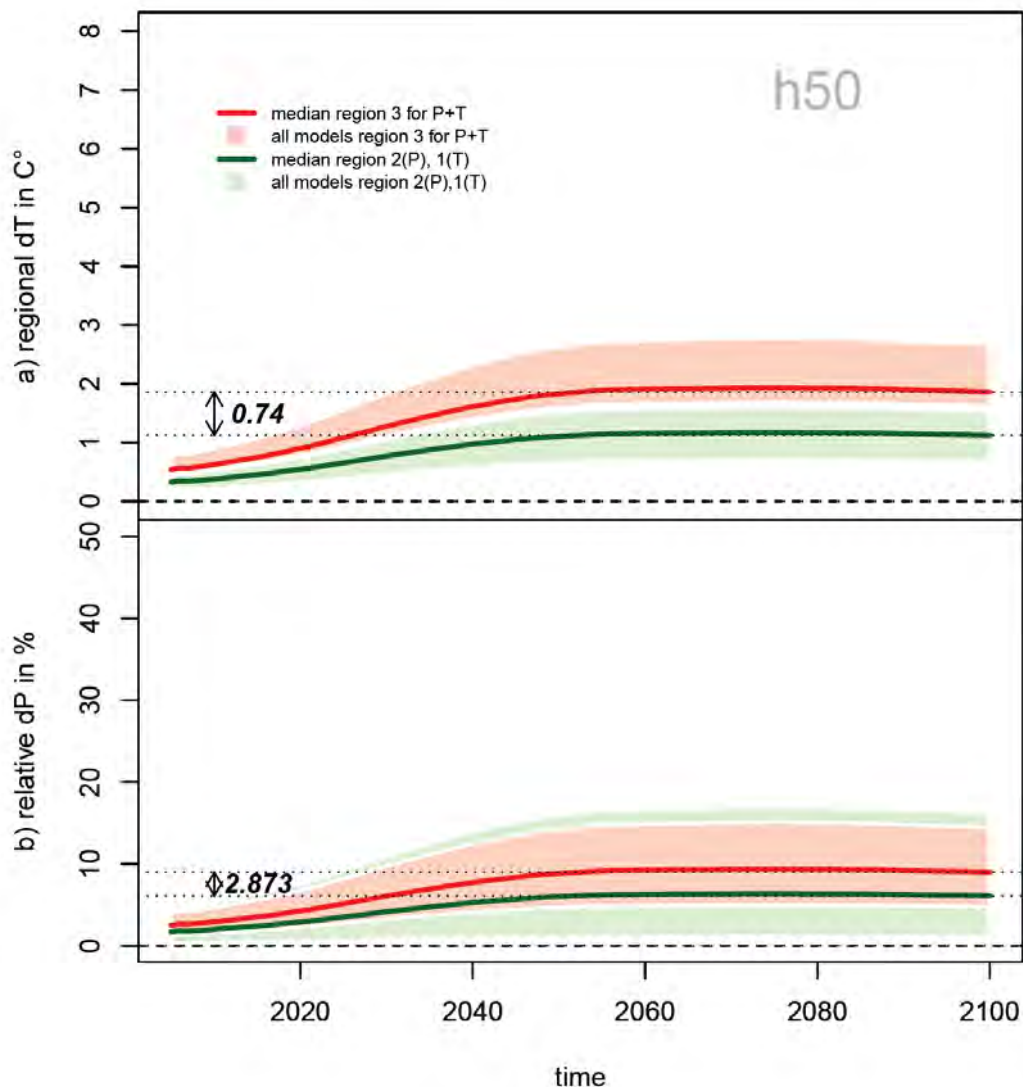
Figure 35: Precipitation and temperature change over the period 2005 to 2100 in scenario H50, a.) the regional annual temperature change for METHOD 1 relating to the whole area (labelled as region 3) and for METHOD 2 (the summer-JJA-temperature) relating to *R*egion 1 and b.) is the precipitation change (both method use the annual precipitation changes) but different regions (results of METHOD 1 are relating to the whole ice sheet and METHOD 2 is). Labeled in light green is the range of all medians of the 22 AOGCMs for METHOD 2, labeled in red is METHOD 1. The bold numbers indicate the resulting differences between the two methods in 2100.
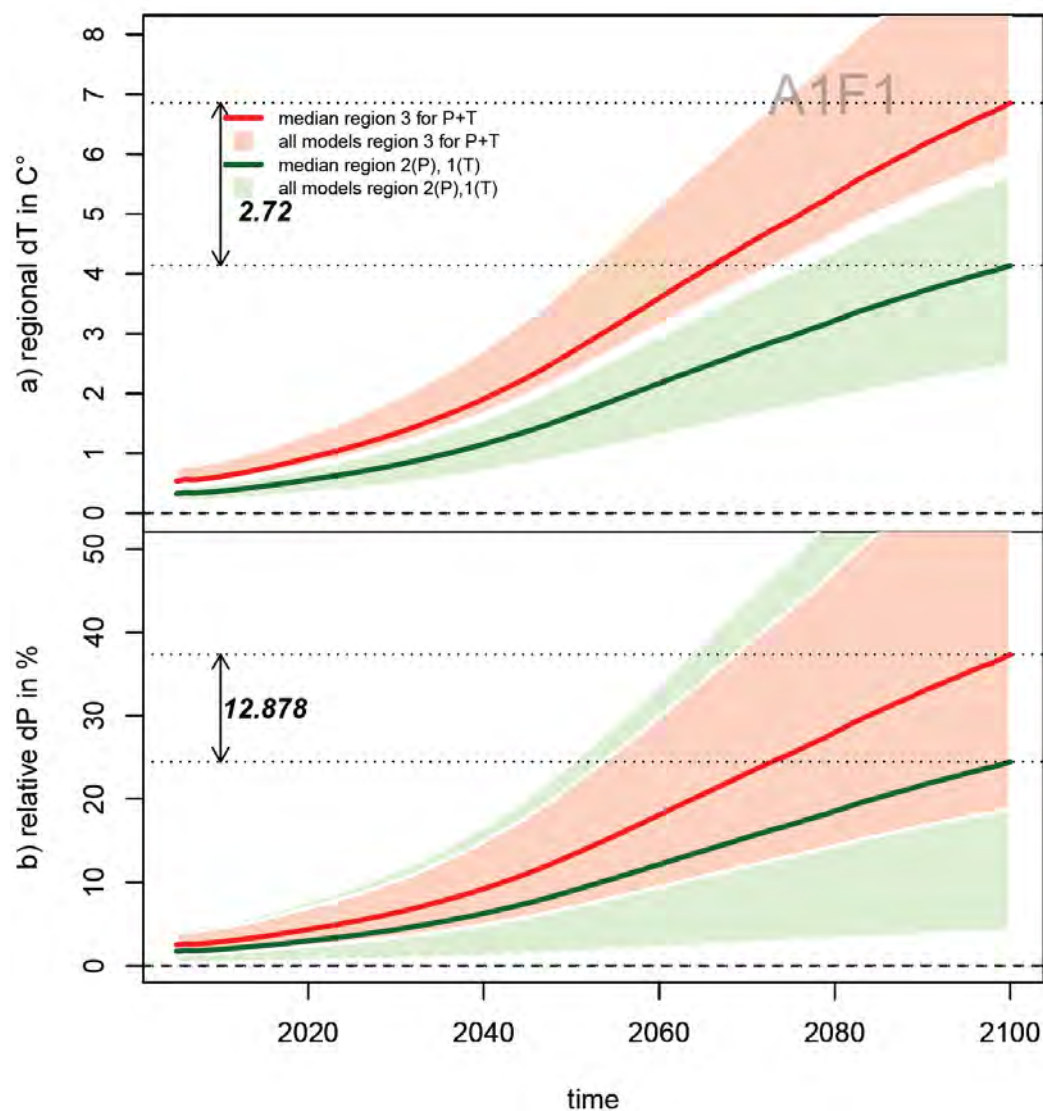
Figure 36: Precipitation and temperature change over the period 2005 to 2100 in scenario A1F1, a.) the regional annual temperature change for METHOD 1 relating to the whole area (labelled as region 3) and for METHOD 2 (the summer-JJA-temperature) relating to Region 1 and b.) is the precipitation change (both method use the annual precipitation changes) but different regions (results of METHOD 1 are relating to the whole ice sheet and METHOD 2 is). Labeled in light green is the range of all medians of the 22 AOGCMs for METHOD 2, labeled in red is METHOD 1. The bold numbers indicate the resulting differences between the two methods in 2100.

B. CDF for each AOGCM

Figure 37: CDF for METHOD 2 for each AOGCM. Each colored line represent the median probability of a single AOGCM. The bold red line is the median of all 22 AOGCMs. The probability refer to an exceeding of the tipping point (0.62 mm/y) at a certain global temperature change.
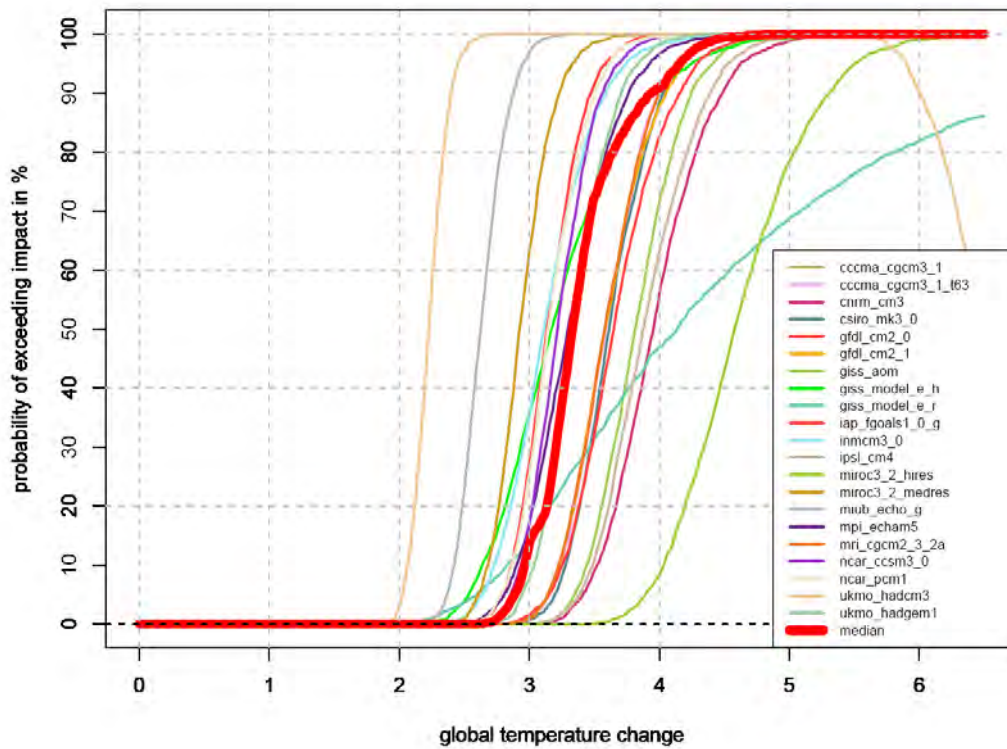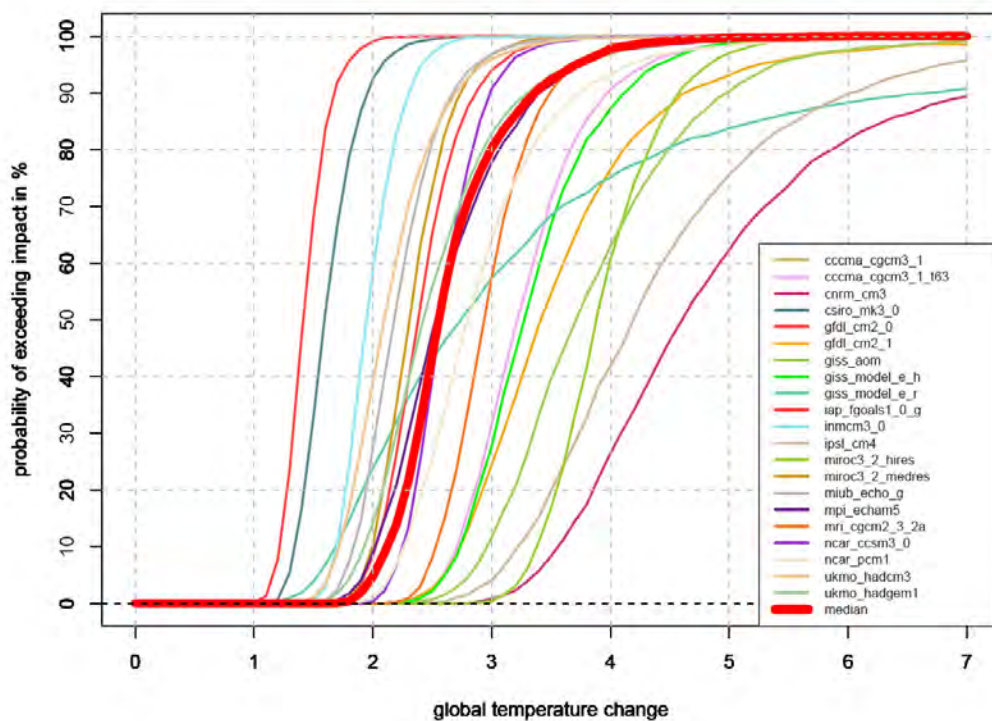
Figure 38: CDF for METHOD 1 for each AOGCM. Each colored line represent the median probability of a single AOGCM. The bold red line is the median of all 22 AOGCMs. The probability refer to an exceeding of the tipping point (0.62 mm/y) at a certain global temperature change.

Chapter 8 Sea Level Rise

Probabilistic projections of sea-level change along the world's coastlines

Mahé Perrette[1*], Riccardo Riva[2], Felix Landerer[3], Katja Frieler[1], Malte Meinshausen[1]

1Potsdam Institute for Climate Impact Research (PIK)

Telegraphenberg A 26, 14412, Potsdam, Germany

2 Delft University of Technology, Delft, Netherlands

3 Jet Propulsion Laboratory / California Institute of Technology, Pasadena, USA

This part of the UFOPLAN work is documented in the manuscript by M. Perrette et al. "Probabilistic projections of regional sea-level rise", to be submitted to Proceedings of the National Academy of Sciences when this report was finalized.

Abstract

Climate change causes global mean sea level to rise due to thermal expansion of seawater[1] and loss of land ice from mountain glaciers, ice caps[2,3] and ice-sheets[4,5]. Locally, where impacts occur, sea-level changes can strongly deviate from the global mean due to ocean dynamics[6-9]. In addition, gravitational adjustments redistribute seawater away from shrinking ice masses[10-12], an effect currently not incorporated in climate models[13]. Here, we provide probabilistic projections of sea level change along the world's coastlines for the 21st century, taking into account uncertainties across the cause-effect chain from greenhouse-gas emissions to ocean heat uptake and regional land-ice melt. At low latitudes, especially in the Indian Ocean and Western Pacific, sea level will likely rise more than the global mean (by 10-20%, possibly up to 45% in Tokyo area). Around the North Atlantic and the North-Eastern Pacific coasts, sea level will rise less than average or, in extreme cases, even drop. Despite large uncertainties for the ice-sheet contributions, the pattern of relative sea level change along the coastlines appears robust. Our probabilistic regional sea level projections provide an improved basis for consistent coastal impact analysis and infrastructure planning for adaptation to climate change.

Analysis

The current understanding of sea-level rise (SLR) remains incomplete as manifested by the inability to close the 20th century sea-level budget in the last IPCC report[13], as well as by the large uncertainty in 21st century projections[14,15]. Current process-based projections can constrain ocean thermal expansion and the retreat of mountain glaciers and ice caps

(MGIC). However, simulations of the Greenland and Antarctic ice-sheets (GIS & AIS) are typically reduced to surface mass balance and slow-evolving components while neglecting fast ice dynamics[4,16]. At the regional level, changes in the ocean's dynamics and density structure due to water temperature and salinity changes (so-called steric changes) have a significant effect[6-9]. The projected regional distribution of steric SLR is highly non-uniform, and deviations from the global mean may be of the same order of magnitude as the global thermal expansion[7]. However, the simulated spatial SLR patterns vary greatly across coupled climate models (GCMs)[8]. In addition to ocean dynamical changes, the shrinking of continental ice masses is accompanied by an instantaneous adjustment of the Earth's gravity field that causes water to migrate away from dwindling ice masses[5,10-12]. The Earth's shape and rotation vector are also affected and further modulate sea-level changes. The number and complexity of processes involved in regional SLR make it difficult to approach the problem in a comprehensive and consistent manner, and subcomponents have so far been treated independently, with the exception of ref 17. In particular, gravitational patterns were long absent from international syntheses such as the IPCC reports, and have received more attention only recently[17,18].

Here, we assess 21st century regional SLR in a consistent probabilistic framework on a global domain. Our general approach is to use probabilistic projections of the global mean contribution of each SLR component (Fig. 1e-h) to scale the associated spatial pattern (Fig. 1a-d). By propagating uncertainties from greenhouse-gas emissions to global and regional SLR, our approach provides an integrated uncertainty analysis – going beyond previous analyses of model ensembles for SRES scenarios[17]. We base regional variations of sea-level

due to ocean density and circulation changes on 12 GCMs from the Coupled Model Intercomparison Project (CMIP3)[19]. For each GCM, we derive a normalized pattern of SLR rise as a function of global mean surface air temperature change based on the SRES A1B scenario. These patterns are then combined with probabilistic temperature projections for the new representative concentration pathways[20] (RCP) to be used in the forthcoming IPCC AR5 report (see methods and supplementary information, SI, for robustness tests with other scenarios). The regional dynamic anomaly (median in Fig. 1a) is added to global mean thermal expansion (Fig. 1e).

The land ice influence on regional SLR depends on the spatial distribution of anticipated ice mass losses[5,10-12]. We created a global MGIC fingerprint which aggregates the effect of 21st century projections for 12 world regions[3] (Fig. 1b; see SI). The global mean MGIC contribution, used to scale the fingerprint, assumes a global surface mass balance sensitivity to air temperature changes, which decreases as the glaciers area shrinks[2,16] (see method and SI). The AIS and GIS fingerprints (Fig 1c-d) take into account the present-day distribution of mass loss. The Antarctic Peninsula is part of the Antarctic MGIC pattern.

Figure 1 (Next page). Sea level fingerprints, their contribution and median 21st century projections. a-l. Sea-level "fingerprints" for ocean dynamics **(a)**, MGIC **(b)**, GIS **(c)** and AIS **(d)**, expressed in unit of regional sea-level rise per unit of global mean temperature change (a) or global mean contribution of the source used for scaling (b-c). The temperature-dependent ocean dynamic anomaly pattern is added to global mean thermal expansion **(e)** while mass additions from land-ice are used for the gravitational patterns **(f-h)**. All four boxes are shown for the four RCP scenarios in the top-down approach and only RCP 4.5 in the bottom-up cases, indicating median and 68% uncertainty range. Panels **(i-l)** show projected total SLR for all components combined (contours every 10 cm). The thick black line corresponds to the global mean on all maps, and grey shading indicates areas of sea-level drop.

a Ocean Dynamics

b Mountain Glaciers & Ice Caps

c Greenland Ice Sheet

d Antarctic Ice Sheet

Sea-level fingerprint (m/m)

Ocean Dynamic Pattern (cm/°C)

e-h Global-Mean Contributions by 2090-2099 rel. 1980-1999

e Steric Sea Level Change

f Mountain Glaciers & Ice Caps

g Greenland Ice Sheet

h Antarctic Ice Sheet

cm

i-l Median Sea Level Change under RCP scenarios (Approach A) 2090-2099 rel. 1980-1999

cm

i RCP3PD 69 [59- 80] cm

j RCP4.5 80 [68-94] cm

k RCP6 79 [67-93] cm

l RCP8.5 99 [83-120] cm
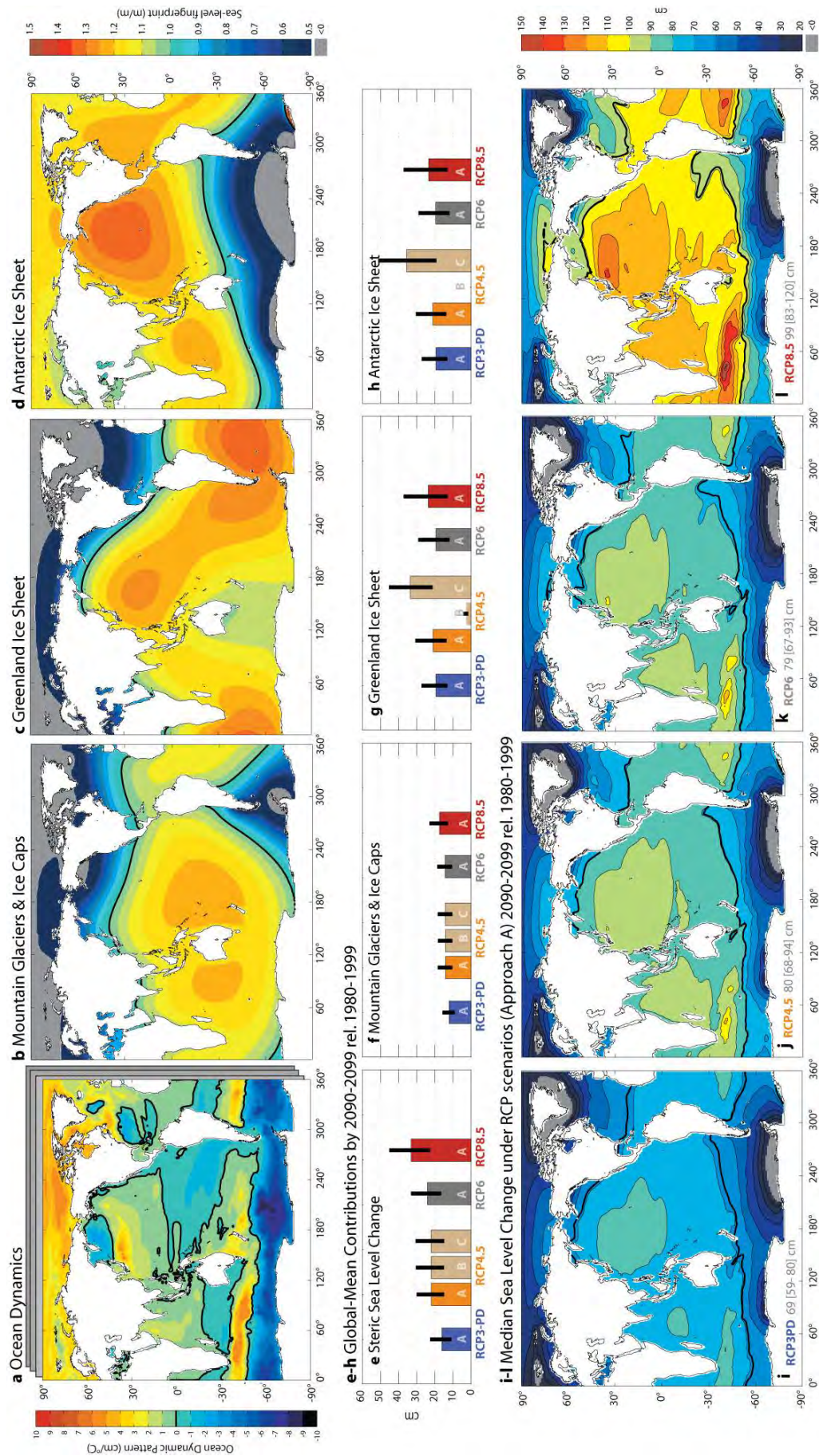
Given the discrepancy between current ice-sheet model simulations and observations[15,21], there is at present little confidence in process-based projections of ice sheet response to warming[14]. We consider three alternative approaches to compute global AIS and GIS contribution to SLR (see SI). The first is a "top-down" approach, where global SLR projections are computed directly using an updated semi-empirical model[22] calibrated with past variations of observed global mean sea level and air temperature. The GIS and AIS are then taken as the residual from total SLR projections after subtracting the steric and the MGIC contributions. Given the large uncertainty, we assume a simplified partitioning between GIS and AIS by varying the distribution uniformly between 1/3 and 2/3. This is roughly consistent with recent observations[12,21], and turns out not to be critical for projected low- and mid-latitude sea level rise (see below, Fig 2c). The second alternative approach, providing a low-end estimate of the role of ice-sheets, assumes an IPCC AR4-like ice-sheet contribution where only Greenland's surface mass balance contributes to the global mean SLR[16], while Antarctica is set to zero (referred to as IPCCAR4*). The third approach considers a higher estimate based on glaciological constraints[23] (PF08). For all RCP scenarios, SLR projections are from 1980-1999 to 2090-2099 with results summarized Table 1.

Table 1. **Global mean projected contributions** between 1980-1999 and 2090-2099 periods. Ranges are the 16th and 84th percentiles. The unit is centimetre or degree Celsius. All numbers are rounded. Note that mountain glaciers and ice caps (MGIC) include those present at Greenland margins and on the Antarctic Peninsula. The crosses ([†]) indicate that ice-sheet contributions are obtained from the "top-down" approach (see main text).

	Thermal expansion	MGIC	GIS	AIS	Total	Global mean temperature
RCP 3-PD, top-down	16 (11, 23)	12 (9, 16)	19 (13, 27) [†]	19 (13, 27) [†]	69 (59, 80)	1.1 (0.8, 1.4)
RCP 4.5, top-down	22 (15, 30)	14 (10, 18)	21 (13, 31) [†]	21 (13, 31) [†]	80 (68, 94)	2.0 (1.6, 2.5)
RCP 6.0, top-down	24 (16, 33)	14 (11, 19)	20 (12, 29) [†]	20 (12, 29) [†]	79 (67, 93)	2.6 (2.1, 3.2)
RCP 8.5, top-down	33 (23, 45)	17 (13, 23)	24 (13, 37) [†]	24 (13, 37) [†]	99 (83, 120)	4.3 (3.5, 5.5)
RCP 4.5, IPCCAR4[*]	22 (15, 30)	14 (10, 18)	3 (2, 4)	0 (0, 0)	39 (31, 49)	2.0 (1.6, 2.5)
RCP 4.5, PF08	22 (15, 30)	14 (10, 18)	33 (21, 45)	35 (20, 51)	106 (86, 125)	2.0 (1.6, 2.5)

The overall, median pattern of rise in the top-down case (Fig. 1i-l) is strongly influenced by the polar ice mass distribution since the latter is assumed to contribute more than 70% of the total rise (Table 1). We find regional variations up to 20% higher than the mean along the East-Asian coast and in the Indian Ocean, and up to 30% lower than the mean in mid-latitude Northern America and Europe (30-50°N). Close to the main ice melt sources (Greenland, Arctic Canada, Alaska, Patagonia and Antarctica), crustal uplift and reduced self-attraction cause an even lower and occasionally negative sea-level change. High-latitude South America is directly influenced by the Patagonian and West Antarctica glaciers and experiences sea-level change up to 30% below the global mean. The median sea-level pattern is quasi scenario-independent in this top-down case, because the proportion of the contributions is approximately constant across the scenarios.
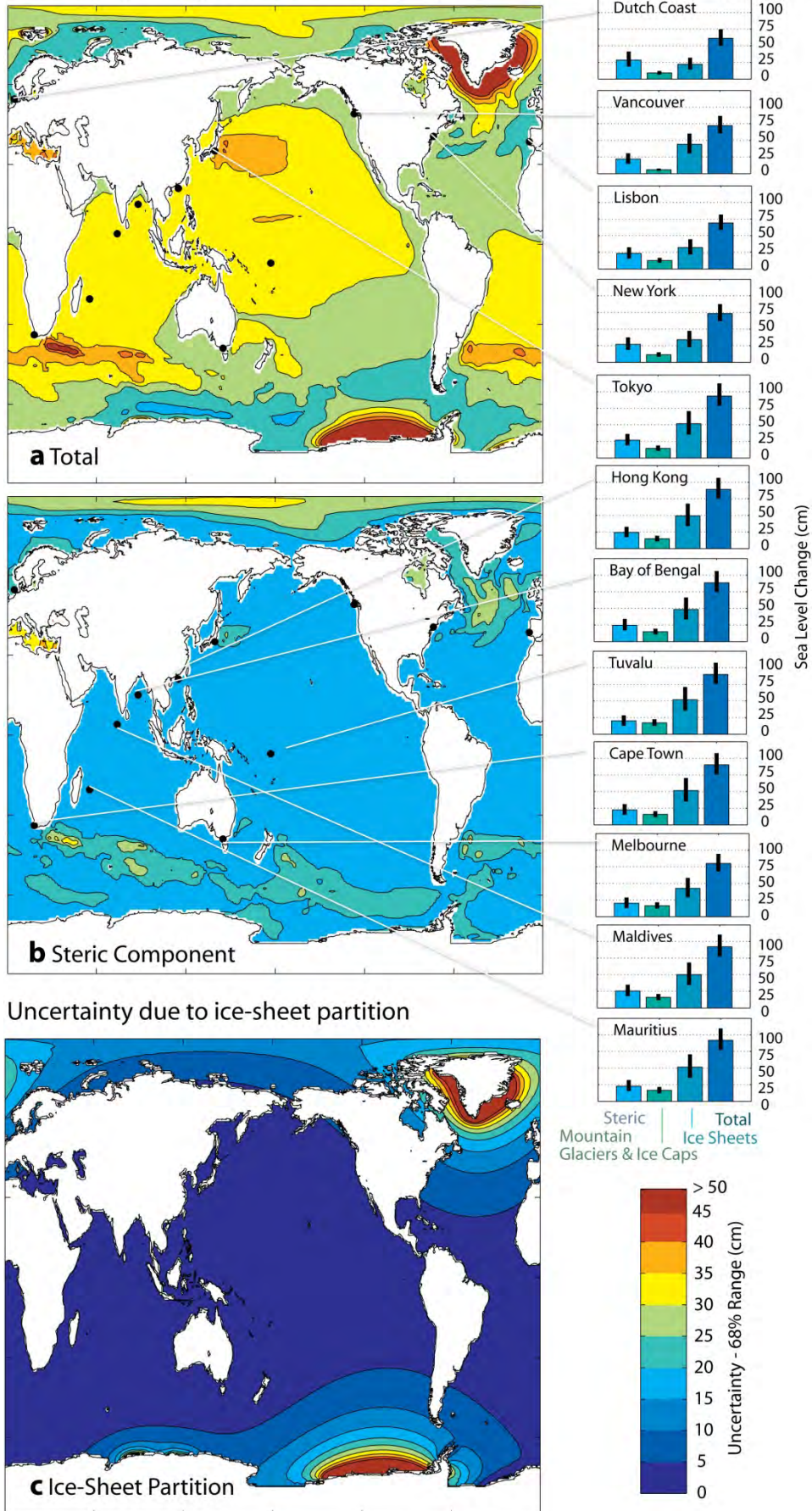
Our approach enables a probability density function of sea-level change to be computed at each grid point to assess associated uncertainties. The uncertainty of regional SLR projections in the top-down case, excluding ice-sheet surroundings, may be up to 35% greater than the global mean SLR uncertainty (Fig. 2a), but can also be lower in regions of relative sea-level fall. Due to the prescribed range in the GIS/AIS contribution, the partitioning uncertainty is very large near the ice-sheets, whereas for regions further away (e.g., in the Pacific and Indian Ocean), this uncertainty is only a few centimetres (Fig. 2c) because the GIS and AIS fingerprints have similar magnitudes in these regions (Fig. 1c,d). A larger-than-average uncertainty is also found near the Gulf Stream, the Kuroshio current and in the Southern Ocean (Fig. 2b). These regions feature strong sea level gradients governed by ocean dynamics, and while individual GCMs tend to consistently show large changes under climate forcing for these current systems, they disagree on the exact location of the changes. Therefore, shifts or adjustments of these currents under external forcing lead to large inter-model spread[8,9].

Figure 2 (next page). Uncertainty in regional sea level change. a-d. Uncertainty (68% range) in sea-level change (a) and its steric component (b), for the RCP 4.5 scenario in the top-down case. The uncertainty resulting from GIS/AIS partition in the top-down approach is illustrated in panel (c), for a total ice-sheet contribution equal to the ensemble median. Contours lines indicate 5-cm intervals. Black dots indicate individual locations appearing in Figure 3, whose individual contributors to selected local SLR locations and their 68% uncertainty range are shown in panel (d).

Uncertainty in Regional Sea Level Change

a Total

b Steric Component

Uncertainty due to ice-sheet partition

c Ice-Sheet Partition

Dutch Coast

Vancouver

Lisbon

New York

Tokyo

Hong Kong

Bay of Bengal

Tuvalu

Cape Town

Melbourne

Maldives

Mauritius

Sea Level Change (cm)

Steric | Total
Mountain | Ice Sheets
Glaciers & Ice Caps

Uncertainty - 68% Range (cm)

> 50
45
40
35
30
25
20
15
10
5
0

Finally, we project sea-level changes in coastal waters along the world's coastlines, for various emission and ice-sheet scenarios (Fig. 3). The median pattern is robust across the scenarios, confirming the expectation of higher-than-average rise at low latitudes, in particular in the Western Pacific and Indian Ocean, and reduced rise at high latitudes. In the IPCCAR4* case, the polar location of MGIC compensates for the small ice-sheet contributions in terms of gravity changes and overcompensates a large dynamic rise in the North Atlantic. In the two approaches where the ice-sheets contribute a large fraction to the total sea-level rise (Fig 3c,f), the uncertainty in the ratio between local and global mean sea-level is relatively small, except near the ice-sheets. These results contrast sharply with the low IPCCAR4* case, where steric expansion is the main source of spread and the uncertainty in the pattern itself may be as large as the uncertainty in the global mean SLR (Fig. 3e). Across all scenarios and ice-sheet contributions, the highest projected SLR is found near Tokyo with a rise of 10 to 45% above the global mean (80% range, Fig. 3a,e).

Figure 3 (next page). Projected sea-level rise along world coastlines. Coloured lines show regional sea-level projections, averaged over coastal areas (<300 km from land, including islands) over latitude, and for various oceans (selected coastlines are indicated in the inlet). Global mean SLR (cm) is indicated by a horizontal black bar on the left for each scenario, with error bars indicating 50%, 68% and 80% uncertainty ranges. Particular locations are also shown (averages within 200 km from the black dots on the map, and vertical dashed lines). The uncertainty ranges for these only describe the relative deviation from the global mean (%), to highlight uncertainty in regional fingerprints. The total uncertainty in regional sea-level, not shown in the figure, is a combination of local (right y-axis) and global (left y-axis) sea-level uncertainties. The normalized scale is also used to aggregate the various RCP scenarios and ice-sheet approaches, but the large difference in total sea-level rise should be kept in mind.
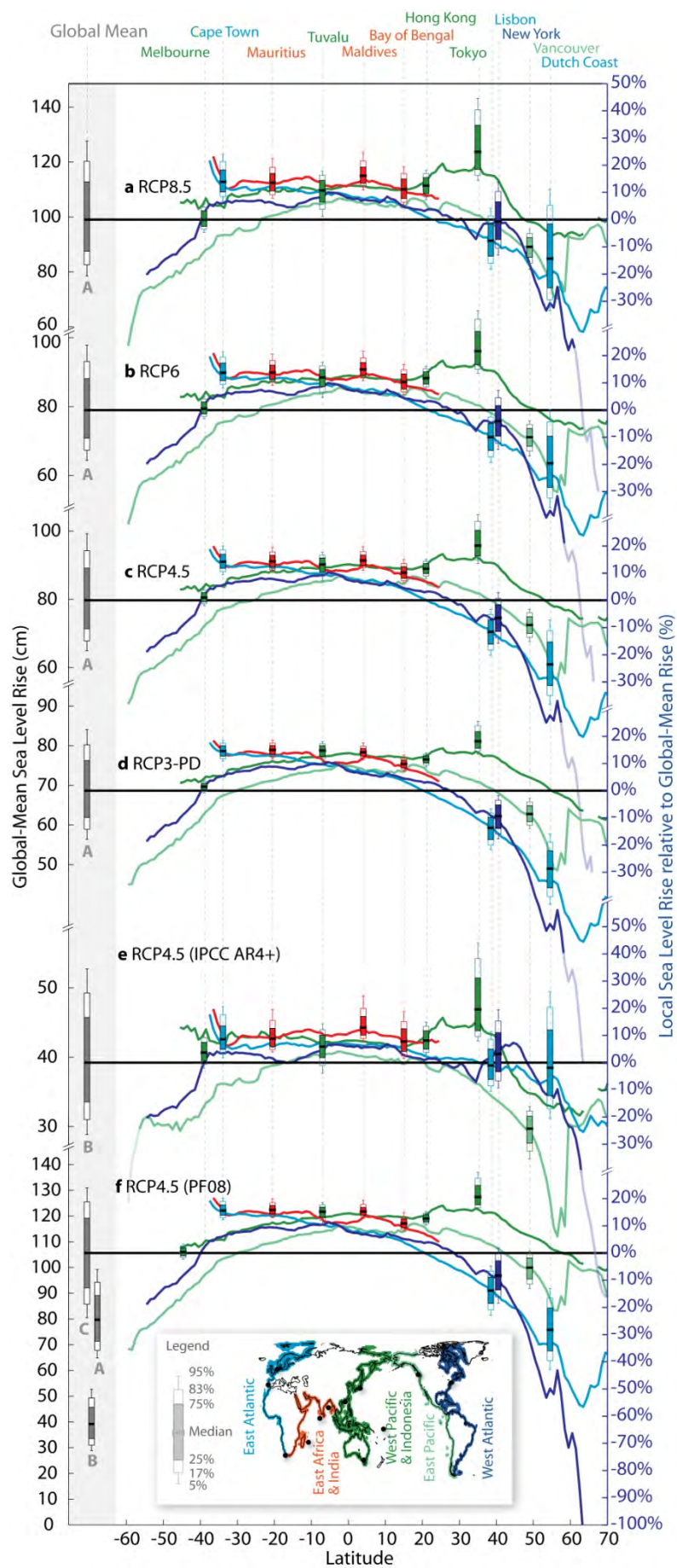
Our projected dynamic changes for the New York region are above average but weaker than in a previous assessment[7]. This is likely because of large, fine-scale differences in dynamic SLR projected across the continental shelf in this location which could lead to different interpretation of local SLR (e.g., single grid cells vs. regional average). Additionally, the RCP45 scenario implies lower surface warming than the SRES A1B scenario used in earlier work. The precise value also depends on the choice of a GCM ensemble. Densely populated coasts along the Bay of Bengal are projected to experience higher-than-average rise (+10 to +20 %) due to the combined effect of ocean dynamics and gravity changes. This result is sensitive to glacier melt in the Himalayas and other high Asian mountains: if losses of glacial mass are greater than projected, gravitational effects would lower sea-level and compensate for the dynamic rise (Fig. S5). Similarly, sea-level around Cape Town rises more than the global mean due to the assumed distribution of ice loss around West Antarctica. A more uniform ice loss over the Antarctic continent would lead to local SLR closer to the global mean[12]. Other uncertainties include assumptions about solid Earth properties in the generation of our gravitational fingerprints.

Our normalized ocean dynamic patterns explain most of the simulated long-term changes during the 21st century (Fig. S3 and S4). Sensitivity tests suggest a small emission scenario dependency of the patterns, in particular for lower scenarios, but the inter-scenario range remains smaller than the inter-model range (Fig. S2-S4). The proposed scaling approach is therefore appropriate, in an ensemble context, to predict dynamic sea-level change for a range of emission scenarios. After 2100, during the stabilization period of the

CMIP3 simulations, the relationship between global mean temperature and dynamic sea-level, derived for the 2000-2100 period, becomes less robust. This indicates that the long-term equilibrium response of regional sea level to global warming might differ from the 21st century patterns. Additionally, our projected regional sea level response does not include the ocean's dynamic response from the intense freshening due to Greenland and Antarctic meltwater discharge[24]. SLR might therefore be underestimated along the North-East coast of America[7,25] in scenarios with large ice sheet contributions. The relatively low spatial resolution of the GCMs and the absence of appropriate weighting based on model skill are limitations to current multi-model projections of local SLR[7-9].

As new component–specific simulations become available, our projections can be updated within the presented framework. In particular, process-based estimates of land-ice melt could replace the semi-empirical top-down approach. When applying our projections to impact analysis and adaptation planning, non-climatic factors such as human-induced modification of land hydrology[26], local subsidence (e.g., from sediments deposition and groundwater pumping[27]) and long-term glacial isostatic adjustment[28] have to be taken into account, the latter being potentially substantial at high-latitudes in the Northern hemisphere. Our probabilistic method and the presented results open new possibilities for impact studies in coastal regions synthesizing a number of uncertainties from emission scenarios to regional sea-level changes in a consistent framework.

Methods

We use the simple carbon-cycle climate model MAGICC 6[29] for observationally-constrained, probabilistic projections of global mean ocean heat uptake and surface air temperature changes[30]. Our projections are based on the new representative concentration pathways (RCP), to be used in the next IPCC report to cover a broad range of future emissions. RCP 8.5 is comparable with A1F1 from IPCC AR4, while RCP 4.5 and RCP 6.0 resemble B1 and A1B, respectively[20].

Ocean thermal expansion is assumed proportional to ocean heat uptake; with scaling coefficients derived from an ensemble of 13 GCMs from the CMIP3 intercomparison (see SI). Regional variations of sea-level due to ocean density and circulation changes are accounted for by using an ensemble of 12 GCMs, based on data availability and on model skills at representing present-day dynamic sea-level[9]. A spatial pattern of SLR for each model is derived by linear regression of dynamic sea-level changes against global mean surface air temperature under the SRES A1B scenario (see SI), with global mean temperature then being used as a predictor for projecting the patterns under the RCP scenarios. The regression explains most long-term changes during the 21st century. The variability of the resulting patterns is large, and each of the GCM patterns is assumed to be equally likely. The global MGIC term is updated from IPCC AR4[2,16] (Fig. 1f), assuming global surface mass balance sensitivity to temperature changes and volume-area scaling (see SI). The results are then scaled-up to account for mountain glaciers present at the margin of the two main ice-sheets, consistently with a recent regionally-explicit model projection for the 2000-2100 period[3] (see SI). Land-ice gravitational fingerprints are obtained by solving the sea-level equation with the

same model as ref. 12. In addition to gravitational effects, these fingerprints account for vertical land motion in the vicinity of the disintegrating ice masses, thereby enhancing local-sea level fall. However, they do not include present-day viscoelastic glacial isostatic adjustments in response to previous glaciations because the rate of this process is nearly constant on the time scales considered here[28] and carries large uncertainties. The various approaches for global mean ice-sheet contribution are detailed in the SI.

References

1 Wigley, T. M. L. & Raper, S. C. B. Thermal expansion of sea water associated with global warming. *Nature* **330**, 127-131 (1987).

2 Wigley, T. M. L. & Raper, S. C. B. Extended scenarios for glacier melt due to anthropogenic forcing. *Geophys. Res. Lett.* **32**, L05704 (2005).

3 Radic, V. & Hock, R. Regionally differentiated contribution of mountain glaciers and ice caps to future sea-level rise. *Nature Geosci* **4**, 91-94 (2011).

4 Gregory, J. M. & Huybrechts, P. Ice-sheet contributions to future sea-level change. *Phil. Trans. R. Soc. London, Ser. A* **364**, 1709-1732 (2006).

5 Bamber, J. L., Riva, R. E. M., Vermeersen, B. L. A. & LeBrocq, A. M. Reassessment of the Potential Sea-Level Rise from a Collapse of the West Antarctic Ice Sheet. *Science* **324**, 901-903 (2009).

6 Landerer, F. W., Jungclaus, J. H. & Marotzke, J. Regional Dynamic and Steric Sea Level Change in Response to the IPCC-A1B Scenario. *J. Phys. Oceanogr.* **37**, 296-312 (2007).

7 Yin, J., Schlesinger, M. E. & Stouffer, R. J. Model projections of rapid sea-level rise on the northeast coast of the United States. *Nat. Geosci.* **2**, 262-266 (2009).

8 Pardaens, A., Gregory, J. & Lowe, J. A model study of factors influencing projected changes in regional sea level over the twenty-first century. *Clim. Dyn.*, 1-19 (2010).

9 Yin, J., Griffies, S. M. & Stouffer, R. J. Spatial Variability of Sea Level Rise in Twenty-First Century Projections. *J. Clim.* **23**, 4585-4607 (2010).

10 Clark, J. A. & Lingle, C. S. Future sea-level changes due to West Antarctic ice sheet fluctuations. *Nature* **269**, 206-209 (1977).

11 Mitrovica, J. X., Tamisiea, M. E., Davis, J. L. & Milne, G. A. Recent mass balance of polar ice sheets inferred from patterns of global sea-level change. *Nature* **409**, 1026-1029 (2001).

12 Bamber, J. L. & Riva, R. E. M. The sea level fingerprint of recent ice mass fluxes. *The Cryosphere* **4**, 621-627 (2010).

13 Bindoff, N. L. *et al.* in *IPCC WG1 Fourth Assessment Report* (eds Solomon, S. *et al.*) (Cambridge Univ. Press, 2007).

14 Lowe, J. A. & Gregory, J. M. A sea of uncertainty. *Nature Reports*, 42-43 (2010).

15 Rahmstorf, S. A new view on sea level rise. *Nature Reports*, 44-45 (2010).

16 Meehl, G. A. *et al.* in *IPCC WG1 Fourth Assessment Report* (eds Solomon, S. *et al.*) (Cambridge University Press, 2007).

17 Slangen, A. B. A., Katsman, C. A., van de Wal, R. S. W., Vermeersen, L. L. A. & Riva, R. E. M. Towards regional projections of twenty-first century sea-level change based on IPCC SRES scenarios. *Clim. Dyn.* **in press**.

18 Katsman, C. A., Hazeleger, W., Drijfhout, S., van Oldenborgh, G. & Burgers, G. Climate scenarios of sea level rise for the northeast Atlantic Ocean: a study including the effects of ocean dynamics and gravity changes induced by ice melt. *Clim. Change* **91**, 351-374 (2008).

19 Meehl, G. A. *et al.* The WCRP CMIP3 multimodel dataset. *Bull. Am. Meteorol. Soc* **88**, 1383–1394 (2007).

20   Moss, R. H. *et al.* The next generation of scenarios for climate change research and assessment. *Nature* **463**, 747-756 (2010).

21   Rignot, E., I. Velicogna, van den Broeke, M. R., Monaghan, A. & Lenaerts, J. Acceleration of the contribution of the Greenland and Antarctic ice sheets to sea level rise. *Geophys. Res. Lett.* **38**, L05503 (2011).

22   Vermeer, M. & Rahmstorf, S. Global sea level linked to global temperature. *Proc. Nat. Acad. Sci. U.S.A.* **106**, 21527 (2009).

23   Pfeffer, W. T., Harper, J. T. & O'Neel, S. Kinematic Constraints on Glacier Contributions to 21st-Century Sea-Level Rise. *Science* **321**, 1340-1343 (2008).

24   Stammer, D. Response of the global ocean to Greenland and Antarctic ice melting. *J. Geophys. Res.* **113**, C06022 (2008).

25   Levermann, A., Griesel, A., Hofmann, M., Montoya, M. & Rahmstorf, S. Dynamic sea level changes following changes in the thermohaline circulation. *Clim. Dyn.* **24**, 347-354 (2005).

26   Wada, Y. *et al.* Global depletion of groundwater resources. *Geophys. Res. Lett.* **37**, L20402 (2010).

27   Poland, J. F. & Davis, G. H. Land subsidence due to withdrawal of fluids. (1969).

28   Peltier, W. R. & Andrews, J. T. Glacial-Isostatic Adjustment—I. The Forward Problem. *Geophys. J. Roy. Astron. Soc.* **46**, 605-646 (1976).

29   Meinshausen, M., Raper, S. & Wigley, T. Emulating coupled atmosphere-ocean and carbon cycle models with a simpler model, MAGICC6–Part 1: Model description and calibration. *Atmos. Chem. Phys* **11**, 1417-1456 (2011).

30   Meinshausen, M. *et al.* Greenhouse-gas emission targets for limiting global warming to 2 C. *Nature* **458**, 1158-1162 (2009).

Acknowledgements

Author contributions

M.P. and M.M. designed the research. M.P. performed the calculations and analysis, with input from all authors. R.R. generated the gravitational fingerprints. F.L. and K.F. provided advice for the PCMDI analysis and GCM pattern downscaling. All authors contributed to writing the paper.

Probabilistic projections of sea-level change along the world's coastlines

Mahé Perrette[1*], Riccardo Riva[2], Felix Landerer[3], Katja Frieler[1], Malte Meinshausen[1]

[1]Potsdam Institute for Climate Impact Research (PIK)

Telegraphenberg A 26, 14412, Potsdam, Germany

[2] Delft University of Technology, Delft, Netherlands

[3] Jet Propulsion Laboratory / California Institute of Technology, Pasadena, USA

1. **Global mean thermal expansion**

The global mean ocean heat uptake is well simulated with the MAGICC 6 model[1,2], however at present the simulation of thermal expansion estimated from general circulation models is not sufficiently accurate for the purposes of this study. In order to project global mean thermal expansion, we make use of the quasi-linear relationship between global mean ocean heat uptake and thermal expansion as displayed in General circulation models (GCMs) (Figure S1a). The slope of the relationship, or scaling coefficient, varies slightly among models, probably because of different depths of heat penetration into the ocean and differences in the background climatological temperature and salinity. These scaling coefficients were used to fit a Gaussian distribution (Figure S1b), before re-sampling and use with MAGICC outputs. The distribution has a mean of 1.12×10^{-25} m/J and a standard deviation of 1.18×10^{-26} m/J. Observation-based estimates typically get a number within the range $1.3-1.6 \times 10^{-25}$ m/J, significantly larger than the GCMs[3]. The difference most likely comes from the fact that the observational estimates are based on the top 700 m, whereas our study concerns the whole water column (the expansivity of seawater is pressure dependent, decreasing with depth).

2. **Dynamic sea-level change**

For dynamic sea-level change projections over the 21st century, we derive a normalized pattern of dynamic sea-level change for each GCM with respect to global mean surface air temperature (GMSAT) change (Figure S2). The ensemble of GCMs has been selected based on model skills at simulating the climatological dynamic topography of the ocean[4]. The

pattern is obtained using a linear regression between both variables over the 2000-2100 period, using yearly data and 1980-1999 as the reference period (no intercept). The linear regression explains most long-term changes over the 21st century (Figure S4), and the derived patterns have relatively little inter-scenario variability as compared to the multi-model spread (Figures S2-S4, Table S1). During the stabilization period (after 2100 in the A1B scenario), the linear relationship is less robust (Figure S4), but this does not affect our projections, which focus on the end of the 21st century. Additional sensitivity experiments (not shown) indicate that GMSAT is better than global mean thermosteric sea-level or the rate of ocean heat uptake at predicting dynamic sea-level change at predicting dynamic sea-level change, in particular for stabilization periods when surface air temperatures have equilibrated, but the oceans continue to take up heat.

3. Mountain glaciers and ice caps

a. Global mean contribution

The mountain glaciers and ice caps (MGIC) contribution H_{gl} (excluding those near the ice-sheets) is computed after Meehl et al.[5], itself based on Wigley and Raper[6]. It assumes global surface mass balance sensitivity, meaning the rate of glacier's ice loss dH_{gl}/dt is proportional to a change in global mean temperature T as compared to pre-industrial equilibrium T_o. To account (1) for a decrease in global SMB sensitivity as the global glacier area decreases, due to the preferential disappearance of more sensitive glacier areas, and (2) for global area versus volume scaling, the projected global SMB sensitivity, b_{gl}, is $b_{gl} = b_0 \ (V_{gl} \ / \ V_o \ )^{1.646}$, where b_0 is the present (1961-2004 average) global SMB sensitivity, and V_{gl} and V_o are the projected and present global glacier volumes (in sea level equivalent) respectively. Thus:

$$dV_{gl}/dt = b_o (T-T_o) (1 - V_{gl}/V_o)^{1.646} \qquad (1)$$

where $b_o = 0.8 \pm 0.2$ mm.yr^{-1}.°C^{-1}, $V_o = 410 \pm 30$ mm and $T_o = -0.41 \pm 0.01$ °C (as compared to 1951-1980). The global SMB sensitivity b_o, and the exponent adopted here are the same as in the IPCC AR4[5], while the total glacier volume V_o is taken from a more recent estimate[7]. T_o is chosen consistently with equation (2) (see section 4.a) and yields a 1961-2004 trend of 0.43 ± 0.12 mm/yr, close to IPCC AR4's estimate[8] (0.43 ± 0.15 mm.yr^{-1}). We did not attempt to tune T_o with more up-to-date observational data since sensitivity tests showed that projections by 2100 are relatively insensitive to the precise specification (not shown). To account for mountain glaciers present at the margin of the two main ice-sheets, we add on the top of MGIC contribution calculated from equation (1) another +21% to Antarctic Peninsula and +4% to Greenland, based on a recent model projection[7].

b. Gravitational fingerprints

We use the same model as Bamber and Riva[9] (BR10) to solve the sea-level equation, which includes self-gravitation, changes in polar wander (Earth rotation vector), shoreline migration and elastic deformation of the solid Earth. As input distribution of ice mass loads necessary to derive the gravitational fingerprints, we use a regionally-explicit 21st century projection of MGIC retreat based on Radic and Hock[7] (RH11). We do not model the 7 regions of RH11 that are projected to individually cause less than 1 mm SLR by 2100, together accounting for about 1% of the total MGIC contribution. We attributed the whole Antarctic MGIC projections from RH11 to the Antarctic Peninsula, ignoring potential contributions from around the margins of the East Antarctic where temperatures are expected to remain cold during the projection period. In Figure S5, we compare a fingerprint identical to ours

but with no load over Greenland with a fingerprint based on estimates for the 2000-2008 period (taken from Table 1 of BR10 and references therein, combined with an estimate for high Asian mountains[10], not considered in BR10). The MGIC present on Greenland are excluded in this comparison since BR10 did not separate MGIC and ice-sheet contributions.

Projected losses for Asian high mountains (incl. Himalayas), the Rocky Mountains and Western Canada are much less than present-day estimates (Figure S5 and Figure S6), meaning possible overestimation of sea-level rise in these regions if the current rate is accurate and sustained (due to the underestimated contribution of both the gravitational drop of the sea surface and the elastic uplift of the solid Earth). On the other hand, Iceland and Arctic Asia regions show large projected contribution to SLR whereas both current observations (BR10) and simulations of the past 1960-2000 period (RH11) indicate no significant contribution to global SLR (Figure S6). Alaska, Arctic Canada and Svalbard show a temporally consistent trend of increasing wastage when aggregating observed and simulated data (Figure S6). Note that the Antarctic Peninsula, Arctic Canada, Alaska, Svalbard and Asian high mountains present a large spread in RH11 projections, which is not accounted for in the present study.

4. Ice-sheets contribution

a. Semi-empirical method (top-down case)

The mismatch between model simulations and present-day observations of SLR have lead to the development of semi-empirical methods[11]. They are based on simple physical considerations and exploit the link between global mean sea-level and surface temperature

(or radiative forcing) in the observational record, for projection of future SLR, with parameters calibrated with available observations[11-13]. These methods typically yield future sea-level projections that can reach more than one metre of rise by 2100, which is significantly higher and in sharp contrast with the IPCC AR4 projections. One caveat in their application is that the semi-empirical relationships between temperature and sea-level variations is calibrated over a relatively narrow range of global mean temperature variation compared to the projected warming to 2100[14], but in the absence of robust physical models that can reliably and explicitly simulate ice sheet response to warming based on first principles, semi-empirical methods still provide a useful, plausible alternative estimate[15].

In our "top-down" setting, global mean sea-level projections are computed after Vermeer and Rahmstorf[13] (VR09), where the rate of sea-level change dH/dt is assumed to be proportional to the temperature anomaly relative to a pre-industrial equilibrium T_o. An additional term proportional to the derivative of global mean temperature dT/dt, captures the rapid response of sea-level to temperature variations, related to mixed-layer dynamics. Therefore:

$$\frac{dH}{dt} = a(T - T_o) + b\frac{dT}{dt} \qquad (1)$$

where a and b are regression coefficients. Similar to VR09, sea-level time-series[16] are corrected from artificial reservoir impoundment (building of dams)[17]. Additionally, here we apply a recent ground-water mining correction[18] before the regression, to only account for climate-induced changes in sea-level. Groundwater mining data date back to the 1950s and need to be extrapolated backward for conjoint use with tide-gauge data. For this purpose,

we assume that groundwater extraction follows a linear relationship with global population data. The negative groundwater mining correction is of the same order of magnitude as the positive reservoir correction and yields about 15 cm lower SLR projections compared to the default VR09 case. We obtain as parameter values: a = 0.50 ± 0.04 cm a^{-1} K^{-1}, b= -5.3 ± 1.3 cm.K^{-1} and T_o = -0.41 ± 0.04 K (expressed as 1951-1980 anomalies). Note also that we used a different regression method than in VR09: here, a linear regression is conducted on the integral equation of (1) after smoothing of temperature, and taking autocorrelation into account. This yields virtually identical parameter values when everything else is held the same as in VR09, albeit improving the error estimates. The joint uncertainty in the model parameters, deduced from the goodness-of-fit with sea-level data, are further inflated by a factor of two and propagated into the projections to provide error bars. The additional inflation of the uncertainty is intended to account for errors other than formal fitting of the model, such as data error and model choice. It adds another 10 cm to the 68% confidence range in projected sea-level by the end of the 21st century (not shown).

b. Bottom-up approaches

In addition to the top-down case, we consider two other approaches, based on bottom-up estimate of the 21st century ice-sheet contribution to sea-level rise and which provide a low and a high estimate for this term.

i. IPCC-like case (IPCC AR4*)

An IPCC AR4-like ice-sheet scenario is obtained by computing Greenland ice sheet (GIS)'s surface mass balance similarly to what was done in the Report[5,19]. Four high-resolution GCM simulations in combination with a degree-day model served at deriving a look-up table of GIS

surface mass balance as a function of temperature and precipitation changes averaged over Greenland[19]. Global simulations with coarser GCMs were then conducted and combined with the look-up tables to derive 2nd order polynomial fits of surface mass balance as a function of GMSAT change[1]. Due to expected increased precipitation over Antarctica and with warming not projected to be high enough to lead them substantial surface melting, ice sheet models presently project sea level lowering from Antarctica over the next century. From observations however it is clear that the Antarctic continent as a whole is in negative mass balance[19-22], with an observed accelerating rate of discharge mainly from the West Antarctic likely due to ocean warming affecting the ice-sheet grounding lines.

ii. High-end glaciological constraint (PF08)

We also consider an extreme case for ice-sheet contribution which was elaborated based on currently observed ice-sheet shrinkage and assumptions about physically plausible future acceleration[23]. This scenario is more speculative and is presented here to cover the full range of anticipated 21st century ice-sheet contribution found in the literature, as a sensitivity case. The intervals considered are 16.5-53.8 cm for Greenland and 12.8-62.9 cm for Antarctica. Since ice-sheet contribution was given without mention of a concomitant temperature change, we assume a uniform probability over the whole ranges, independently of GMSAT projections. Such estimates are not implausible: Rignot and colleagues[22] have recently

---

[1] The polynomial fits are available at http://www.met.rdg.ac.uk/~jonathan/data/ar4_ice_sheet_smb.html

shown that continued acceleration of the loss observed between 1992 to 2009 from both ice

sheets would raise sea level by approximately 56 cm by 2100 compared to 2009.

References

1   Meinshausen, M. *et al.* Greenhouse-gas emission targets for limiting global warming to 2 C. *Nature* **458**, 1158-1162 (2009).

2   Meinshausen, M., Raper, S. & Wigley, T. Emulating coupled atmosphere-ocean and carbon cycle models with a simpler model, MAGICC6–Part 1: Model description and calibration. *Atmos. Chem. Phys* **11**, 1417-1456 (2011).

3   Domingues, C. M. Improved estimates of upper-ocean warming and multi-decadal sea-level rise. *Nature* **453**, 1090-1094 (2008).

4   Yin, J., Griffies, S. M. & Stouffer, R. J. Spatial Variability of Sea Level Rise in Twenty-First Century Projections. *J. Clim.* **23**, 4585-4607 (2010).

5   Meehl, G. A. *et al.* in *IPCC WG1 Fourth Assessment Report* (eds Solomon, S. *et al.*) (Cambridge University Press, 2007).

6   Wigley, T. M. L. & Raper, S. C. B. Extended scenarios for glacier melt due to anthropogenic forcing. *Geophys. Res. Lett.* **32**, L05704 (2005).

7   Radic, V. & Hock, R. Regionally differentiated contribution of mountain glaciers and ice caps to future sea-level rise. *Nature Geosci* **4**, 91-94 (2011).

8   Lemke, P. *et al.* in *IPCC WG1 Fourth Assessment Report* (eds Solomon, S. *et al.*) (Cambridge University Press, 2007).

9   Bamber, J. L. & Riva, R. E. M. The sea level fingerprint of recent ice mass fluxes. *The Cryosphere* **4**, 621-627 (2010).

10   Matsuo, K. & Heki, K. Time-variable ice loss in Asian high mountains from satellite gravimetry. *Earth Planet. Sci. Lett.* **290**, 30-36 (2010).

11   Rahmstorf, S. A Semi-Empirical Approach to Projecting Future Sea-Level Rise. *Science* **315**, 368-370 (2007).

12   Grinsted, A., Moore, J. C. & Jevrejeva, S. Reconstructing sea level from paleo and projected temperatures 200 to 2100 AD. *Clim. Dyn.* **34**, 461-472 (2009).

13   Vermeer, M. & Rahmstorf, S. Global sea level linked to global temperature. *Proc. Nat. Acad. Sci. U.S.A.* **106**, 21527 (2009).

14   Lowe, J. A. & Gregory, J. M. A sea of uncertainty. *Nature Reports*, 42-43 (2010).

15   Rahmstorf, S. A new view on sea level rise. *Nature Reports*, 44-45 (2010).

16   Church, J. A. & White, N. J. A 20th century acceleration in global sea-level rise. *Geophys. Res. Lett.* **33**, L01602 (2006).

17   Chao, B. F., Wu, Y. H. & Li, Y. S. Impact of artificial reservoir water impoundment on global sea level. *Science* **320**, 212-214 (2008).

18   Wada, Y. *et al.* Global depletion of groundwater resources. *Geophys. Res. Lett.* **37**, L20402 (2010).

19   Gregory, J. M. & Huybrechts, P. Ice-sheet contributions to future sea-level change. *Phil. Trans. R. Soc. London, Ser. A* **364**, 1709-1732 (2006).

20   Rignot, E. *et al.* Recent Antarctic ice mass loss from radar interferometry and regional climate modelling. *Nature Geosci* **1**, 106-110 (2008).

21   Velicogna, I. Increasing rates of ice mass loss from the Greenland and Antarctic ice sheets revealed by GRACE. *Geophys. Res. Lett.* **36**, L19503 (2009).

22   Rignot, E., I. Velicogna, van den Broeke, M. R., Monaghan, A. & Lenaerts, J. Acceleration of the contribution of the Greenland and Antarctic ice sheets to sea level rise. *Geophys. Res. Lett.* **38**, L05503 (2011).

23   Pfeffer, W. T., Harper, J. T. & O'Neel, S. Kinematic Constraints on Glacier Contributions to 21st-Century Sea-Level Rise. *Science* **321**, 1340-1343 (2008).

Table S1. Global statistics for the linear regression of dynamic sea-level against global mean temperature. The table indicates for each model the global mean temperature (column name: "Tg") and global mean thermal expansion ("TSL"), the spatial root mean square of the regression coefficient for A1B over the 2000-2100 period ("Reg. coeff.") and the error associated with the regression ("Reg. error"). Additionally, it provides an estimate of the inter-scenario variability of the regression coefficient as the difference between the default pattern with patterns derived from a low ("B2 error") and a high ("A2 error") SRES emission scenario, as well as with a pattern computed from A1B over the 2000-2200 period ("2200 error"). The prediction error between 1980-1999 and 2090-2999 (difference between direct model projection and prediction from the regressed A1B pattern) is also shown for the three SRES scenarios ("Pred. A1B", 'Pred. B1" and "Pred. A2"). Differences are computed as spatial root mean square with appropriate area-weighting. Missing values correspond to simulations missing in CMIP3.

| GCM code	Tg °C	TSL cm	Reg. coeff. cm/°C	Reg. error cm/°C	B1 error cm/°C	A2 error cm/°C	2200 error cm/°C	Pred. A1B cm	Pred. B1 cm	Pred. A2 cm
BCCR BM2.0	2.9	-	3.5	0.2	1.2	0.6	-	1.9	2.4	3
CCCMA CGCM 3.1	2.5	-	3.2	0.1	0.5	0.4	-	1.2	1.5	1.8
GFDL CM2.0	2.8	22	2.8	0.2	4.6	0.5	0.9	1.6	6.7	2.3
GFDL CM2.1	2.4	23	3.1	0.2	1.0	0.7	1.5	2.1	2.2	3.4
GISS MODEL EH	2.3	17	5.0	0.3	-	-	-	4.1	-	-
IPSL CM4	3.2	-	3.4	0.1	0.7	0.5	-	2.3	3.4	3.0
MIROC3.2 HIRES	4.3	29	2.9	0.1	0.7	-	-	2.0	2.8	-
MIROC3.2 MEDRES	3.3	27	4.1	0.2	1.8	0.6	2.6	3.1	7.7	2.0
MPI ECHAM5	3.3	24	2.6	0.2	0.7	0.6	1.0	2.1	2.2	2.9
NCAR CCSM3.0	2.7	25	2.6	0.2	0.9	0.5	-	1.9	2	3.8
UKMO HADCM3	2.9	21	3.4	0.2	1.1	1.3	0.9	2.0	3.5	4.3
UKMO HADGEM1	3.3	-	2.2	0.2	-	0.7	0.8	2.0	-	4.1
Inter-model range of the regression coefficient:						4.0 cm/°C (68%)	-	8.5 cm/°C (90%)		
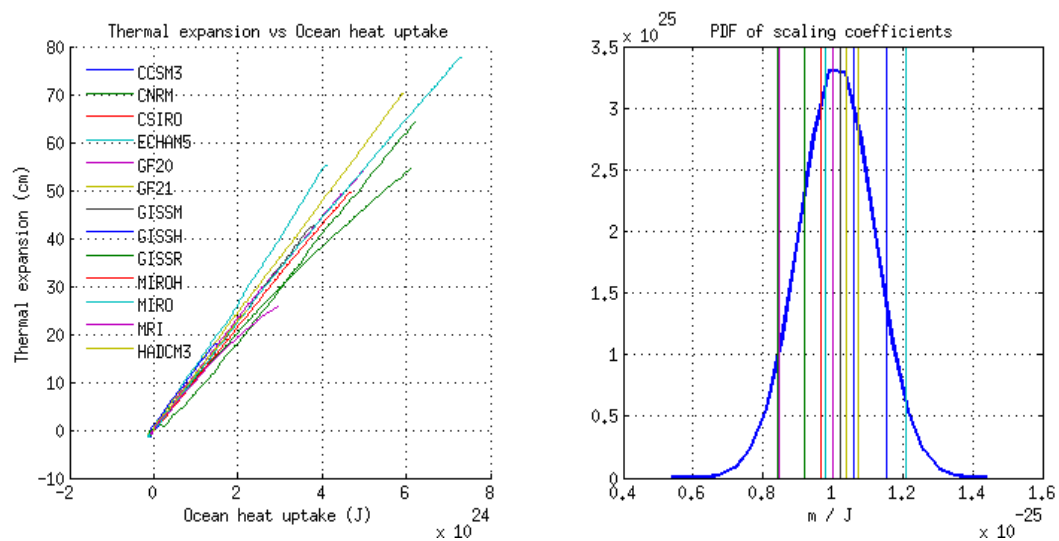
Figure S1. Global mean thermal expansion vs. ocean heat uptake in a sample of CMIP3 AOGCMs (left) and actual values of the corresponding regression coefficients with the fitted Gaussian distribution used for MAGICC scaling.
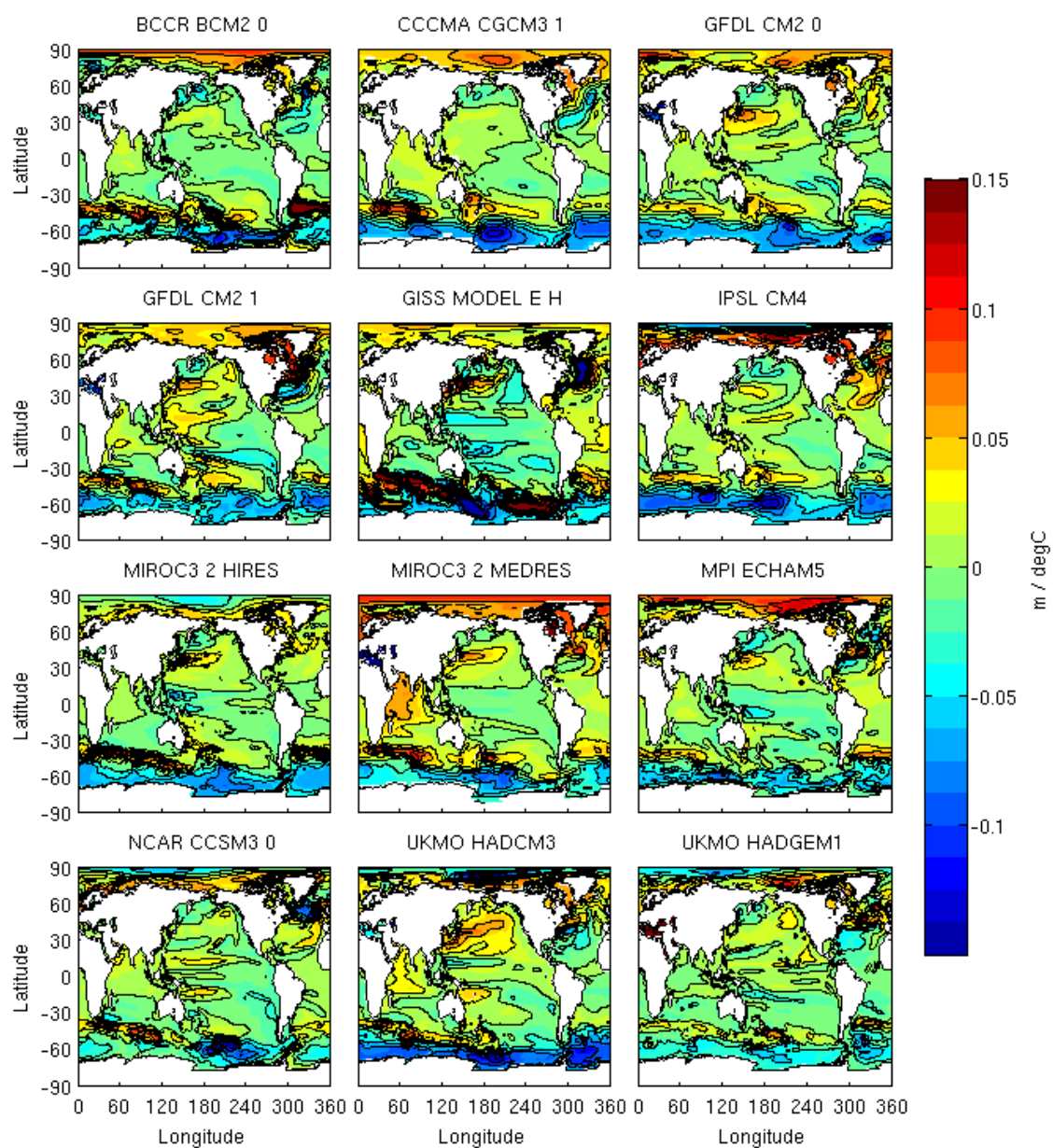
Figure S2. Regression coefficients of dynamic sea-level change against global mean temperature (in m.°C^{-1}) for the SRES A1B scenario over the 2000-2100 period. Contour line intervals are 0.025 m/°C.
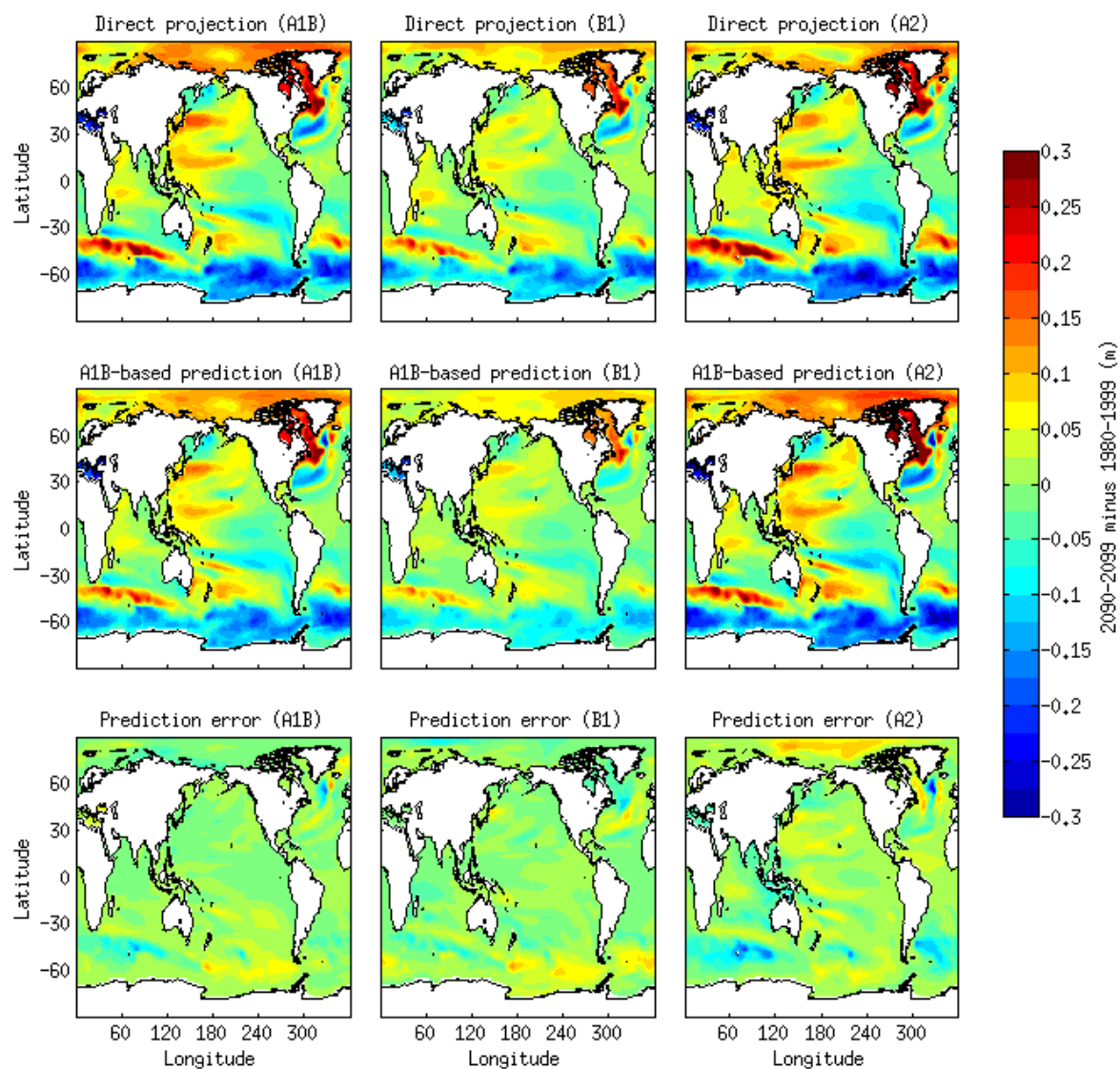
Figure S3. Comparison between direct model projections (GFDL CM2.1) between 1980-1999 and 2090-2099 averages (top) with predicted patterns using the regression method (middle), for the SRES scenarios A1B, B1, and A2 (from left to right). The difference between the predicted and projected values is also shown (bottom). Note that the predictions always use the same regression pattern derived from A1B scenario.
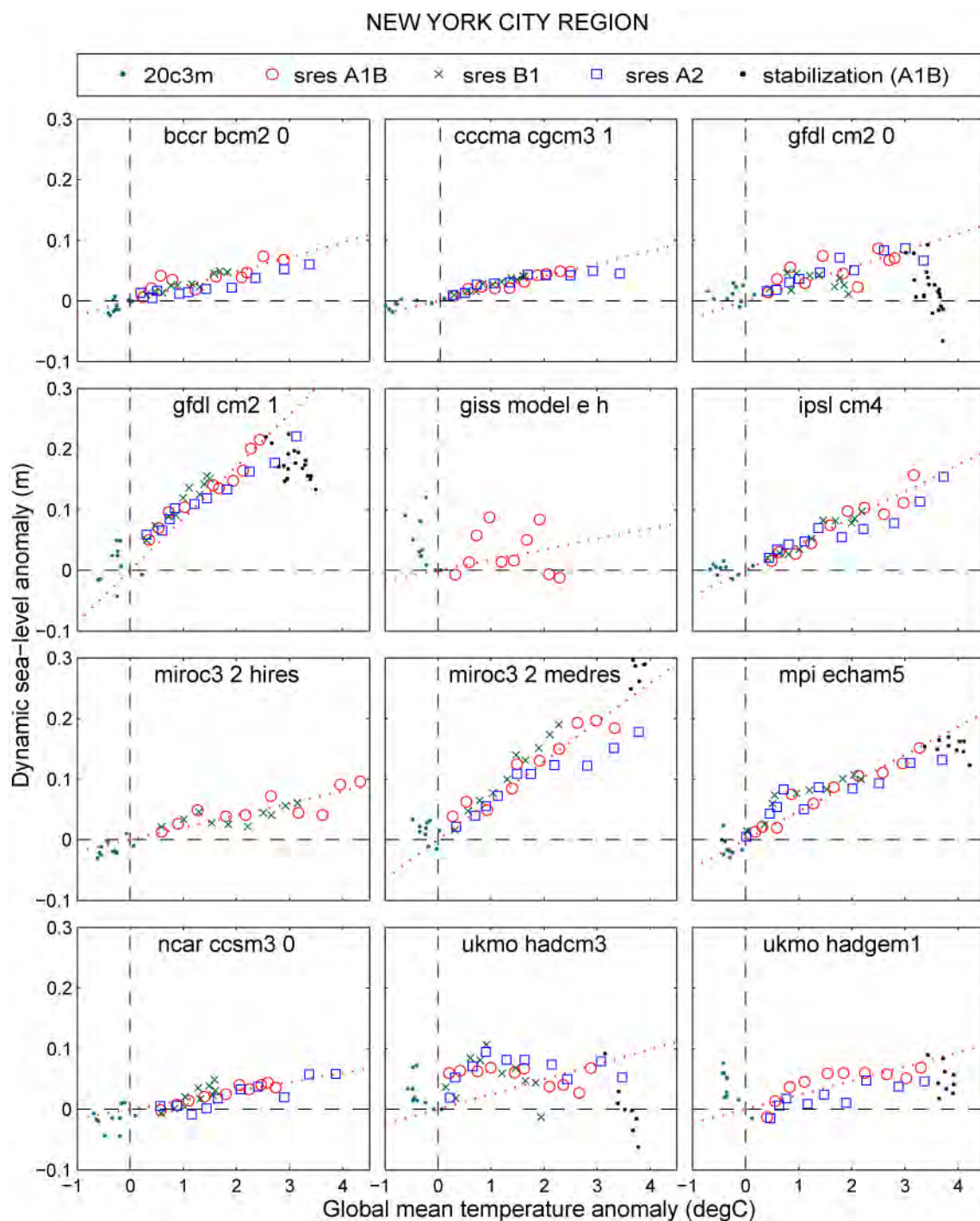
Figure S4. Scatter plot of dynamic sea-level anomaly in New York City region against global mean surface air temperature anomaly (with respect to a 1980-1999 reference period). The data represent three SRES scenarios (A1B, B1, A2), a simulation of the 20th century (20c3m) and the stabilization period of the A1B scenario (after 2100), as indicated in the legend. The markers are 10-year averages. The dotted line is a linear regression over 2000-2100 for the SRES A1B scenario using yearly values, as used to derive patterns of figure Figure S2. The data are retrieved as an average within 200km of the geographical coordinates [40.5°N, 73.5°W] on model's own grids.
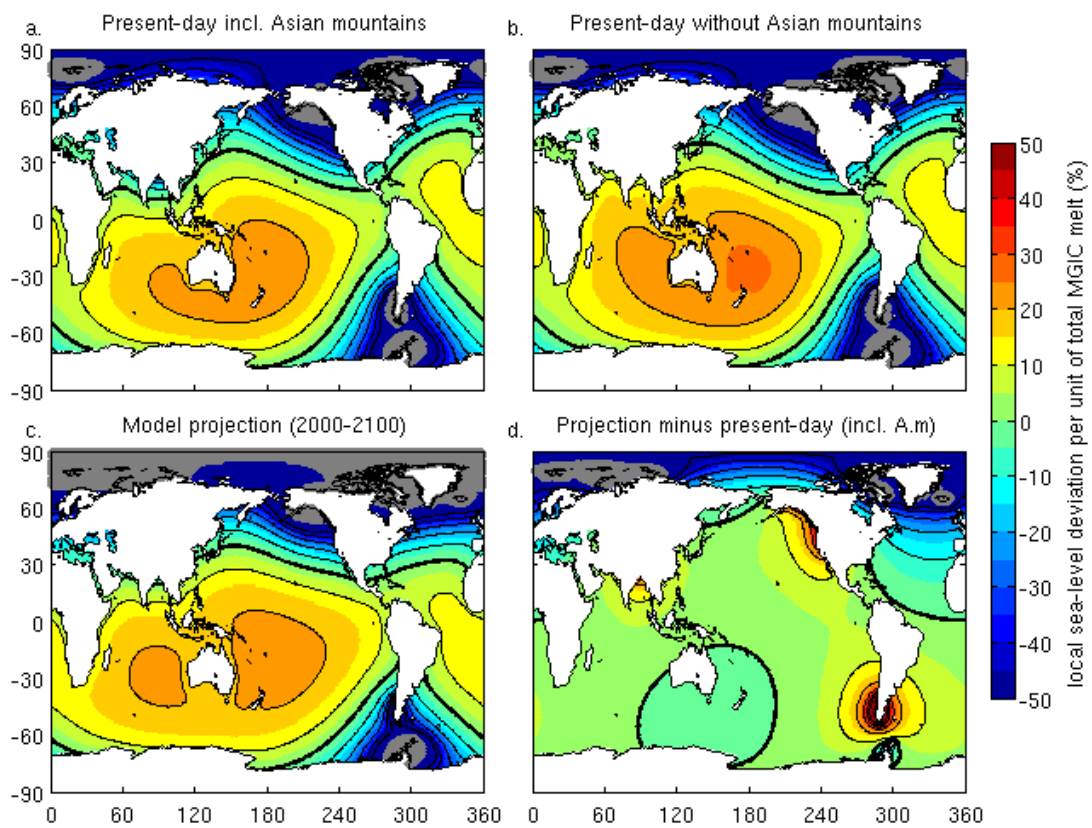
Figure S5. MGIC gravitational fingerprints (in % of total MGIC source spread uniformly across the oceans) computed after (a) observations from BR10 with an independent estimate for Asian high mountains[10], (b) BR10 alone (who did not include Asian high mountains) and (c) Radic and Hock's[7] model simulations of 21st century MGIC loss. (d) Difference between (c) and (a) (both were normalized beforehand as on the figure, because only relative loads are important for our scaling approach). Contour line intervals are every 10%. The thick black line indicates the global mean sea-level change. Gray area is less than -100%, meaning sea-level fall.
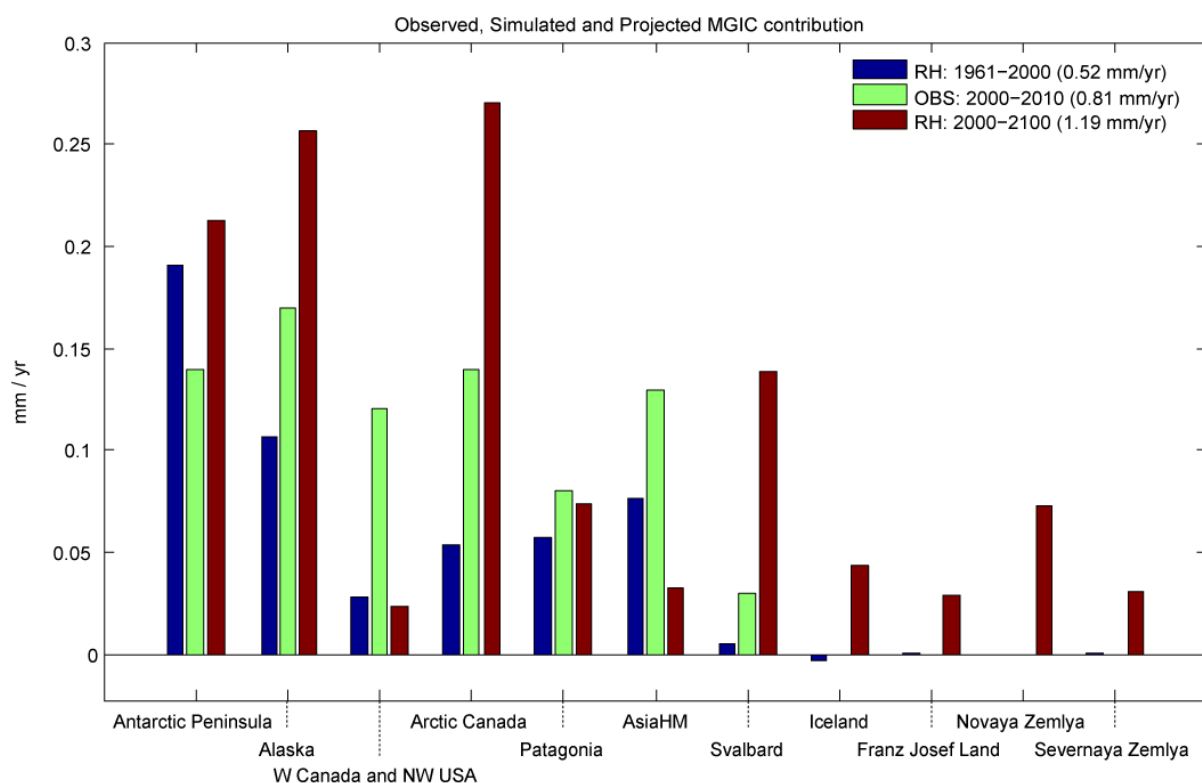
Figure S6. MGIC contribution to SLR as simulated for the past 1961-2000 period (RH11, blue), observed over the present 2000-2008 period (BR10, green) and projected over the 2000-2100 period (RH11, red). This shows that relative variations between past and present values are generally consistent with the difference in the patterns presented in Figure S5. RH11 data obtained from their table S6.

PS: The good news: Fewer fatalities from skiing accidents.
Tony McMichael